Nonlinear instabilities and filamentation of Bessel beams

Ismail Ouadghiri Idrissi

UBFC
UNIVERSITÉ
BOURGOGNE FRANCHE-COMTÉ

UFC
UNIVERSITÉ
DE FRANCHE-COMTÉ

THÈSE DE DOCTORAT DE L'ÉTABLISSEMENT UNIVERSITÉ BOURGOGNE FRANCHE-COMTÉ

PRÉPARÉE À L'UNIVERSITÉ DE FRANCHE-COMTÉ

École doctorale n°37
Sciences Pour l'Ingénieur et Microtechniques

Doctorat d'Optique et Photonique

par

ISMAIL OUADGHIRI-IDRISSI

Nonlinear instabilities and filamentation of Bessel beams

Instabilités non linéaires et filamentation des faisceaux de Bessel

Thèse présentée et soutenue à Besançon, le 10 décembre 2018

Composition du Jury :

BERNAL-ARTAJONA MARIA-PILAR	Directeur de recherche à l'Institut FEMTO-ST	Président du jury
COUAIRON ARNAUD	Directeur de recherche à l'École Polytechnique	Rapporteur
SZAMEIT ALEXANDER	Professeur à l'Université de Rostock	Rapporteur
JEDRKIEWICZ OTTAVIA	Chargé de recherche à l'Université de l'Insubrie	Examinateur
DUDLEY JOHN M.	Professeur à l'Université de Franche-Comté	Examinateur
COURVOISIER FRANÇOIS	Chargé de recherche à l'Institut FEMTO-ST	Directeur de thèse

N° | X | X | X |

école doctorale **sciences pour l'ingénieur et microtechniques**

Title: Nonlinear instabilities and filamentation of Bessel beams

Keywords: Bessel beams, filamentation, spatial beam shaping, nonlinear instabilities, filamentation modeling, laser-plasma interactions.

Abstract:

Bessel beams are solutions of Helmholtz equation. They can propagate while conserving their transverse intensity profile in space even in filamentation regime. This feature is very advantageous in high power laser applications such as plasma waveguide generation and laser ablation because they can generate homogeneous plasma channels in dielectrics. However, for moderate to low focusing conditions, Bessel pulses can sustain nonlinear instabilities, which consist in the modulation of the central core intensity along the propagation. Such a feature can prevent efficient energy deposition which hampers the applicability of Bessel pulses. The aim of this thesis is to investigate the possibility to control laser-generated plasma channels using spatially-reshaped Bessel pulses. In a first part, we have developed an experimental method based on a spatial light modulator to modify the evolution of the on-axis intensity of Bessel beams in the linear propagation regime. To study and control Kerr-induced instabilities, we developed, in a second part, a novel model based on four wave mixing interactions in Bessel beams. We have then demonstrated a novel approach to control these instabilities via on-axis intensity shaping. Bessel filamentation models in transparent media were then studied. Most models used in literature are based on nonlinear Schrödinger equation for light propagation and Drude model for laser-matter coupling. Experimental results on Bessel filamentation in glass showed propagation-invariant features in contrast with numerical simulations. Several corrections to this model were discussed. Our results show that such models are insufficient to explain our experimental results and thus the need to develop a more suitable one.

Titre : Nonlinear instabilities and filamentation of Bessel beams

Mots-clés : Faisceaux de Bessel, filamentation, Mise en forme spatial de lumière, instabilités non-linéaires, modélisation de filamentation, interaction laser-plasma.

Résumé :

Un faisceau de Bessel est un champ électromagnétique résistant à la diffraction. il peut se propager en préservant son profile transversal d'intensité même en régime de filamentation. Ceci est très avantageux pour les applications laser de haute puissance, en particulier parce qu'ils permettent de générer des canaux de plasma homogènes dans les diélectriques. Cependant, à haute intensité, les impulsions laser ultracourtes subissent, dans certaines conditions expérimentales (faible focalisation), des instabilités non linéaires entraînant la modulation d'intensité du lobe central au cours de la propagation, ce qui peut être néfaste pour ces applications comme l'usinage des matériaux transparents. L'objectif de cette thèse est de contrôler la génération de canaux de plasma par impulsions de Bessel via le contrôle du profil spatial de ces impulsions. Nous avons dans une première partie, développé une méthode expérimentale pour manipuler le profil d'intensité axiale en régime linéaire. La seconde partie concerne l'étude et le contrôle des instabilités non linéaires induites par l'effet Kerr. Nous avons développé un modèle théorique du mélange à quatre ondes dans les faisceaux de Bessel et avons démontré une nouvelle approche pour manipuler ces instabilités par une mise en forme appropriée de l'intensité axiale des faisceaux de Bessel. Nous avons ensuite étudié la validité des modèles de filamentation basés l'équation non linéaire de Schrödinger et le modèle de Drude. Les résultats expérimentaux de la filamentation des faisceaux de Bessel dans le verre ont montré un comportement invariant par propagation, contrairement aux modèles numériques. Nous avons testé et amendé les modèles de dynamiques de plasma et de propagation. Nos simulations sont comparées à des résultats expérimentaux. Nous montrons que les corrections que nous avons pu apporter par rapport à l'état de l'art sont insuffisantes et rendent nécessaire une autre forme de modèle.

UBFC UNIVERSITÉ BOURGOGNE FRANCHE-COMTÉ

Université Bourgogne Franche-Comté
32, avenue de l'Observatoire
25000 BesanÃğon, France

"One of the beautiful things about science is that it allows us to bumble along, getting it wrong time after time, and feel perfectly fine as long as we learn something each time."

Martin A. Schwartz

ACKNOWLEDGMENTS

At the end of my thesis, I would like to express my sincerest gratitude to those who helped me to accomplish my research works. I take this opportunity to thank all the researchers and lecturers in Optics department for establishing a highly educative Master program (Master PICS) which allowed me to lay a solid foundation to build my research carrier. I am really happy to be given the opportunity to work at FEMTO-ST Institute of the university of Bourgogne Franche-Comté in Besançon. The institute provides a highly satisfactory work environment which facilitates my progress.

I would like to specifically give my appreciation and thanks to my thesis supervisor François Courvoisier. I believe I would not have been able to complete my thesis if not for you. You have always been available to discuss and answer my questions. Your remarks have many times pointed out the flaws in my results and showed me the way to rectify them. You taught me many things and never hesitated to share you knowledge with me. Particularly, I will never forget your support during the hardest times when I faced my difficult issues in order to persevere until the day of the thesis defense and even afterwards. So, thank you so much. I am really indebted to you.

I sincerely thank all the members of the research team for helping in many of my tasks. A great thank to Remo Giust, a specialist in theoretical optics. Since the majority of my work concerned theoretical and numerical studies, I usually had to consult with him about the validity of my calculations and equations. I always feel at ease with him whenever I converse with him especially thank to his keen sens of humor. These discussions were very productive and allowed me to take less detours before obtaining satisfactory results.

Special thanks to Luca Furfaro, the laser engineer of our team. He accompanied me when setting-up and conducting my experiments on Bessel beam shaping. He always took the time to teach me how to behave and take precautions while dealing with high power lasers before and during experiments. I appreciate his strict attitude regarding laser manipulation which is required to avoid any possible accident.

I also would like to thank Luc Froehly, a specialist in linear Optics, for helping me in my experiments. He gave me the opportunity to use his own experimental setup. This allowed me to perform many experiments using different equipments from those in our laboratory and conduct a comparative study when analyzing my results. Moreover, I am thankful to him for taking the time to answer my questions and give me advice whenever he is available.

I am also thankful to Maxime Jacquot for his answers to my technical questions regarding beam shaping using spatial light modulators. His mastery of this domain is truly worth of praise. I specifically present my thanks to John M. Dudley for his relevant remarks regarding the papers I have submitted so far. His opinions were always spot-on and greatly facilitated the acceptance of my submitted papers. I take this occasion to re-thank him for giving me crucial points on conducting successful research works.

I present my thanks to the rest of the team members Pierre A. Lacourt, Cyril Billet, my

former fellow Ph.D students Abel Gil Villalba, Rémi Meyer, Benoit Morel and also my previous colleagues, and particularly Chen Xie and Gaurav Raj with whom I shared and discussed many of our results.

I would like to renew my thanks and appreciation to all members of the Jury for being present to evaluate my thesis works: Dr. Arnaud Couairon, Prof. Alexander Szameit and Dr. Ottavia Jedrkiewicz who took the time to come from so far away, Maria-Pilar Bernal-Artajona who presided the Jury and of course John M. Dudley and my thesis supervisor François Courvoisier.

Lastly, I warmly thank my family members, specifically my parents and brothers for their unreserved support during all these years. You never hesitated to provide help whenever needed and support me in all of my endeavors. I truly owe you so much.

Thank you all!

CONTENTS

General introduction 1

1 Bessel beams in linear and filamentation regimes 5

1.1 Non-diffracting Bessel beams . . . 5

1.1.1 Definition . . . 5

1.1.2 Apodized Bessel beams . . . 6

1.1.2.1 Diffraction-free length: Bessel zone . . . 8

1.1.2.2 Size of the central core of Bessel beams . . . 8

1.1.2.3 Self-reconstruction of Bessel beams . . . 8

1.1.2.4 Superluminal velocity of Bessel beams . . . 9

1.1.3 Experimental generation of Bessel beams . . . 9

1.1.3.1 Categories of Bessel beam generators . . . 10

1.1.3.2 Experimental realization of Bessel beams: phase and amplitude modulation . . . 10

1.1.3.3 Beam shaping instruments and experimental methods . . . 11

1.1.4 Bessel pulses . . . 15

1.1.5 Applications of Bessel beams in the linear regime . . . 17

1.2 Bessel Filamentation . . . 18

1.2.1 Brief history on filamentation . . . 18

1.2.2 Nonlinear processes involved in filamentation . . . 19

1.2.2.1 Kerr self-focusing . . . 20

1.2.2.2 Photoionization . . . 21

1.2.2.3 Plasma absorption and Avalanche ionization . . . 22

1.2.2.4 Plasma defocusing . . . 23

1.2.3 Filamentation modeling of Gaussian beams . . . 23

1.2.3.1 Modeling scenarii . . . 23

1.2.3.2 Modeling equations . . . 24

1.2.4 Bessel Filamentation . . . 25

1.2.4.1 Nonlinear Bessel beam . . . 25

1.2.4.2 Bessel filament: Nonlinear Unbalanced Bessel beam (NL-UBB) . . . 26
1.2.4.3 Filamentation regimes . . . 28
1.2.5 Applications of Bessel filamentation . . . 29
1.2.5.1 Laser-induced plasma waveguide . . . 30
1.2.5.2 Electric discharge guiding . . . 31
1.2.5.3 Generation of THz radiation . . . 32
1.2.6 Bessel filamentation and Laser micro-nano machining . . . 33
1.2.6.1 Physical processes of laser interaction with transparent materials . . . 34
1.2.6.2 High aspect ratio laser processing . . . 35
1.3 Contributions of my thesis . . . 37
1.3.1 On-axis intensity shaping of Bessel beams . . . 37
1.3.2 Control of nonlinear instabilities in unsteady Bessel filaments . . . 37
1.3.3 Modeling of Bessel filamentation . . . 38

2 Arbitrary on-axis intensity shaping of Bessel beams 39
2.1 Theoretical background . . . 40
2.2 Spatial amplitude and phase shaping using a single SLM . . . 42
2.2.1 Fourier-space beam shaping . . . 42
2.2.2 Direct-space beam shaping . . . 43
2.3 Our experimental approach . . . 45
2.3.1 Experimental setup . . . 45
2.3.2 Computation of the phase mask . . . 46
2.3.2.1 The expression of the light field at the first diffraction order 47
2.3.2.2 The expression of the functions M and F . . . 48
2.4 Theoretical and numerical analysis . . . 49
2.4.1 Plane wave spectrum and wave propagation . . . 50
2.4.1.1 Field decomposition into plane waves . . . 50
2.4.1.2 Plane wave propagation . . . 51
2.4.1.3 Reconstruction of the light field along propagation . . . 51
2.4.2 Physically realizable target fields . . . 52
2.4.2.1 Effect of spectral truncation on retrieved on-axis intensity profiles . . . 52
2.4.2.2 Constraints on the target intensity profile . . . 53
2.4.2.3 Constraints on the geometrical parameters . . . 55

2.4.2.4 Limitations imposed by the SLM . . . 56
2.5 Numerical and experimental results . . . 56
2.5.1 Numerical simulation results . . . 57
2.5.1.1 Computation of the phase mask used in experiments . . . 57
2.5.1.2 Evolution of the Bessel beam generated by the SLM . . . 57
2.5.1.3 Impact of the encryption method . . . 59
2.5.2 Experimental results and discussion . . . 60
2.6 Conclusion . . . 62

3 Nonlinear dynamics and control of Kerr-induced instabilities in Bessel beams 63

Introduction . . . 63
3.1 Theoretical background . . . 65
3.1.1 Third order nonlinear polarization . . . 65
3.1.2 Reduced FWM model . . . 67
3.1.2.1 Derivation of Helmholtz equation . . . 67
3.1.2.2 Derivation of Helmholtz equation for $\theta_4 = 0$ . . . 69
3.1.2.3 Normalized propagation equation . . . 69
3.1.3 Analysis of the TPM integral . . . 70
3.1.3.1 Numerical computation . . . 71
3.1.3.2 Analytical computation . . . 72
3.2 Analysis of Kerr-induced instabilities in Bessel beams . . . 75
3.2.1 Numerical simulation model in a pure Kerr medium . . . 76
3.2.2 Numerical simulation results . . . 77
3.2.3 Interpretation of new frequency generation . . . 78
3.2.3.1 Description of the theory of Ref. [Gadonas et al., 2001] . . . 79
3.2.3.2 First approximation: Generation of the axial wave seed . . . 80
3.2.3.3 Second approximation: growth of new spectral components 82
3.2.4 Interpretation of longitudinal intensity modulation . . . 86
3.2.5 Summary . . . 87
3.3 Soft and abrupt intensity transitions . . . 88
3.3.1 Numerical analysis . . . 89
3.3.2 Intuitive interpretation . . . 90
3.3.3 Theoretical analysis . . . 92
3.3.3.1 Theoretical considerations . . . 92

3.3.3.2 First approximation: impact on axial wave seed 93
3.3.3.3 First approximation: cascaded feature of spectral broadening 95
3.3.3.4 Second approximation: growth of unstable modes 96
3.3.4 Summary 98
3.4 Control of nonlinear instabilities using shaped intensity profiles 100
3.4.1 Numerical simulation results 100
3.4.2 Intuitive interpretation 101
3.4.3 Theoretical analysis 103
3.4.4 Control of the growth of unstable modes (second approximation) . . 105
3.4.5 Summary 106
3.5 Bessel filamentation using shaped longitudinal intensity profiles 107
3.5.1 Filamentation model 107
3.5.2 Decrease of the critical intensity above which MPA prevails over Kerr effect 109
3.5.3 Control of laser-induced plasma channels 110
Conclusions 111

4 Filamentation of Bessel beams 113
4.1 Filamentation modeling 114
4.1.1 Nonlinear propagation equations and related approximations 115
4.1.1.1 Scalar wave equation 115
4.1.1.2 Nonlinear envelope equation 116
4.1.2 Laser-matter coupling terms of nonlinear propagation equation . . . 117
4.1.2.1 Nonlinear polarization 117
4.1.2.2 Nonlinear absorption 117
4.1.2.3 Plasma current density 118
4.1.2.4 Equation of plasma density evolution in time and avalanche ionization 119
4.2 Bessel filamentation in fused silica: experiments and simulation 120
4.2.1 Experimental results 120
4.2.1.1 Experimental setup and methodology 120
4.2.1.2 Experimental parameters and results 121
4.2.2 Numerical results and discussion 122
4.2.2.1 Filamentation model and improvements 122
4.2.2.2 Numerical model and parameters 124

4.2.2.3 Results for an input energy of 0.26 μJ 125
4.2.2.4 Results for an input energy of 0.72 μJ 126
4.3 Conclusions 132

Conclusion and perspectives **135**

Appendix of chapter 2 **149**
2.A Demonstration of the light field expression at the first diffraction order 149
2.B Analytical computation of the spatial spectrum 150
Case of a flat-top profile with parabolic ramps 151
Case of a linear ramp profile with parabolic decay 151

Appendix of chapter 3 **153**
3.A. Derivation of Helmholtz equation for a J_0 function 153
3.B Analytical computation of a TPM integral defined for $\beta_1 = \beta_2$ and $\beta_3 = \beta_4$ . . . 154
3.C Expression of the idler wave for two-frequency pump and signal waves . . . 156

Bibliography **168**

GENERAL INTRODUCTION

The advent of ultrafast lasers, which is a generic term for picosecond and femtosecond lasers, has opened the way to numerous fields for research and applications in physics, materials science, chemistry, biology, materials processing among others. The high power that such lasers generate has brought light-matter interactions to new heights. Of particular interest, experiments on the interaction of pulsed laser beams with transparent media showed an increase in light intensity along the beam propagation. This effect, called Kerr self-focusing, has caught a major interest and was extensively studied since such an effect allows to overcome transverse intensity spreading of light beams as dictated by linear diffraction. Indeed, a conventional light beam, called Gaussian beam, can only remain localized in space over a short distance called Rayleigh length. In this regard, these experiments showed that Kerr self-focusing yields transversely-localized light beams in space that are formed over propagation distances higher than Rayleigh length. Such a phenomenon was referred to as "filamentation" [Shen, 1975].

Light filaments formed using laser pulses with durations lower than a hundred of picoseconds were relatively small in length. The advent of femtosecond light sources in 1980s allowed the discovery of unprecedented regimes of light-matter interactions and filamentation. In 1995, Braun et al. discovered that high intensity ultrafast pulses remain focused in air over distances greater than 20 m. Other experiments showed that 2-kilometer long filaments could be formed in air [Couairon et al., 2007]. These results have opened the way to novel potential applications such LIDAR (Light Detection And Ranging) [Iwasaki et al., 2003], plasma waveguide generation [Durfee et al., 1993], controlled electric discharge [Clerici et al., 2015], THz radiation [Bitman et al., 2012] or high aspect ratio laser machining [Tzortzakis et al., 2001].

Numerous studies on the filamentation of femtosecond Gaussian beams were reported [Couairon et al., 2007]. The process of Gaussian filament formation involves many linear and nonlinear effects, specifically diffraction, dispersion, Kerr self-focusing, nonlinear absorption and plasma defocusing. As light intensity increases due to Kerr self-focusing, the probability of nonlinear absorption becomes greater and leads to the generation of a plasma of free-electron-holes. This plasma plays the role of a defocusing lens and attenuate light intensity. Kerr self-focusing can be triggered afterwards if the light field remains sufficiently intense. A long filament can then be formed as a result of the interplay between these focusing and defocusing effects [Couairon et al., 2007].

Although Gaussian filaments are widely used, they have drawbacks which hamper their applicability. The formation of Gaussian filaments involves spatio-temporal dynamics which makes it difficult to control. Hence in applications where the generation of uniform plasma channels is needed such as materials processing [Courvoisier et al., 2016b], the use of Gaussian filaments is limited. In this regard, spatial beam shaping into Bessel light modes has emerged as an alternative to Gaussian beams [Polesana et al., 2008]. Indeed, the above described filamentation process involves pronounced spatio-temporal

dynamics which reshape input Gaussian pulses into light fields with conical waveform similar to that of Bessel pulses. Hence, Gaussian pulses, initially shaped into Bessel pulses, sustain less spatio-temporal dynamics and can propagate according to a propagation-invariant regime.

Bessel beams were proposed as a propagation-invariant solution to Helmholtz equation in linear propagation regime and thus they are diffraction-free [Durnin, 1987]. By definition, a Bessel beam is made of the superposition of plane waves propagation along the surface of a cone making the same angle with the propagation axis. Its transverse amplitude profile consists of an intense central core surrounded be several peripheral rings of lower intensity. In practice, Bessel beams can only be generated over limited propagation length where they can preserve their diffraction-resistant properties.

The use input Bessel beams as an alternative to conventional Gaussian beams was proposed before 1990. The long line focus of axicon-focused laser pulses was extremely attractive to generate uniform plasma channels over many Rayleigh lengths. For instance, Bunkin et al. used axicon-focused nanosecond laser beams in their experiments to generate long and uniform laser sparks (laser-generated-plasma of free-electrons in air or generally in gases) [Bunkin et al., 1983]. In contrast, laser sparks engendered by input Gaussian pulses were non-uniform and more limited in spatial extent. The advantages of Bessel beams over Gaussian beams were reported in many fields of applications such high aspect ratio machining, materials processing, generation of THz radiation and plasma waveguides, etc. However, depending on laser and geometrical parameters, Bessel beams can undergo nonlinear instabilities leading to strong intensity modulation of the central core of Bessel beams along propagation [Polesana et al., 2007, Cooley et al., 2006]. Such a feature hampers the applicability of Bessel pulses, for example, in the generation of uniform plasma waveguides in gases and high aspect ratio nano-holes in transparent solids [Gaizauskas et al., 2006].

This thesis has been conducted in the framework of spatial beam shaping of high power laser pulses and its application in micro-nano ablation of transparent materials. Our group has previously demonstrated that a single pulsed Bessel beam can realize ablation traces with an aspect ratio higher than 100:1 [Bhuyan et al., 2010]. Actually, these results were obtained for Bessel beams with high cone angles, typically superior to 9° in glass. However, for Bessel beams with lower cone angles, for which longer plasma channels can be generated, the above mentioned nonlinear instabilities take place, which may prevent the generation of uniform ablation traces. For this reason, and by means of spatial beam shaping of Bessel pulses, we aim to investigate the possibility to reduce the extent of nonlinear instabilities and control the uniformity of laser-generated plasma channels.

My thesis consists of four chapters. The first describes Bessel beams, their experimental generation, their properties in linear and nonlinear regimes and their applications. We will review the main advantages of Bessel beams over conventional Gaussian beams in different applications. Nonlinear instabilities in Bessel beams will also be discussed. We will present their causes and the solutions proposed in previous works to mitigate their extent.

To introduce our approach in controlling nonlinear instabilities using beam shaping, we first need to develop an experimental approach suitable for the above mentioned applications. In fact, the central core intensity of conventional Bessel beams varies along propa-

gation. It usually has a bell-shaped evolution, which, as we will see, predetermines their nonlinear propagation behavior. Hence, our approach consists in controlling the central intensity at each point of the propagation distance. In the second chapter, we will therefore present numerical and experimental results on on-axis intensity shaping of Bessel beams using spatial light modulator. We show that our experimental technique ensures a relatively high energy throughput which is suitable for high power laser applications.

In the third chapter, we will present theoretical and numerical studies on nonlinear instabilities in Bessel beams and their control using on-axis intensity shaping. To this end, we developed a theoretical model based on four wave mixing interactions. This model allows to unravel the major features occurring in the unsteady nonlinear propagation regime, i.e. where nonlinear instabilities arise. Afterwards, we will recall how nonlinear instabilities can be controlled as reported in the literature and use our model for further investigation. We will discuss the possibility to control the growth of nonlinear instabilities by suitable on-axis intensity shaping of Bessel beams in pure Kerr media and show that our results are also valid in the filamentation regime where plasma is generated.

Finally, we will study the modeling of Bessel filamentation in transparent media in the case of high angle focusing. Experimental results obtained by our group show that high-angle Bessel beams are stationary and remain highly focused even at ablation-level intensities. However, these results could not be reproduced numerically: simulation results show that Bessel beams undergo significant transverse spreading in space. After recalling the derivation of the nonlinear Schrödinger equation (NLSE), we propose several possible corrections.

1

BESSEL BEAMS IN LINEAR AND FILAMENTATION REGIMES

Bessel beams are a special class of diffraction-free beams. While conventional light fields, such as Gaussian beams, are bound to transversely spread along propagation, Bessel beams can propagate while conserving an invariant transverse beam shape. Indeed, Bessel beams were found to be an exact solution to light propagation equation in free space. However, this is only valid in infinite space where the transverse beam intensity has no physical limit. Hence, ideal Bessel beams, which consequently carry infinite energy, are physically non-realizable. In practice, only approximated versions of Bessel beams can be realized. Experimentally-generated Bessel beams present many interesting properties, particularly long and localized focus volume and self-healing features, which have found a wide range of applications.

In this thesis, my work concerns the applications of Bessel pulses in high power laser applications, and particularly laser micro-nano machining. In such applications, use is made of invariant-propagation regimes of filamentation which allow a coherent energy deposition of the Bessel pulse in nonlinear samples.

In the first section, I shall review Bessel beams, their properties and present some of their applications in the linear propagation regime.

In the second section, I will discuss the different properties and features of Bessel filaments in nonlinear Kerr media and present some of their different applications. Then, I will specifically discuss the application of Bessel pulses in plasma shaping and present the outline of my work in this field.

1.1/ NON-DIFFRACTING BESSEL BEAMS

1.1.1/ DEFINITION

In linear physics, the propagation of light in free space is characterized by diffraction. Any light field with finite transverse intensity distribution can undergo transverse spreading along the propagation direction. Taking for example a Gaussian beam with a beam waist w_0 and a wavelength λ, the distance at which it can remain transversely localized in space before spreading is given by Rayleigh length $D_R = \pi w_0^2/\lambda$. However, there exists special types of optical waves which are intrinsically immune to diffraction. These

optical waves are referred to as nondiffracting beams. They are theoretically introduced as beam-like exact solutions of the propagation equation with a propagation-invariant transverse intensity.

Let's consider the scalar propagation equation in vacuum given by:

$$(\frac{\partial^2}{\partial z^2} + \Delta_\perp - \frac{1}{c^2}\frac{\partial^2}{\partial t^2})E(x,y,z,t) = 0 \tag{1.1}$$

where $\Delta_\perp$ is the transverse laplacian characterizing the transverse variation of the optical field $E(x,y,z,t)$; (x,y) refer to the transverse variables, z is the longitudinal coordinate, t is the time variable and c is the vacuum light velocity. Propagation-invariant solutions to this equation account for optical fields whose time averaged intensity $I(x,y,z) \propto |E(x,y,z,t)|^2$ is constant along propagation. We consider monochromatic solutions in the form $E(x,y,z,t) = A(x,y)\exp[i(k_z z - \omega t)]$ where k_z and ω are the longitudinal spatial frequency (propagation constant) and angular frequency respectively. Durnin has introduced Bessel beams as cylindrically-symmetric and monochromatic wave solutions whose field amplitude $A(x,y)$ takes the form of the zeroth order Bessel function of the first kind J_0 as follows [Durnin, 1987]:

$$E(x,y,z,t) = \exp[i(k_z z - \omega t)] \int_0^{2\pi} \exp[ik_r(x\cos\phi + y\cos\phi)]\frac{\mathrm{d}\,\phi}{2\pi} \tag{1.2}$$

$$E(x,y,z,t) = \exp[i(k_z z - \omega t)]\, J_0(k_r r) \tag{1.3}$$

where ϕ is the azimuth angle, $r = \sqrt{x^2+y^2}$ is the radial coordinate and k_r is the corresponding transverse spatial frequency such as the wavevector k of the beam is written as $k^2 = k_r^2 + k_z^2$.

Equation (1.2) shows that a Bessel beam is formed by the superposition of an infinite number of plane waves propagating at different azimuth angles ϕ and forming the same angle with the propagation axis z. This angle, denoted the cone angle θ, is defined as a function of the spatial frequency k_r as follows: $\theta = \mathrm{asin}(k/k_r)$. This superposition yields a propagation-invariant interference pattern which consists of an intense central core surrounded by multiple secondary rings of lower intensity (see Fig. (1.1,left)). In the far field, Bessel beams take the form of a ring of radius k_r (see Fig. (1.1,right)). For an ideal J_0 beam, it can be represented by Dirac function which corresponds to the inverse Hankel transform of the function J_0. For experimentally-generated Bessel beams, the spectral distribution is centered around the central frequency $k_{r0} = k\sin(\theta)$ with a width that is inversely proportional to the aperture radius.

1.1.2/ APODIZED BESSEL BEAMS

The nondiffracting wave solution presented in the previous section is only valid in infinite space. Indeed, the energy contained in a J_0 Bessel beam is infinite and thus it cannot be realized physically. This stems from the fact that a Bessel beam has an infinite number of secondary rings, each carrying the same amount of energy as that contained in the central core [Durnin, 1987].

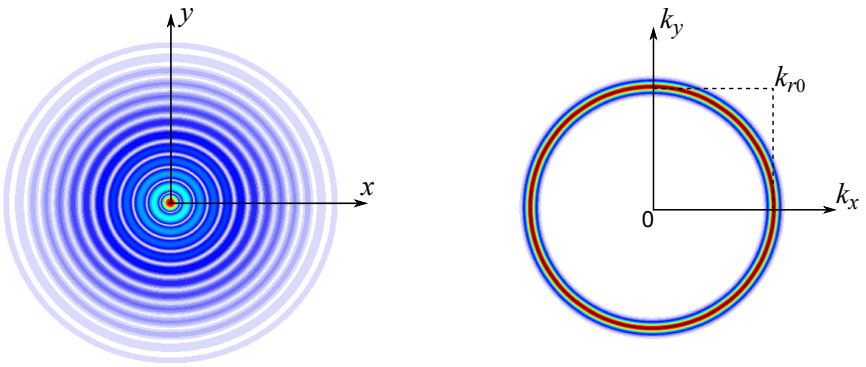

Figure 1.1: Transverse spatial distribution of Bessel beam in (left) near and (right) far fields.

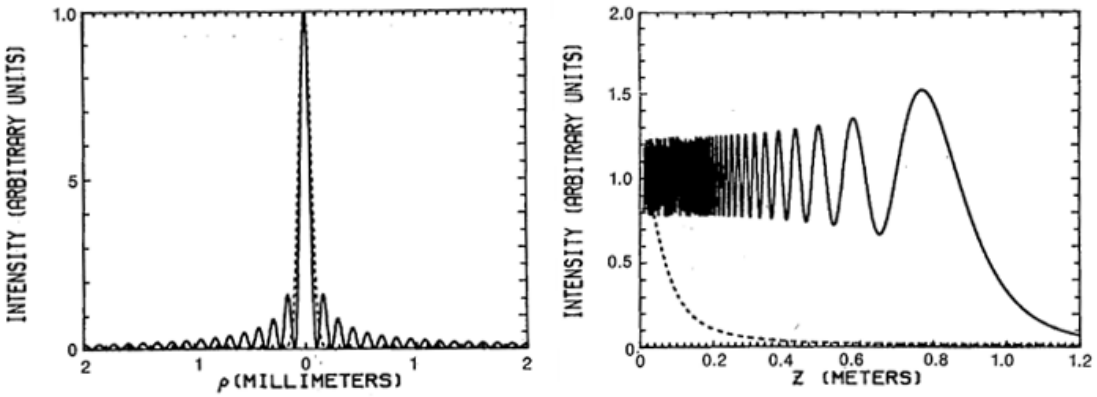

Figure 1.2: Transverse intensity distribution of a Bessel beam (solid line) and Gaussian beam (dashed line) whose width is equal to that of the Bessel central core. (right) On-axis intensity evolution of (solid line) an apertured Bessel beam and (dashed line) a Gaussian beam. [From Ref. [Durnin, 1987]].

To physically realize a Bessel beam, a spatial truncation of the beam is required. Durnin performed a numerical study on the propagation of apodized Bessel beams and compared simulation results with those of Gaussian beam propagation [Durnin, 1987]. He considered a Bessel beam truncated at an aperture radius of 2 mm. Its main lobe Full Width at Half Maximum (FWHM) is chosen to be initially (at a plane $z = 0$) identical to that of the Gaussian beam and is equal to $100\ \mu m$ as shown in Fig. (1.2,left).

Figure (1.2,right) shows the evolution along propagation of the central core intensity of both beams. Over a long propagation distance, the on-axis intensity of the Bessel beam oscillates around its initial value (at $z = 0$) with a decreasing frequency. Most importantly, the Bessel beam maintains an invariant spot size of the central core and only drops in intensity at a propagation distance of about $z = 1$ m. In contrast, the Gaussian beam exhibits a noticeable intensity decay at about 1 cm which corresponds to its Rayleigh length. Thus, even though the spatial apodization of Bessel beams leads to the reappearance of diffraction effects, a truncated Bessel beam can still maintain its nondiffracting properties over a propagation length that can be several orders of magnitudes higher than the Rayleigh length corresponding to its main lobe size.

1.1.2.1/ DIFFRACTION-FREE LENGTH: BESSEL ZONE

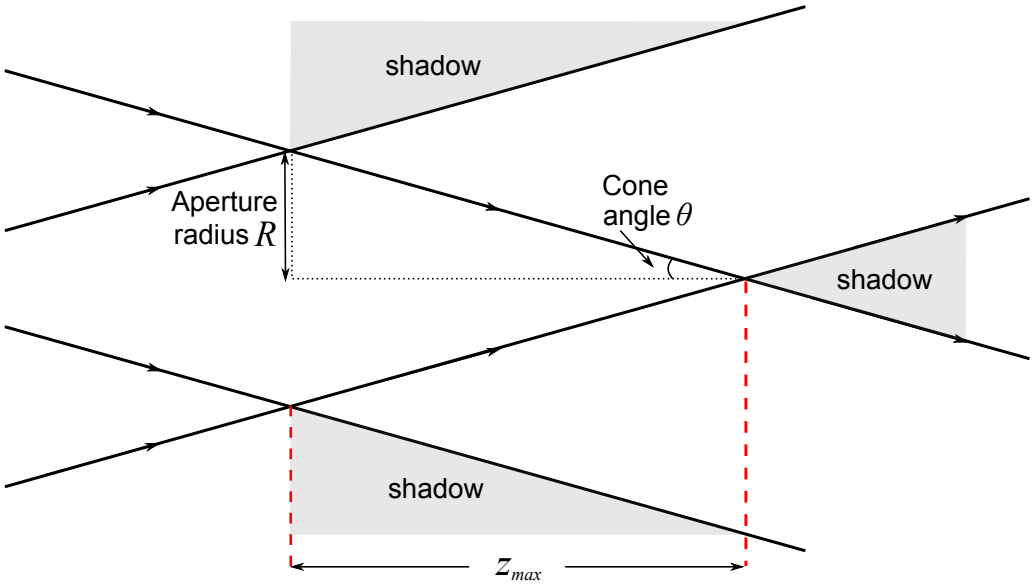

Figure 1.3: Geometrical estimation of the Bessel zone. [After Ref. [Durnin, 1987]].

Numerical simulations thus show that Bessel beams with finite aperture can remain focused over a longer propagation distance compared to Gaussian beams. This diffraction-free length, termed "Bessel zone", can be estimated geometrically as shown in Fig. (1.3) [Durnin, 1987]. We recall that a Bessel beam is made of the interference of infinite number of plane waves that all cross the optical axis at an angle θ. The fact that a Bessel beam is truncated means that the range at which their interference takes place is limited by the size of the aperture. Moreover, their interference extent will also depend on their angle of incidence at the aperture, i.e. the cone angle θ. Thus, one can define the Bessel zone, denoted z_{max}, as the propagation range where the truncated plane waves interfere. For an aperture of radius R, the Bessel zone can be geometrically estimated by the relation:

$$z_{max} \approx R/\tan(\theta) \tag{1.4}$$

Contrary to Gaussian beams whose Rayleigh length is geometrically determined by the beam waist, Bessel beams offer two degrees of freedom to define the Bessel zone.

1.1.2.2/ SIZE OF THE CENTRAL CORE OF BESSEL BEAMS

The Full Width at Half Maximum (FWHM) of the central core of Bessel beams is given by: $W = 2.27/k_{r0}$ [Tiwari et al., 2012] . Thus, the central core size does not depend on the aperture radius which allows preserving the nondiffracting length of Bessel beams with the possibility of decreasing the central core diameter.

1.1.2.3/ SELF-RECONSTRUCTION OF BESSEL BEAMS

One can view the long focus volume of Bessel beams as a quasi-homogeneous energy distribution along the propagation distance because of their conical flow of energy. At a

given propagation distance z_1, only a portion of the plane waves, constructing the Bessel beam, interfere at the central core while the other portion gives rise to the side lobes. Then, at a point $z_1 + \mathrm{d}z$, it is the interference of another portion of plane waves that gives rise to the central core. In other words, the photons generating the central core at the point z_1 are not the same as those generating it at the point $z_1 + \mathrm{d}z$. Consequently, if one were to put an obstacle at the point z_1, then the Bessel beam will be blocked at this point but will inevitably be reconstructed at a later point $z_2 = z_1 + \Delta z$, as shown in Fig. (1.4). This gives rise to the self-reconstruction or self-healing property of Bessel beams.

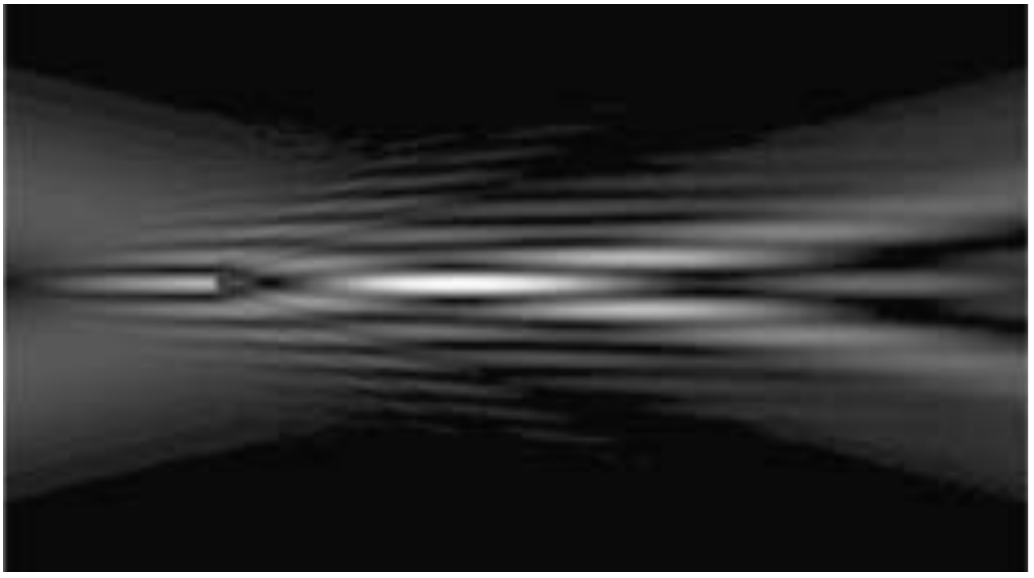

Figure 1.4: Self-reconstruction property of Bessel beams. [From Ref. [McGloin et al., 2005]]

1.1.2.4/ SUPERLUMINAL VELOCITY OF BESSEL BEAMS

Thanks to its conical structure, the wavefront of a Bessel beam is tilted with respect to the propagation axis at an angle θ (the cone angle). Hence, the phase velocity of Bessel beams, given by the relation $v_\phi = \omega/k_z = c/\cos(\theta)$, is higher than light velocity. The phase velocity is then termed "superluminal". However, this effect is merely geometrical and only applies to the apparent speed of the central core intensity. Indeed, considering the conical superposition of plane waves, the central core of Bessel beams is seen to move faster than the light velocity. Nonetheless, the energy flow of the beam remains subluminal and thus no information can be transmitted at the superluminal velocity of the wavepacket generated on the optical axis [McGloin et al., 2005, Saari et al., 1997].

1.1.3/ EXPERIMENTAL GENERATION OF BESSEL BEAMS

Since Durnin first introduced the nondiffracting Bessel beams and their potential applications, many techniques have been developed in order to experimentally generate these optical fields and study their properties.

1.1.3.1/ CATEGORIES OF BESSEL BEAM GENERATORS

Bessel beam generation methods consist in transforming an input light field into the desired spatial distribution of Bessel beams. Generally, the aim is to produce a superposition of plane waves propagating on a cone which would form a Bessel beam. In practice, there are two different ways to achieve this conical interference:

Direct-space beam shaping: The first approach aims to directly transform the wavefront of an incident beam into a conical one. This allows generating an approximation of the transverse distribution of a J_0 Bessel function that is a characteristic of a Bessel beam in real space. Hence, this approach is termed "Direct-space shaping".

Fourier-space beam shaping: In contrast with direct-space shaping, this approach allows generating a Bessel beam according to a two-step process. The first step consists in shaping the transverse intensity profile of an incident beam into a ring-like pattern which is equivalent to a Bessel beam distribution in the far-field. The next step lies in transforming the ring-like shape into a J_0 Bessel function distribution using the Fourier transform property of lenses in the paraxial regime [Durnin et al., 1989].

1.1.3.2/ EXPERIMENTAL REALIZATION OF BESSEL BEAMS: PHASE AND AMPLITUDE MODULATION

Any light field can be defined by its amplitude and phase distributions. In practice, whether it is space- or Fourier-space beam shaping, both can be performed by applying either an amplitude or phase modulation (or both) to an incident beam.

Phase-only modulation: This modulation type is usually more adapted to direct-space beam shaping. The formation of a Bessel beam can be achieved by applying an azimuthally-symmetric phase $\Phi(r)$ to an input light field. An example of experimental schemes for Bessel beam generation is described in Fig. (1.5). In this scheme, an input beam, of complex amplitude U_{inc}, passes through an optical system which contains the desired spatial phase $\Phi(r)$. At the output of this optical system, the incident beam will acquire a conical wavefront which can be described by a transmission function that is expressed as $\exp(i\,\Phi(r))$. Hence, the resulting field U_{out} is given by:

$$U_{out} = U_{inc}\exp(i\,\Phi(r)) \tag{1.5}$$

The longitudinal extent of the beam (Bessel zone) is constrained by both the numerical aperture of the optical system and the radius of the incoming beam.

Amplitude-only modulation: In opposition to phase-only modulation, amplitude-only modulation is usually used for Fourier-space beam shaping. An example of experimental configuration is presented in Fig. (1.6). An amplitude mask is firstly applied to an input beam in order to shape its transverse intensity into a ring-like pattern. Then, by using Fourier transformation, the ring beam can be transformed into the target Bessel beam.

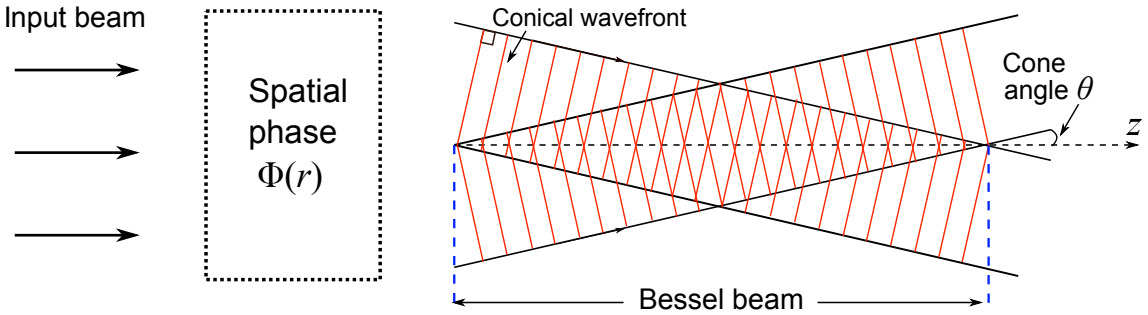

Figure 1.5: Experimental scheme for Direct-space Bessel beam generation using phase-only modulation.

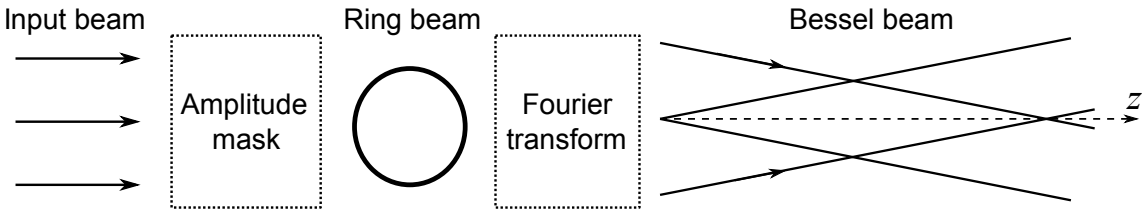

Figure 1.6: Experimental scheme for Fourier-space Bessel beam generation using amplitude-only modulation.

Note that simultaneous modulation of both amplitude and phase can also be performed. This point will be discussed in the chapter 2.

1.1.3.3/ BEAM SHAPING INSTRUMENTS AND EXPERIMENTAL METHODS

Many instruments have been proposed to generate Bessel beams such as holograms [Turunen et al., 1988], spatial light modulators [Davis et al., 1993, Froehly et al., 2014], axicons [Polesana et al., 2007], digital micro-mirror devices [Gong et al., 2013] and optical fibers [Steinvurzel et al., 2011]. Other techniques are based on more sophisticated procedures such thermal nonlinear optical effects [Zhang et al., 2014]. In the following, we will present the major experimental methods used in previous works, especially those largely used in high power laser applications. We will specifically describe these techniques according to the above described beam shaping categories .

Circular slit at the back focal plane of a lens: This experimental method was first introduced by Durnin et al. [Durnin et al., 1989]. It allows the generation of Bessel beams from Fourier space using amplitude-only modulation [Durnin et al., 1989]. The experimental setup is described in Fig. (1.7). It consists of an annular aperture with a diameter d and a width Δd. It is placed at the back focal plane of a lens of a focal distance f and a radius R. An incident beam passing through the slit will be shaped into a ring beam. The lens will then perform a Fourier transform of the ring beam to generate an approximation of a J_0 beam with a cone angle $\theta = \tan^{-1}(d/2f)$.

However, the energy throughput of this method is considerably low since most of the energy is blocked at the annular aperture. Furthermore, the quality of the constructed Bessel beam depends on the width of the aperture Δd. Normally, the incident light am-

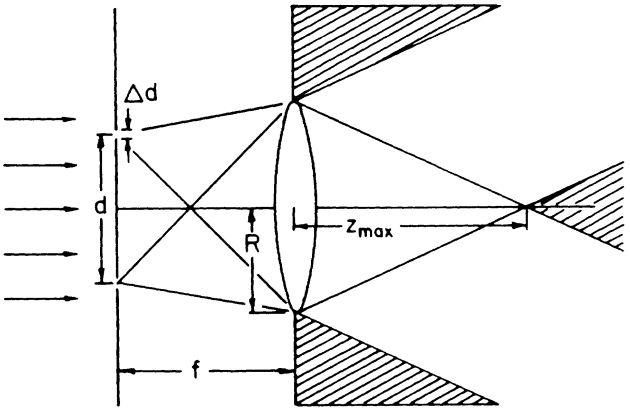

Figure 1.7: Bessel beam generator based on a annular aperture placed at the object focal plane of a lens. [From Ref. [Durnin et al., 1989]]

plitude will be modulated after passing the annular slit and this modulation can only be negligible in case $\Delta d \ll \lambda f/R$ [Durnin et al., 1989]. Thus, this approach is less used in practice, especially in high power laser applications.

Axicons: An axicon is an optical element that is manufactured in the form of a glass cone. It was first introduced by Mcleod as a means to construct images from a given source over a continuous straight line [McLeod, 1954, McLeod, 1960]. Even before the introduction of J_0 beams by Durnin et al., axicons had already been used as an alternative to conventional lenses since laser beams focused by this optical element (axicon) have a long focus volume [Bunkin et al., 1983].

Axicons allow the generation of Bessel beams in direct space via phase-only modulation. Thanks to its conical form, an incident beam passing through an axicon, with a base angle γ and a refraction index n_{ax}, will acquire an axisymmetric linear phase in the form:

$$\Phi(r) = -2\pi \sin[\theta(\gamma, n_{ax})]\, r/\lambda \tag{1.6}$$

Thus, the optical field at the output of the axicon will have an axially symmetric wavefront making an angle θ with the propagation axis, which generates an approximation of a J_0 beam, as depicted in Fig. (1.8). The value of θ is obtained using the Snell law $\sin(\gamma + \theta) = n_{ax} \sin(\gamma)$ [Polesana et al., 2008].

Axicons, and specifically refractive axicons, have the property to generate Bessel beams from incident Gaussian beams with a very high energy throughput, and thus they have been largely used in high power laser applications, such as materials processing [Courvoisier et al., 2016b]. However, manufactured axicons may suffer from some imperfections, especially at the axicon tip, which cause the generated-Bessel-beams to undergo on-axis intensity modulations [Čižmár et al., 2009]. Such undesired features can be avoided using spatial filtering as reported in [Čižmár et al., 2008].

Holographic optical elements: Holography was first introduced by Gabor in 1948 as an imaging technique. In contrast to photography where only intensity information of an object is recorded, holography allows recording both amplitude and phase information.

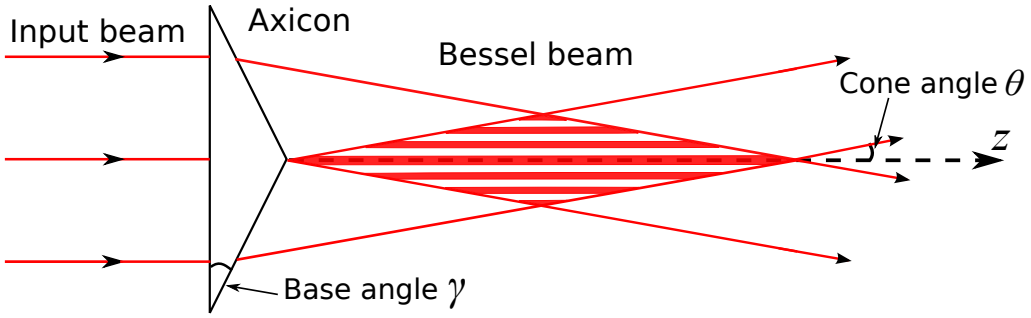

Figure 1.8: Bessel beam generation using an axicon.

The principle of holography can be described as follows: the object to be imaged is illuminated by a coherent light source (laser). Then, the reflected light (object beam) is superposed to another light beam of the same wavelength which has not seen the object (reference beam). This superposition yields an interference pattern which contains information on the amplitude and phase of the object beam. Then, this pattern, called hologram, is recorded on an appropriate material. To reconstruct the wavefront of the object beam, one simply needs to illuminate the recorded hologram by the reference beam [N.Kim et al., 2017].

The concept of holography was further extended to computer (or digital) holography where holograms can be designed by computer. A major property of computer holography is that the object is not necessary to construct a hologram [Tricoles, 1987]. One can design an ideal wavefront and, by means of numerical simulation of light propagation theory, it is possible to record numerical data of the corresponding hologram. This type of holograms is referred to as Computer Generated Hologram (CGH) [Tricoles, 1987]. Computer holography can be used to design and fabricate optical elements by recording CGHs into an appropriate material. Such optical elements are called holographic optical elements (HOEs) [Kim et al., 2009].

HOEs have been largely used in a wide range of applications and particularly as Bessel beam generators [Turunen et al., 1988, Vasara et al., 1989, Cox et al., 1991, Paterson et al., 1996]. In this regard, the wavefront information to be recorded is a spatial phase distribution that is identical to that applied by an axicon. However, in contrast to the continuous phase distribution of an axicon, information in holograms takes the form of a fringe-like pattern. Therefore, Bessel beam generators based on holograms are often referred to as "diffractive axicons".

There are different types of holograms depending on the mode of information transmission to an incident laser light. In Ref. [Turunen et al., 1988], Turunen et al. proposed a Bessel beam generator where the desired beam wavefront is recorded on an amplitude-binary hologram according to the experimental scheme depicted in Fig. (1.5). Similarly to axicons, it acts as a transmission function described by a multiplicative complex function in the form $\exp(i\Phi(r))$ where $\Phi(r)$ is defined by Eq. (1.6).

In this example, the hologram takes the form of concentric rings whose width depends on the geometrical parameters of the target field as shown in Fig. (1.9,left). However, note that because of the fringe pattern of holograms, the light field passing through the hologram will be diffracted at different diffraction orders [Vasara et al., 1989]. As a result, the energy conversion of holographic elements is generally lower than that provided by

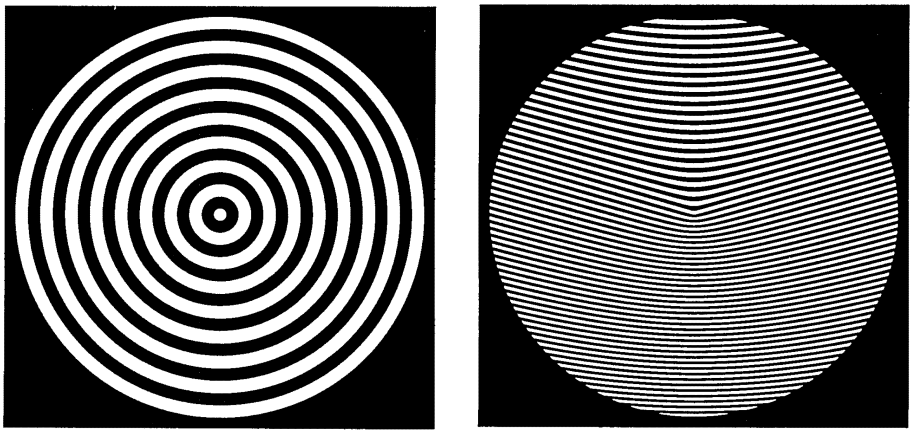

Figure 1.9: Example of a binary-amplitude hologram for Bessel beam generation (left) without and (right) with carrier frequency. [from Ref. [Vasara et al., 1989]]

axicons. To obtain a good beam quality, spatial filtering is required in order to separate the diffraction order which contains the target light information from the others. Generally, this spatial filtering can be performed by adding a linear phase ramp (or a carrier frequency [Vasara et al., 1989]) to the hologram. An example of holograms with carrier frequency is shown in Fig. (1.9,right).

Regarding the diffraction efficiency of the target diffraction order, it is of the order of $10\ \%$ for binary-amplitude holograms. Generally phase holograms are mostly used to generate Bessel beams since not only they provide a higher diffraction efficiency ($\approx\ 40\%$) [Vasara et al., 1989], but also higher quality Bessel beams. Of particular interest, blazed holograms can potentially provide a diffraction efficiency close to 100% [Turunen et al., 1988]. However, this largely depends on the manufacturing process.

Phase-only spatial light modulators: Spatial Light Modulators (SLMs) refer to active optical components designed to manipulate the spatial distribution of light such as phase, amplitude and polarization. These components apply computer-generated holograms onto incident light beams with the benefit of reconfigurability. A spatial light modulator that is specifically designed to manipulate the light spatial phase is referred to as phase-only SLM.

In our work, we specifically use SLMs based on Liquid-Crystal-On-Silicon (LCOS) technology. They are referred to as LCOS-SLM. The active surface of a LCOS-SLM is made of a matrix of pixels. Each pixel is composed of parallel-aligned liquid crystal layers arranged between a transparent and reflecting surfaces.

Under the effect of an external electric field, it is possible to freely control the alignment of liquid crystals. Due to the rod-like shape of these crystals, an applied electric voltage can induce a birefringence. Hence, by controlling the voltage applied at each pixel of the active surface, it is possible to control the effective refractive index at each of these pixels. In other words, LCOS-SLMs offer the possibility to control the wavefront of light fields interacting with a SLM at each pixel.

In order to actively control the arrangement of liquid crystals, a SLM device is connected to a computer. Wavefront patterns (or phase masks) can be numerically computed and

are used to control the electric voltage applied on the liquid crystal pixels.

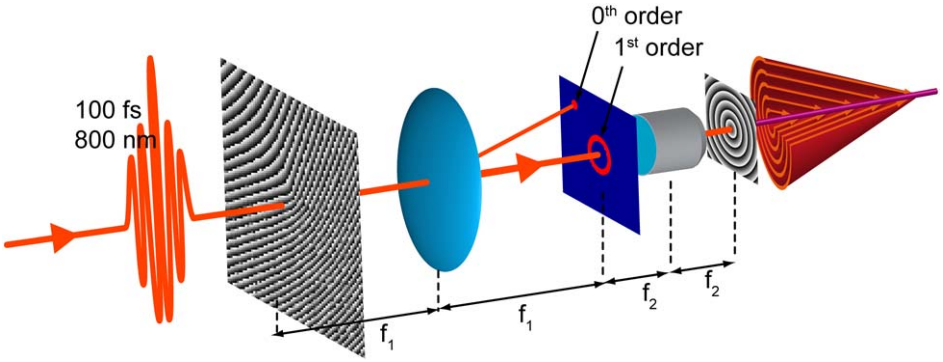

Figure 1.10: Experimental setup for femtosecond Bessel beam generation from direct-space using a phase-only SLM. Image taken from Ref. [Froehly et al., 2014].

Phase-only SLMs have attracted a major interest and have been largely deployed as Bessel beam generators [Davis et al., 1993, Chattrapiban et al., 2003, Froehly et al., 2014]. Bessel beams are generated in the same manner as that used in holographic techniques. Figure (1.10) shows an experimental setup to generate Bessel beams from direct space using a phase-only SLM. An incident laser beam, passing through the active surface of a SLM, is diffracted at different diffraction orders.

In this example, the phase mask is composed of an azimuthally-symmetric wavefront pattern (information of the Bessel beam to be generated) to which a linear phase ramp is added to separate the different diffraction orders. Since information of the Bessel beam is solely contained in the first diffraction order, a spatial filtering system is set up to filter out all undesired diffraction orders, especially the zeroth one. This system is called "4f system"; it is made of one lens and a microscope objective. The SLM is placed at the focal of the lens to convert the beam at the SLM plane into the corresponding spatial spectrum at the image plane of the lens. The spatial filtering is then performed in this image plane. Then the microscope objective is used to reconstruct the Bessel beam in direct space.

While axicons and holographic elements can produce Bessel beams with specific geometrical properties, phase-only SLMs are more versatile since one can freely modify the imprinted phase mask using computer-generated holograms. The versatility of phase-only SLMs makes them a powerful tool for spatial beam shaping. Of particular interest, a single phase-only SLM can be used for simultaneous spatial amplitude and phase shaping, which very useful for arbitrary shaping of the on-axis intensity of Bessel beams. We will specifically discuss this topic in chapter 2.

1.1.4/ BESSEL PULSES

So far, we have only discussed monochromatic Bessel beams in the form of continuous waves. Actually, a Bessel pulse, which is made of a superposition of Bessel beams with different temporal frequencies, is still a propagation-invariant solution of the propagation equation in the linear regime. The spatial shaping of laser pulses into Bessel beams using the above described methods is still valid, but the spatio-temporal properties of the spatially-shaped pulses differ depending on the Bessel beam generator. We consider

Bessel pulses generated by refractive and diffractive axicons and compare their spatio-temporal properties based on their respective group velocity.

The on-axis group velocity v_g is given by:

$$v_g = (\mathrm{d}k_z/\mathrm{d}\omega)^{-1} \tag{1.7}$$

where $k_z = n(\omega)\omega/c\cos(\theta(\omega))$, ω is the angular frequency of the pulse and $n(\omega)$ is the frequency-dependent refractive index of the propagation medium. We consider the case of cone angles defined in the paraxial approximation, i.e. $\cos(\theta) \approx 1 - \theta^2/2$. In this case, Eq. (1.7) can be derived as follows:

$$v_g = \frac{c}{n(\omega)\,\cos(\theta)}\left(1 + \frac{\omega}{n(\omega)}\frac{\partial[n(\omega)]}{\partial\omega}\cos(\theta) - \omega\,\tan(\theta)\frac{\partial[\theta]}{\partial\omega}\right)^{-1} \tag{1.8}$$

In the particular case where the dispersion of the propagation medium is negligible [Alexeev et al., 2002], i.e. $\partial[n(\omega)]/\partial\omega = 0$, the expression of v_g is reduced to [Klewitz et al., 1998]:

$$v_g = \frac{c}{n(\omega_0)\,\cos(\theta)}\frac{1}{1 - \tan(\delta)\tan(\theta)} \tag{1.9}$$

where $\tan(\delta) = \omega(\partial\theta/\partial\omega)$ and δ is interpreted as the pulse tilt angle [Klewitz et al., 1998]. For a Bessel beam generated by a refractive axicon, its cone angle is frequency-dependent [Froehly et al., 2014]. Considering an axicon with positive dispersion, the angular dispersion is found to be positive and thus it yields a superluminal group velocity $v_g > v_\phi = c/n(\omega_0)\cos(\theta)$ that is even superior to the phase velocity [Klewitz et al., 1998]. Bessel beams generated by annular slits also exhibit the same property [Saari et al., 1997]. Superluminal speed of the central core of Bessel pulses has been investigated in a number of experiments. Alexeev et al. measured a superluminal ionization speed induced by axicon-generated Bessel pulses [Alexeev et al., 2002]. Such a feature was also demonstrated by measuring the terahertz radiations focused by axicons in comparison with the ones measured without any optical element [Lloyd et al., 2003]. Of particular interest, Saari and Reivelt [Saari et al., 1997] showed that Bessel pulses exhibiting a superluminal velocity are X-shaped in the longitudinal plane and thus such pulses are referred to as "Bessel-X pulses". Direct measurement of their spatio-temporal field was performed using the interferometric technique SEA TADPOLE [Bowlan et al., 2009]. Note that Bessel-X pulses are different from the dispersion-free X waves since the former can still undergo dispersion effects.

However, if we use diffractive axicons, such as those produced by holograms and spatial light modulators, Bessel beams are generated with a frequency-independent cone angle [Froehly et al., 2014]. Hence, the angular dispersion is negative [Klewitz et al., 1998]. As shown in Fig. (1.11,b), the pulse front remains perpendicular to the propagation axis as the pulse propagates whereas the wavefront is tilted at the angle θ with respect to the propagation direction. The spatio-temporal aspects of Bessel beams generated by phase-only SLM were particularly studied in [Froehly et al., 2014]. While locally, the Bessel pulse velocity is superluminal, the overall traveling speed is subluminal and is given by $v_g = c\cos(\theta)$. Such a pulse is termed "Pulsed Bessel beam" and its temporal profile is usually modeled by a temporal Gaussian envelope [Courvoisier et al., 2016b].

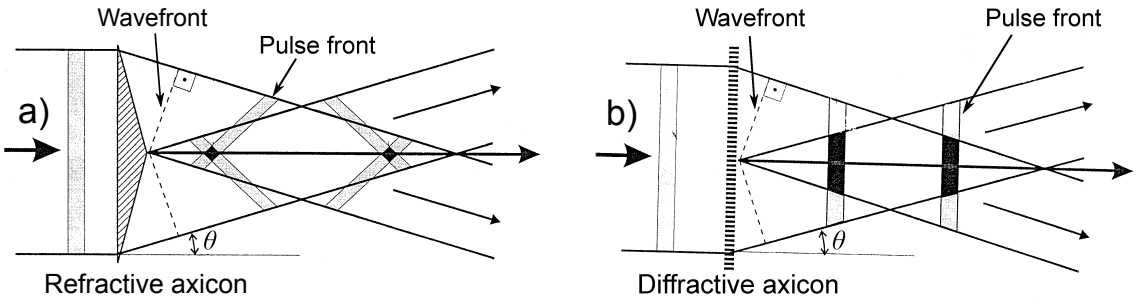

Figure 1.11: Group velocity of a Bessel pulse for two types of Bessel beam generators: a) refractive and b) diffractive axicon. Image taken from [Klewitz et al., 1998].

1.1.5/ APPLICATIONS OF BESSEL BEAMS IN THE LINEAR REGIME

Thanks to their peculiar properties, specifically their diffraction-resistant and self-healing features, Bessel beams have found a wide range of applications such as imaging, optical micro-manipulation [Arlt et al., 2001], optical guiding, spectroscopy, etc. In imaging applications, the long focal volume of Bessel beams allows a longer penetration depths in samples compared to Gaussian beams, especially in biological tissues. Such a property has been used in numerous imaging techniques such as microscopy [Fahrbach et al., 2010], optical coherence elastography [Fang et al., 2017], optical coherence tomography [Lee et al., 2008], Phakometry [Lambert et al., 2016], dark-field microscopy [Lei et al., 2008], etc.

The self-reconstruction property of Bessel beams was shown to be very advantageous in many applications. In imaging applications, this feature allows Bessel beams to be more resistant to highly scattering media [Fahrbach et al., 2012] which has further extended their applicability. Figure (1.12,left) shows simulation results of the propagation of a Bessel beam along a cluster of spheres which represents a scattering medium. While scattering is clearly seen in the peripheral rings, the central core of the beam hardly deviates from a straight line along its propagation length.

Figure (1.12,right) shows a comparison between fluorescence images of biological samples (two Drosophila egg chambers) obtained by Gaussian and Bessel beams. In the case of Gaussian illumination, the incident beam is significantly scattered from the propagation axis (dashed line) after passing through the first chamber. As a result, only the edges of the second chamber are illuminated. In contrast, this second chamber is well imaged by the Bessel beam thanks to its resistance to scattering from the first chamber.

Bessel beams can also be used as optical tweezers to manipulate multiple particles at different locations along their propagation length [Garces-Chavez et al., 2002]. Thanks to its self-healing property, a Bessel beam can reconstruct itself after interacting with each particle. Hence, the use of a single Bessel beam gives the possibility to manipulate multiple particles even it they are located in two different cells as shown in Fig. (1.13).

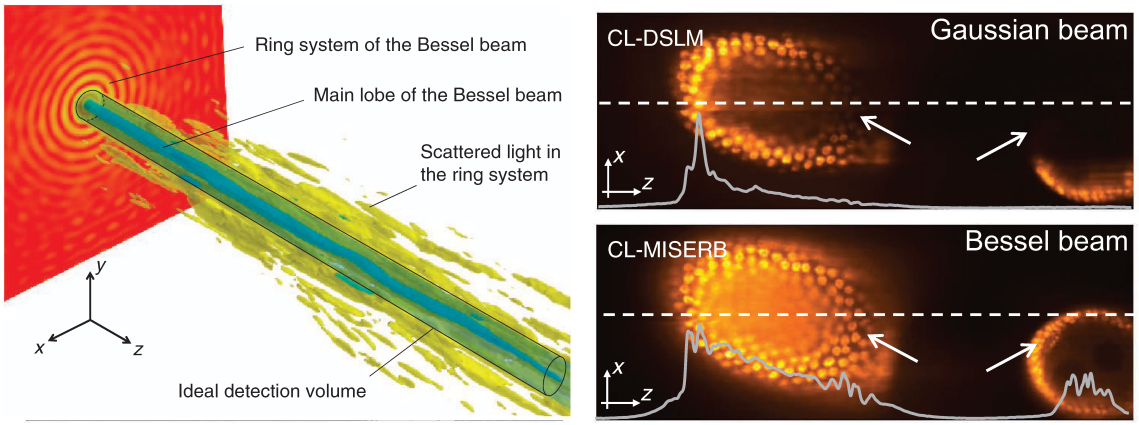

Figure 1.12: (left) Simulation of Bessel beam propagation in a thick medium as reported in [Fahrbach et al., 2010] and (right) comparison depth imaging performance of Gaussian and Bessel beams. Images taken from [Fahrbach et al., 2010].

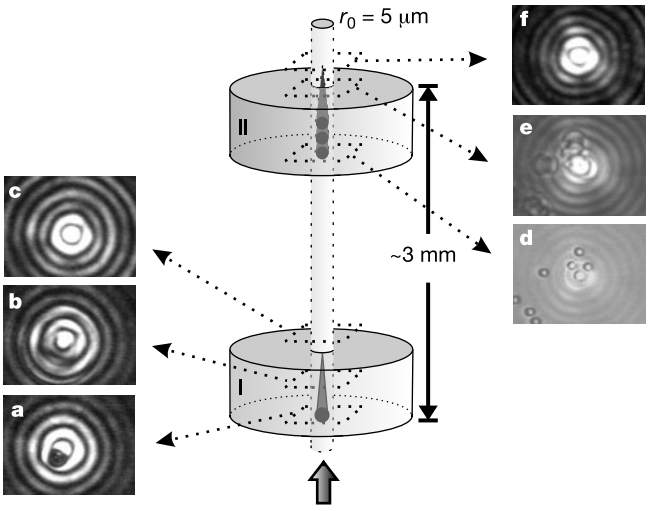

Figure 1.13: Setup for manipulation of particles placed in two different cells separated by a distance of 3 mm. Image taken from Ref. [Garces-Chavez et al., 2002].

1.2/ Bessel Filamentation

1.2.1/ Brief history on filamentation

As mentioned above, generally, any beam-like wave tends to transversely spread as it propagates in free space. Before the introduction of propagation-invariant solutions to the wave equation, nonlinear effects have been proposed as a solution to overcome diffraction and generate localized wave-packets over long propagation distances.

The discovery of Kerr-self focusing in 1964 was the point of beginning. Hercher et al. have studied the interaction of nanosecond laser pulses with glass and found that such pulses can induce weak but noticeable damage [Shen, 2009]. This experiment showed the increase in light intensity along propagation, thus suppressing the intrinsic light spreading.

To explain this effect, Chiao et al. proposed a self-trapping model according to which a

waveguide is generated because of the self-action of the light field in nonlinear regime [Shen, 2009]. Talanov and Kelly have shown that light self-focusing only takes place when the input laser power is higher than a threshold value [Chiao et al., 2009]. At the conclusion of these studies, the concept of filamentation has been introduced as "an intense streak of light parallel to the direction of beam propagation" [Shen, 1975].

However, before the advent of femtosecond laser sources, the observed light filaments had relatively small propagation lengths. In transparent condensed media, the typical length of light filaments was of the order of $1\ mm$. Laser pulses with tens of picoseconds and longer pulse durations usually induce damage in the propagating media which prevent the formation of longer filaments [Tzortzakis et al., 2001]. In the 1980s, the laser technology has been further developed thanks to two major advancements. Firstly, laser energy amplification techniques, such as the chirped pulse amplification (CPA) method, were introduced allowing the amplification of laser power up to the petawatt level. Secondly, research in solid-state lasers, such as Titanium-sapphire-based laser, had given rise to the femtosecond laser technology. Hence, it has become possible to confine a great amount of energy in an ultrashort time frame, which led to the exploration of new regimes of laser-matter interactions.

In 1995, Braun et al. studied the nonlinear propagation of a 50-mJ 200-fs laser pulse in air. They demonstrated that such a laser pulse could remain transversely localized in space over distances greater than 20 m. This showed that self-focusing effect still occurred at such propagation distances thus producing a filament with unprecedented propagation length. Prior to this experiment, use was usually made of pulses with longer pulse duration ($> 100\ ps$) and laser intensity superior to $10^{14}\ W/cm^2$ to generate light filaments on the order of few centimeters [Durfee et al., 1993]. However, in the experiment of Braun et al., the femtosecond laser pulse intensity was only on the order of $10^{13}\ W/cm^2$. This showed that light filaments can be effectively formed using femtosecond laser sources with lower input energy. Other experiments showed that 2-kilometer long filaments could also be formed in air [Couairon et al., 2007]. These results have opened the way to novel potential applications and thus rejuvenated the interest of the scientific community on filamentation.

In transparent condensed media, Tzortzakis et al. used a femtosecond laser pulse to generate, for the first time, a 2-cm long filament in fused silica [Tzortzakis et al., 2001]. The filament was formed from a 2-μJ input Gaussian pulse with a pulse duration of 160 fs. In comparison to linear propagation regime where the beam diameter significantly increases along propagation, the filament remains transversely localized over a longer propagation distance (see Fig. (1.14) for more details). Note that, in this experiment, the laser pulse was weakly focused in the sample. In case of a tightly focused laser pulse, the pulse may induce a damage or at least a local matter modification in the medium which may prevent the formation of a long filament [Sudrie et al., 2002].

1.2.2/ NONLINEAR PROCESSES INVOLVED IN FILAMENTATION

Along the filamentation process, many nonlinear effects are involved. In the following, we will briefly describe some of these effects:

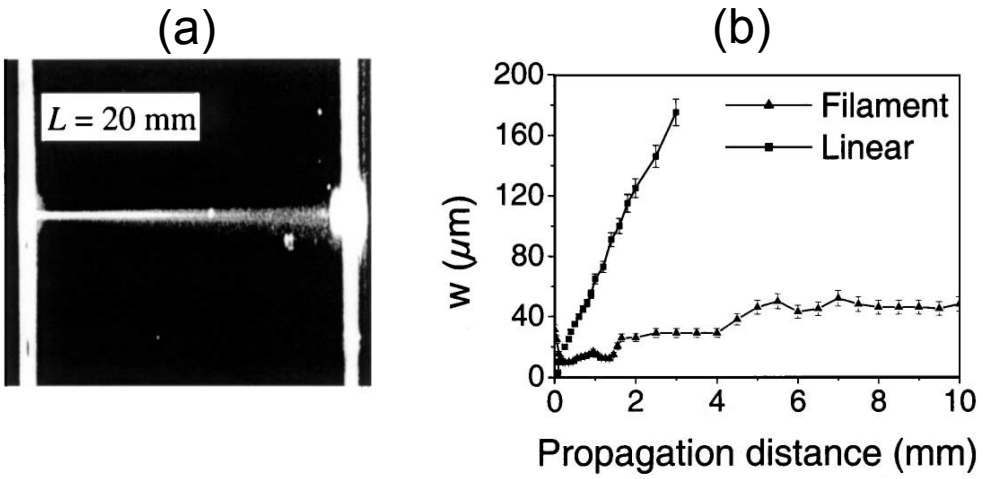

Figure 1.14: (a) A photograph of the self-guided filament in fused silica at input energy of 2 μJ. (b) Measured diameter of the filament along its propagation compared to that measured in linear propagation regime at low input energy (50 nJ). Figures taken from Ref. [Tzortzakis et al., 2001].

1.2.2.1/ KERR SELF-FOCUSING

Kerr effect is a third order nonlinear effect. It mainly takes place in isotropic and centrosymmetric materials where second order nonlinearity is negligible (or nonexistent).

Kerr nonlinearity consists in inducing refractive index change in the propagating medium by the action of the laser field on itself. The refractive index n thus becomes intensity-dependent according to the formula $n = n_0 + n_2 I$ where I is the laser intensity. In case n_2 is positive, Kerr nonlinearity plays, in the spatial domain, the role of a focusing lens as illustrated in Fig. (1.15). This leads to an increase in intensity and allows overcoming transverse intensity spreading induced by diffraction [Couairon et al., 2007].

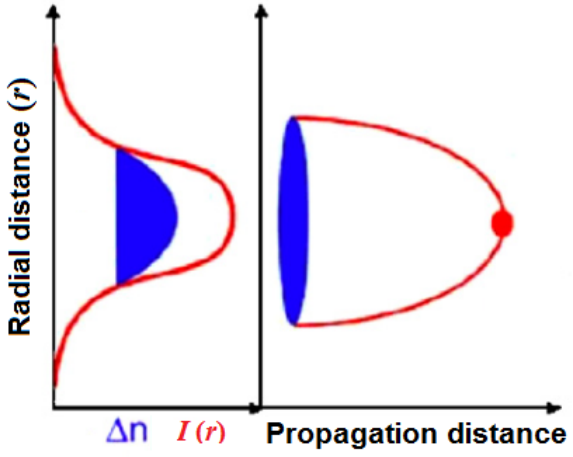

Figure 1.15: Illustration of Kerr effect which acts as a focusing lens. Image taken from Ref. [Couairon et al., 2007].

1.2.2.2/ PHOTOIONIZATION

Photoionization of transparent materials refers to a physical process according to which electrons in the valence band (bound electrons) are transferred to the conduction band by means of optical energy absorption. In transparent materials, the gap energy between the valence band and conduction band, denoted U_i, is much higher than single photon energy E_{1ph}, which allows light to be transmitted through the material. Thus, the ionization of transparent materials is only possible at high intensities where the probability of nonlinear light absorption is measurable [Couairon et al., 2007].

The probability of photoionization, denoted W_{PI}, can be described by Keldysh formula as follows [Sudrie et al., 2002]:

$$W_{PI} = \frac{2\omega_0}{9\pi}\left(\frac{\omega_0 m}{\hbar\sqrt{\Gamma}}\right)^{3/2} Q(\gamma, U_i, \omega_0) \tag{1.10}$$

where ω_0 is the angular frequency, m is the reduced mass of electron and hole, $\Gamma = \gamma^2/1+\gamma^2$ and $\gamma = \omega_0\sqrt{mU_i}/qE$ is referred to as adiabaticity parameter with q is the electric charge and E is the electric envelope. Q is a function of laser and material parameters. As an example, Fig. (1.16) shows the photoionization rate computed for fused silica with a potential gap $U_i = 9$ eV.

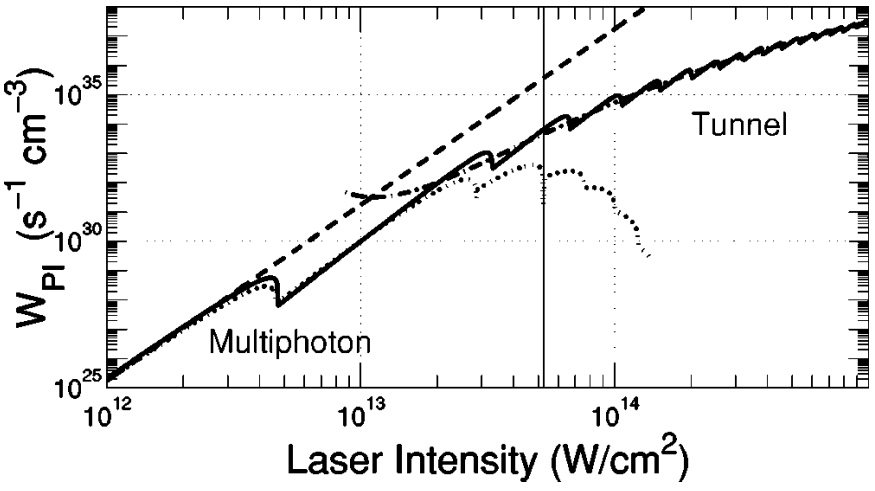

Figure 1.16: Ionization rate for fused silica with gap U_i =9 eV computed with Keldysh's formulation for multiphoton ionization ($\gamma \gg 1$, dotted curve) and tunnel ionization ($\gamma \ll 1$, dash-dotted curve) and from the general formula valid in the intermediate regime (solid line). The multiphoton rate is shown by the dashed line. Figure taken from Ref. [Couairon et al., 2005].

Keldysh formula effectively covers two extreme cases of ionization process, that we can distinguish from the value of the γ parameter. For a laser wavelength of $\lambda = 800$ nm, the parameter γ is equal to unity for an intensity of 35 TW/cm^2. If $\gamma \gg 1$, corresponding to weak intensities, photoionization can be assimilated to multiphoton ionization. It consists of the absorption of multiple photons of energie E_{1ph} to overcome the potential gap (see Fig. (1.17 ,left)). For $\gamma \ll 1$, the laser intensity is strong enough to deform the structure of the atomic potential (see Fig. (1.17,right)) as to suppress the potential barrier

[Couairon et al., 2007] . This leads to electron transition from the valence to the conduction band through tunneling effect. This ionization process is termed tunnel ionization.

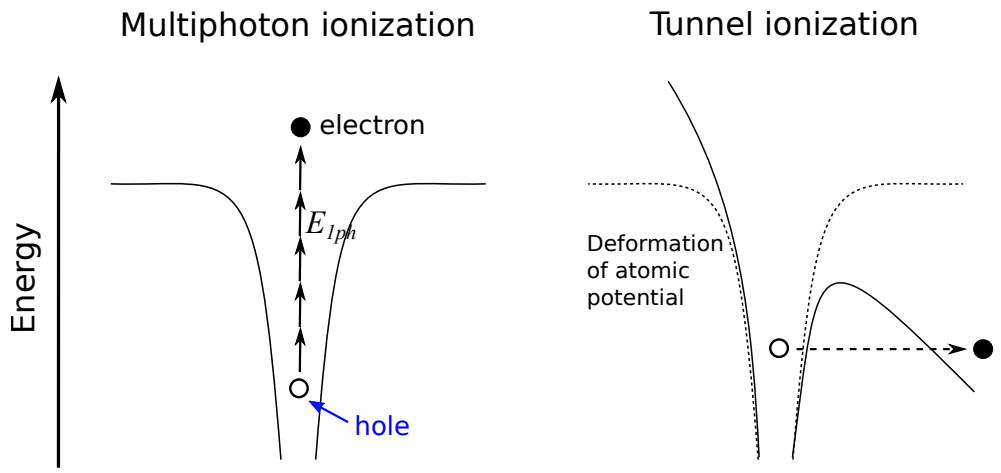

Figure 1.17: Illustration of multiphoton (left) and tunnel (right) ionizations. E_{1ph} refers to the energy of a single photon. [After Ref.[Couairon et al., 2007]].

1.2.2.3/ Plasma absorption and Avalanche ionization

Photoionization leads to electron transition from the valence to conduction band. Considering laser pulse interaction with transparent materials, photoionization occurs in the leading part of the pulse whereas its trailing part interacts with the induced free-electrons. In this stage, free-electrons absorb light through inverse Bremsstrahlung effect [Vogel et al., 2005], which can be assimilated to Joule heating or successive single photon absorption [Rethfeld, 2004]. In the event the energy gained is superior to a critical value, high-energy electrons can collide with valence electrons which acquire enough energy to transit to the conduction band. These processes are illustrated in Fig. (1.18) and take place repeatedly for as long as the light field is present.

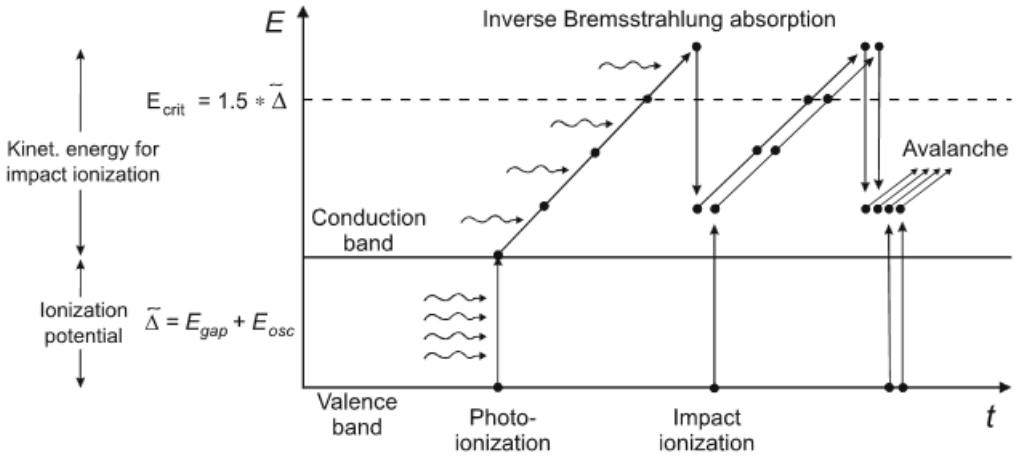

Figure 1.18: Illustration of avalanche ionization. Image taken from Ref. [Vogel et al., 2005].

1.2.2.4/ PLASMA DEFOCUSING

In contrast to Kerr self-focusing, free-electron plasma plays the role of a defocusing lens. Its effect consists in reducing the refractive index of the medium and is approximately expressed by the relation $n \approx n_0 - \rho/2\rho_{cr}$ where ρ is the density of laser-generated plasma and ρ_{cr} is the critical plasma density (it corresponds to plasma frequency equal to that of the laser field).

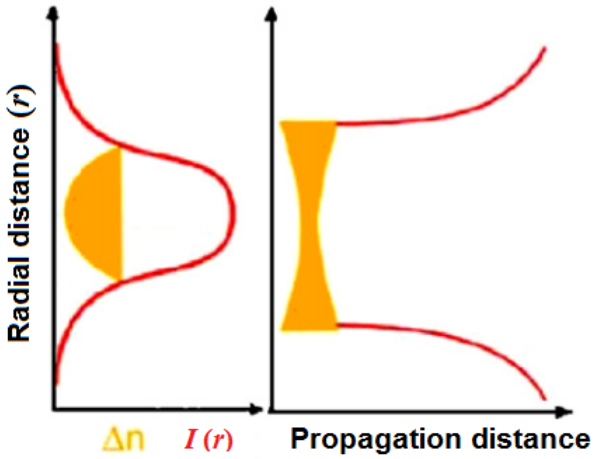

Figure 1.19: Illustration of plasma defocusing effect. Image taken from Ref. [Couairon et al., 2007].

1.2.3/ FILAMENTATION MODELING OF GAUSSIAN BEAMS

1.2.3.1/ MODELING SCENARII

Many models have been introduced to describe light filaments. As discussed above, the first experimentally observed filaments were obtained for nanosecond pulse duration. They were seen as transversely localized light rays propagating over multiple Rayleigh lengths [Shen, 1975]. The first model introduced is the self-trapping theory which states that a filament is formed from an interplay between nonlinear self-focusing and diffraction [Chiao et al., 2009]. Another model is named the moving focus. It states that an input pulse can be fragmented into independent time slices each having its own nonlinear focus length [Shen, 1975, Brodeur et al., 1997].

These two models were sufficient to explain many of the filamentation aspects in the regime of long pulse duration and the formation of short filaments. However, regarding femtosecond filaments such as that reported by Braun et al.[Braun et al., 1995], the nonlinear dynamical processes involved are more complicated and require a more complicated model to describe their features. Specifically, it was shown that such filaments undergo significant spatio-temporal deformations such as pulse splitting [Mlejnek et al., 1998] which cannot be explained by these two models.

A more advanced model states that light filaments are formed through a nonlinear interplay between Kerr self-focusing and the generated plasma defocusing [Couairon et al., 2007]. After an initial increase in intensity due to self-focusing, the light

intensity increases so much that, at some point, the light field will self-collapse. However, nonlinear absorption of light takes place and decreases the light intensity. Meanwhile, a plasma of electron-hole is locally generated and significantly decreases the refractive index of the medium and thus plays the role of a diverging lens. The nonlinear absorption and plasma defocusing will then decrease light intensity which will transversely spreads. If the light field power is still above the self-focusing threshold, then it will once again increase in intensity thanks to Kerr nonlinearity. Therefore a cycle of focusing and defocusing will persist for as long as the pulse power is greater than the self-focusing threshold. These dynamics are illustrated in Fig. (1.20).

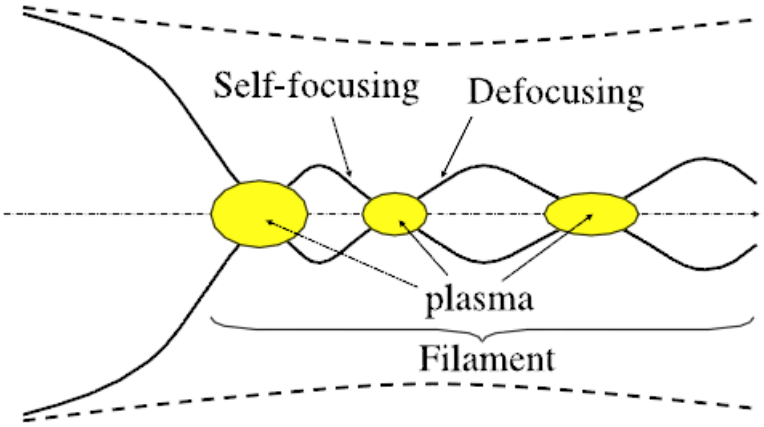

Figure 1.20: Illustration of filament formation according to a cycle of nonlinear focusing and defocusing effects. Image taken from Ref. [Couairon et al., 2007].

These nonlinear dynamics have been shown to lead to progressive reshaping of the initial Gaussian intensity profile into a Bessel-like wave [Dubietis et al., 2004]. Actually, it was experimentally demonstrated that light filaments can reconstruct themselves when an obstacle is placed along their propagation path, which is reminiscent of the self-healing property of Bessel beams. Thus, it was shown that an initial spatial reshaping of Gaussian beams into Bessel beams yields more stable and controllable formation of filaments [Polesana et al., 2008].

1.2.3.2/ MODELING EQUATIONS

For numerical simulation, light filamentation is usually modeled by the following nonlinear propagation equation [Couairon et al., 2007]:

$$\frac{\partial A}{\partial z} = \frac{i}{2k}\nabla_\perp^2 A - i\frac{k^{(2)}}{2}\frac{\partial^2 A}{\partial t^2} + [N_{Kerr}(|A|^2) + N_{PI}(|A|^2) + N_{Plasma}(\rho)]A \tag{1.11}$$

This equation is derived according to the scalar approximation and describes the propagation of the envelope A of a linearly polarized electric field E, written as $E = \Re[A\exp(ikz - i\omega_0 t)]$. It has been used to explain the major properties of filamentation of Gaussian beams [Sudrie et al., 2002, Couairon et al., 2007] and also Bessel beams [Polesana et al., 2005, Polesana et al., 2008, Dubietis et al., 2007] whether in gases, transparent liquids or solids. The first two terms of the right hand side of this equation account for linear effects: the operator $\nabla_\perp^2$ stands for transverse laplacian and accounts

for diffraction while the other term accounts for dispersion through the group velocity dispersion (GVD) coefficient $k^{(2)}$. This equation also takes into account the major nonlinear effects involved in filamentation, namely Kerr nonlinearity N_{Kerr}, photoionization $N_{PI}(|A|^2)$ and light coupling to laser-induced plasma $N_{Plasma}(\rho)$ where ρ is the plasma density.

This equation is coupled to the time evolution of plasma density described by the following equation [Couairon et al., 2007]:

$$\frac{\partial \rho}{\partial t} = [W_{PI} + W_{ava}\rho](1 - \rho/\rho_{at}) - \rho/\tau_r \tag{1.12}$$

where W_{ava} alludes to avalanche ionization and τ_r is the relaxation time of free-electrons.

Although many features of filamentation could be described by this model, filamentation modeling is still a hot topic since other features remain unexplained especially those regarding the propagation-invariant property of Bessel beams in this regime [Courvoisier et al., 2016b]. We will further discuss this point in chapter 4 where we will show how to derive the nonlinear propagation equation, the approximations involved and the different models of light-plasma coupling used in literature.

1.2.4/ Bessel Filamentation

The propagation of Bessel beams in Kerr media was investigated numerically and experimentally by many groups [Andreev et al., 1991, Gadonas et al., 2001, Sogomonian et al., 2000, Klewitz et al., 1998, Polesana et al., 2008, Dota et al., 2012]. The concept of filamentation of Bessel beams is a bit different from that of Gaussian beams. As stated above, Gaussian filaments are formed by the interplay between Kerr self-focusing and nonlinear losses. However, Bessel beams are intrinsically diffraction-resistant and thus are "self-guided" without the need of Kerr self-focusing. Nonetheless, these nonlinear dynamics still take place in Bessel filaments. Let us first discuss the effect of Kerr nonlinearity on Bessel beams.

1.2.4.1/ Nonlinear Bessel beam

The effect of Kerr nonlinearity has been first considered in pure Kerr media, i.e. where nonlinear losses are negligible [Gadonas et al., 2001, Johannisson et al., 2003]. Considering the nonlinear propagation model of Eq. (1.11) and neglecting nonlinear losses (photoionization and plasma terms), it is reduced to a nonlinear Schrödinger equation (NLSE) as follows:

$$\frac{\partial A}{\partial z} = \frac{i}{2k}\nabla_\perp^2 A + i\,kn_2/n\,|A|^2 A \tag{1.13}$$

In Refs. [Gadonas et al., 2001, Johannisson et al., 2003], dispersion was neglected and Kerr nonlinear term N_{Kerr} is written as $i\,kn_2/n\,|A|^2$ where k is the wavenumber of the light field; n and n_2 are the linear and nonlinear refractive indices respectively.

Numerical simulation results of this equation showed that the central core of Bessel beams undergoes intensity modulation along the propagation distance as seen in Fig.

(1.21, left). This nonlinear intensity modulation will be referred to as "nonlinear instabilities" [Ouadghiri-Idrissi et al., 2017]. In the spectral domain, it was shown that Bessel beams can sustain Kerr-induced spectral distortions which lead to the generation of two additional spectral components: an axial wave component of spatial frequency $k_r = 0$ and a secondary conical wave with a spatial frequency $k_r = \sqrt{2}k_{r0}$ where k_{r0} is the spatial frequency of the incident Bessel beam [Gadonas et al., 2001, Pyragaite et al., 2006]. Experimental evidence of the appearance of these two components was reported in [Gadonas et al., 2001, Pyragaite et al., 2006, Polesana et al., 2007]. An example is shown in Fig. (1.21,right).

The observed longitudinal intensity modulation was interpreted by the phase retardation between the input Bessel beam and the self-induced axial wave [Gadonas et al., 2001, Polesana et al., 2008]. We will further discuss these nonlinear instabilities in chapter 3.

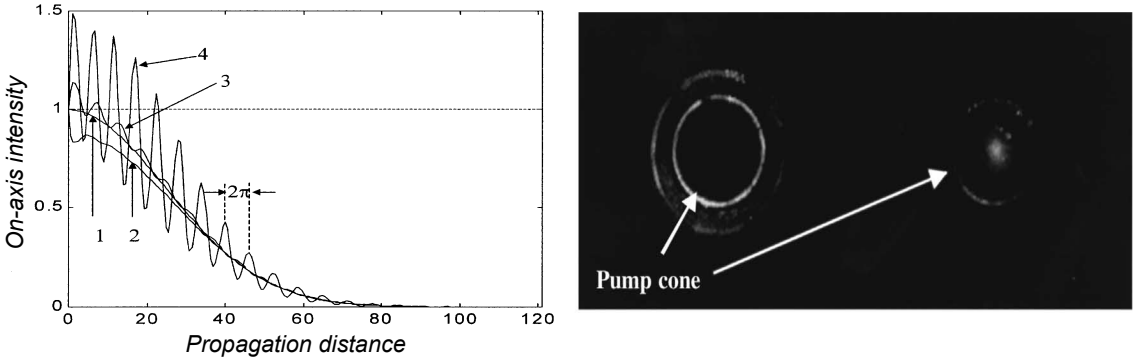

Figure 1.21: (left) Evolution of the central core intensity along propagation in the linear (1) and nonlinear regimes (2-4) where nonlinearity is increased from (2) to (4). (right) Experimental observation of spatial spectrum of Bessel beam transmitted through a benzene cell in the nonlinear regime. Images taken from Ref. [Gadonas et al., 2001].

Johannisson et al. discussed solutions of nonlinear Schrödinger equation (NLSE). Near the central core of Bessel beams, it was shown that the NLSE has an approximate solution of the form:

$$A = A_0 J_0\left(\sqrt{2k(\delta + \delta_{NL})}r\right) \exp(-i\delta z) \tag{1.14}$$

where A_0 is the peak amplitude, $\delta = k_{r0}^2/2k$ and $\delta_{NL} = kn_2/n\,|A_0|^2$ are the linear and nonlinear phase shifts of the beam central core. For a medium with positive nonlinear refractive index, a Bessel beam sustains ring compression in the near-field as shown in Fig. (1.22).

The NLSE was shown to have no stationary solutions [Johannisson et al., 2003]. Johannisson et al. discussed the possibility of partial or global collapse with increased beam intensity and explained these nonlinear dynamics in terms of interplay between Kerr effect and diffraction.

1.2.4.2/ BESSEL FILAMENT: NONLINEAR UNBALANCED BESSEL BEAM (NL-UBB)

In order to achieve a stable propagation regime of Bessel beams which is desired for high power laser applications, stationary solutions of the nonlinear propagation equation have been thoroughly investigated.

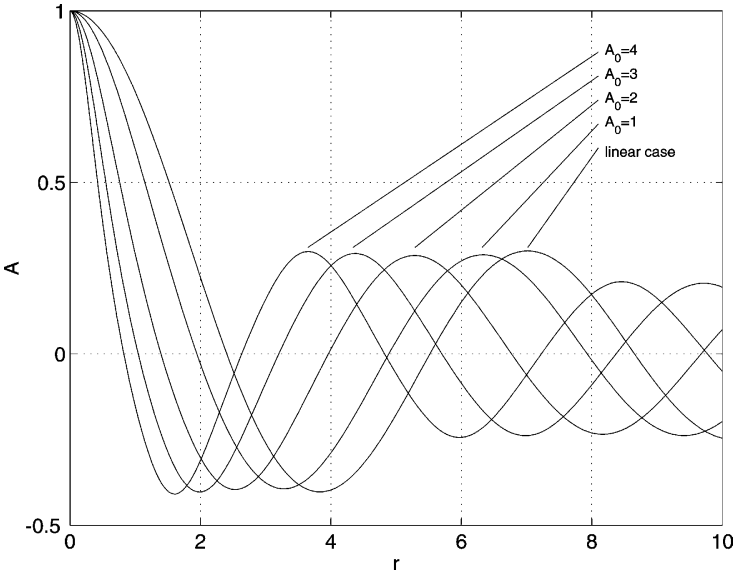

Figure 1.22: Numerical results: radial compression of Bessel beams in a Kerr medium for increased peak amplitude. Image taken from [Johannisson et al., 2003].

Porras et al. investigated the stability of Bessel beams in the presence of nonlinear losses (NLL), precisely multiphoton absorption (MPA) [Porras et al., 2004, Porras et al., 2015]. Considering the filamentation model of Eq. (1.11) and neglecting laser-plasma coupling, the propagation equation reads:

$$\frac{\partial A}{\partial z} = \frac{i}{2k}\nabla_{\perp}^2 A + i\,k\,n_2/n|A|^2 A - \frac{1}{2}\sigma_K K\hbar\omega_0|A|^{2\,K-2}A \tag{1.15}$$

where the photoionization term is written as $N_{PI} = -1/2W_{PI}K\hbar\omega_0/|A|^2$. Here, photoionization is approximated to multiphoton ionization, i.e. $W_{PI} = \sigma_K|A|^{2\,K}$ where σ_K is multiphoton ionization rate and K is the number of photons absorbed to overcome the potential gap U_i. Asymptotically, this equation has a propagation-invariant solution of the form:

$$A = \frac{A_0}{2}\left[b_{out}H_0^{(1)}\left(\sqrt{2k\delta}r\right) + b_{in}H_0^{(2)}\left(\sqrt{2k\delta}r\right)\right]\exp(-i\delta\,z) \tag{1.16}$$

This solution consists of the superposition of an inward and outward Hankel functions $H_0^{(2)}$ and $H_0^{(1)}$ with different amplitudes $|b_{in}|$ and $|b_{out}|$ respectively with $|b_{in}| \geq |b_{out}|$ [Porras et al., 2015]. In case $|b_{in}| = |b_{out}|$, this equation is reduced to $J_0\left(\sqrt{2k\delta}r\right)\exp(-i\delta\,z)$ which corresponds to an ideal Bessel beam. In the filamentation regime, however, these two amplitudes are different and thus the solution (1.16) can be interpreted as a non-diffracting Bessel beam with unbalanced amplitudes of its inward and outward Hankel components. Hence, it is referred to as NonLinear Unbalanced Bessel Beam (NL-UBB).

The amplitudes of the two Hankel components are related by $|b_{in}|2 - |b_{out}|^2 = k\,N_\infty/A_0^2$ where N_∞ refers to power loss due to nonlinear absorption. This relation shows that an input Bessel beam is reshaped into a NL-UBB due to nonlinear losses. This power loss was shown to engender an inward energy flux to compensate it [Porras et al., 2004, Polesana et al., 2006] and also leads to a loss of contrast of the beam side lobes (see Fig. (1.23)).

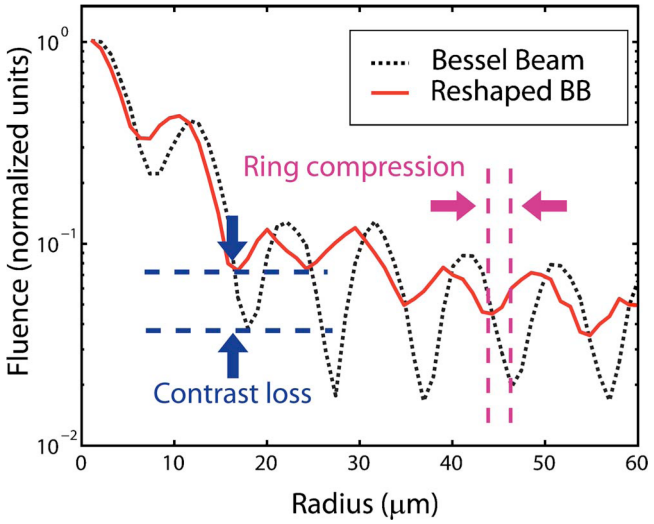

Figure 1.23: Magnification of the fluence profile (logarithmic scale of normalized units) of the reshaped Bessel beam (BB) (solid line) after the nonlinear propagation through a 5-mm-long fused silica sample, compared with the linearly propagated Bessel beam (dotted line) through the same sample. Image taken from Ref. [Polesana et al., 2006].

1.2.4.3/ FILAMENTATION REGIMES

The presence of nonlinear losses does not necessarily imply the formation of NL-UBB. Modulation instability analysis showed that NL-UBBs can only be formed in case nonlinear losses prevail over Kerr nonlinearity [Porras et al., 2004]. This condition can be satisfied if the Bessel beam intensity "I" exceeds a critical value I_c which can approximately be defined by the following relation [Couairon et al., 2012]:

$$I \geq I_c \equiv \left(\frac{2kn_2/n}{\sigma_K U_i}\right)^{1/(K-2)} \tag{1.17}$$

Hence, depending on the peak intensity of Bessel beams, three different regimes of Bessel filamentation have been defined [Polesana et al., 2008]:

- Weakly nonlinear regime: this filamentation regime occurs in case the light power is high enough to trigger Kerr nonlinearity but not high enough to generate a dense plasma.

- Steady filamentation regime: it is characterized by a smooth spatial reshaping of the beam into NL-UBB (see Fig. (1.24,left)). As discussed above, the high increase in intensity of the central core is continuously absorbed and replenished from the peripheral rings.

- Unsteady filamentation regime: in this regime, even though the Bessel pulse remains spatially localized, it undergoes noticeable spatio-temporal dynamics such as pulse splitting [Couairon et al., 2007]. Since Kerr nonlinearity is predominant, Kerr-induced instabilities step in which lead to the appearance of periodic strong intensity peaks as presented in Fig. (1.24,right).

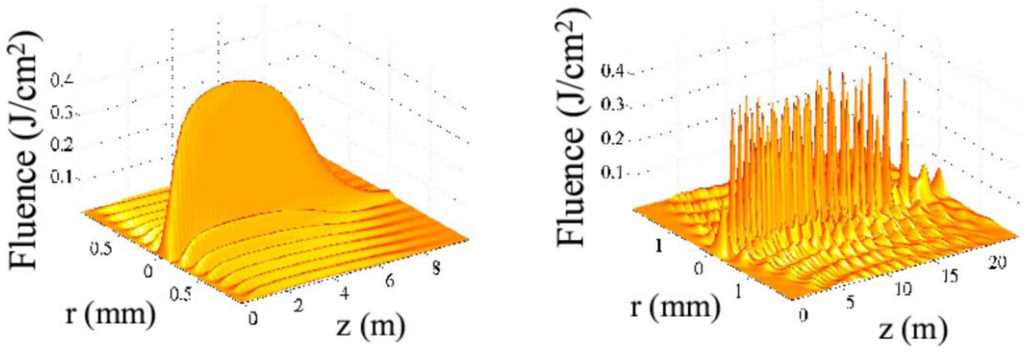

Figure 1.24: Simulation results of the filamentation of two Bessel beam beams with different cone angles: Fluence distribution along propagation for (left) $\theta = 0.15°$ and (right) $\theta = 0.05°$. Image taken from [Polesana et al., 2008].

Numerically, both steady and unsteady regimes were studied using different filamentation equation models. Whether or not light-plasma coupling is accounted for, the reshaping of input Bessel beam into a NL-UBB can be demonstrated. In addition, their experimental demonstration was performed in [Porras et al., 2004, Polesana et al., 2007]. The unsteady regime was also particularly observed in glass [Gaizauskas et al., 2006].

Note that, in the literature, two kinds of nonlinear instabilities were reported. One is caused by Kerr nonlinearity which was described above. The other one is induced by laser-generated plasma and was mainly reported to occur in gases (see Fig. 1.25) [Cooley et al., 2006]. Indeed, Bessel pulses were shown to generate plasma waveguides in gases [Durfee et al., 1993]. A waveguide is characterized by a specific longitudinal wavenumber k_g according to which a propagating mode can be channeled through it. In some cases, Bessel beams can be self-trapped in these waveguides [Fan et al., 2002]. In case the self-trapped beam has a different wavenumber, an intensity beating, resulting from the superposition of both modes, can be induced which may further be amplified by plasma absorption [Cooley et al., 2006].

Although there are some similarities between these instabilities, plasma-induced instabilities were found to greatly depend on the gas pressure but independent of the Bessel cone angle, in contrast with Kerr-induced instabilities. In this thesis, we will solely consider Kerr instabilities since we are more interested in Bessel filamentation in transparent solids. Furthermore, these instabilities were also demonstrated in gases [Gadonas et al., 2001] which will make our results valid in gaseous media as well.

1.2.5/ APPLICATIONS OF BESSEL FILAMENTATION

Filamentation has found a wide range of applications such as laser-generated plasma waveguides [Durfee et al., 1993], electrical discharge guiding [Clerici et al., 2015], pulse compression, high power terahertz generation, charged particle acceleration, laser ablation [White et al., 2008], materials processing [Amako et al., 2003], etc. Although Gaussian filaments are widely used, they have some drawbacks which hamper their applicability in some these applications. For instance, the formation of Gaussian filaments

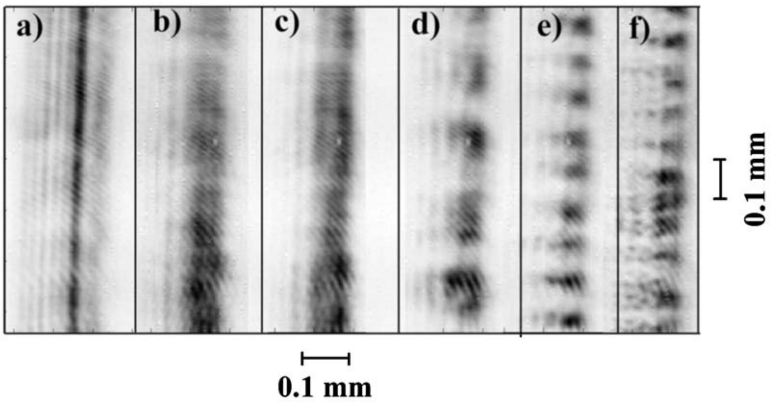

Figure 1.25: Shadowgrams of channels formed in argon for different pressures: (a) 200 torr, (b) 280 torr, (c) 300 torr, (d) 340 torr, (e) 370 torr, and (f) 420 torr. Laser pulse: 100 ps FWHM, $\lambda = 1064$ nm, and peak intensity 5×10^{13} W/cm^2; and axicon base angle $25°$. Image taken from Ref. [Cooley et al., 2006].

involves spatio-temporal dynamics which makes it difficult to control. Hence in applications where the generation of uniform plasma channels is needed, such as materials processing [Courvoisier et al., 2016b], the use of Gaussian filaments is limited. In this regard, spatial beam shaping into Bessel light modes has emerged as an alternative to Gaussian beams.

Actually, the idea to use input Bessel beams as an alternative to conventional Gaussian beams was proposed before 1987. The long line focus of axicon-focused laser pulses was extremely attractive to generate uniform plasma channels over many Rayleigh lengths. For instance, Bunkin et al. used axicon-focused nanosecond laser beams in their experiments to generate long and uniform laser sparks (laser-generated-plasma of free-electrons in air or generally in gases) [Bunkin et al., 1983]. In contrast, laser sparks engendered by input Gaussian pulses were non-uniform and more limited in spatial extent. In this section, we will present some applications of filamentation and highlight the advantages of Bessel beams over Gaussian beams.

1.2.5.1/ LASER-INDUCED PLASMA WAVEGUIDE

The generation of plasma waveguides makes use of the expansion properties of laser-induced electron-plasmas. A laser filament first produces a plasma channel whose number density is maximal at the spatial center of the beam. Afterwards, the plasma expands in space and its maximal density is gradually shifted away from the center of the beam. At a time frame of the order of 1 nanosecond, the plasma density becomes minimal over the axis of the channel (Fig. 1.26). As explained above, a free-electron plasma induces a local reduction in the refraction index of the medium. This means that a plasma channel with minimal on-axis density yields a maximal on-axis refraction index, which can be seen as a waveguide [Durfee et al., 1993].

The concept of laser channeling using plasma waveguides using two laser pulses was first introduced by Durfee et al. [Durfee et al., 1993]. It consists, in a first step, in generating a plasma channel using a high energy laser pulse. Then, by launching a second pulse

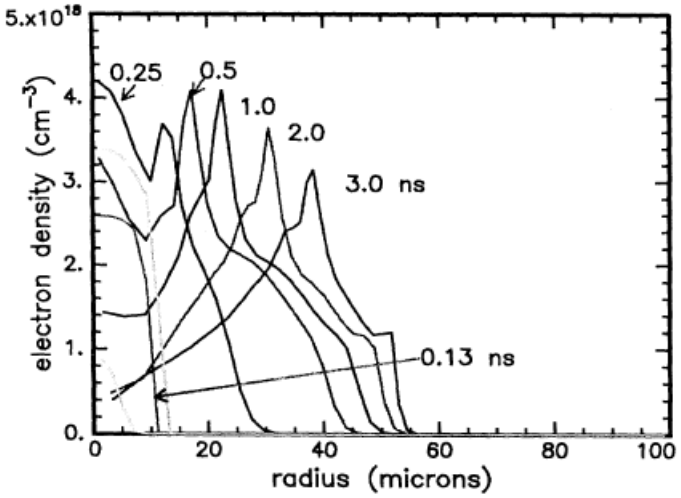

Figure 1.26: Calculation of 30 torr Argon time response to a 100 ps laser pulse with a peak intensity of 400 TW/cm^2, a spot size of 10 μm and a wavelength of 1.064 μm. The rapid rise in electron density at early times was seen to be due to direct ionization by the laser. The pulse, Gaussian in time, peaks at 0.125 ns. Image taken from Ref. [Durfee et al., 1993].

with an appropriate delay, this second pulse will be channeled over the whole length of the laser spark.

In Ref. [Durfee et al., 1993], Durfee et al. also compared the performance of laser sparks generated by Gaussian and Bessel pulses by measuring laser scattering of the guided second pulse. The experimental setups used to this end are described in Figs. (1.27,a,b). For Gaussian-induced spark, the second pulse is significantly scattered and thus only partly guided (see Fig. 1.27,c). As for the Bessel-pulse-induced spark, the second pulse (Gaussian) is quasi-perfectly guided over the whole plasma channel except at both ends of the latter (see Fig. 1.27,d). Indeed, the fluorescence image shows that the initial laser spark generated by the Bessel pulse is long, uniform and highly localized in space. Furthermore, its length is about 24 the Rayleigh length of its central spot. These results showed a more effective confinement of laser pulses using plasma channels induced by Bessel pulses than those generated by Gaussian pulses [Durfee et al., 1993, Durfee et al., 1995].

1.2.5.2/ ELECTRIC DISCHARGE GUIDING

Electric discharge refers to high-intensity electric current propagating along unpredictable paths in gases. Actually, the propagation of such electric current follows the path where the gas density is the lowest, which is extremely difficult to predict. Light filamentation has emerged as a potential solution to guide and control these structures.

The principle of guiding electric discharges is also based on the generation of laser sparks. Here, use is made of the local decrease in the gas density thanks to plasma generation. As a result, the gas density along the laser filament will be minimal and will act as guide for electric discharges.

In Ref. [Clerici et al., 2015], Clerici et al. compared experimental results of electric dis-

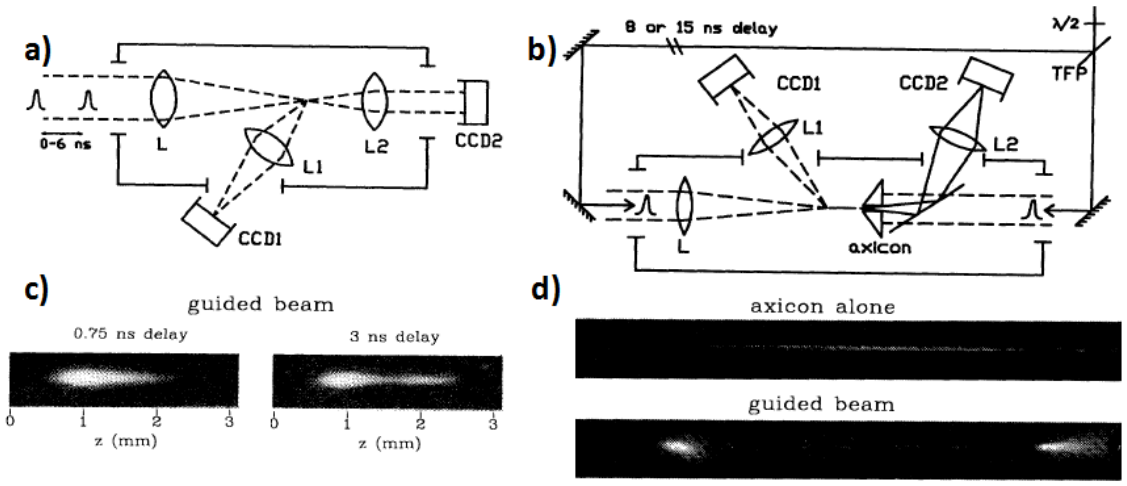

Figure 1.27: Experimental setup for guiding laser pulses using laser-generated plasma channel using (a) a lens and (b) using an axicon. (c) Fluorescence images from sparks generated by Gaussian pulses in Argon for different delays and (d) fluorescence images of (top) Bessel-induced spark and (bottom) the scattered light of the second pulse at a delay of 15 ns at the channel entrance and exit. Images taken from [Durfee et al., 1993].

charge guiding using Gaussian and Bessel beams as shown in Fig. (1.28). It is clear that the guided discharge current is more localized in space and more uniform in the case of Bessel-induced filaments.

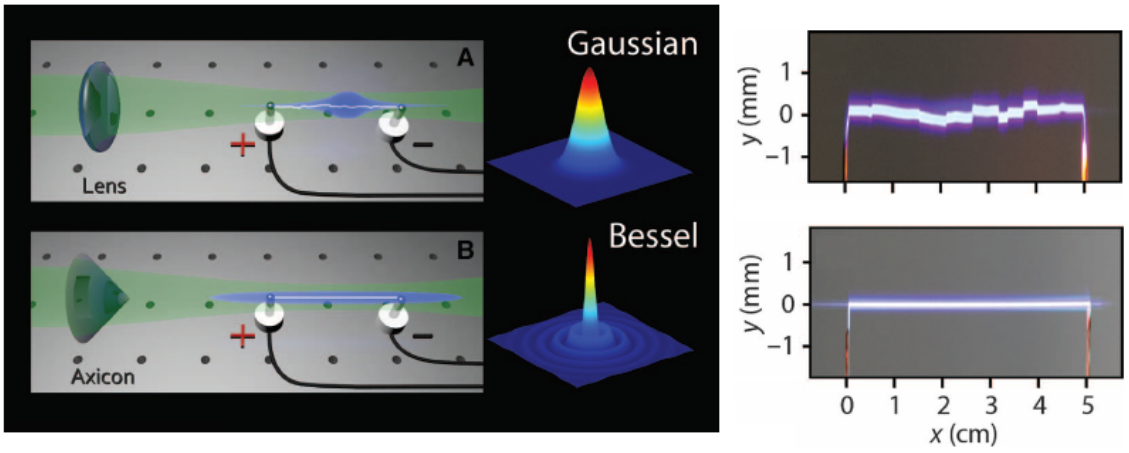

Figure 1.28: Guiding of electric discharge using laser sparks generated by a) a pulsed Gaussian beam and b) a Bessel pulse. Image taken from Ref. [Clerici et al., 2015].

1.2.5.3/ Generation of THz radiation

In the wake of the generation of free-electron plasma, space charge separation could induce an electric discharge oscillating at frequencies in terahertz range [Hamster et al., 1993, Bystrov et al., 2005]. This charge separation can be induced by various mechanisms and specifically the ponderomotive force. The generation of terahertz radiation can be performed using both Gaussian and Bessel beams

[Akhmedzhanov et al., 2009].

Generally, terahertz radiation is more efficiently generated using Gaussian beam, especially if an external electric field is applied in the electric discharge zone [Akhmedzhanov et al., 2009]. For Gaussian beams, the intensity distribution of terahertz radiation is generally asymmetric. It gains an axisymmetric distribution when an external electrostatic field is applied. As for Bessel beams, the generated-terahertz radiation is radially polarized and is axially symmetric in the form of a Cerenkov cone [Akhmedzhanov et al., 2009]. Furthermore, the superluminal velocity of the Bessel beam has been shown to contribute to the generated THz field. Another point of difference is that the application of an external electric field does not increase the energy conversion of THz radiations, in contrast with THz radiations induced by Gaussian beams [Akhmedzhanov et al., 2009].

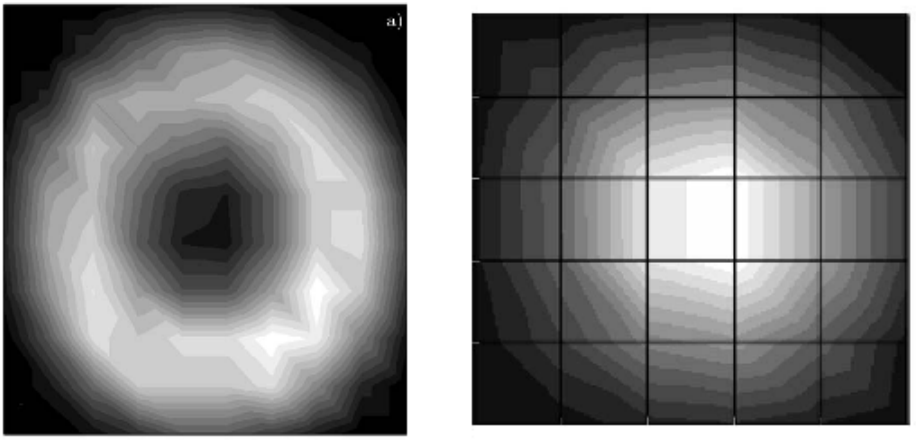

Figure 1.29: Transverse intensity distribution of THz radiations generated by (left) Bessel beam and (right) Gaussian beam [Akhmedzhanov et al., 2009].

Despite the lower energy conversion rate of THz radiations generated by Bessel beams, such THz radiations still hold important advantages over those generated by Gaussian beams. For instance, it was demonstrated in Ref. [Zhang et al., 2011] that Bessel beams can significantly improve the depth of focus in THz imaging. It was also demonstrated that Bessel beams undergo reduced spherical aberration when imaging objects embedded in a dielectric medium. In Ref. [Bitman et al., 2012], the imaging depth was shown to increase by a factor of 3.5 using broadband THz Bessel beams compared to THz Gaussian beams.

1.2.6/ BESSEL FILAMENTATION AND LASER MICRO-NANO MACHINING

In gases, light filamentation can take place without concern of matter damage in contrast with solid materials. For this reason, gases are preferred over transparent solids in many applications of filamentation, such as the generation of plasma waveguides and THz radiations. However, matter damage induced by high power laser has been exploited in many applications such materials processing, fabrication of waveguides, laser surgery, etc. Laser technology is now largely used in industry since it can be used to process any kind of materials with an extreme precision (down to tens of nanometers) [Gil-Villalba et al., 2015, Gattass et al., 2008].

1.2.6.1/ PHYSICAL PROCESSES OF LASER INTERACTION WITH TRANSPARENT MATERIALS

Generally, femtosecond pulses are more appropriate for laser ablation than laser pulses with long duration [Chichkov et al., 1996] because the thermodynamical gradients are higher and thus less burr is formed around the crater. The process of laser ablation is not an instantaneous process. It involves several physical effects as described in Fig. (1.30). Firstly, laser energy is absorbed through nonlinear processes, namely photo-ionization, inverse Bremsstrahlung effect, and impact ionization. As a result, a plasma of free-electron-holes is generated. These processes take place on a time scale ranging from few femtoseconds to few picoseconds.

The second step involves the thermalization of laser-generated free-electrons. This results in energy transfer between free-electrons (carrier-carrier scattering) and local energy transfer from the electrons to the lattice (carrier-phonon scattering). Then, at a time scale superior to few tens of picoseconds, a shock wave emission and thermal diffusion take place as a result of energy transfer from the locally heated lattice to its surrounding. At this stage, depending on the energy absorbed by the lattice, the material phase can evolve from the solid state to liquid, gas or even plasma phase. Then, at about a few nanoseconds, the material will be re-solidified.

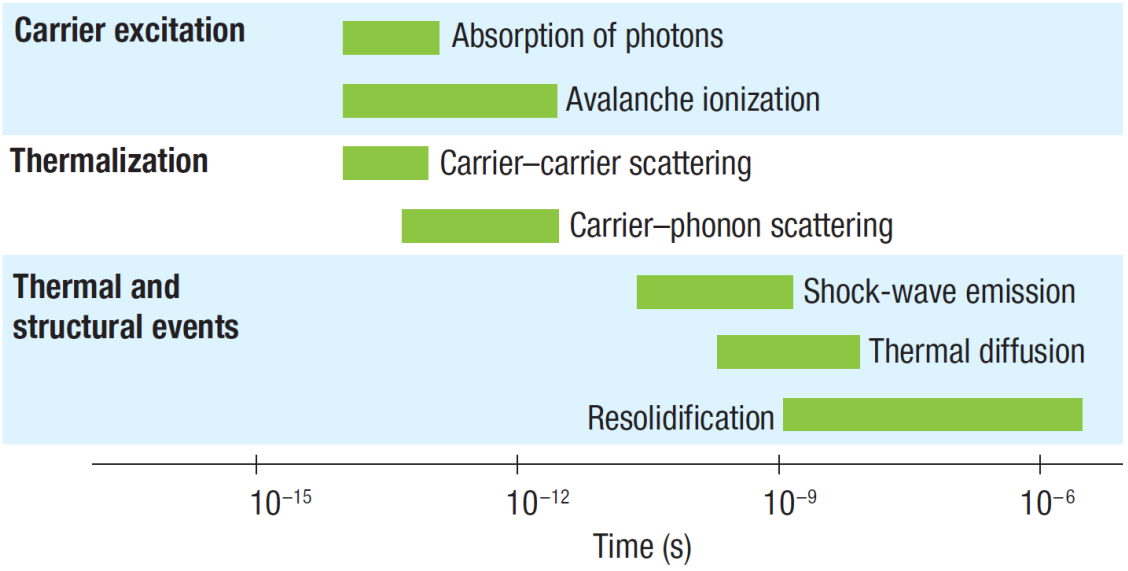

Figure 1.30: Timescale of the physical phenomena associated with the interaction of laser pulses with transparent materials. The green bars represent typical timescales for the relevant process. Image taken from Ref. [Gattass et al., 2008].

As shown in Fig. (1.30), the energy transfer from free-carrier to the lattice takes place in the picosecond time range. Further hydrodynamics interactions occur at times higher than hundreds of picoseconds. Thus, femtosecond laser pulses do not affect energy transfer to the lattice and further processes. The main interaction process in the femtosecond time scale is electron heating which will prevent further damage due to shock waves and thermal diffusion [Gamaly et al., 2013].

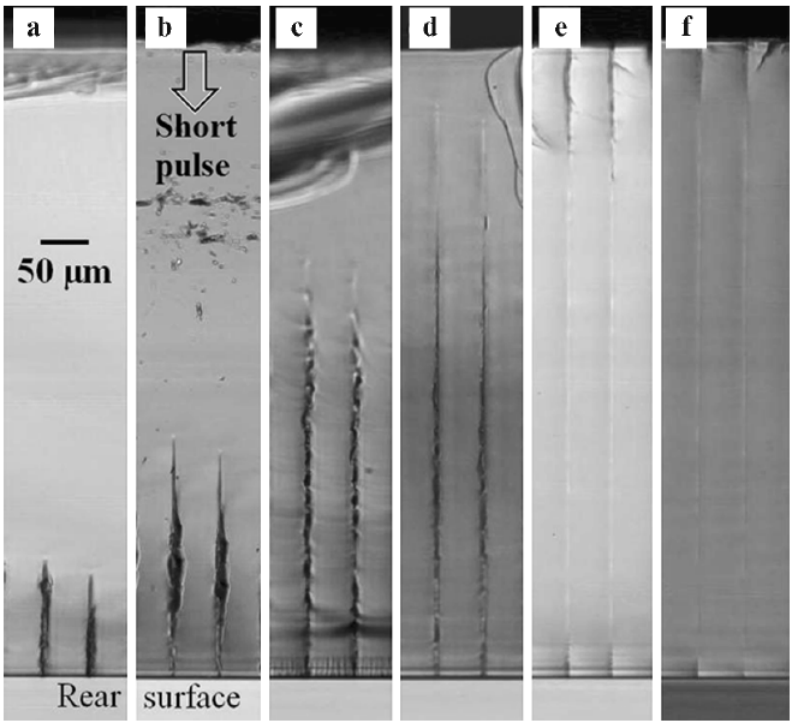

Figure 1.31: Impact of increased spherical aberrations in elongating laser induced-channels [Ahmed et al., 2014].

1.2.6.2/ HIGH ASPECT RATIO LASER PROCESSING

There are two different categories of the application of laser pulses in materials processing: laser surface processing and high aspect ratio materials processing. Light filamentation is well suited for high-aspect-ratio processing of transparent materials. It has been shown that Bessel filaments could perform deep drilling in transparent materials with an aspect ratio superior to 100:1 [Bhuyan et al., 2010], which is unattainable for Gaussian filaments [Ahmed et al., 2014] and other drilling technologies such as DRIE [Wu et al., 2010] and electrochemical discharge machining [Jui et al., 2013]. Of course, this in only valid in transparent materials since opaque media prevent the establishment of conical energy flux and thus the formation of filaments.

Laser-induced channels using femtosecond Gaussian beams: White et al. demonstrated deep laser drilling in fused silica with an aspect ratio greater than 20:1 using single-shot femtosecond Gaussian beams [White et al., 2008]. Herbstman et al. also showed that single-shot femtosecond Gaussian beams can induce sub-micro channels in glass with a length greater than the Rayleigh range [Herbstman et al., 2010]. These experiments showed that the aspect ratio of laser-induced channels can be further enhanced by filamentation. It was later demonstrated that the enhancement of filamentation by means of spherical aberrations can further increase the length of laser-induced channels (Fig. 1.31). This was performed by placing thick glass plates between focusing optical element and samples [Ahmed et al., 2014].

Generally, laser-drilled channels using Gaussian filaments are not uniform, which is clearly shown in Fig. 1.31. Indeed, and as discussed above, light filaments formed from

input Gaussian beams are generally difficult to control because of the pronounced spatio-temporal reshaping involved in the filament formation. Therefore, it is hard to predict the conditions for which long and uniform nanochannels can be formed.

Laser-induced channels using femtosecond Bessel beams: In contrast to Gaussian filaments, propagation-invariant Bessel filaments can be directly formed in the steady nonlinear propagation regime. High-aspect ratio laser drilling was demonstrated using single-shot pulsed Bessel beams [Bhuyan et al., 2010, Bhuyan et al., 2011, Bhuyan et al., 2014, Mitra et al., 2015]. In the example shown in Fig. ([Courvoisier et al., 2016b],top), the nanochannel has an aspect ratio of about 100:1 and was drilled using a 230-fs Bessel pulse with a input energy of 3.1 μJ and a cone angle of $\theta = 11^\circ$ in glass. In addition, the process of laser drilling using femtosecond Bessel beams was demonstrated to be highly reproducible [Bhuyan et al., 2010] which was attributed to the robustness of Bessel filaments to spatio-temporal reshaping (such as transverse beam break-up) at ablation-level intensities. These experiments showed that Bessel beams are more advantageous than Gaussian beams in transparent materials processing applications.

The sequence of Bessel-beam laser drilling is shown in Fig. ([Courvoisier et al., 2016b],bottom), the conical structure of Bessel beams yields a uniform energy deposition over the whole Bessel zone of the beam, which results in the generation of uniform plasma channels. Afterwards, the energy gained by the plasma is transfered to the lattice whose phase is changed as a result. Then, an elongated void is left after that the phase-modified material is removed from the sample or compressed on the channel sides. The void formation mechanism is not yet clear.

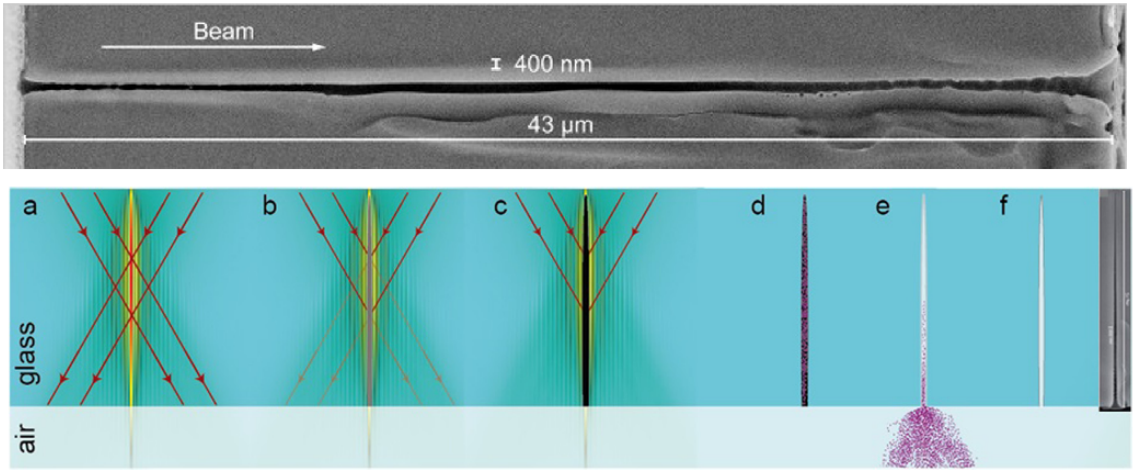

Figure 1.32: (top) SEM image of a nanochannel drilled by a single-shot femtosecond Bessel beam [Bhuyan et al., 2010] and (bottom) Sequence of glass drilling using Bessel beams [Courvoisier et al., 2016b].

One can further increase the dept of nanochannel (and thus the aspect ratio) by decreasing the cone angle. However, in this case, the Bessel filaments may propagate according to the unsteady filamentation regime. As previously discussed, this regime is characterized by the modulation of longitudinal intensity of the beam central core and one may obtain periodic ablation traces instead of uniform channels [Gaizauskas et al., 2006].

1.3/ CONTRIBUTIONS OF MY THESIS

In the high power laser applications described above, Bessel beams are usually generated using either refractive or diffractive axicons. A Bessel beam generated using these optical elements exhibits a significant variation of central core intensity along propagation. Generally, one has to use only a portion of the Bessel zone where the central core intensity is nearly constant [Bhuyan et al., 2010]. In addition, the longitudinal distribution of laser-generated plasma depends on the exact intensity value at a given propagation distance. For example, Hine et al. showed that, by modulating the on-axis intensity of Bessel beams, the longitudinal density distribution of the generated electrons varies according to the chosen intensity profile [Hine et al., 2016]. This shows that plasma shaping is necessary to extend the applicability of Bessel beams and further improve laser-based technologies. For example, plasma shaping can allow further control over matter modification such as the amount of the induced-damage and refraction index modification. This thesis is focused on three points:

1.3.1/ ON-AXIS INTENSITY SHAPING OF BESSEL BEAMS

The first step in controlling longitudinal plasma distribution is the capability to arbitrarily shape the on-axis intensity profile of Bessel beams. So far, this point has been extensively studied by some groups [Čižmár et al., 2009, Zamboni-Rached, 2004, Zamboni-Rached et al., 2005]. Prior to our work, arbitrary shaping of Bessel beams was performed using either Fourier-space beam shaping [Čižmár et al., 2009] or using amplitude-only SLMs [Vieira et al., 2014]. Both beam shaping techniques generally yield very low energy throughput which makes them unsuitable in high power laser applications.

In the second chapter, I will present my work on on-axis intensity shaping of Bessel beams by means of phase-only SLM. I will describe our experimental procedure and present our numerical and experimental results.

1.3.2/ CONTROL OF NONLINEAR INSTABILITIES IN UNSTEADY BESSEL FILAMENTS

As described in the previous section, Bessel beams can propagate according to unsteady nonlinear regime which may prevent the formation of uniform plasma channels. This undesired effect has been shown to be caused Kerr-induced instabilities. These instabilities consist in the generation of new spectral components through four wave mixing process [Gadonas et al., 2001]. The observed longitudinal intensity modulation was thus interpreted as the interference of the input conical beam with the newly generated spectral components. This effect will, of course, prevent controlling plasma shapes.

Actually, this issue has been studied previously and various means have been proposed to avoid it [Porras et al., 2004, Polesana et al., 2007]. One way is to enhance nonlinear losses, specifically, multiphoton absorption in order to compensate for Kerr induced nonlinearities [Couairon et al., 2012]. This can be achieved by increasing the cone angle and/or the intensity of the input Bessel beam. However, this means that one should avoid some experimental configurations [Porras et al., 2004, Polesana et al., 2008]. The inter-

est of low cone angle Bessel beams, for which Kerr-induced instabilities are predominant, is their long focal distance as well as the possibility to reduce the diameter of laser ablated traces [Bhuyan et al., 2014]. In the third chapter, I will analytically and numerically discuss the causes of these instabilities. I will also show the possibility to control these instabilities by means of on-axis intensity shaping of Bessel beams.

1.3.3/ MODELING OF BESSEL FILAMENTATION

The last point concerns the modeling of the propagation of Bessel pulses in the filamentation and ablation regimes. As discussed above, filamentation modeling remains a hot topic since there are still some features that could not be explained by existing models. In our group, we have performed many experiments on Bessel filamentation in glass and especially fused silica. Our results show that Bessel filaments can conserve their propagation-invariant features even at ablation-level intensities. However, numerical simulations based on generalized nonlinear Schrödinger equation [Polesana et al., 2008, Couairon et al., 2007] predict that the Bessel filaments exhibit a spatial expansion of the central core. Regarding the topic of this thesis, filamentation modeling is necessary in order to study the effect of on-axis intensity shaping of Bessel beams on the distribution of laser-induced plasma. In the fourth chapter, I will present numerical simulation results using different existing models. I will compare results and point out the necessity to develop a novel model to explain the propagation-invariance of Bessel filaments in the ablation regime.

2

ARBITRARY ON-AXIS INTENSITY SHAPING OF BESSEL BEAMS

INTRODUCTION

We have discussed in the first chapter the main properties of quasi-Bessel beams. One of the drawbacks of spatial apodization is that since the nondiffracting length is limited in space, the intensity of the Bessel beam varies significantly from the beginning to the end of the Bessel zone. Such undesired feature restricts the applicability of Bessel beams in applications [Čižmár et al., 2009]. For instance, in optical trapping, optical forces used to manipulate micro-particles depend on the intensity value of the laser beam [Arlt et al., 2001] . In materials processing, precise value of the beam intensity along the propagation distance is often required for high aspect ratio drilling. In these applications, only a restricted area of the Bessel zone where the intensity is quasi-constant is generally used [Bhuyan et al., 2010]. Hence, arbitrary shaping of the on-axis intensity of Bessel beams offers the possibility to extend their applicability in many fields of applications.

The first research studies on controlling the on-axis intensity of Bessel beams were focused on generating Bessel beams with constant intensity profile. In the early 1990s, axicons with logarithmic phase retardation have been developed [Sochacki et al., 1993]. However, although this optical element can generate Bessel beams with flat-top intensity profile, it exhibits significant intensity oscillations [Sochacki et al., 1993, Golub et al., 2010]. In addition, the cone angle of such Bessel beam varies along the propagation distance, which limits the applicability of logarithmic axicons.

In 2004, Zamboni-Rached first introduced a theoretical approach to arbitrarily shape the on-axis intensity of Bessel beams [Zamboni-Rached, 2004, Zamboni-Rached et al., 2005]. His approach is based on superposing Bessel beams with the same temporal frequency but having different transverse spatial frequencies. It was shown that the on-axis intensity pattern of the resulting Bessel beam can be expanded in Fourier series. Hence, for a given profile of the on-axis intensity in finite propagation length, it is possible to compute the corresponding spatial distribution in Fourier space. This formalism has been generalized to dispersive media and further developed to engineer the beam polarization along propagation [Vieira et al., 2015].

In 2009, Cizmar and Dholakia developed a similar approach which is also based on the superposition of J_0 beams with different transverse wavenumbers [Čižmár et al., 2009]. Instead of Fourier series expansion, the spectral distribution of the target Bessel beam

is computed using the inverse Fourier transform of the corresponding on-axis intensity profile.

Regardless of the theoretical approach, longitudinal intensity shaping of Bessel beams requires simultaneous modulation of the amplitude and phase of an input light beam [Vieira et al., 2014, Čižmár et al., 2009]. Generally, optical elements, including spatial light modulators (SLMs), can modulate either the amplitude or the phase separately. Hence, for simultaneous amplitude and phase modulation, it is necessary to use two optical elements. However, it was demonstrated that both information can be encoded on a single spatial light modulator [Kirk et al., 1971, Davis et al., 1999, Bolduc et al., 2013, Arrizón et al., 2005, Mendoza-Yero et al., 2014, Clark et al., 2016, Arrizón et al., 2007].

Prior to our work, the experimental methods based on SLMs were shown to generate arbitrarily shaped Bessel beams with high beam quality but with very low energy throughput [Čižmár et al., 2009, Li et al., 2014, Vieira et al., 2014, Vieira et al., 2015]. Cizmar et al. experimentally demonstrated the generation of Bessel beam of modified on-axis intensity profiles using a single phase-only SLM. Li et al. also used the same technique to generate axially shaped self-imaging bottle beams [Li et al., 2014]. Experimental results showed good agreement between simulation and experiments. Vieira et al. reported the generation of such modified Bessel beams using single amplitude-only SLM [Vieira et al., 2014, Vieira et al., 2015].

In this thesis, our objective is to generate Bessel beams with arbitrary longitudinal intensity profile which we aim to apply in laser filamentation in Kerr media. Thus, we chose an experimental technique that yields relatively high beam quality and also a high energy throughput.

In the first section, we will first present the theoretical framework of arbitrary manipulation of the on-axis intensity of Bessel beams as described in [Čižmár et al., 2009]. In the second section, we will present different techniques based on a single SLM. We will then specifically present our chosen method based on both reproduced beam quality and energy throughput. Afterwards, we will present our numerical and experimental results.

2.1/ THEORETICAL BACKGROUND

Let $U(x, y, z = 0)$ [1] be the complex amplitude of the light field defined in a transverse plane (x, y) at an initial propagation point $z = 0$ and $S(k_x, k_y, z = 0)$ the corresponding spatial spectrum. Here, k_x and k_y are the spatial frequencies corresponding to the transverse variables x and y. The optical amplitude is computed from the beam spectrum $S(k_x, k_y, z = 0)$ via inverse Fourier transform as follows:

$$U(x, y, z = 0) = \frac{1}{4\pi^2} \int_{-\infty}^{\infty} S(k_x, k_y, z = 0) \mathrm{e}^{i(k_x x + k_y y)} \, \mathrm{d}k_x \, \mathrm{d}k_y \tag{2.1}$$

Since a Bessel beam is azimuthally independent, the optical field can be calculated from

[1] In this thesis, I choose to express the amplitude in terms of $W^{1/2}/cm$ instead of V/cm, unless stated otherwise.

its corresponding spectrum using Hankel transformation [Čižmár et al., 2009]:

$$U(r, z = 0) = \frac{1}{2\pi} \int_0^\infty S(k_r, z = 0) J_0(k_r r) k_r \, \mathrm{d}k_r \tag{2.2}$$

r is the radial variable and is defined by $r = \sqrt{x^2 + y^2}$; k_r is the corresponding spatial frequency and is defined by $k_r = \sqrt{k_x^2 + k_y^2}$. From this expression, we can deduce the axial pulse envelope $U(r = 0, z)$ at the center of the Bessel beam (r = 0) [Čižmár et al., 2009]. Provided that $k_r = \sqrt{k^2 - k_z^2}$, where k_z is the longitudinal spatial frequency, $dk_r = -k_z dk_z / k_r$. Thus, equation (2.2) becomes:

$$U(r, z = 0) = -\frac{1}{2\pi} \int_0^\infty S(\sqrt{k^2 - k_z^2}, z = 0) J_0(k_r r) k_z \, \mathrm{d}k_z \tag{2.3}$$

N.B. in Ref. [Čižmár et al., 2009], there is no (-) sign in equation (2.3) which naturally has no impact on the on-axis intensity profile.

For $z > 0$, the integrand of equation (2.3) is multiplied by the propagation term $\mathrm{e}^{ik_z z}$. Given that the Bessel function $J_0(k_r r)$ is equal to 1 for $r = 0$, the field on-axis envelope $U(r = 0, z)$ is given by:

$$U(r = 0, z) = -\frac{1}{2\pi} \int_0^k k_z S(\sqrt{k^2 - k_z^2}, z = 0) \mathrm{e}^{ik_z z} \, \mathrm{d}k_z \tag{2.4}$$

where $k = 2\pi/\lambda$ is the wavevector and λ is the wavelength of the input beam. We note that the superior limit of this integral is k and not ∞ since evanescent modes do not propagate over distances superior to the light wavelength as considered here [Čižmár et al., 2009]. This expression shows that the on-axis envelope is defined as the inverse Fourier transform of the function $k_z S(\sqrt{k^2 - k_z^2}, z = 0)$ provided that the latter is equal to 0 outside the interval $[0, k]$. $U(r = 0, z)$ can be written as $\sqrt{I(z)}\mathrm{e}^{ik_{z0}z}$, where $I(z)$ is an arbitrary form of the on-axis intensity and $k_{z0} = k\cos(\theta)$ where θ is the conical angle [Čižmár et al., 2009]. This phase term thus defines a conical beam (Bessel beam). Consequently, the beam spatial spectrum can be computed from the corresponding on-axis intensity as follows [Čižmár et al., 2009]:

$$S(\sqrt{k^2 - k_z^2}, z = 0) = \frac{1}{k_z} \int_{-\infty}^{+\infty} \sqrt{I(z)} \mathrm{e}^{i(k_{z0} - k_z)z} \, \mathrm{d}z \tag{2.5}$$

Therefore, it is possible to shape a Bessel beam with any physically realizable form of the on-axis intensity in the linear regime thanks to Eq. (2.5).

2.2/ SPATIAL AMPLITUDE AND PHASE SHAPING USING A SINGLE SLM

According to Eq. (2.5), in order to experimentally realize Bessel beams with arbitrary shape of the on-axis intensity, it is necessary to perform a simultaneous modulation of the amplitude and phase of an incoming beam [Čižmár et al., 2009]. Throughout the years, many methods have been proposed to this end. Most of these techniques are based on phase-only holograms imprinted on a SLM. There is also an experimental approach to encode the complex field information on a digital micro-mirror device (DMD) [Rodenburg et al., 2014]. However, the quality of Bessel beams produced by DMDs is generally lower [Gong et al., 2013] than that generated by SLMs [Čižmár et al., 2009], which is not suitable for high power laser applications.

Actually, SLMs can either modulate or phase of an input beam and generally cannot perform both tasks simultaneously. Hence, the most basic method is to use two SLMs to independently modulate the amplitude and phase of an input light field [Neto et al., 1996]. However, this method presents many drawbacks since the use of two SLMs is costly and more importantly it yields a very low diffraction efficiency. Fortunately, many other methods have been reported where both amplitude and phase can be encoded in a single hologram. We can categorize these techniques depending on the reconstruction space. A computer-generated hologram can be designed to reconstruct a Bessel beam either in direct space or Fourier space.

We recall that we aim to generate arbitrarily-shaped Bessel beams for high power laser applications. In this regard, the experimental technique we choose should guarantee a relatively high energy throughput which is appropriate for these applications. Furthermore, this technique should allow a high control over the peak intensity reached by the shaped Bessel beam along propagation. In this section, we will present a brief overview on amplitude and phase shaping techniques and compare their performances. Since we are interested in arbitrary beam shaping, we solely consider techniques based on SLMs. Then, we will specifically present our chosen technique and describe the experimental setup used in our experiments.

2.2.1/ FOURIER-SPACE BEAM SHAPING

Cizmar et al. proposed an amplitude and phase beam shaping technique using a phase-only SLM [Čižmár et al., 2009] which was applied to generate quasi-Bessel beams from Fourier space. Amplitude modulation imposes that information of the target field can only be encoded into a limited area of the phase mask. As it is the case for Fourier-space Bessel beam generators, this area correspond to a ring [Čižmár et al., 2009], as shown in Fig. (2.1,left). The expression of the target Bessel beam is firstly computed using Eq. (2.5). Then, the corresponding hologram is computed using numerical iteration according to Gerchberg-Saxton algorithm.

Actually, this experimental technique is very precise and allows the generation of high quality beams. Target on-axis intensity profiles of Bessel beams can be reproduced with high accuracy [Čižmár et al., 2009, Li et al., 2014]. An example is shown in Fig. (2.1,right) where a comparison is made between numerical and experimental results of the generation of a Bessel beam with constant on-axis intensity. However, since the area

where the amplitude and phase are encoded on the SLM is very small, most of the light diffracted from the SLM will be lost. Hence, this experimental approach yields a very low energy throughput.

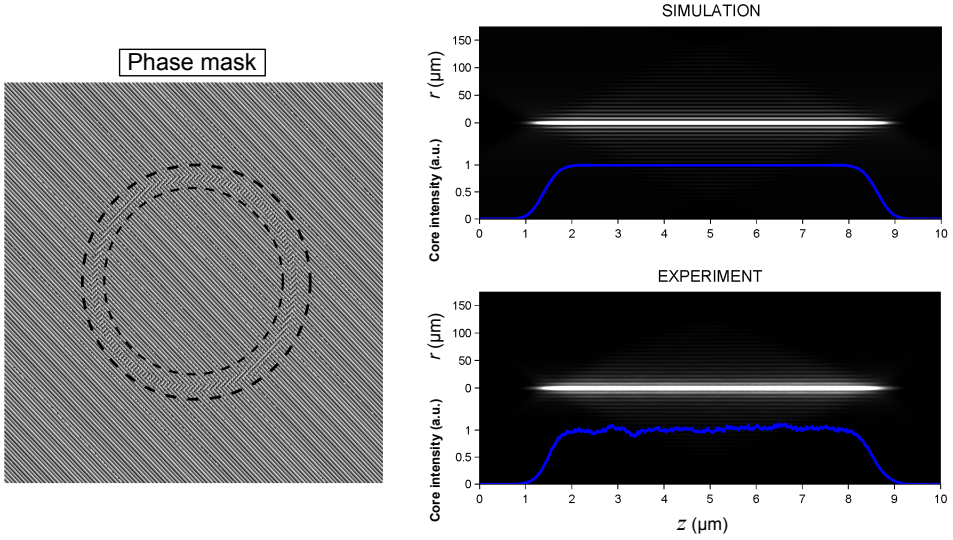

Figure 2.1: (left) phase-only hologram for arbitrary on-axis intensity shaping and (right) comparison between numerical and experimental results of the generation of a Bessel beam with constant on-axis intensity profile. Images taken from [Čižmár et al., 2009].

2.2.2/ DIRECT-SPACE BEAM SHAPING

In order to generate Bessel beams with relatively high energy throughput, it is better to encode information of the target Bessel beams in direct-space since the spatial amplitude of Bessel beams in this space occupies a larger area compared to that in Fourier space.

Prior to our work, and to our knowledge, only one experimental technique was used to arbitrarily shape the on-axis intensity of Bessel beams from direct space [Vieira et al., 2014, Vieira et al., 2015]. This technique was introduced by Arrizon et al. and consists in encoding the amplitude and phase of a target field on a single amplitude-only hologram [Arrizón et al., 2007]. In contrast with the iterative nature of the technique reported by Cizmar in [Čižmár et al., 2009], this one is deterministic which allows direct computation of the hologram given the exact expression of the target field. An example is shown in Fig. (2.2) where the target on-axis intensity shape is made of three flat-top profiles.

This technique is indeed very accurate since it guarantees a good consistency between theoretical and experimental results. Nonetheless, it is actually recommended to encode the amplitude and phase modulation on phase-only hologram instead of an amplitude-only one. As shown in Fig. (2.3), a polarizer and an analyzer optical components are added in order to perform amplitude modulation. Consequently, the energy throughput of an amplitude-only SLM is generally lower than that provided by a phase-only SLM. For this reason, we choose an experimental method based on a phase-only SLM.

There is no unique way to encode the target amplitude and phase onto a single phase-only hologram [Kirk et al., 1971, Davis et al., 1999, Bolduc et al., 2013, Arrizón et al., 2005, Mendoza-Yero et al., 2014]. One technique consists in decomposing the target field into a superposition of two fields with two different phase profiles. The

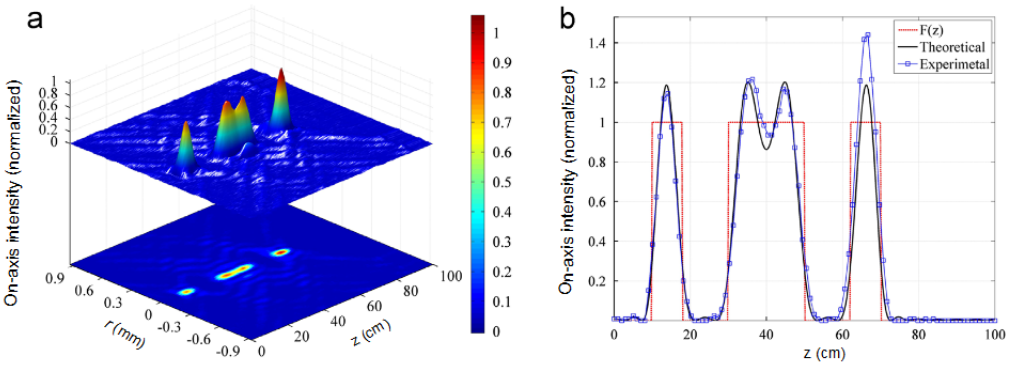

Figure 2.2: Numerical and experimental data of a Bessel beam whose intensity profile is made of three separate flat-top shapes (a) 3D intensity map and (b) the corresponding on-axis intensity profiles. Images taken from [Vieira et al., 2014].

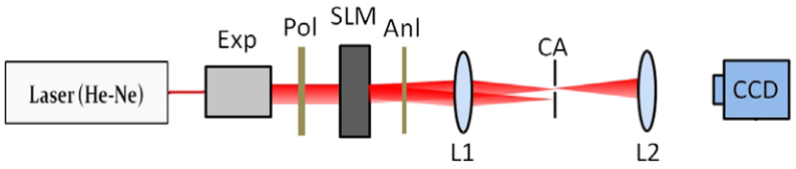

Figure 2.3: Experimental setup for amplitude and phase shaping using an amplitude-only hologram. Exp: beam expander, Pol: polarizer, Anl: analyzer and CA: circular aperture mask. Figure is taken from [Vieira et al., 2014].

phase mask is then expressed as a function of these two phase profiles and consists of two interlaced phase holograms. This technique allows the reconstruction of the target field at the zeroth diffraction order [Mendoza-Yero et al., 2014].

A second approach allows the generation of the target field in the first order of diffraction: the amplitude is obtained by modulating the level of phase wrapping, which is directly linked to the diffraction efficiency. This approach was first introduced by Davis et al. [Davis et al., 1999].

To illustrate its principle, let's consider a one dimensional refractive blazed grating which can be assimilated to a column of a phase-only hologram. Normally, a blazed hologram should have a maximal phase depth of 2π in order to maximize the diffraction efficiency. Theoretically, a light beam incident to such grating would be totally deflected at the first diffraction order, as depicted in Fig. (2.4,a). If the phase depth is decreased, for example, to π, then a part of the incident beam passes through the grating unmodulated which results in a decrease in the diffraction efficiency. Thus, only a part of the incident beam is deflected at the first diffraction order. The rest is deflected in the unmodulated zeroth diffraction order. However, it is this undesired effect that is used to modulate the amplitude: if the phase depth is modulated according to a specific pattern, one can include amplitude modulation in a phase-only hologram. This feature is illustrated in Fig. (2.4,c).

This technique was further improved by Bolduc et al. [Bolduc et al., 2013]. As we will show in the next section, the approach of Davis et al. does not allow retrieving the target field accurately. Bolduc et al. showed how to accurately encode the amplitude and phase of the target field on a single phase-only hologram. In our work, we choose this improved technique since it is theoretically very accurate as reported in Ref. [Bolduc et al., 2013].

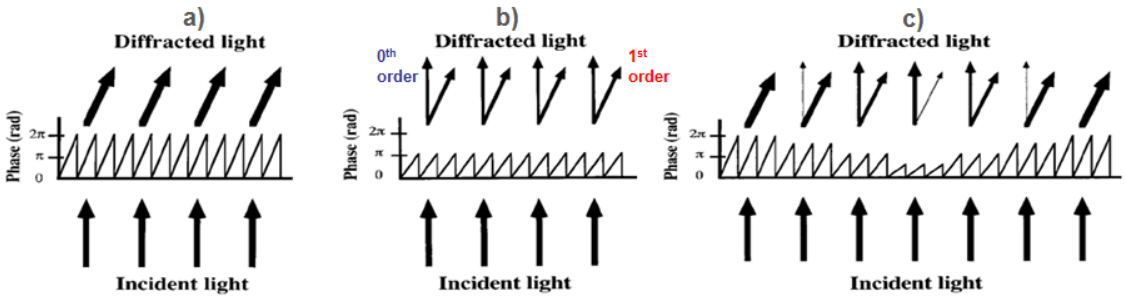

Figure 2.4: Principle of amplitude and phase beam shaping using a single phase-only hologram. Images taken from Ref. [Davis et al., 1999]

Indeed, Clark et al. [Clark et al., 2016] compared the performances of different techniques including the methods of Arrizon et al. [Arrizón et al., 2005, Arrizón et al., 2007], the method of Davis et al. [Davis et al., 1999] and the improved version proposed by Bolduc et al. They showed that the latter is the most accurate. In addition, the energy throughput of these techniques is similar and ranges between 12 and 18 $\%$. Hence, the method of Bolduc et al. holds an advantage over the other methods as stated in Ref. [Clark et al., 2016]. In the next section, we will present a detailed description of this technique. We will first describe our experimental setup and then show how to compute the expression of the phase mask corresponding to target fields.

2.3/ OUR EXPERIMENTAL APPROACH

2.3.1/ EXPERIMENTAL SETUP

In our experiments, we used a Liquid Crystal On Silicon phase-only SLM (LCOS-SLM) provided by Hamamatsu which belongs to the series X10468-02. We present its characteristics in table (2.1).

Quantity	Value
Wavelength	$750 - 850\ nm$
Active area	$[16\ mm, 12\ mm]$
Number of pixels	[792, 600]
Pixel pitch	x $20\ \mu m$
Modulation depth	$\geq 2\pi$

Table 2.1: SLM characteristics used in our experiments.

Our setup is described in Fig. (2.5). The light source is an amplified Titanium:Sapphire (Ti:Sa) laser emitting 120 fs pulses at a wavelength of 800 nm. Its transverse intensity shape is assimilated to a Gaussian distribution of diameter 4.7 mm at $1/e^2$. The beam is polarized at the same direction as that of the SLM liquid crystals. The laser field is set in an oblique-incidence configuration with respect to the SLM at a small angle of 7°.

The back-reflected field is separated at different diffraction orders which then pass through a 4f optical system with a total demagnification factor of 1/55. This system is made of two optical elements: the first is a lens, with a focal distance f_1 of 1 m, placed

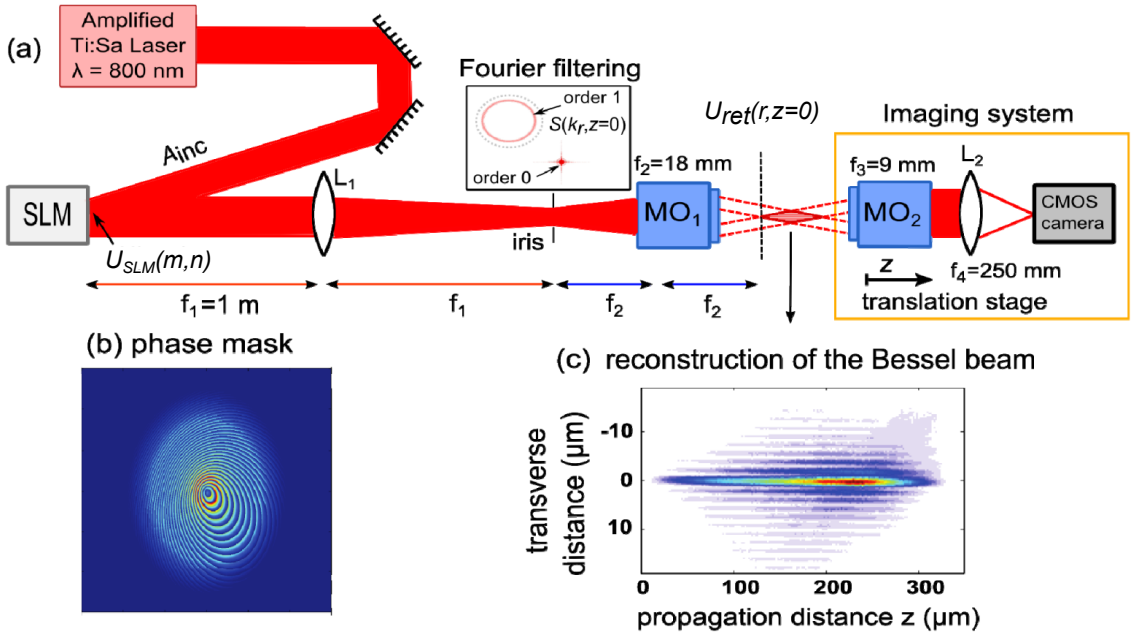

Figure 2.5: Experimental setup using LCOS-SLM . A_{inc} is the amplitude of the incident laser beam, $U_{SLM}(m,n)$ is the beam spatial envelope reflected on the SLM, $S(k_r, z=0)$ is the spatial spectrum and $U_{ret}(r, z=0)$ is the retrieved Bessel beam envelope (b) Example of the phase mask applied on the SLM; (c) Experimentally measured Bessel beam intensity distribution.

exactly at a distance equal to its focal length from the SLM. This allows constructing the amplitude distribution of the laser beam in the far field (Fourier plane). This then allows to spatially separate the different diffraction orders to prepare spatial filtering. Knowing that information of the shaped Bessel beam is carried by the first diffraction order (which is the spatial spectrum expressed in Eq. (2.5)), we use an iris around this diffraction order and filter out all the other undesired ones. The second element is a microscope objective (MO1) with numerical aperture $NA = 0.3$. It is placed at a distance equal to its focal length away from the Fourier plane of the first lens L1. This allows performing the second optical Fourier transformation to reconstruct the Bessel beam in the real (direct) space at the longitudinal position $z = 0$ which corresponds to the image focal point of MO1.

The imaging system has a magnification of 27.7 and consists of a microscope objective MO2 (NA = 0.4), an imaging lens L2 and a CMOS camera (pixel pitch 5.2 μm), placed on a motorized translation stage. We sequentially reconstruct the beam propagation by recording images along the propagation distance z.

2.3.2/ COMPUTATION OF THE PHASE MASK

Let us consider a target light field $U_{tar}(x,y)$ with a spatial amplitude $A_{tar}(x,y)$ and phase $\phi_{tar}(x,y)$ written as:

$$U_{tar}(x,y) = A_{tar}(x,y)\exp[i\phi_{tar}(x,y)] \tag{2.6}$$

The target is defined in a transverse plane (XOY) where x and y are transverse spatial

coordinates. Considering a phase mask $\psi(x,y)$ imprinted on a SLM, an incident laser field $U_{inc}(x,y) = A_{inc}(x,y)\exp[i\phi_{inc}(x,y)]$ on the SLM will acquire the imprinted phase profile and is then expressed as:

$$U_{SLM}(x,y) = U_{in}(x,y)\exp[i\psi(x,y)] \tag{2.7}$$

Recall that our chosen technique is based on modulating the phase depth to control the amount of energy diffracted at each group of pixels of the SLM. Hence, the phase-only hologram can be expressed by a phase function $F(x,y)$ wrapped over 2π multiplied by a normalized amplitude function $M(x,y)$ which plays the role of a modulation function. The phase-only hologram, denoted $\psi(x,y)$, is then written as:

$$\psi(x,y) = M(x,y) \cdot \mathrm{mod}[F(x,y), 2\pi] \tag{2.8}$$

Different ways were suggested to define the functions $M(x,y)$ and $F(x,y)$. The common point between them is that the modulation function should depend on target amplitude $A_{tar}(x,y)$ while $F(x,y)$ depend on the target spatial phase $\phi_{tar}(x,y)$. We will first show how Davis et al. [Davis et al., 1999] defined the functions $M(x,y)$ and $F(x,y)$ and present the improvements proposed by Bolduc et al. [Bolduc et al., 2013]. Note that this technique was originally developed for incident light fields with uniform intensity distribution. We will show how to generalize this approach to non-uniform light sources.

2.3.2.1/ THE EXPRESSION OF THE LIGHT FIELD AT THE FIRST DIFFRACTION ORDER

A light beam, of amplitude A_{inc}, incident to the SLM will acquire a spatial phase in the form of the multiplicative $\exp(i\psi(x,y))$. Considering the pixelization of the back-reflected field, the continuous transverse variables x and y will be reduced to discrete variables defined at the SLM pixels m and n respectively. The back-reflected field, denoted U_{SLM}, can be written as:

$$U_{SLM}(m,n) = A_{inc}\exp(i\psi(m,n)) \tag{2.9}$$

Davis et al. considered the special case of an incident plane wave ($A_{inc} = 1$). They showed that the quantity $U_{SLM}(m,n)$ can be expanded into a Fourier-Taylor series. It is given by:

$$U_{SLM}(m,n) = \sum_{-\infty}^{+\infty} U_q(m,n)\exp(iq\,F(m,n)) \tag{2.10}$$

The index q can be interpreted as the diffraction order of the back-reflected. The coefficients $U_q(m,n)$ are written as:

$$U_q(m,n) = \exp\{i[q - M(m,n)\pi]\}\mathrm{sinc}\{\pi[q - M(m,n)]\} \tag{2.11}$$

The retrieved light beam at the first diffraction order, denoted U_{ret}, is then expressed as [Bolduc et al., 2013]:

$$U_{ret}(m,n) = -\mathrm{sinc}[\pi\,(M(m,n) - 1)]\exp[i(F(m,n) + \pi M(m,n)))] \tag{2.12}$$

2.3.2.2/ THE EXPRESSION OF THE FUNCTIONS M AND F

Davis et al. first proposed to linearly scale the target amplitude distribution $A_{tar}(x,y)$ to the target phase function $\phi_{tar}(x,y)$. In other words, the functions $M(x,y)$ and $F(x,y)$ are simply assimilated to $A_{tar}(x,y)$ and $\phi_{tar}(x,y)$ respectively [Davis et al., 1999]. The phase mask has then the following expression:

$$\psi(x,y) = A_{tar}(x,y) \cdot \mathrm{mod}[\phi_{tar}(x,y), 2\pi] \tag{2.13}$$

Equation (2.12) shows that the amplitude of the reconstructed light field is $A_{ret}(m,n) = -\mathrm{sinc}[\pi\,(A_{tar}(m,n) - 1)]$ whereas its phase is $\phi_{ret}(m,n) = \phi_{tar}(m,n) + \pi A_{tar}(m,n)$. Hence, the target amplitude and phase are not accurately retrieved using the method of Davis et al.

Bolduc et al. introduced an improved method where the expressions of the functions $M(x,y)$ and $F(x,y)$ are chosen so that the reconstructed light beam at the first diffraction order has the exact expression of the target light beam $U_{tar}(x,y)$. Identifying Eqs. (2.6) and (2.12) yields:

$$M(x,y) = 1 + \frac{1}{\pi}\mathrm{sinc}^{-1}(A_{tar}(x,y)) \tag{2.14}$$

$$F(x,y) = \phi_{tar}(x,y) - \pi M(x,y) \tag{2.15}$$

Bolduc et al. have also compared the performance of both techniques in the generation of a light beam whose transverse intensity is made of the superposition of two Laguerre-Gaussian modes. In their experiment, they approximated the modulation function $M(x,y)$ by $A_{tar}(x,y)$ as it was suggested by Davis et al. whereas they kept the proposed expression of phase function $F(x,y)$ given by Eq. (2.15). Since, this expression allows removing the coupling between the phase and amplitude in the phase mask, their experiment highlighted the impact of phase-amplitude decoupling on the quality of reconstructed beams.

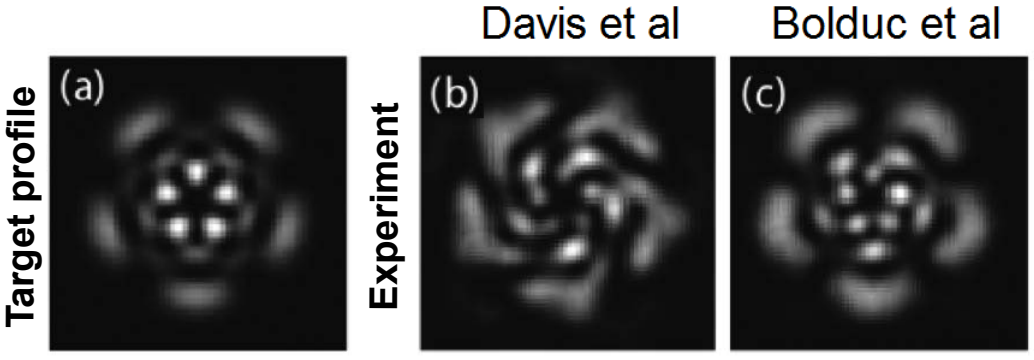

Figure 2.6: Qualitative comparison of the method of Davis et al. [Davis et al., 1999] and that of Bolduc et al. [Bolduc et al., 2013]. The target intensity profile purposely has small features to accentuate the difference between the two methods. The experimentally recorded images are taken in the far-field of a HOLOEYE SLM. Image taken from [Bolduc et al., 2013].

As shown in Fig. (2.6), the target field was fairly reproduced using the approximated version of the method of Bolduc et al. compared to that of Davis et al. As mentioned

above, Clark et al. compared the performances of these two methods [Clark et al., 2016] and showed that, when it comes to precision and beam quality, the method proposed by Bolduc et al. generally yields the best results.

Note that major works on amplitude and phase shaping only consider uniform incident beams. For incident beams with a Gaussian intensity profile, such as those emitted by femtosecond laser sources, one has to use a beam expander to approximate the incident laser beam to a plane wave. Since we aim to optimize the energy conversion of our setup, we have considered the intensity distribution in the computation of phase masks. This point was also considered by Clark et al. in their paper [Clark et al., 2016] where the non-uniformity of the incident light field was accounted for in the expression of phase masks. Thus, accounting for the incident beam amplitude A_{inc}, and considering that the corresponding phase is flat, we show that the expression of the phase mask can be written as (see appendix section 4.3):

$$M(x,y) = 1 + \frac{1}{\pi}\mathrm{sinc}^{-1}(A_{tar2}(x,y)) \tag{2.16}$$

$$F(x,y) = \phi_{tar}(x,y) - \pi M(x,y) \tag{2.17}$$

where $A_{tar2} = A_{tar}/A_{inc}$ and should be normalized: $0 \leq A_{tar2} \leq 1$.

To summarize, the design of our phase masks is performed in the following sequence:

1. We compute the spatial spectrum corresponding to a Bessel beam with a specific profile of the on-axis intensity using Eq. (2.5).
2. We compute the corresponding optical envelope U_{tar} in real space using 2D inverse Fourier transform.
3. We experimentally measure the intensity profile of the incident laser beam $|A_{inc}|^2$ and then compute and normalize the quantity $A_{tar2} = A_{tar}/A_{inc}$.
4. We compute the functions M and F to prepare their encryption on our SLM.

2.4/ THEORETICAL AND NUMERICAL ANALYSIS

We have described in section 2.1 the theory of arbitrary shaping of the on-axis intensity of Bessel beams reported in Ref. [Čižmár et al., 2009]. As stated in Eq. (2.5), i.e: $S(\sqrt{k^2 - k_z^2}, z = 0) = \frac{1}{k_z}\int_{-\infty}^{+\infty} \sqrt{I(z)}\mathrm{e}^{i(k_{z0}-k_z)z}\,\mathrm{d}z$, this theory consists in computing the spatial spectrum $S(\sqrt{k^2 - k_z^2}, z = 0)$ of a Bessel beam for a target profile of the on-axis intensity $I(z) \equiv I(r = 0, z)$. Of particular interest, we pointed out the fact that the spatial spectrum should be strictly defined in the range of longitudinal frequencies $k_z \in [0 - k]$ where k is the wavenumber of the beam. This point was discussed by Cizmar et al. [Čižmár et al., 2009]; they showed that spatial spectra defined outside this frequency range cannot be fairly reproduced. Hence, the concept of arbitrary shaping of Bessel beams is constricted to target on-axis intensity shapes that are physically realizable.

In this section, we will discuss the physical limitations imposed on spatial spectra of Bessel beams and their impact on retrieved on-axis intensity profiles. To this end, we will use numerical simulations of the propagation of Bessel beams in the linear regime. Firstly, we will briefly describe our numerical approach to study the linear propagation of shaped Bessel beams. Then we will introduce physical criteria allowing fair reproduction of target fields of Bessel beams and present our numerical simulation results.

2.4.1/ PLANE WAVE SPECTRUM AND WAVE PROPAGATION

In this chapter, we consider the propagation of Bessel beams in the linear regime, i.e. in case the light power is low enough to not trigger nonlinear effects. Our numerical method is based on the plane wave spectrum representation since it is easy to implement and allows accurate computation of scalar optical fields at any point of the propagation distance. Let's first recall the principle of this numerical approach and then briefly present our numerical algorithm.

We consider a light wave defined by the complex amplitude $U(x, y, z)$ in the spatial domain; its temporal component is neglected. Note that since our modified Bessel beams are theoretically computed using the scalar approximation, we consider that these optical fields are linearly polarized along a given direction $\mathbf{e}_x$ and that this polarization is conserved along propagation.

The light wave is defined on a transverse plane (x, y) and propagates along a propagation axis z that is perpendicular to the plane (x, y). We consider that the light wave is initially defined at a plane $(x, y, z = 0)$ and it is represented by $U(x, y, z = 0)$. Our aim is to compute the complex amplitude $U(x, y, z = Z)$ of the wave at a plane $(x, y, z = Z)$ that is parallel to the plane $(x, y, z = 0)$.

The propagation of the light field $U(x, y, z = 0)$ in the linear regime can be described by Helmholtz equation:

$$(\frac{\partial^2}{\partial z^2} + \nabla_\perp^2 + k^2)U(x, y, z) = 0 \tag{2.18}$$

where $\nabla_\perp^2 = \dfrac{\partial^2}{\partial x^2} + \dfrac{\partial^2}{\partial y^2}$ is the transverse Laplacian and stands for diffraction. According to the plane wave spectrum approach is performed in three steps:

2.4.1.1/ FIELD DECOMPOSITION INTO PLANE WAVES

The complex amplitude of the input light field is decomposed into an infinite number of plane waves. It is written as:

$$U(x, y, z = 0) = \frac{1}{4\pi^2} \int_{-\infty}^{\infty} S(k_x, k_y, z = 0) \mathrm{e}^{i(k_x x + k_y y)} \, \mathrm{d}k_x \, \mathrm{d}k_y \tag{2.19}$$

This expression is seen as an inverse two-dimensional Fourier transform of the spatial spectrum $S(k_x, k_y, z = 0)$ of the light field. Similarly, the complex amplitude of the wave

at the plane $(x, y, z = Z)$ can also be expressed as a function of its spatial spectrum as follows:

$$U(x, y, z = Z) = \frac{1}{4\pi^2} \int_{-\infty}^{\infty} S(k_x, k_y, z = Z) \mathrm{e}^{i(k_x x + k_y y)} \, \mathrm{d}k_x \, \mathrm{d}k_y \tag{2.20}$$

2.4.1.2/ PLANE WAVE PROPAGATION

The second step consists in computing the spatial spectrum $S(k_x, k_y, z = Z)$ of the field at the distance $z = Z$ as a function of $S(k_x, k_y, z = 0)$ where $Z > 0$. In this regard, we consider the fact that the complex amplitude of the field $U(x, y, z = Z)$ should satisfy the Helmholtz equation (2.18). By inserting Eq. (2.20) in Eq.(2.18), we obtain:

$$\frac{\partial^2 S(k_x, k_y, z = Z)}{\partial z^2} + (k^2 - k_x^2 - k_y^2) S(k_x, k_y, z = Z) = 0 \tag{2.21}$$

An elementary solution to this differential equation can be written in the following form:

$$S(k_x, k_y, z = Z) = S(k_x, k_y, z = 0) \exp(i \, k_z z) \tag{2.22}$$

where $k_z^2 = k^2 - k_x^2 - k_y^2$ and the term $\exp(i \, k_z z)$ can be referred to as "propagator". In case $k_x^2 - k_y^2 > k^2$, i.e. $k_z < k$, the effect of propagation yields a change in the relative phase of each component of the spatial spectrum. In contrast, if $k_z > k$, then the propagator is positive and the light field is exponentially attenuated.

2.4.1.3/ RECONSTRUCTION OF THE LIGHT FIELD ALONG PROPAGATION

The third step consists in reconstructing the complex amplitude of the field in real space $U(x, y, z = Z)$ using Eq. (2.20). The expression of the complex amplitude of the optical field at any point of the propagation axis $z > 0$ can be written as:

$$U(x, y, z) = \frac{1}{4\pi^2} \int_{-\infty}^{\infty} S(k_x, k_y, z = 0) \exp[i(k_x x + k_y y + k_z z)] \, \mathrm{d}k_x \, \mathrm{d}k_y \tag{2.23}$$

N.B: Since Bessel beams are axially symmetric, we can also express the spatial spectrum of the beam using Hankel transform which is equivalent to 2D Fourier transform. This implies that the two transverse coordinates (x, y) are reduced to a single variable $r = \sqrt{x^2 + y^2}$ which allows reducing the initially two-dimensional problem to a one-dimensional one. The expression of the optical field then becomes:

$$U(r, z) = \frac{1}{2\pi} \int_{0}^{\infty} S(k_r, z = 0) J_0(k_r r) \exp(i \, k_z z) \, k_r \, \mathrm{d}k_r \tag{2.24}$$

This formalism will be specifically used in our numerical simulations of the propagation of Bessel beams in the nonlinear and filamentation regimes. In this chapter, we will

solely use the formalism based on 2D Fourier transform since we intend to study the propagation of Bessel beams with shaped on-axis intensities reconstructed by our phase-only holograms. This will also allow us to study the effect of incident laser beam and compare numerical and experimental results.

2.4.2/ PHYSICALLY REALIZABLE TARGET FIELDS

In this section, we will discuss the physical limitations related to arbitrary shaping of the on-axis intensity of Bessel beams. According to the theoretical approach presented in section 2.1, one can directly compute the spatial spectrum $S_{tar}(k_z)$ as a function of a target on-axis intensity profile $I_{tar}(z)$ (Eq. 2.5), i.e. $S_{tar}(k_z) = \frac{1}{k_z}\int_{-\infty}^{+\infty} \sqrt{I_{tar}(z)}e^{i(k_{z0}-k_z)z}\,dz$. To accurately reproduce the target intensity profile, Cizmar et al. showed that the computed spatial spectrum should be confined in the frequency range $k_z \in [0 - k]$ [Čižmár et al., 2009].

Actually, in experimental conditions, the lower limit of this spectral range is actually not zero but it is defined by the numerical aperture (NA) of the system. Hence, a lower cutoff frequency $k_z^{min} = k\sqrt{1-NA^2}$ is introduced. We also note that numerical sampling can also induce an effective numerical aperture.

In the following, we will particularly discuss the two physical limits related to the spatial spectrum: the lower limit is related to the numerical aperture (NA) of the experimental setup while the upper limit is related to the laser wavelength.

2.4.2.1/ EFFECT OF SPECTRAL TRUNCATION ON RETRIEVED ON-AXIS INTENSITY PROFILES

To study the effect of spectral truncation of the target spatial spectrum $S_{tar}(k_z)$, we consider a response function $R(k_z)$ that is equal to 1 in the range $k_z \in [k_z^{min} - k]$ and is zero outside this range. We define a truncated spatial spectrum S_{tr} as follows:

$$S_{tr}(k_z) \equiv S_{tar}(k_z).R(k_z) \quad \text{where} \quad R(k_z) = \begin{cases} 1 & , k_z \in [k_z^{min} - k] \\ 0 & , \text{otherwise} \end{cases} \tag{2.25}$$

Using Eq. (2.4), we compute the corresponding on-axis complex amplitude $U_{tr}(r=0,z)$:

$$\begin{aligned} U_{tr}(r=0,z) &= -\frac{1}{2\pi}\int_0^k k_z S(k_z).R(k_z)\exp(i\,k_z z)\,dk_z \\ &= U_{tar}(r=0,z) \otimes H(z) \end{aligned} \tag{2.26}$$

where $U_{tar}(r=0,z) = \sqrt{I_{tar}}(z)\exp(i\,k_{z0}z)$ is the target on-axis amplitude, $\otimes$ stands for the convolution product and $H(z)$ is the Fourier transform of the response function which yields:

$$H(z) = (k - k_z^{min})\text{sinc}\Big(\frac{k-k_z^{min}}{2}z\Big)\exp\Big(\frac{k+k_z^{min}}{2}z\Big) \tag{2.27}$$

Equations (2.26) and (2.27) show that the retrieved on-axis intensity undergoes periodic oscillations because of the convolution product with the sinc function.

2.4.2.2/ CONSTRAINTS ON THE TARGET INTENSITY PROFILE

In order to avoid the on-axis oscillations induced by spectral truncations, the intensity variations in target on-axis intensity I_{tar} should be lower than the oscillation period of the sinc function $\mathrm{sinc}[(k - k_z^{min})\, z/2]$ of Eq. (2.27) or specifically the full width at half maximum of its central lobe ΔH. The latter reads:

$$\Delta H = 4\pi/(k - k_z^{min}) \tag{2.28}$$

Let us reconsider, as an example, the case of an intensity profile in the form of a flat-top profile as depicted in Fig. (2.7,c-green curve). In the ideal case, this intensity profile, denoted I_{cst0}, is characterized by abrupt intensity variations, i.e. infinite slopes at both ends of the beam longitudinal extent. It is expressed as:

$$I_{cst0} = \begin{cases} I_{max} & , z_i \leq z \leq z_f \\ 0 & , \text{otherwise} \end{cases} \tag{2.29}$$

where z_i and z_f denotes the beam terminations. In Fig. (2.7), we choose $z_i = 51\ \mu m$ and $z_f = 289\ \mu m$ and consider a cone angle of 13°.

According to our discussion, it is obvious that the spatial spectrum computed from this intensity profile will be truncated by the response function $R(k_z)$. We analytically resolve Eq. (2.5) (see page 40) to compute the spatial spectrum $S(k_z, z = 0)$ corresponding to this profile. We show in Fig. (2.7,a-blue dashed line) the modulus of the computed spectrum. The spectrum takes the form of a sinc-like function and extends outside the range $k_z \in [k_z^{min} - k]$.

We numerically study the effect of spectral apodization of this spatial spectrum on the retrieved on-axis intensity profile. We simulate the propagation of the corresponding Bessel beam using the plane wave spectrum approach as described above. The results are shown in Fig. (2.7,b-blue dashed line) where we clearly notice truncation-induced on-axis intensity oscillations.

In order to avoid this undesired aspect, we use parabolic intensity transitions at both ends of the flat-top profile as shown in Fig. (2.7,c-green line). This profile, denoted I_{cst}, can be described by Eq. (2.30).

$$I_{cst} = \begin{cases} I_{max}(z/z_i)^2 & , 0 \leq z \leq z_i \\ I_{max} & z_i \leq z \leq z_f \\ I_{max}(1 - \dfrac{z - z_f}{z_{max} - z_f})^2 & , z_f \leq z \leq z_{max} \\ 0 & , \text{otherwise} \end{cases} \tag{2.30}$$

Here, z_i and z_f in Eq. (2.30) are the same as in Eq. (2.29) and $z_{max} = 340\ \mu m$. We choose parabolic variation because it allows reaching zero intensity values in contrast with

the Gaussian apodization proposed in Ref. [Čižmár et al., 2009]. In addition, it provides smoother intensity variation compared to other profiles such as exponential ones.

In our experimental conditions (as shown in our setup of Fig. 2.5), we use a microscope objective with numerical aperture $NA = 0.3$ which corresponds to $k_z^{min} = 0.945\,k$. Thus, according to Eq. (2.28), the lowest intensity variation above which intensity oscillations can be avoided is $\Delta H = 34\ \mu m$.

Using Fig. (2.7,c), we estimate the intensity variation induced by the parabolic intensity decay at the edges of the flat-top profile, i.e. at the points z_i or z_f. In this figure, we plot a line tangent to the parabolic profile (dotted line) at the point z_i and find that this intensity variation is approximately 33 μm, which is approximately equal to the theoretical value ΔH. Hence, the target on-axis intensity profile I_{cst} is expected to be retrieved with practically no oscillations.

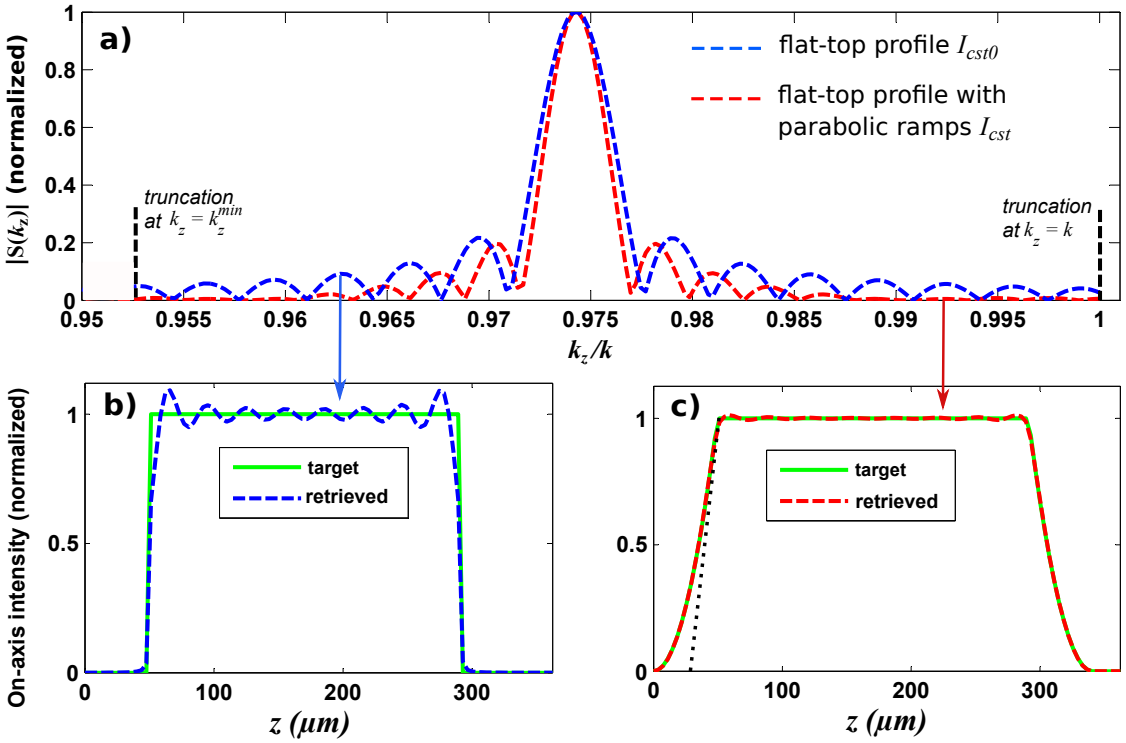

Figure 2.7: Comparison of the spatial spectra for two flat-top on-axis intensity profiles with and without parabolic ramps. The two truncations of the spectrum at $k_z = k$ and $k_z = k_z^{min}$ are specifically shown. The spectrum is expressed in the image plane of the SLM ($\theta = 13°$). (bottom) Retrieved on-axis intensity for the target intensity profile (b) without and (c) with parabolic variations (with typical variation length of about $\Delta H = 33\ \mu m$ for our experimental conditions).

We plot in Fig. (2.7,a-red dashed line) the modulus of the spatial spectrum corresponding to the improved on-axis intensity profile I_{cst}. We notice that the sinc-like oscillations of the spectrum are significantly damped in this case compared to the case of profile I_{cst0}. The spatial spectrum is consequently confined in the spectral range which allows to fairly conserve the target spectral distribution.

In Fig. (2.7,c), we show simulation results of the linear propagation of the corresponding beam and compare the retrieved on-axis intensity profile with the target. The target on-

axis intensity profile is reproduced with a maximal relative error of about 1%. It is then clear that, to fairly retrieve a target on-axis intensity profile, it is necessary to avoid abrupt intensity variations over propagation distances inferior to the quantity ΔH.

2.4.2.3/ CONSTRAINTS ON THE GEOMETRICAL PARAMETERS

Another point that should be accounted for to avoid spectral truncation is the beam geometrical parameters, namely the cone angle θ and the spot size of the input light beam. If we reconsider the spectrum depicted in Fig. (2.7,a), we notice that $|S(k_z)|$, that is centered around the frequency $k_{z0} = k\cos(\theta)$, is placed nearly in the middle of the definition range $k_z \in [k_z^{min} - k]$. Indeed, the variation of the cone angle will shift the position of the central frequency near the edges of this frequency range. Regarding the effect of the input beam spot size, we recall that the spectral width of the spatial spectrum is inversely proportional to the beam size. Hence, for low enough value of the beam spot size, the spectral width will be large enough to cause the spatial spectrum to be extended outside this range.

N.B: Note that since the input spatial amplitude of modified Bessel beams is generally different from that Gaussian profiles (see Fig. (2.8,right)), it is not appropriate to characterize the transverse spatial extent of the input beam by the beam waist w_0. Hence, we will define a quantity w_b which refers to the half width at $1/e^2$ of the maximal amplitude and refer to it as "beam radius".

For a lower cone angle, the center of the spectrum defined at $k_z = k_{z0}$ will be shifted closer to the cutoff frequency $k_z = k$ which will lead to spectrum truncation regardless of the shape of the target intensity. This point is clearly shown in Fig. (2.8,left, blue line). In this figure, we show the modulus of the spatial spectrum computed from the same on-axis intensity profile I_{cst} described by Eq. (2.30). We use a cone angle $\theta = 6.1°$ and a beam radius $w_b = 75\ \mu m$. For a higher cone angle, the spectrum will be truncated at the low cutoff frequency $k_z = k_z^{min}$. In this case, one can use an optical element with higher numerical aperture to avoid this truncation.

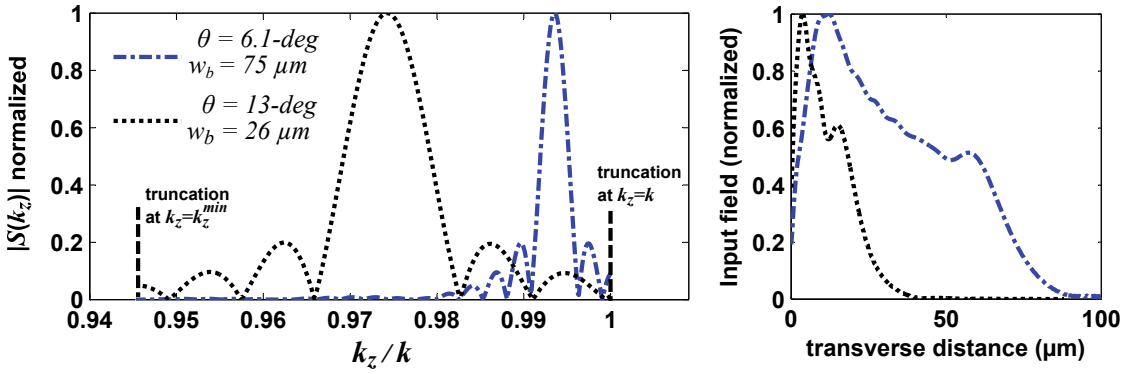

Figure 2.8: (left) Modulus of the spatial spectrum retrieved for the target on-axis intensity profile I_{cst} defined Eq. (2.30) and (right) the corresponding input spatial amplitude for (dashed dotted line) cone angle $\theta = 6.1°$ and $w_b = 75\ \mu m$ and (dotted black line) cone angle $\theta = 13°$ and $w_b = 26\ \mu m$.

In the same figure (2.8,black dotted lines), we show the effect of beam radius of the input beam. We consider the same target on-axis intensity I_{cst} with a cone angle $\theta = 13°$ and

a lower value of the beam radius $w_b = 26\ \mu m$. The input amplitude of corresponding the Bessel beam is shown in Fig. (2.8,right). We plot in Fig. (2.8,left) the modulus of its spatial spectrum which is cut off at both edges of the spectral range $k_z \in [k_z^{min} - k]$.

2.4.2.4/ LIMITATIONS IMPOSED BY THE SLM

To avoid spectral truncation, it is necessary to utilize a beam radius as high as possible. However, this is limited by the size of optical elements. For example, our SLM has an active area of [16 mm, 12 mm]. For axially symmetric beams, such as Bessel beams, the maximal area than can be utilized is [12 mm, 12 mm], which corresponds to a maximum aperture radius of $w_{SLM} = 6\ mm$ in the SLM plane. Considering the demagnification factor (1/55) of our setup, this corresponds to $w_{image} = 110\ \mu m$. In this case, the minimal cone angle one can use to avoid spectral truncation is about 3 mrad in the SLM plane, which corresponds to 10° in the image plane.

Regarding the maximal cone angle, we mentioned that it depends on the numerical aperture of the experimental setup. Nonetheless, one should also take into account other factors such as spatial filtering and the diffraction efficiency of the setup.

Actually, the encryption of a computer-generated hologram onto a SLM implies the sampling of the phase mask on the SLM pixels. In other words, the phase value is fixed over the area of each pixel of the SLM. A good sampling should satisfy Shannon theorem which states that a single period should be encoded on at least two pixels.

Let us consider a linear phase ramp, wrapped over 2π, which is used to separate the different diffraction orders. This phase ramp is given by the function $\phi_{lin} = 2\pi \sin(\alpha)/\lambda$, with a period $p = \lambda / \sin(\alpha)$. Shannon theorem indicates that the maximal angle that can be used is given by $\alpha_{max} \approx \lambda/2\Delta$, where Δ is the SLM pixel pitch. Considering our SLM characteristics, this corresponds to $\alpha_{max} = 20$ mrad. This implies the possibility to use high deflection angles and thus high values of the cone angle.

However, the diffraction efficiency of our SLM decreases with the spatial frequency (and thus decreases with the deflection angle α). In our experimental conditions, and accounting for other SLM imperfections, we used a maximal angle of 6 mrad for both the cone angle of Bessel beams θ and the deflection angle of reference waves α.

2.5/ NUMERICAL AND EXPERIMENTAL RESULTS

In this section, we will compare experimental and numerical results of the linear propagation of modified Bessel beams according to the experimental setup described in Fig. 2.5. We consider two different on-axis intensity profiles. In addition to the flat-top intensity shape, we also consider an intensity profile in the form of a linear ramp and parabolic intensity decay. We discuss the performance of our beam shaping method, specifically its energy throughput and the accuracy of the retrieved on-axis intensity.

2.5.1/ NUMERICAL SIMULATION RESULTS

In our numerical simulations, we consider the parameters of our SLM as described in table (2.1), namely a number of sampling points $N = 600$ and an aperture diameter of 12 mm in the SLM plane. This allows to study the effect of the SLM pixelization on the retrieved on-axis intensity profile.

Note that we compute Fourier transformation using the FFT function. Normally, this function requires a number of sampling points in the form of 2^p where p is an integer. Fortunately, our numerical simulations show that we can still obtain the same results even if use $N = 600$, which does not satisfy the formula $N = 2^p$. Indeed, we compared results for $N = 600$ and $N = 1024$ and found that they are in very good agreement.

Regarding the target on-axis intensity shape, we consider, as a case study, the case of a Bessel beam with flat-top intensity profile and parabolic ramps as described previously by Eq. (2.30). It is exactly as the one shown in Fig. 2.7,c,green line): We use a cone angle of 4 $mrad$ in the SLM plane, corresponding to $13°$ in the image plane of the 4f system. The longitudinal parameters are $z_i = 51$, $z_f = 289$ and $z_{max} = 340$ μm in the image space.

2.5.1.1/ COMPUTATION OF THE PHASE MASK USED IN EXPERIMENTS

We recall that the expression of the phase mask is given by: $\psi(x,y) = M(x,y)\text{mod}[(F(x,y)+\phi_{ref}, 2\pi]$. The exact version states that $M(x,y)$ and $F(x,y)$ are respectively expressed as:

$$M(x,y) = 1 + \frac{1}{\pi}\text{sinc}^{-1}[A_{tar2}(x,y)] \tag{2.31}$$

$$F(x,y) = \phi_{tar}(x,y) - \pi M(x,y) \tag{2.32}$$

where A_{tar2} depends on the incident amplitude profile A_{inc} as $A_{tar2} = A_{tar}/A_{inc}$. We use a deviation angle α = 5.5 mrad in the linear phase ramp ϕ_{ref}.

We show in Fig. (2.9.a) the experimentally measured intensity $|A_{inc}|^2$ of the laser beam and we compare in Fig. (2.9.b,c) the phase mask distributions in case of uniform and non-uniform laser illuminations respectively. We notice that the inclusion of non-uniform light distribution in the phase mask allows to adjust the phase height to the light amplitude in each pixel of the SLM. In other words, at the transverse spatial positions where the light intensity is weak, the phase height at these positions is higher compared to the case of uniform illumination.

2.5.1.2/ EVOLUTION OF THE BESSEL BEAM GENERATED BY THE SLM

Let us consider, in our simulations, an incident laser beam with the same intensity distribution shown in Fig. (2.9,a) and study its evolution through the 4f system after interacting with the phase mask presented in Fig. (2.9,c). We firstly analyze its transverse field distribution at the common focal plane of the lens and microscope objective (see setup of Fig. (2.5), page 45) and the image plane of the 4f system.

We recall that the laser beam incident on the SLM acquires the imprinted phase profile ψ in the form of a multiplicative $\exp(i\psi)$. We compute the corresponding field distribution

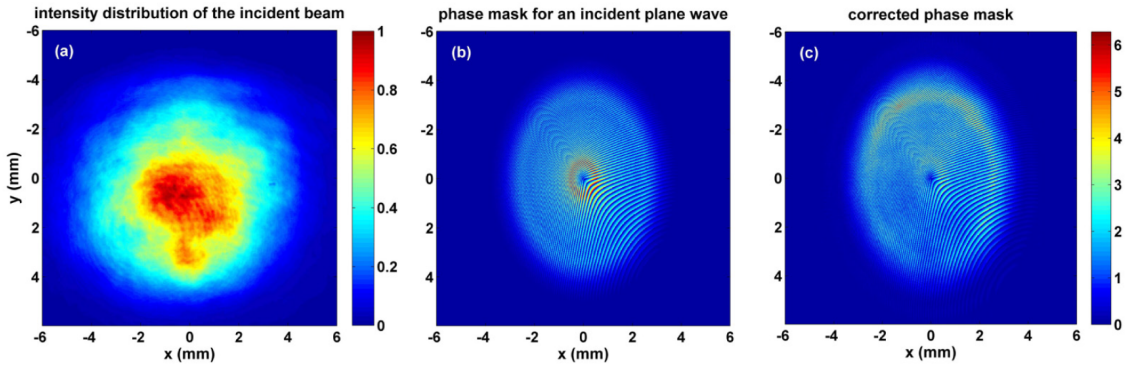

Figure 2.9: Image of the incident beam intensity at the SLM plane, (b) phase mask corresponding to a uniform light illumination ($A_{inc} = 1$) and (c) phase mask corresponding to the incident laser beam.

$S(x_f, y_f)$ at the common focal plane (Fourier plane) using 2D Fourier transform. We show in Fig. (2.10, a-b) the field distribution before and after spatial filtering. The use of a reference wave with a deviation angle of 5.5 mrad allowed about 6-mm-separation between the zeroth diffraction order and the ring center of the first order. Nonetheless, there are still residual ring-like structures in the first diffraction order which stem from higher orders of diffraction.

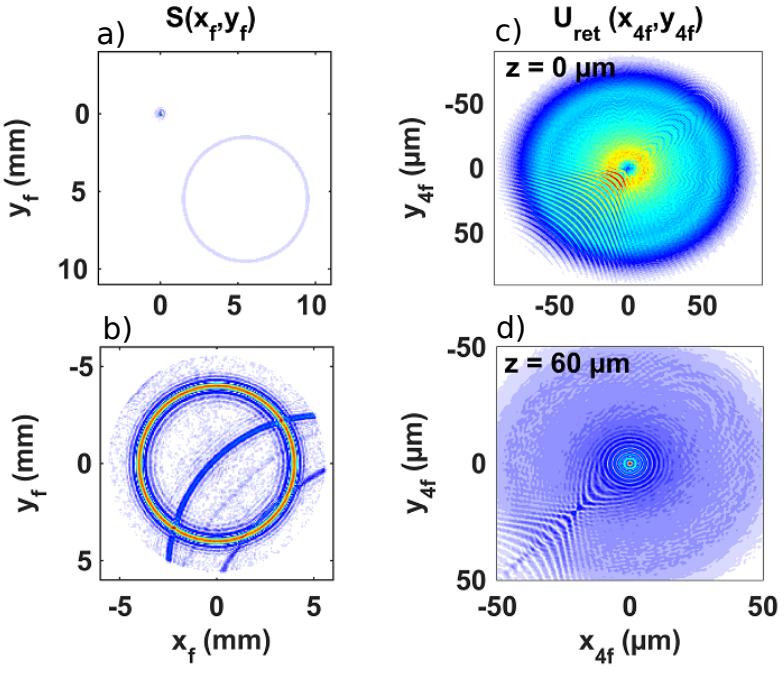

Figure 2.10: Computation of the field distribution at the common focal plane of the lens and microscope objective (see setup of Fig. (2.5), page 45) of our 4f system (a) before and (b) after spatial filtering and centering. Reconstruction of the optical field distribution in the image space at (c) $z = 0\ \mu m$ and (d) $z = 60\ \mu m$. the subscripts "f" and "4f" added to the transverse coordinates (x_f, y_f and x_{4f}, y_{4f}) refer to the Fourier plane and image plane of the 4f system respectively

We compute the inverse Fourier transform of the filtered field at the first diffraction order

to reconstruct the Bessel beam in real space. We show in Fig. (2.10,c) the amplitude distribution of the reconstructed Bessel beam $U_{ret}(x_{4f}, y_{4f})$. We notice the presence of disturbances in the form of fringe-like patterns. These disturbances are caused by the non-filtered diffraction orders which interfere with the light field that stems from the first order. However, numerical simulations show that these disturbances tend to propagate away from the propagation axis and thus do not further interfere with the central core of the beam. This feature is displayed in Fig. (2.10,d) where we show the amplitude of the Bessel beam at a propagation point $z = 60\ \mu m$.

We show in Fig. (2.11) the distribution of the retrieved on-axis intensity of the SLM-reconstructed Bessel beam. We compare it to the case where the Bessel beam is computed directly from the target intensity profile (ideally retrieved). We notice that the target intensity profile is fairly reproduced with a maximum relative error of 3 % compared to less than 2 % in the ideal case. This then shows the validity of our approach.

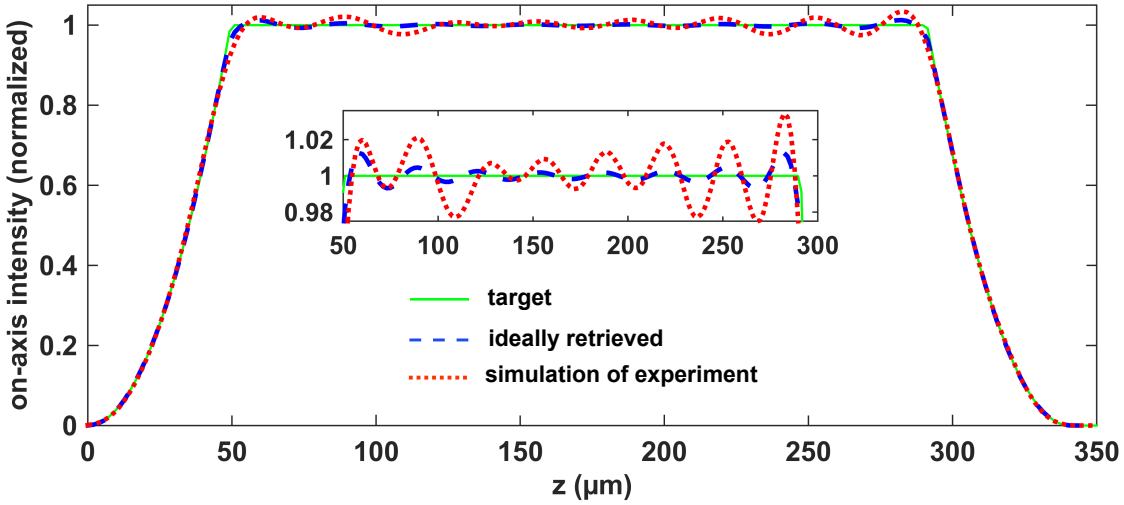

Figure 2.11: Comparison of (green line) target on-axis intensity profile with the one retrieved in case (blue dashed line) the Bessel beam is computed directly from the target on-axis intensity [ideally retrieved] and (dotted red line) in case it is generated by the SLM.

2.5.1.3/ IMPACT OF THE ENCRYPTION METHOD

So far, we have used the exact expression of the phase mask, given by Eq. (2.32), to exactly encode the amplitude and phase of the target field. In Ref. [Bolduc et al., 2013], and as previously discussed, Bolduc et al. proposed an approximate expression of the phase mask to facilitate its computation and showed that this approximation can still allow fair reconstruction of target fields. Actually, the inverse sinc function in the expression of modulation function $M(x, y)$ was seen to be time consuming and thus an approximation was proposed. Here, we will verify whether or not the proposed approximation is suitable for on-axis intensity shaping.

We recall that the approximate version proposed by Bolduc et al. [Bolduc et al., 2013] consists in assimilating the expression of $M(x, y)$ to A_{tar2} (defined in page57) while keeping the same expression of the phase term $F(x, y)$ as in Eq. (2.32). We simulate the propagation of the same Bessel beam (as in Fig. (2.11)) using these two different phase

masks and compare in Fig. (2.12) the corresponding retrieved on-axis intensity shapes.

In contrast with the exact version, it is clear that the approximate version proposed by Bolduc et al. does not fairly reconstruct the target intensity profile. The reproduced intensity profile in this case (triangles) largely deviates from the targeted one. We also considered other profiles, such as one in the form of linear slope and parabolic decay (Figure not shown). We observed in this case that the approximate approach yields an oscillating on-axis intensity with a large relative error. This shows that such an approximation should be avoided in the case of on-axis intensity shaping of Bessel beams.

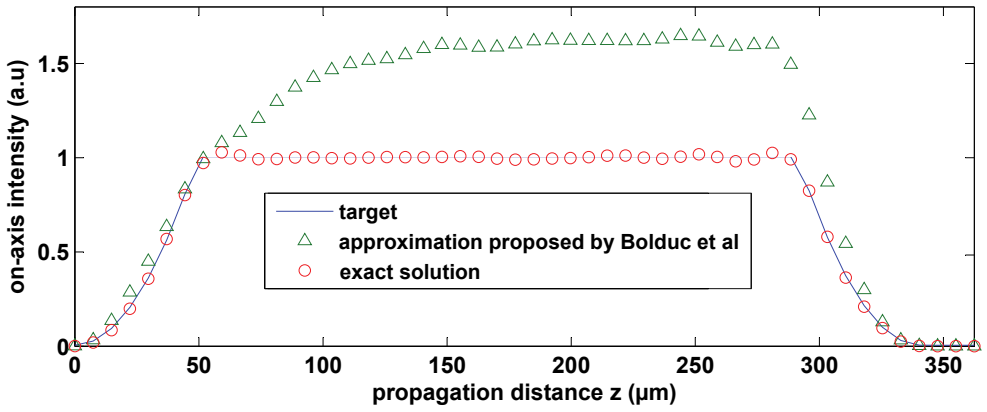

Figure 2.12: Comparison between the target on-axis intensity profile of a modified Bessel beam with flat on-axis intensity and the ones retrieved using (triangles) the approximation proposed in Ref. [Bolduc et al., 2013] and (circles) our implementation of this method [Ouadghiri-Idrissi et al., 2016].

2.5.2/ EXPERIMENTAL RESULTS AND DISCUSSION

We show a comparison between simulation results and experimental data in case of Bessel beams with two different profiles: one is flat-top intensity profile we have used so far as in Fig. (2.11). The other is in the form of a linear ramp along with a parabolic intensity decay. This intensity decay is formulated in the same way as in the flat-top intensity profile (see Eq. (2.30)). In this regard, we consider three Bessel beams with different values of the intensity slope but exhibiting the same intensity decay. We use in all cases a cone angle of 4 $mrad$ in the SLM plane (13° in the image plane).

Regarding the computation of the phase masks, we take into account, in all cases, the non-uniformity of the input laser beam whose intensity is described in Fig. (2.9,a). We use a reference wave with a deviation angle of 5.5 mrad.

In Fig. (2.13,bottom), we compare the numerically and experimentally retrieved on-axis intensity profiles in all cases: the intensity distributions of the experimentally generated beams are in excellent agreement with the target and numerical results. The mean relative error is inferior to 4 % which is experimentally acceptable.

The energy throughput slightly varies from one mask to another due to the variation of

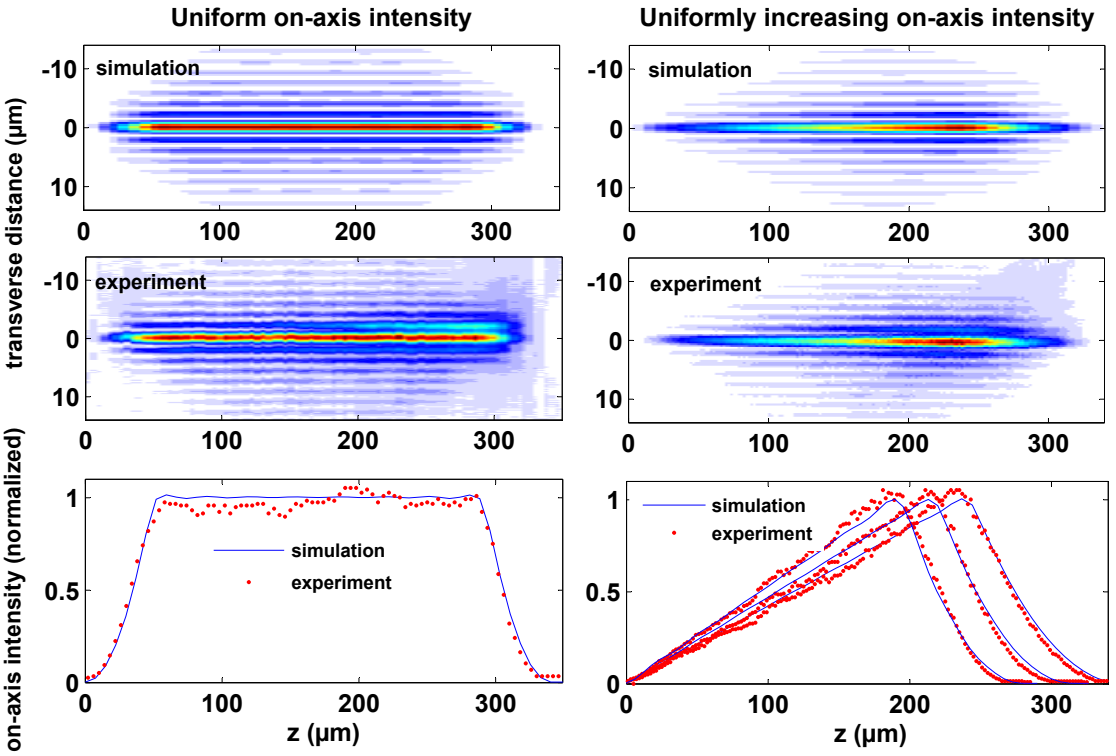

Figure 2.13: Numerical and experimental data of the intensity distribution along the propagation axis of Bessel beams with (left) uniform and (right) uniformly growing on-axis intensity profiles.

the beam radius of the target field (corresponding to its chosen longitudinal extent). We experimentally estimate the energy throughput by measuring the ratio of the power of the first diffraction order to that of the input beam. In the case of Bessel beam with flat-top profile, we find an efficiency value of about 10 %.

Numerically, we estimate the energy throughput by computing the power ratio of the light field after and before spatial filtering. We find that it is higher than the experimental value by a factor of 2. This may be due to other imperfections of the SLM that were not accounted for in our numerical model.

In our work, we numerically studied the effect of the input beam intensity distribution on the retrieved Bessel beam. Our results show that the input intensity (with homogeneous distribution) does not affect the retrieved on-axis intensity distribution. However, it allows increasing the energy throughput of the system. We have numerically measured this quantity in the case of a uniform illumination and compared it to the non-uniform illumination case. In the first case we found an efficiency of 11 % compared to about 23 % in the second case.

We can obtain better energy conversion factors if the input field distribution is optimized. For example, we found an energy conversion of about 60 % in the case of an incident Gaussian beam with a beam waist of 4 mm. Experimentally, this generally needs the implementation of a another optical element to appropriately shape the laser beam.

2.6/ CONCLUSION

In this chapter, we have presented our numerical and experimental works on arbitrary on-axis intensity shaping of Bessel beams using a single-phase only SLM. We firstly presented the theoretical background of on-axis intensity shaping which was reported by Cizmar et al. [Čižmár et al., 2009]. It is based on the interference of multiple J_0 beams of the same temporal frequency but of different longitudinal wavenumbers. According to this theory, the spatial spectrum of Bessel beams can be computed from any arbitrary target profile of the on-axis intensity, provided that the latter is physically realizable.

This approach requires the shaping of both the spatial amplitude and phase of an incident beam. We presented experimental techniques which allow performing this task. Our chosen approach satisfies our requirements on high energy throughput and high reconstructed beam accuracy. The latter (i.e. high beam accuracy) is necessary since the Bessel beam intensity should be accurately controlled at each point of the propagation distance. The high energy throughput concerns the applicability of this technique in high power laser applications. To this end, we adopted an experimental approach allowing precise reconstruction of arbitrarily-shaped Bessel beams from direct space using a single phase-only SLM. This approach was first introduced by Bolduc et al. [Bolduc et al., 2013] which we further improved and generalized for non-uniform SLM illumination.

Afterwards, we numerically studied the physical limitations applied to target on-axis intensity profiles of Bessel beams and the corresponding spatial spectra. The spatial spectrum should be confined in a spectral frequency range delimited by the beam wavelength at the upper limit and the numerical aperture of the experimental system at the lower one. In case the spectrum is defined outside this range, the retrieved on-axis intensity will exhibit on-axis oscillations. To avoid these truncation-induced oscillations, we showed that target intensity profiles should exhibit smooth intensity variations. We also discussed constraints applied to the cone angle and beam size of the target Bessel beam.

Finally, we presented our numerical study of SLM pixelization impact on retrieved optical fields and compared results with our experimental data. Our results showed a very good agreement between simulations and experiments which validate our chosen experimental approach. We also discussed the energy throughput of our technique. Our measurements showed that it is typically around 10 % and that it depends largely on the transverse size of the target beam. We also discussed the possibility to improve the energy throughput by means of intensity shaping of the incident laser field.

3

NONLINEAR DYNAMICS AND CONTROL OF KERR-INDUCED INSTABILITIES IN BESSEL BEAMS

INTRODUCTION

The nonlinear propagation of Bessel beams in transparent Kerr media has caught a major interest and found many applications. We have discussed in the first chapter the major properties of Bessel filaments and some of these applications. Particularly, Bessel beams allow for homogeneous energy deposition over long propagation distances in transparent materials. Consequently, Bessel pulses can sustain steady propagation regime of filamentation which is very advantageous in high power laser applications [Courvoisier et al., 2016b, Durfee et al., 1993]. Nevertheless, despite the robustness of these beams, they may undergo, in some conditions, nonlinear instabilities, which restrict their applicability [Polesana et al., 2008, Cooley et al., 2006].

Nonlinear instabilities refer to the modulation of the central core intensity of Bessel beams along the propagation distance [Alexeev et al., 2002]. Instabilities induced by Kerr nonlinearity were particularly investigated by Gadonas et al. [Gadonas et al., 2001]. Considering four wave mixing interactions and using phase-matching arguments, they showed that a Bessel beam can sustain Kerr self-action which deforms its angular spectrum to generate two additional spectral components: an axial wave component and a secondary conical wave whose cone angle is $\sqrt{2}$ times the incident one (outer ring) [Gadonas et al., 2001, Pyragaite et al., 2006]. Their numerical simulations highlighted peak intensity modulation of Bessel beams along propagation which was explained by the interference of the conical beam with the axial wave component.

In order to achieve a stable propagation regime of Bessel beams, stationary solutions of the nonlinear propagation equation have been thoroughly investigated. Porras et al. investigated the stability of Bessel beams in the presence of nonlinear losses (NLL), precisely multiphoton absorption (MPA) [Porras et al., 2004]. They showed that stable Bessel filaments can only be formed (steady filamentation regime) if MPA prevails over Kerr self-focusing. This condition can be satisfied for relatively high input power and high cone angles [Porras et al., 2004, Couairon et al., 2012].

In filamentation applications such as materials processing, specific values of the cone angle and input power can be required [Courvoisier et al., 2016b]. Polesana et al.

investigated the effect of the exact positioning of Bessel beams in nonlinear media on the stability of Bessel filaments [Polesana et al., 2007, Polesana et al., 2008]. They showed that a Bessel beam will smoothly reshape into a stable filament only if it is progressively formed inside the Kerr medium. However, if the Bessel beam, with the same values of the input power and cone angle, is formed prior entering the nonlinear sample, it will exhibit significant instabilities which consist in quasi-periodic intensity modulation along propagation (unsteady filamentation regime) as shown in Fig. 3.1. These two input conditions are referred to as smooth and abrupt intensity transitions respectively. According to Ref. [Polesana et al., 2007], experimental and numerical results showed that the growth of the axial wave and outer ring is greatly enhanced in the case of abrupt intensity transition. Theoretically, this increase in intensity growth was attributed to enhanced longitudinal phase-matching between the input conical wave and these newly-generated spectral components [Polesana et al., 2007]. In contrast, the growth of these components was shown to be impeded in the smooth transition case. Hence, although nonlinear instabilities can still occur in the case of smooth intensity transition [Polesana et al., 2008], these results showed the possibility to reduce nonlinear instabilities even for specific values of the cone angle and input power.

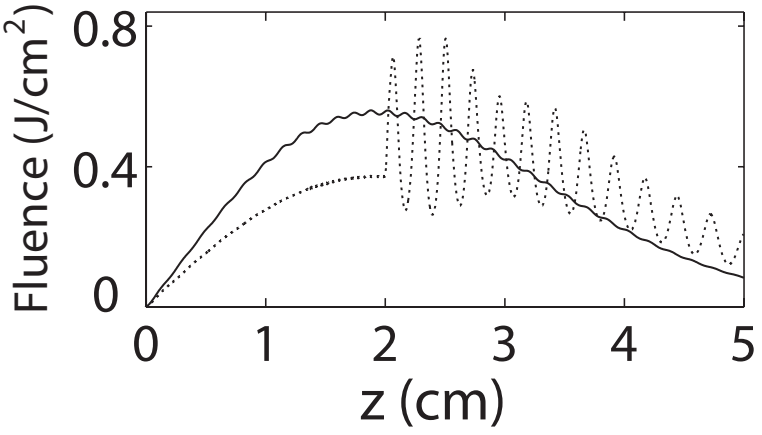

Figure 3.1: Numerical simulation results of Ref. [Polesana et al., 2008] comparing the on-axis fluence of a pulsed Bessel beam in the case of smooth (solid line) and abrupt (dotted line) intensity transitions. The abrupt intensity transition is considered at the interface between air (linear medium) and water (nonlinear medium) at the point $z = 2$ cm.

In this chapter, we will present a novel approach to control Kerr-induced instabilities by means of on-axis intensity shaping of Bessel beams. In the first section, we will first introduce a detailed theory in order to give more insight to the FWM interactions involved in the generation and growth of new spectral components. Since Kerr-induced instabilities were shown to be mainly caused by the generation of new spatial spectral components [Gadonas et al., 2001], we restrict our work to monochromatic waves. We use the slowly varying envelope approximation for Bessel beams as in Ref. [Tewari et al., 1996]. We calculate the third order nonlinear polarization and then derive the Helmholtz equation.

In the second section, we review the theoretical interpretations of Kerr-induced instabilities and investigate related nonlinear dynamics. Using the theory of Gadonas et al. [Gadonas et al., 2001] and our model, we show that nonlinear spectral distortions in Bessel beams are established in two steps. The first consists in an initial spectral broadening which leads to the generation of an "axial wave seed". The second step is

the establishment of four wave mixing (FWM) interactions leading to the amplification of the axial wave seed and generation of an outer ring.

In the third section, we further investigate nonlinear instabilities in the case of smooth and abrupt intensity transitions. We consider our theoretical model to explain how nonlinear instabilities are mitigated in the smooth transition case and enhanced in the other case.

In the fourth section, we introduce our approach to control nonlinear instabilities by means of on-axis intensity shaping of Bessel beams. Using numerical simulations in pure media (where only Kerr nonlinearity is accounted for), we show that nonlinear spectral distortions can be reduced for specific longitudinal intensity profiles of Bessel beams. We further discuss the limitation of our approach and show the possibility of further improvements.

Finally, we numerically show that our results are also valid in the filamentation regime, where photoionization and laser-generated plasma are accounted for. We specifically show that Bessel filaments can be further stabilized for Bessel beams with optimized longitudinal intensity profiles. We also show that such modified Bessel beams can generate more uniform plasma channels compared to those generated by conventional Bessel-Gauss beams.

3.1/ THEORETICAL BACKGROUND

In 1996, Tewari et al. introduced a theoretical model to describe and explain enhanced third harmonic generation (THG) in Bessel beams [Tewari et al., 1996]. Our theoretical model follows the same approach. Instead of THG nonlinear terms, we will solely consider Four wave mixing (FWM) interactions to study nonlinear spectral distortions in Bessel beams which are related to Kerr-induced instabilities. Hence, we will later refer this theory to as "reduced FWM model".

Firstly, we will compute the third order nonlinear polarization and then select the relevant nonlinear terms which we consider having direct impact on the generation of new spectral components. Afterwards, we will include these terms in the Helmholtz equation which we will analytically and numerically study.

3.1.1/ THIRD ORDER NONLINEAR POLARIZATION

In Kerr media, information on nonlinear effects is contained in the third order nonlinear polarization $\mathbf{P}_{NL}$.It is written as follows:

$$\mathbf{P}_{NL} = \varepsilon_0 \chi^{(3)} \mathbf{EEE} \tag{3.1}$$

where $\mathbf{E}$ is the total electric field and $\chi^{(3)}$ is the third order susceptibility. According to previous works [Gadonas et al., 2001], nonlinear instabilities are mainly caused by spatial distortions of Bessel beam spectra. Hence, for the sake of simplicity, we neglect time contribution and consider that the interacting waves oscillate at the same temporal frequency ω_0. Of course, it is possible to extend our model to the non-monochromatic case to give more insight into other Kerr-induced phenomena such as temporal spectral broadening and stimulated Raman scattering [Polesana et al., 2007, Dubietis et al., 2007]. This will be the subject of future works.

In the framework of four wave mixing interactions, we consider the interaction of two intense pump waves, denoted $\mathbf{E}_1$ and $\mathbf{E}_2$, with a signal wave $\mathbf{E}_3$ to generate an idler wave $\mathbf{E}_4$. The idler wave is then assumed to be generated at the same angular frequency ω_0. In addition, we consider that these four waves $\mathbf{E}_j$ are linearly polarized along the same axis $\mathbf{x}$ and possessing different longitudinal spatial frequencies k_{zj}. The expression of each of these waves is given by:

$$\mathbf{E}_j = \frac{1}{2} E_j \mathbf{x} \qquad\qquad E_j = A_j \exp[i(\omega_0 t - k_{zj} z)] \; + \; c.c \tag{3.2}$$

where A_j is the complex amplitude of the electric field $\mathbf{E}_j$. The total electric field can be written as:

$$\mathbf{E} = \sum_{j=1}^{4} \mathbf{E}_j \tag{3.3}$$

We substitute Eq. 3.3 in Eq. 3.1 and only consider nonlinear polarization terms $\mathbf{P}_{NL}^{(4)}$ related to the idler wave $\mathbf{E}_4$. We obtain:

$$\mathbf{P}_{NL}^{(4)} = \frac{1}{8} \varepsilon_0 \chi^{(3)} \mathbf{x} [E_4^3 + 3(E_1^2 + E_2^2 + E_3^2) E_4 + 6(E_1 E_2 E_3)] \tag{3.4}$$

We substitute Eq. 3.2 in Eq. 3.4, and only keep terms preserving the same frequency ω_0. Writing Eq. 3.4 in the same form as Eq. 3.2, we obtain:

$$\mathbf{P}_{NL}^{(4)} = \frac{1}{2} \mathbf{x} \; p_{NL,\,\omega_0}^{(4)} \exp[i(\omega_0 t - k_{z4} z)] \; + \; c.c \tag{3.5}$$

where

$$\begin{aligned} p_{NL,\,\omega_0}^{(4)} = \frac{3}{4} \varepsilon_0 \chi^{(3)} \Big[& |A_4|^2 A_4 + 2\,(|A_1|^2 + |A_2|^2) A_4 \\ & + 2\,(A_1 A_2^* A_3 \mathrm{e}^{-i(k_{z1} - k_{z2} + k_{z3} - k_{z4}) z} + A_1^* A_2 A_3 \mathrm{e}^{-i(-k_{z1} + k_{z2} + k_{z3} - k_{z4}) z} \\ & + A_1 A_2 A_3^* \mathrm{e}^{-i(k_{z1} + k_{z2} - k_{z3} - k_{z4}) z}) + ... \Big] \end{aligned} \tag{3.6}$$

This equation is similar to that reported in [Agrawal, 2013] which was demonstrated for nonlinear interactions in optical fibers. The first and second terms of Eq. 3.6 are responsible for self phase modulation (SPM) and cross phase modulation (XPM) respectively. The last three terms correspond generally to non-degenerate FWM processes. As stated above, Kerr-induced FWM interactions are responsible for the generation of new spectral components (axial wave and outer ring), which are responsible for nonlinear instabilities. We will later show that, according to the theory of Gadonas et al. Ref. [Gadonas et al., 2001], the first two FWM terms (second line of Eq. 3.6) are responsible for the generation of the axial wave while the other leads to the generation of the outer ring through parametric amplification [Gadonas et al., 2001]. In previous works on modulation instability in nonlinear fibers, both XPM and FWM-induced parametric amplification were accounted for [Agrawal, 2013]. In our case, since we consider three FWM terms, the inclusion of XPM will further complicate the resolution and analysis of our model. Thus, we will only consider the three FWM terms.

3.1.2/ REDUCED FWM MODEL

In our theory, we limited Kerr-nonlinearity to three FWM terms as stated above. Hence, our model is referred to as "reduced FWM model". In the following, we will derive the propagation equation where we implement the previously computed third order polarization. We then solve the resulting equation in spectral domain to study the generation and growth of new spectral components.

3.1.2.1/ DERIVATION OF HELMHOLTZ EQUATION

The starting point is the following wave equation given by:

$$\Delta \mathbf{E}_4 - \frac{\varepsilon_r}{c^2}\frac{\partial^2 \mathbf{E}_4}{\partial t^2} = \mu_0 \frac{\partial^2 \mathbf{P}_{NL}^{(4)}}{\partial t^2} \tag{3.7}$$

$\mathbf{E}_4$ was defined in Eq. 3.2. For simplicity, we will only consider ideal Bessel beams defined by the J_0 Bessel function. The complex amplitudes of the four interacting waves A_j are defined as follows:

$$\begin{aligned} A_j &= J_0(k_{rj} r)\mathrm{e}^{i\phi_j}, \qquad && j = 1,2,3 \\ A_4 &= a_4(z)\, J_0(k_{r4} r) \end{aligned} \tag{3.8}$$

where k_{rj} is the transverse spatial frequency of the amplitude A_j. Here, we considered the approximation of undepleted pump where the intensity of the pump waves remains constant along propagation. To further simplify the problem and subsequent analytical analysis, we assume that the signal wave also remains constant. Thus, our conclusions would generally only be valid for relatively short propagation distances.

Note that we also took into account the input phase of each wave. Actually, since we defined each wave at a specific spatial frequency k_{rj}, the input phase ϕ_j is then interpreted as a spectral phase related to the frequency k_{rj}. As in Ref. [Tewari et al., 1996], we are solely interested in the axial behavior of A_4 which is referred to as axial complex envelope and is denoted $a_4(z)$. The evolution of this complex envelope along propagation will be analyzed according to the Helmholtz equation which will later be derived.

Since we developed an expression of $\mathbf{P}_{NL}^{(4)}$ with the same form as $\mathbf{E}_4$, we can develop Eq. 3.7 without the complex conjugate terms. We obtain:

$$2ik_{z4}\frac{\partial a_4(z)}{\partial z} J_0(k_{r4}) = \frac{k^2}{\varepsilon_0 n^2} p_{NL}^{(4)} \tag{3.9}$$

where n is the linear refractive index and $k = \sqrt{k_{rj}^2 + k_{zj}^2}$ is the wavenumber in the nonlinear medium. This formula is demonstrated in Appendix 3.A (page 153). Substituting Eq. 3.8 in Eq. 3.9 and neglecting SPM and XPM terms in the expression of $p_{NL}^{(4)}$, it becomes:

$$\begin{aligned} \frac{\partial a_4(z)}{\partial z} J_0(k_{r4} r) = \frac{-2i\,k\,n_2}{n\cos(\theta_4)} J_0(k_{r1} r) J_0(k_{r2} r) J_0(k_{r3} r)\, [&\exp(-i\Delta k_{z1} z)\mathrm{e}^{i\Delta\phi_1} + \exp(-i\Delta k_{z2} z)\mathrm{e}^{i\Delta\phi_2} \\ &+ \exp(-i\Delta k_{z3} z)\mathrm{e}^{i\Delta\phi_3}]. \end{aligned} \tag{3.10}$$

where $n_2 = (3/8)\chi^{(3)}/n$ and the functions Δk_{zj} and $\Delta\phi_j$ are defined by Eqs. 3.11 and 3.12.

$$\begin{aligned}\Delta k_{z1} =& k_{z1} + k_{z2} - k_{z3} - k_{z4}\\ \Delta k_{z2} =& k_{z1} - k_{z2} + k_{z3} - k_{z4}\\ \Delta k_{z3} =& -k_{z1} + k_{z2} + k_{z3} - k_{z4}\end{aligned} \tag{3.11}$$

and

$$\begin{aligned}\Delta\phi_1 =& \phi_1 + \phi_2 - \phi_3\\ \Delta\phi_2 =& \phi_1 - \phi_2 + \phi_3\\ \Delta\phi_3 =& -\phi_1 + \phi_2 + \phi_3\end{aligned} \tag{3.12}$$

Here, we define the longitudinal phase matching conditions (LPM) for $\Delta k_{zj} = 0$.

In order to remove the J_0 function from the left-hand-side of Eq. 3.10, Tewari et al. suggested to multiply both parts of this equation by $rJ_0(k_{r4}r)$ and integrate over 0 to $+\infty$. In other words, we apply Hankel transformation on both sides of the propagation equation. Hence, this allows the analysis of the propagation equation in the spectral domain.

We recall that, in the spatial frequency domain, a Bessel beam takes the form of a ring (Bessel ring) with a radius $k_{r0} = k\sin(\theta)$ where θ is the cone angle. While an ideal Bessel beam is composed of a single frequency k_{r0}, the spatial spectrum of a quasi-Bessel beam is distributed over multiple frequencies centered around k_{r0}. In this regard, we generally consider that the frequencies k_{r1} and k_{r2} of pump waves can be different from k_{r0}.

On the left part of Eq. 3.10, we encounter the integral $\int_0^{+\infty} rJ_0^2(k_{r4}r)\mathrm{d}r$. According to Lommel [Tewari et al., 1996], this integral is infinite and is given by:

$$\int_0^{+\infty} rJ_0^2(k_{r4}r)\mathrm{d}r = \frac{1}{k_{r4}}\delta(0) \tag{3.13}$$

In our work, we consider a finite upper limit of this integral which is denoted r_f. According to Ref. [DLMF,], the integral $\int_0^{+r_f} rJ_0^2(k_{r4}r)\mathrm{d}r$ is equal to $r_f^2/2(J_0^2(k_{r4}r_f) + J_1^2(k_{r4}r_f))$. Using the asymptotic expressions of both Bessel functions [DLMF,], i.e.

$$J_\alpha(k_{r4}r) = \sqrt{\frac{2}{\pi k_{r4}r}}\cos\left(k_{r4}r - \frac{\alpha\pi}{2} - \frac{\pi}{4}\right), \qquad \alpha = 1,\, 2 \tag{3.14}$$

then, this integral can be approximated to:

$$\int_0^{r_f} rJ_0^2(k_{r4}r)\mathrm{d}r = \frac{r_f}{\pi k_{r4}} \tag{3.15}$$

which is also proportional to $\frac{1}{k_{r4}}$. Hence, we can avoid an infinite value of this integral and simplify our equation as demonstrated in [Tewari et al., 1996]. Equation 3.10 then becomes:

$$\frac{\partial a_4(z)}{\partial z} = i\,C_0 \tan(\theta_4) I_{TPM}[\exp(-i\Delta k_{z1} z)\mathrm{e}^{i\Delta\phi_1} + \exp(-i\Delta k_{z2} z)\mathrm{e}^{i\Delta\phi_2} + \exp(-i\Delta k_{z3} z)\mathrm{e}^{i\Delta\phi_3}]. \tag{3.16}$$

where $C_0 = -2\pi k^2 n_2 / n r_f$ and I_{TPM} is the Transverse Phase Matching integral. In contrast with Ref. [Tewari et al., 1996], I_{TPM} is defined for a finite upper integral limit and is given by:

$$I_{TPM} = \int_0^{r_f} J_0(k_{r1}\, r)\, J_0(k_{r2}\, r)\, J_0(k_{r3}\, r)\, J_0(k_{r4}\, r)\, r\, \mathrm{d}r \tag{3.17}$$

3.1.2.2/ Derivation of Helmholtz equation for $\theta_4 = 0$

Equation 3.16 is not valid in case the idler wave frequency is zero ($\theta_4 = 0$). In this special case, the integral $\int_0^{+r_f} r J_0^2(k_{r4} r)\mathrm{d}r$ is reduced to $\int_0^{+r_f} r\mathrm{d}r$, which yields $r_f^2/2$. Thus, the idler wave is assimilated to an apertured plane wave instead of a J_0 beam. Then, Eq. 3.16 is written as:

$$\frac{\partial a_4(z)}{\partial z} = -i\,\frac{4\,kn_2}{n r_f^2} I_{TPM0}[\exp(-i\Delta k_{z1} z)\mathrm{e}^{i\Delta\phi_1} + \exp(-i\Delta k_{z2} z)\mathrm{e}^{i\Delta\phi_2} + \exp(-i\Delta k_{z3} z)\mathrm{e}^{i\Delta\phi_3}]. \tag{3.18}$$

The TPM integral is reduced to a product of three Bessel functions instead of four and is written as:

$$I_{TPM0} = \int_0^{r_f} J_0(k_{r1}\, r)\, J_0(k_{r2}\, r)\, J_0(k_{r3}\, r)\, r\, \mathrm{d}r \tag{3.19}$$

3.1.2.3/ Normalized propagation equation

In this section, we will normalize our propagation equation 3.16 and then generalize it to account for broad spatial spectra of input quasi-Bessel beams. As we will show in the following sections, it is necessary to consider the contribution of multiple spectral components to describe the nonlinear evolution of the spatial spectrum of the beam. This generalization will be performed by summing the normalized equation over all frequencies of the pump and signal waves.

Let's use the following normalized parameters as in Ref. [Gadonas et al., 2001]:

- $\beta_j = k_{rj}/k_{r0},\ j = 1, 2, 3, 4.$

- $\nu = k_{r0} r.$

Regarding LPM conditions, let's consider as an example the first condition Δk_{z1} and generalize it to the other two conditions. We have:

$$\begin{aligned}\Delta k_{z1} =& k_{z1} + k_{z2} - k_{z3} - k_{z4}\\ =& k\,[\cos(\theta_1) + \cos(\theta_2) - \cos(\theta_3) - \cos(\theta_4)]\\ =& k\,[1 - \theta_1^2/2 + 1 - \theta_2^2/2 - 1 + \theta_3^2/2 - 1 + \theta_4^2/2]\end{aligned}$$

Here, we used the approximation $\cos(\theta_j) \approx 1 - \theta_j^2/2$. We multiply and divide this equation by k to express it by the transverse frequencies $k_{rj} \approx k\,\theta_j$:

$$\begin{aligned}\Delta k_{z1} &= -\frac{1}{2\,k}\left[k_{r1}^2 + k_{r2}^2 - k_{r3}^2 - k_{r4}^2\right] \times \frac{k_{r0}}{k_{r0}} \\ &= -\frac{k_{r0}^2}{2\,k}\left[\beta_1^2 + \beta_2^2 - \beta_3^2 - \beta_4^2\right]\end{aligned}$$

We define the characteristic distance $L_p = 2\,k/k_{r0}^2$ which is equivalent to the Rayleigh range of the central core of Bessel beams [Gadonas et al., 2001]. We then define the following normalized parameters: $\xi = z/L_p$; $\Delta k_{zm} = -\Delta\beta_{zm}/L_p$ where

$$\begin{aligned}\Delta\beta_{z1} &= \beta_1^2 + \beta_2^2 - \beta_3^2 - \beta_4^2 \\ \Delta\beta_{z2} &= \beta_1^2 - \beta_2^2 + \beta_3^2 - \beta_4^2 \\ \Delta\beta_{z3} &= -\beta_1^2 + \beta_2^2 + \beta_3^2 - \beta_4^2\end{aligned} \tag{3.20}$$

Finally, to generalize our theoretical model to a distribution of spectral components, we use a triple integral of Eq. 3.16 over all possible frequencies of the pump and signal waves. It becomes:

$$\begin{aligned}\frac{\partial a_4(\xi,\theta_4)}{\partial\xi} = i\,C_0\tan(\theta_4)\int_0^{+\infty} \mathrm{d}\beta_1 S_1(\beta_1)\int_0^{+\infty} \mathrm{d}\beta_2 S_2(\beta_2) \\ \times\int_0^{+\infty} \mathrm{d}\beta_3 S_3(\beta_3)\, I_{TPM}\sum_{m=1}^{3}\exp(i\Delta\phi_m + i\Delta\beta_{zm}\xi)\end{aligned} \tag{3.21}$$

where I_{TPM} is rewritten as:

$$I_{TPM} = \frac{1}{k_{r0}^2}\int_0^{\nu_f} J_0(\beta_1\nu)\,J_0(\beta_2\nu))\,J_0(\beta_3\nu)\,J_0(\beta_4\nu)\,\nu\,\mathrm{d}\nu \tag{3.22}$$

and $\nu_f = k_{r0}r_f$ and $S_j(\beta_j)$, $j = 1,2,3$, stand for the amplitude distribution of the spectral components of the pump and signal waves respectively. The complex spatial spectra are given by: $\tilde{S}_j(\beta_j) = S_j(\beta_j)\exp[i\phi_j(\beta_j)]$. Recall that we interpreted the input phase term ϕ_j as the spectral phase $\phi_j(\beta_j)$ related to the frequency β_j. For simplicity, we will keep on using the notation ϕ_j.

Note that the notation $S_j(\beta_j)$ does not imply that each interacting wave has its specific spectral distribution. It was only introduced to show that each of these waves is defined in a specific range of frequencies. We will later define these domains and present our arguments.

3.1.3/ Analysis of the TPM integral

The transverse phase matching (TPM) integral is a finite integral of the product of four zeroth order Bessel functions. To compute this integral, it is necessary to use some

approximations or perform numerical integration. We will analyze this integral numerically and analytically and compare our results with those reported in [Gadonas et al., 2001]. We will show that I_{TPM} peaks at specific *transverse* spatial frequencies which we will refer to as transverse phase matching conditions. We will also show that I_{TPM} is inversely proportional to the central frequency and demonstrate that Kerr nonlinearity decreases with the value of the cone angle.

3.1.3.1/ NUMERICAL COMPUTATION

To numerically compute this integral, we first define a vector ν representing the transverse coordinate. we also define two vectors β_3 and β_4 representing all possible values of the spatial frequencies of the signal and idler waves A_3 and A_4.

As discussed above, since the spatial spectrum of a quasi-Bessel beam contains many frequencies, the spatial frequencies β_1 and β_2 of the pump waves can be different from the central frequency $\beta_0 = 1$. We then define a matrix $[R, P, Q]$ from the vectors ν, β_3, β_4. If $\beta_3 = \beta_4$ or β_3 has a specific value, then we define a 2×2 matrix.

To verify the validity of our calculations, We compared our results with those of Ref. [Gadonas et al., 1999]. To this end, we considered a Gaussian apodization and choose the same parameters as those of this reference. The integral is written as:

$$I_{TPM} = \int_0^{r_f} \exp(-\nu^2/g^2) J_0(\beta_1 \nu)\, J_0(\beta_2 \nu)\, J_0(\beta_3 \nu)\, J_0(\beta_4 \nu)\, \nu \, \mathrm{d}\nu \tag{3.23}$$

where $g = k_{r0} d_0$ and d_0 contains information on the waist of the Gaussian envelope of the pump and signal waves [Gadonas et al., 1999]. To compute the integral, we use the function "sum" of the matrix R multiplied by the product of the four Gaussian enveloped Bessel functions over the matrix R. Figure 3.2 shows a comparison between Fig. (2) of Ref. [Gadonas et al., 1999] and our numerical result. There is a very good consistency between the two curves which validates our calculations.

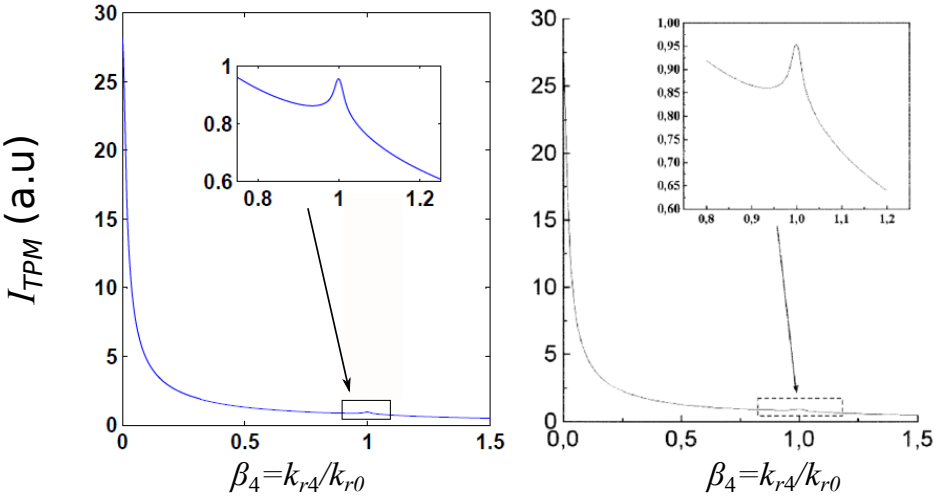

Figure 3.2: Comparison between (right) Fig. (2) of Ref. [Gadonas et al., 1999] and (left) our numerical computation of Eq. 3.23. The parameters β_3 and β_4 are denoted p and q in Ref. [Gadonas et al., 1999].

3.1.3.2/ ANALYTICAL COMPUTATION

To simplify the analytical resolution of this integral, we consider the asymptotic approximation of Bessel functions of the zeroth order that is expressed as $J_0(\nu) \approx \sqrt{\frac{2}{\pi\nu}}\cos(\nu - \pi/4)$ [DLMF,].

This asymptotic formula has a singularity for $\nu = 0$ and can only be used in a range $[\nu_0, +\infty[$, where $\nu_0 > 0$ is a constant. For lower values of ν (up to ν_0 which can be determined numerically), we can develop the function $J_0(\nu)$ in Tailor series up to the first order to simplify the analytical computation of the TPM integral. In this case, $J_0(\nu)$ can be approximated to:

$$J_0(\nu) \approx \begin{cases} 1 - \nu^2/4 & ,0 \leq \nu \leq \nu_0 \\ \sqrt{\frac{2}{\pi\nu}}\cos(\nu - \pi/4) & ,\nu_0 \leq \nu \end{cases} \tag{3.24}$$

To verify the validity of this approximation, we compare the variation of the function $J_0(x)$, defined by the Matlab function "*besselj*(0,ν)", with the approximation given by Eq. 3.24. We choose $\nu_0 = 1.1$. Fig. 3.3 shows that this approximation fairly reproduces the Bessel function $J_0(\nu)$.

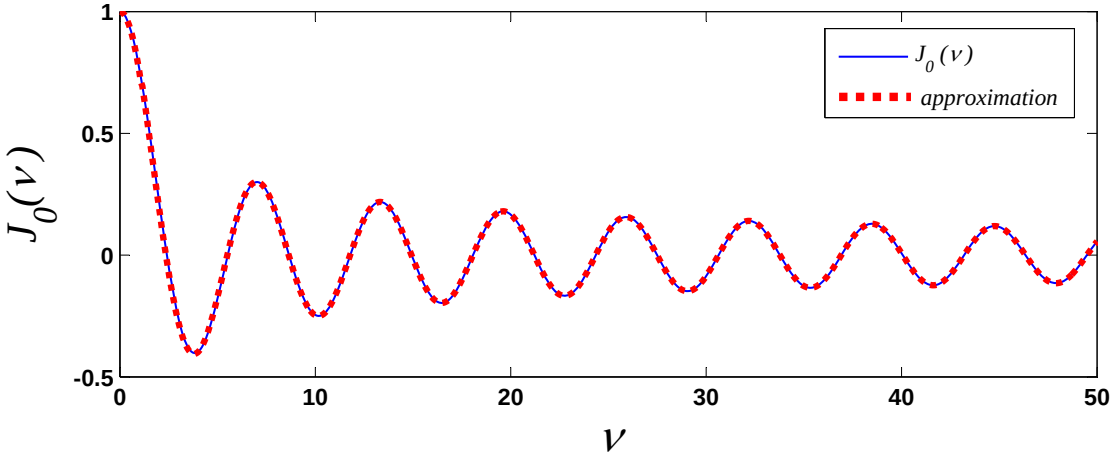

Figure 3.3: Comparison between the variation of $J_0(\nu)$, defined by the Matlab function "*besselj*(0,ν)", with its approximate expression given by Eq. 3.24 where $\nu_0 = 1.1$.

In order to make use of this approximation, we should consider that the argument of each Bessel function of the TPM integral $I_{TPM} = 1/k_{r0}^2 \int_0^{+\nu_f} J_0(\beta_1\nu)\, J_0(\beta_2\nu))\, J_0(\beta_3\nu)\, J_0(\beta_4\nu)\, \nu\, \mathrm{d}\nu$ can be different from the other. That is to say, each function has a specific value of the breakpoint ν_0.

For simplicity, let's first consider the case where $\beta_1 = \beta_2$ and $\beta_3 = \beta_4$ which corresponds to two identical pump waves interacting with a signal wave to yield an idler wave at the same frequency as that of the signal. For analytical integration, we can consider infinite upper limit.

CASE OF TWO IDENTICAL PUMP WAVES

In this case, the TPM integral consists of the squared product of just two Bessel functions:

$$I_{TPM} = 1/k_{r0}^2 \int_0^{+\infty} J_0^2(\beta_1\, \nu)\, J_0^2(\beta_4\, \nu)\, r\, \mathrm{d}r \tag{3.25}$$

The breakpoints of the Bessel functions $J_0(\beta_1\, \nu)$ and $J_0(\beta_4\, \nu)$ are $\nu_1 = 1.1/\beta_1$ $\nu_4 = 1.1/\beta_4$ respectively. In our calculations, we compute I_{TPM} as a function of β_4 for a given value of β_1. Since the breakpoint ν_4 varies as a function of β_4, the approximative expression of I_{TPM} integral depends on whether $\nu_1 < \nu_4$ or $\nu_1 > \nu_4$.
In the case where $\beta_4 < \beta_1$ $(\nu_1 < \nu_4)$, the integral 3.22 can be written as $I_{TPM} = I_1 + I_2 + I_3$ where:

$$I_1 = \int_0^{\nu_1} 1/k_{r0}^2 (1 - \frac{(\beta_1\, \nu)^2}{4})^2 (1 - \frac{(\beta_4\, \nu)^2}{4})^2 \nu\, \mathrm{d}\nu \qquad , \ \nu\epsilon[0, \nu_1] \tag{3.26}$$

$$I_2 = \int_{\nu_1}^{\nu_4} \frac{2}{k_{r0} k_{r1}\, \pi} \cos^2(\beta_1\, \nu - \pi/4)\, (1 - \frac{(\beta_4\, \nu)^2}{4})^2 \mathrm{d}\nu \qquad , \ \nu\epsilon[\nu_1, \nu_4] \tag{3.27}$$

$$I_3 = \int_{\nu_4}^{+\infty} \frac{4}{k_{r1}\, k_{r4}\, \pi^2} \frac{\cos^2(\beta_1\, \nu - \pi/4) \cos^2(\beta_4\, \nu - \pi/4)}{\nu} \mathrm{d}\nu \qquad , \ \nu\epsilon[\nu_4, +\infty] \tag{3.28}$$

We obtain similar expressions for $\beta_4 > \beta_1$. More details can be found in Appendix 3.B (page 154). These integrals can be solved analytically. The solution to these integrals shows that only the third integral I_3 presents singularities, which we interpret as transverse phase matching (which are referred to as transverse spatial resonances in Ref. [Gadonas et al., 2001]):

$$\begin{aligned} I_3 = \frac{1}{2\, k_{r1} k_{r4} \pi^2} \Big\{ & - \mathrm{Ci}[2(\beta_1 + \beta_4)\, \nu] + \mathrm{Ci}[2(\beta_1 - \beta_4)\, \nu] \\ & + 2\, \mathrm{Si}(2\beta_1\, \nu) + 2\, \mathrm{Si}(2\beta_4\, r) + \ln(\nu) \Big\}_{\nu_4}^{+\infty} \end{aligned} \tag{3.29}$$

where $\mathrm{Ci}(x)$ and $\mathrm{Si}(x)$ stand for the cosine and sine integrals respectively and are defined as follows: $\mathrm{Ci}(x) = \int_0^{+\infty} \frac{\cos(t)}{t} \mathrm{d}t$ and $\mathrm{Si}(x) = \int_0^{+\infty} \frac{\sin(t)}{t} \mathrm{d}t$. Knowing that the integral $\mathrm{Ci}(x)$ exhibits a singularity for $x = 0$, the TPM integral then exhibits a singularity for $\beta_4 = \beta_1$. Although this expression is not valid for $\beta_4 = 0$, the fact that I_3 is inversely proportional to β_4 suggests that the TPM integral exhibits a resonance at this frequency too.

Fig. 3.4 shows a comparison between the numerical and analytical computation of the TPM integral. The angle of the signal wave β_4 varies from 0.005 and 1.5. We observe a strong resonance at lower cone angles and a weak resonance at the pump cone angle (20 mrad). These results are in qualitative agreement with those obtained by Gadonas et al. as well as my numerical computation of this integral (Fig. 3.4 [red dotted line]).

N.B: Notice that I_{TPM} is inversely proportional to the central frequency k_{r0}. This shows that this integral is smaller for higher values of cone angles. Thus, this partly explains why nonlinear instabilities are weaker for high cone angles.

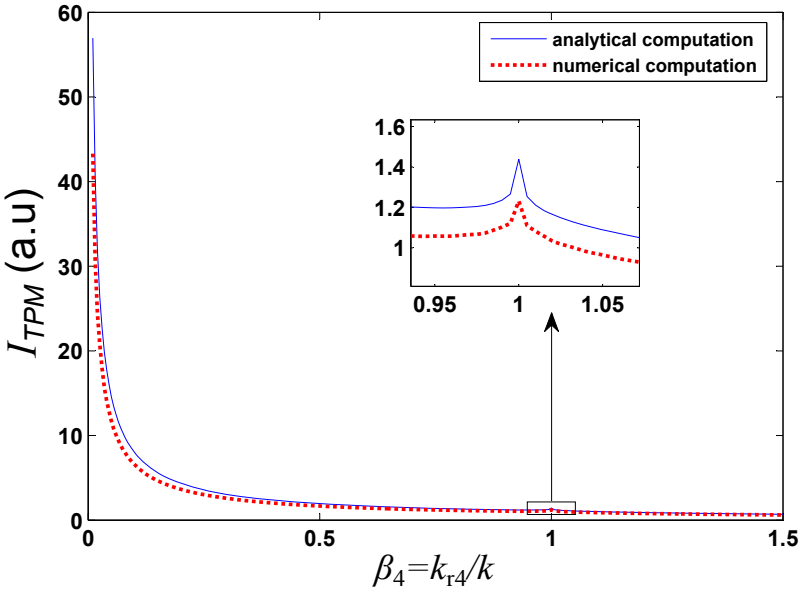

Figure 3.4: (blue line) Analytical and (red dotted line) numerical computation of the TPM integral given by Eq. 3.25.

CASE OF DIFFERENT INTERACTING WAVES

In the case where all spatial frequencies are different, the resolution of Eq. 3.22 is more complicated since there are two other breakpoints. However, the resonance conditions are only found in case the Bessel function is approximated by the second formula of Eq. 3.24. In the case $\beta_4 > \beta_j$, $j = 1, 2, 3$, the expression of the TPM integral is given by:

$$\begin{aligned} I_{TPM} = \frac{1}{2\sqrt{k_{r1}k_{r2}k_{r3}k_{r4}}\pi^2}\Big\{&\mathrm{Ci}[(\beta_1+\beta_2-\beta_3-\beta_4)\,\nu] + \mathrm{Ci}[(\beta_1-\beta_2+\beta_3-\beta_4)\,\nu] \\ &+ \mathrm{Ci}[(\beta_1-\beta_2-\beta_3+\beta_4)\,\nu] + \mathrm{Ci}[(\beta_1+\beta_2+\beta_3+\beta_4)\,\nu] \\ &- \mathrm{Si}[(\beta_1-\beta_2-\beta_3-\beta_4)\,\nu] + \mathrm{Si}[(\beta_1+\beta_2+\beta_3-\beta_4)\,\nu] \\ &+ \mathrm{Si}[(\beta_1+\beta_2-\beta_3+\beta_4)\,\nu] + \mathrm{Si}[(\beta_1-\beta_2+\beta_3+\beta_4)\,\nu]\Big\}_{\nu_4}^{+\infty} \end{aligned} \tag{3.30}$$

From this expression, and since the function "Si" is always finite, we deduce three different resonance conditions corresponding to the conditions for which the function Ci exhibits singularities:

$$\Delta\beta_1 = \beta_1+\beta_2-\beta_3-\beta_4;\ \Delta\beta_2 = \beta_1-\beta_2+\beta_3-\beta_4 \text{ and } \Delta\beta_3 = -\beta_1+\beta_2+\beta_3-\beta_4 \tag{3.31}$$

For two identical pump waves $\beta_1 = \beta_2 = 1$, these conditions are reduced to $\beta_3 = \beta_4$ and $\beta_3 + \beta_4 = 2$. These two conditions are identical to those reported in Ref. [Gadonas et al., 2001] (see Fig. (2) of Ref. [Gadonas et al., 2001] shown in Fig. 3.5). However, if we consider the results of Gadonas et al. (the same figure 3.5), they stated that transverse spatial resonances can occur for two more conditions. They are noted as: $\beta_3 = \beta_4 + 2$ and $\beta_4 = \beta_3 + 2$. These two conditions were determined considering numerical integration of the TPM integral. In our case, we assume that these conditions refer the cutoff frequencies over which the TPM integral is zero [Tewari et al., 1996]. Therefore, they will not be accounted for in our analysis.

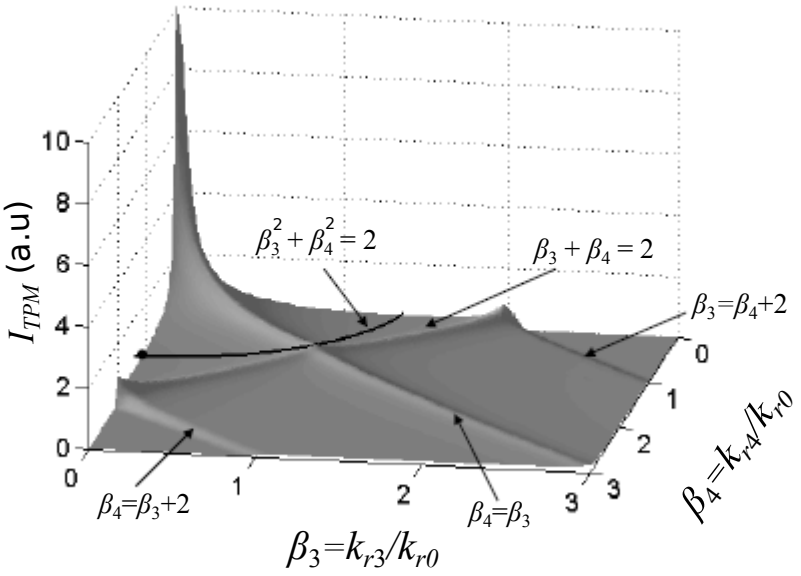

Figure 3.5: Figure (2) of Ref. [Gadonas et al., 2001]: Results of the numerical computation of the TPM integral written as: $I_{TPM} = \int_0^{+\infty} \exp(-2\nu^2/g^2) J_0^2(\nu)\ J_0(\beta_3\,\nu)\, J_0(\beta_4\,\nu)\,\nu\,\mathrm{d}\nu$. The parameters β_3 and β_4 are denoted p and q in Ref. [Gadonas et al., 2001].

CASE OF TWO IDENTICAL PUMP WAVES AND $\beta_4 = 0$

Considering the particular case where $\beta_4 = 0$, the TPM integral reads:

$$I_{TPM0} = 1/k_{r0}^2 \int_0^{+\infty} J_0^2(\beta_1\,\nu)\, J_0(\beta_3\,\nu)\, r\,\mathrm{d}r \tag{3.32}$$

For $\beta_1 = 1$, an analytical solution to this integral can be written as [DLMF,]:

$$I_{TPM0} = \frac{1}{\pi\beta_3\sqrt{1-\beta_3^2/4}} \tag{3.33}$$

This equation exhibits a singularity for two spatial frequencies, namely $\beta_3 = \beta_4 = 0$ and $\beta_3 = 2$. Notice that these two TPM conditions can be obtained from the general TPM conditions described by Eqs. 3.31. Hence, although the TPM integral 3.22 is only defined for $\beta_4 > 0$, the case where $\beta_4 = 0$ can still be taken into account for values close to zero.

3.2/ ANALYSIS OF KERR-INDUCED INSTABILITIES IN BESSEL BEAMS

Before introducing our approach in controlling nonlinear instabilities in Bessel beams, we propose to use our reduced FWM model to analyze their different features. To this end, we first present and analyze numerical simulation results of nonlinear propagation of a Bessel beam. We will specifically analyze FWM interactions leading to the generation and growth of new spectral components. We will then use our model to interpret these nonlinear dynamics.

3.2.1/ NUMERICAL SIMULATION MODEL IN A PURE KERR MEDIUM

Our numerical simulations are based on standard nonlinear Schrödinger equation (NLSE) [Gadonas et al., 2001, Porras et al., 2004, Polesana et al., 2008]. To highlight the effect of Kerr-induced instabilities, we will, in a first approximation, only consider Kerr nonlinearity and neglect other nonlinear effects (nonlinear losses), as in Ref. [Gadonas et al., 2001]. The propagation equation we solve is then written as:

$$\frac{\partial A}{\partial z} = \frac{i}{2k_0}\Delta_\perp A + ik_0 n_2 |A|^2 A \tag{3.34}$$

where A is the linearly polarized monochromatic complex amplitude of the laser electric field, $\Delta_\perp = 1/r\partial/\partial r + \partial^2/\partial r^2$ is the transverse Laplacian operator, r and z are the radial and axial coordinates, k_0 is the wave vector in vacuum ($k = n\,k_0$ in the medium), n and n_2 are the linear and nonlinear refractive indices.

Nonlinear instabilities were shown to depend on the input beam conditions [Polesana et al., 2007]. These conditions are depicted in Fig. (3.6). In case the Bessel beam is progressively formed in the medium (Fig. (3.6,left)), nonlinear instabilities were shown to be negligible. In contrast, instabilities were shown to be enhanced in case the beam is formed prior entering the sample in such a way as its peak intensity coincides with the point of laser-matter contact (Fig. (3.6,middle)). These conditions are thus referred to smooth and abrupt intensity transitions.

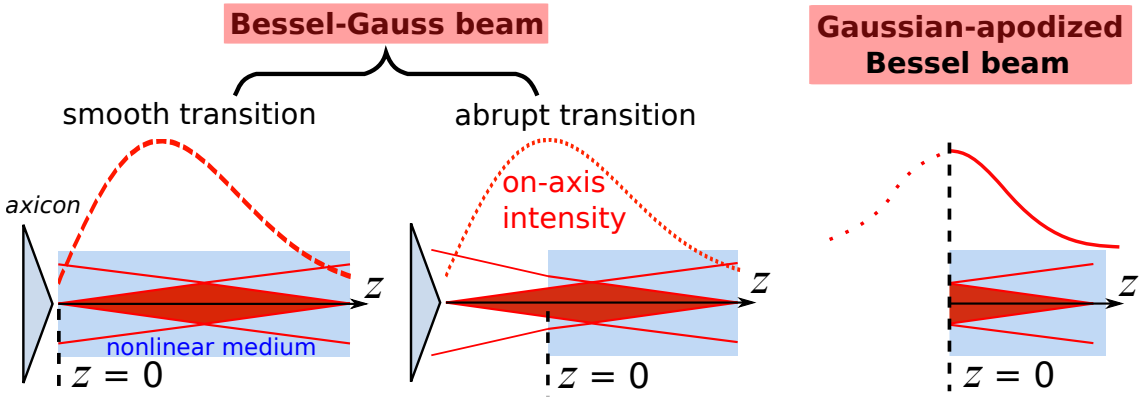

Figure 3.6: Input conditions for numerical simulations reported in (left) Ref. [Polesana et al., 2008] and (right) Ref. [Gadonas et al., 2001].

In their analysis of nonlinear instabilities in Bessel beams [Gadonas et al., 2001], Gadonas et al. modeled quasi-Bessel beams with a Gaussian-apodized Bessel function: $A_{GJ0}(r, z = 0) = \exp(-r^2/w_0^2)\, J_0(k\, r\, \sin(\theta))$. In their simulations, the Bessel beam, at $z = 0$, is at its maximum intensity as depicted in Fig. (3.6,right). They showed that nonlinear intensity modulation appears right after entering the nonlinear medium. This feature is similar to the abrupt input condition, like the one shown in [Polesana et al., 2007]. This model does not correspond to quasi-Bessel beams that are usually used experimentally, i.e. those generated by axicons. In the following, we will consider an axicon-generated Bessel beam [Polesana et al., 2007, Polesana et al., 2008], which we will refer to as Bessel-Gauss beam, propagating according to the smooth intensity transition case.

The input field is then modeled by a Gaussian beam with a spatial phase characterizing the axicon conical focusing:

$$A_{BG}(r, z = 0) = \exp\Big(- \frac{r^2}{w_0^2} - k\, r\, \sin(\theta)\Big) \tag{3.35}$$

where w_0 is the beam waist defined at 1/e of the central amplitude and θ is the cone angle of the beam in the nonlinear medium.

Although nonlinear instabilities are reduced in smooth transition case, they can still take place in case Kerr nonlinearity prevail over nonlinear losses, which corresponds to relatively low peak intensities of Bessel beams and low cone angles [Polesana et al., 2007, Porras et al., 2004, Couairon et al., 2012]. In our simulations, since nonlinear losses are neglected, the input power and Bessel cone angle are chosen as to induce significant on-axis intensity modulation. We use a relatively low value of the cone angle $\theta = 4°$ as to enhance nonlinear FWM interactions. The peak intensity is chosen to be high enough to trigger Kerr nonlinearity but low enough to not lead to optical collapse, i.e. nonlinear losses in this case are physically small and can be neglected in a first step (weakly nonlinear filamentation regime [Polesana et al., 2008]). We chose a maximal intensity $I_{max} = 14.5\ TW/cm^2$ corresponding to an input power $P_{in} = 47.6\ MW$. Parameters of our simulations are summarized in table 3.1.

$\lambda\ (\mu m)$	n	n_2 (m^2/W)	θ (°)	$w_0\ (\mu m)$	$P_{in}\ (MW)$
0.8	1.45	$2.48\ 10^{-20}$	4	300	47.6

Table 3.1: Numerical parameters used in simulations. The values of n and n_2 correspond to those of fused silica [Gulley et al., 2010].

Note that our nonlinear propagation equation (3.34) is solved using cylindrical symmetry. Thus, potential azimuthal modulation instabilities are not accounted for.

3.2.2/ NUMERICAL SIMULATION RESULTS

Simulation results are shown in Fig. (3.7). In Fig. (3.7,a), we plot the intensity evolution as a function of the radial distance r and propagation distance z. The beam intensity is seen to undergo longitudinal modulation not only along the central core but also in the peripheral rings. The on-axis intensity is shown in Fig. (3.7,b), where these intensity oscillations, with a period of $\approx 180.5\ \mu m$, are clearly apparent.

In Fig. (3.7,c) the spatial spectrum $|S(k_r, z)|^2$ is displayed as a function of the propagation distance. We recall that the spatial spectrum of a Bessel beam in the linear regime is in the form of a ring centered around the Bessel transverse frequency $k_{r0} = 0.55\ \mu m^{-1}$. In our simulations, we make use of azimuthal symmetry of the beam and thus we only display the evolution of a cross-section along the propagation distance. After an initial stage of spectral broadening around the central frequency k_{r0}, we notice the generation of two particular spectral components at $k_r \approx 0$ and $k_r \approx 1.5 k_{r0}$. These components are referred to an axial wave and outer ring respectively.

As discussed above, the observed longitudinal intensity modulation can be explained as the interference of these newly-generated waves with the input conical beam. In the

literature, although both spectral components are considered as part of nonlinear instabilities, the axial wave is the only one that is usually considered to interact with the input Bessel beam [Gadonas et al., 2001, Polesana et al., 2008]. Furthermore, we notice in Fig. (3.7,c) parabolic-like structures in the spatial spectrum that appear before the growth of the axial wave. What is the contribution of the outer ring in nonlinear intensity modulation? and what is the cause of these spectral structures and what is their role in subsequent nonlinear distortions? In the following, we will bring an answer to these questions.

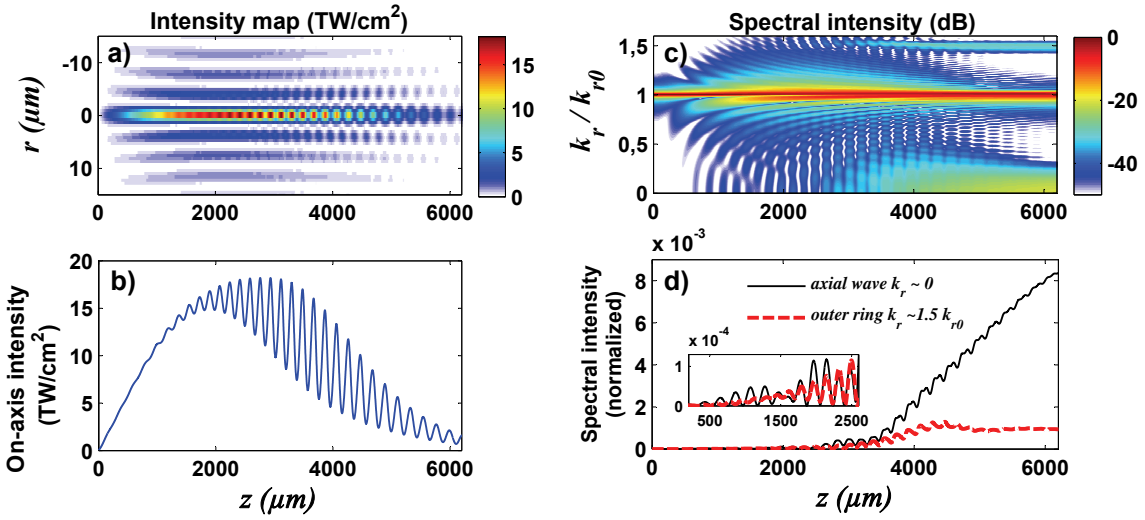

Figure 3.7: NLSE simulation results: (a) intensity distribution of a Bessel–Gauss (BG) beam propagating in a pure nonlinear Kerr medium ($n_2 = 2.4810^{-16}$ cm^2/W), as a function of the radial and propagation distances r and z, (b) the corresponding on-axis intensity, (c) the spatial spectrum distribution $|S(k_{rj}|^2/|S(k_{r0}|^2|$ along the propagation distance (logarithmic scale dB) and (d) the on-axis spectral intensity of the axial wave (solid line) and outer ring in linear scale (dashed line). The intensity of both spectral components are normalized to the maximal intensity value of the central frequency.

3.2.3/ Interpretation of new frequency generation

In abrupt input condition, the axial wave was shown to be directly generated and thus leads to instantaneous on-axis intensity modulation [Polesana et al., 2007]. In soft input condition, which is the case of Fig. (3.7), both the axial wave and outer ring are gradually generated and amplified as shown in Fig. (3.7,c,d). Up to $z = 2600\ \mu m$, the axial wave and outer ring ($k_r \approx 0$ and $k_r \approx 1.5k_{r0}$) are not efficiently generated and exhibit an oscillatory behavior. The magnitude of their spectral intensity is very low and is below -40 dB. After this propagation point, we notice a significant increase in the spectral intensity of both spectral components in an oscillating fashion. Notice the near linear growth of the axial wave which is similar to the one reported in [Gadonas et al., 2001]. Considering the beam spectral expansion, which exhibits parabolic-like structures, all spectral components that are further away from the main ring (Bessel ring) show the same oscillatory behavior. To explain these features, let's first recall the theory of Gadonas et al..

In our reduced FWM model, we considered all the FWM interactions that, according to our estimate, contribute the most to nonlinear instabilities. However, this does not tell

us whether these FWM interactions take place all at once or that they step in according to a specific order. In this regard, the theory of Gadonas et al., reported in Ref. [Gadonas et al., 2001], shows that nonlinear interactions occur at a specific order and not necessarily at the same time. We will discuss this point later in this section.

We will first recall and describe the theory of Gadonas et al. We will specify the similarities between this theory and our reduced FWM model. Then, we will further discuss the different features of nonlinear spectral distortions of Bessel beams observed in our simulations.

3.2.3.1/ DESCRIPTION OF THE THEORY OF REF. [GADONAS ET AL., 2001]

The theory reported by Gadonas et al. [Gadonas et al., 2001] allowed describing the nonlinear processes leading to the generation of both the axial wave and outer ring. This theory is based on standard nonlinear Schrödinger equation (NLSE) expressed by Eq. (3.34). Considering the same normalized parameters as described previously (section 3.1.2.3, page 69), this equation becomes:

$$\frac{\partial B}{\partial \xi} - i\Delta_{\perp n} B = i\gamma |B|^2 B \tag{3.36}$$

where the input optical envelope is simply modeled by a J_0 beam $A_0(r) = \sqrt{I_0} J_0(\nu)$ and $B_0 = J_0(\nu)$. The nonlinear medium is assumed to be of weak nonlinear coefficient $\delta_{NL} = n_2 k_0 I_0$ compared to the linear phase shift of a J_0 beam $\delta = k_{r0}^2/2k$, i.e. $\gamma = \delta_{NL}/\delta \ll 1$. In this case, the solution of Eq. (3.36) was written as:

$$B = B_0(\nu) + B_1(\nu, \xi) + B_2(\nu, \xi) + ... \tag{3.37}$$

such that $B_{j-1} \propto \gamma^{j-1}$, $j \in \mathbb{N}^*$. Finally, considering quantities of the same order, i.e. B_j, $\gamma^{(j-1)} B_{j-1}$,etc, one can develop a series of nonlinear propagation equations to calculate each of the quantities B_j as a function of B_{j-1} [Gadonas et al., 2001]:

$$\frac{\partial B_1}{\partial \xi} - i\Delta_{\perp n} B_1 = i\gamma |B_0|^2 B_0 \qquad \text{, first approximation} \tag{3.38}$$

$$\frac{\partial B_2}{\partial \xi} - i\Delta_{\perp n} B_2 = i\gamma (2|B_0|^2 B_1 + B_0^2 B_1^*) \qquad \text{, second approximation} \tag{3.39}$$

These two equations indicate that the solution B_1 depends on nonlinear interaction of input beam $B_0 = J_0(\nu)$ with itself while the solution B_2 depends on the interaction of B_0 with the self-generated wave B_1. It is then clear that the two nonlinear interactions described according to the second approximation can only take place after the one described in the first approximation.

In the following, we will separately consider the nonlinear interactions described by Eqs. (3.38) and (3.39). Then, we will solely take into account nonlinear terms specific to each equation and insert them in our reduced FWM model. Afterwards, We will compare our theoretical results with numerical simulation results of Fig. (3.7).

3.2.3.2/ FIRST APPROXIMATION: GENERATION OF THE AXIAL WAVE SEED

According to the first approximation (Eq. 3.38), the solution B_1 is a result of the interaction of three identical waves $B_0 = J_0(\nu)$. In the framework of FWM process, this corresponds to the interaction of two identical pump waves with a signal wave identical to the pump. In this case, the longitudinal phase-matching (LPM) condition for the idler wave states that $\beta_4 = \beta_3 = 1$. Such an interaction is reminiscent of self-phase modulation (SPM) according to which the pump wave self-induces a nonlinear phase shift. In the following, we will refer to this term as SPM (that is solely applied to the idler wave). Regarding the transverse phase-matching (TPM) condition, the TPM integral is written as:

$$I_{TPM}^{1st} = 1/k_{r0}^2 \int_0^{\nu_f} J_0^3(\nu) J_0(\beta_4\, \nu)\, \nu\, \mathrm{d}\nu \tag{3.40}$$

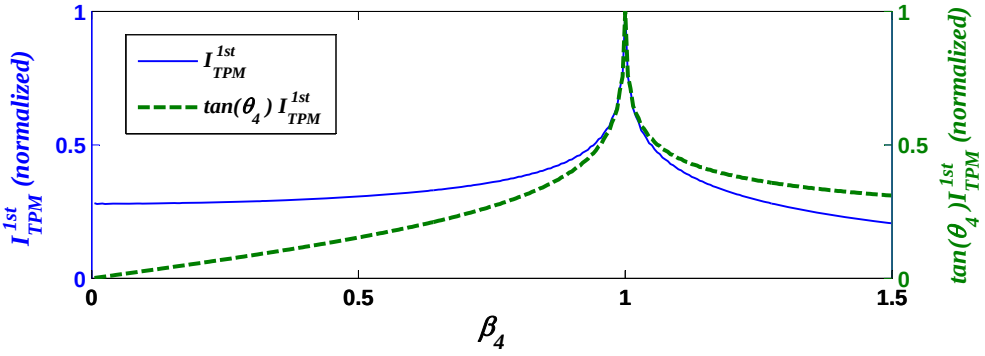

Figure 3.8: Numerical computation of the TPM integral in the case of the first approximation according to Eq. (3.8, (solid line) and $\tan(\theta_4)\, I_{TPM}^{1st}$ (dashed line). These two quantities are normalized to their specific maximal value.

Its numerical computation shows that transverse resonance occurs also for $\beta_4 = 1$ (see Fig. (3.8)). According to Ref. [Gadonas et al., 2001], Bessel beams are robust to Kerr nonlinearity of the first approximation and no new frequency can be efficiently generated. However, although the TPM integral is maximal at $\beta_4 = 1$, it is not zero at other spatial frequencies. Unfortunately, this theory does not tell us the behavior of the idler wave along propagation. In this regard, we consider our reduced FWM model described by Eq. (3.21).

Considering the same conditions as in the first approximation, we consider two single and identical pump waves and a signal wave each defined at $\beta_1 = \beta_2 = \beta_3 = 1$. We ignore the input spectral phases ϕ_j (we will discuss their impact in the next section). The expression of the corresponding input spatial spectra is written as:

$$\tilde{S}_j(\beta_j) = \delta(\beta_j - 1), \quad j = 1, 2, 3 \tag{3.41}$$

By inserting Eq. (3.41) in Eq. (3.21) and integrating over ξ, we find:

$$a_4(\xi, \theta_4) = 3i\, C_0\, \tan(\theta_4)\, I_{TPM}^{1st} \xi \exp[0.5i(1 - \beta_4^2)\xi] \,\mathrm{sinc}[0.5(1 - \beta_4^2)\xi] \tag{3.42}$$

We compute the squared absolute value $I_4(\xi,\theta_4) = |a_4(\xi,\theta_4)|^2$ of Eq. (3.42) and we obtain:

$$I_4(\xi,\theta_4) \propto (I_{TPM}^{1st})^2 \frac{\tan^2(\theta_4)}{(1-\beta_4^2)^2} \sin^2\left[0.5(1-\beta_4^2)\xi\right] \tag{3.43}$$

The on-axis envelope of the idler wave $a_4(\xi,\theta_4)$ is then expressed as a function of the same TPM integral I_{TPM}^{1st}. Notice that the LPM terms $\Delta\beta_{zm}$ are all reduced to $(1-\beta_4^2)$. The dependence of $I_4(\xi,\theta_4)$ on this LPM term is expressed as $[\sin(0.5(1-\beta_4^2)\xi)/(1-\beta_4^2)]^2$. This term states that I_4 oscillates at a period $p(\theta_4) = \lambda/n|\cos(\theta_4) - \cos(\theta_0|)$. This term also indicates that I_4 only has significant values at low propagation distances and in case $\beta_4 = 1$, i.e. in case LPM condition is satisfied. Thus, we express the z-evolution of the idler wave as a function of both TPM integral and LPM terms.

As in Ref. [Tewari et al., 1996], I_4 is proportional to $tan^2(\theta_4)$ which shows that the magnitude of the idler wave would be lower for low cone angles as shown in Fig. (3.8).

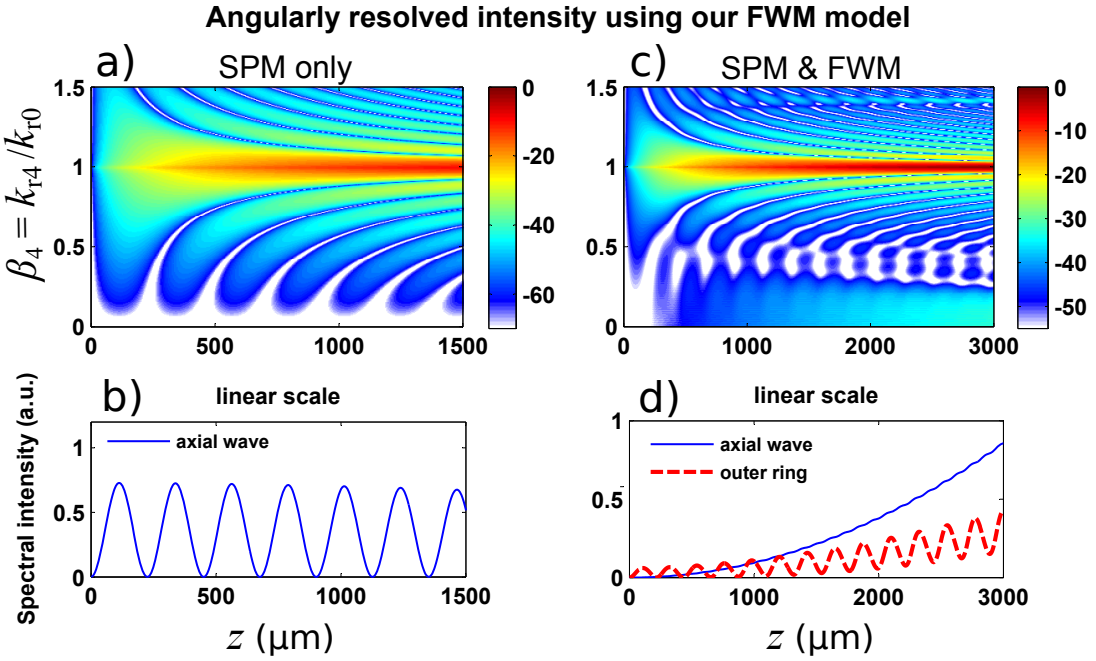

Figure 3.9: Evolution of angularly-resolved intensity (dB) of the idler wave along propagation in case (a-b) the idler wave is generated by SPM only (first approximation: $\beta_1 = \beta_2 = \beta_3 = 1$, i.e. the input spatial spectra of the pump and signal waves are defined by Eq. (3.41)) and (c-d) the idler wave is resulted from both SPM and other FWM interactions [second approximation: i.e. the spatial spectrum of pump wave is defined by Eq. (3.41) while that of the signal wave is written by Eq. (3.46), i.e. $\tilde{S}_3(\beta_3) = \delta(\beta_3 - 1) + \delta(\beta_3 - 0.01)$].

In Fig. (3.9, left), we show the spectral intensity map of the idler wave according to Eq. (3.42) and specifically plot the variation of the axial wave along propagation. Here, we consider the same cone angle $\theta = 4°$ as in our numerical simulation of the NLSE (Fig. (3.7)). This figure shows that the idler wave is intense around the central frequency and increases in intensity along propagation. However, the intensity decreases for frequencies that are away from the central one. On the one hand, this is due to the magnitude of the TPM integral which is maximal at $\beta_4 = 1$. On the other hand, and as

we stated above, the intensity $|a_4|^2$ decreases in magnitude along propagation except if the same condition $\beta_4 = 1$ is satisfied. In addition, this intensity drop is sharper for low frequencies since a_4 is proportional to $\tan(\theta_4)$. Of particular interest, we notice that the idler wave oscillates for frequencies that are away from the central frequency $\beta_4 = 1$ and exhibits parabolic-like structures.

Comparing these results to our numerical simulation results of Fig. (3.7,right) (page 78), we notice a qualitative agreement up to $z = 2600\ \mu m$. Hence, the nonlinear dynamics observed prior to the intensity amplification of the axial wave (spectral broadening, parabolic-like structures) can be interpreted as SPM-like interactions. The oscillating behavior of the axial wave was also reproduced by our FWM model. Here, the oscillation period $p = \lambda/n(1 - \cos(\theta_4))$ yields 226 μm which is about the same as that obtained numerically in Fig. (3.7,d), i.e $p_{num} \approx 226\ \mu m$. Hence, this SPM term is the origin of the axial wave seed which is further amplified for propagation distances $z > 2600\ \mu m$.

The parabolic-like patterns obtained from the NLSE simulation results (Fig. 3.7,c) are also well described by our reduced FWM model. According to Eq. 3.42, these parabolic-like structures stem from the term $\xi \mathrm{sinc}[0.5(1 - \beta_4^2)\xi]$. This term is maximal in case the LPM condition is satisfied, i.e. $\beta_4 = 1$. In case $\beta_4 \neq 1$, this term indicates that $a_4(\xi, \beta_4)$ oscillates at frequency-dependent propagation length $p(\theta_4) = \lambda/n|\cos(\theta_4) - \cos(\theta_0|)$. This shows that the oscillation period is longer for spatial frequencies that are closer to the central one. As depicted in Fig. (3.9,left), this gives rise to the observed parabolic-like patterns.

At low propagation, we can then deduce that SPM is the most efficient Kerr-induced effect since the Bessel beam has yet to reach its peak intensity. As the intensity increases along propagation, other Kerr-induced effects become more and more efficient which leads to further spectral distortions, that is the generation of the axial wave and outer ring.

3.2.3.3/ SECOND APPROXIMATION: GROWTH OF NEW SPECTRAL COMPONENTS

Let us now consider the second approximation of Eq. (3.39) as stated in the theory of Gadonas et al. [Gadonas et al., 2001], i.e. $\dfrac{\partial B_2}{\partial \xi} - i\Delta_{\perp n} B_2 = i\gamma(2|B_0|^2 B_1 + |B_0|^2 B_1^*)$ and analyze the nonlinear dynamics observed for $z > 2600\ \mu m$.

As stated above, the solution B_2 depends on the interaction of B_0 with the self-generated wave B_1. According to Eq. (3.39), the solution B_2 depends on two nonlinear interactions, namely $2|B_0|^2 B_1$ and $|B_0|^2 B_1^*$. These two terms refer both to the interaction of two identical pump waves, defined at $\beta = 1$ with a signal wave that was self-generated beforehand by the SPM term (which is qualitatively depicted in Fig. (3.9, left)). In contrast with the first approximation, the signal wave in this case is defined at all spectral components contained in B_1.

Regarding TPM conditions, these two terms have both same TPM integral [Gadonas et al., 2001], which is:

$$I_{TPM}^{2nd} = 1/k_{r0}^2 \int_0^{r_f} J_0^2(\nu)\, J_0(\beta_3\, \nu)\, J_0(\beta_4\, \nu)\, \nu\, \mathrm{d}\nu \tag{3.44}$$

This integral was shown to manifest two main transverse resonances (Fig. 3.5), namely for $\beta_3 = \beta_4$ and $\beta_3 + \beta_4 = 2$ and particularly $\beta_3 = \beta_4 = 0$. Regarding LPM conditions, they

depend on the interaction term [Gadonas et al., 2001]:

- The first term $(2|B_0|^2B_1)$ is maximal for $\beta_4 = \beta_3$. The axial wave, which is defined at $\beta_4 = 0$, actually satisfies both LPM and TPM conditions which explains its significant intensity growth along propagation. In this regard, we can assimilate the term "$2|B_0|^2B_1$" to cross phase modulation (XPM) applied to the axial wave.

- The second term $(B_0^2B_1^*)$ yields $\beta_4 = \sqrt{2-\beta_3^2}$. This LPM condition does not correspond to any transverse spatial resonance. Hence, the efficiency of the corresponding nonlinear interaction depends on the spectral intensity of the signal wave. In other words, the axial wave in this case is the only spectral component that can take the role of a signal wave ($\beta_3 \approx 0$) since it is amplified through a XPM-like nonlinear process. Consequently, the idler wave is generated at $\beta_4 = \sqrt{2}$, which corresponds to the outer ring, according to a parametric amplification [Gadonas et al., 2001].

In the following, we will refer to these two terms as "FWM" since they are the only ones that efficiently generate new frequencies. In addition, in contrast with SPM effect of the first approximation, these two interactions involve two intense pump waves with a weak signal wave which correspond to the conventional picture of FWM processes. We illustrate these two interactions in Fig. (3.10).

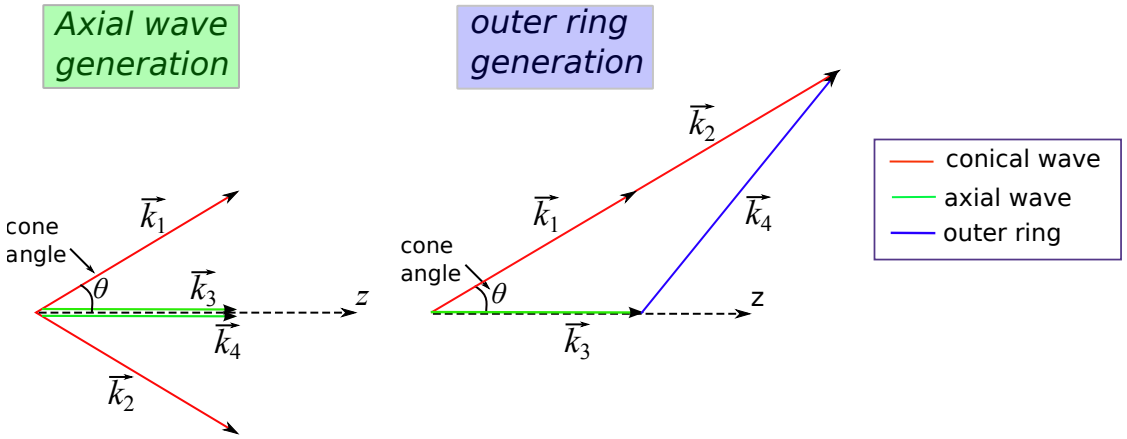

Figure 3.10: Illustration of FWM interactions of the second approximation, described by Eq. (3.39) satisfying the corresponding LPM conditions.

The theory of Gadonas et al. thus allows predicting the nonlinear FWM processes leading to the generation and growth of the axial wave and outer ring. However, this theory cannot describe other features related to the nonlinear evolution of the spatial spectrum of Bessel beams. For instance, according to the NLSE simulation results described in Fig. (3.7,right) (page 78), the spatial spectrum displays interference patterns and that both the axial wave and outer ring exhibit an oscillatory behavior along propagation. In this regard, we will use our reduced FWM model in order to explain these features.

We consider the interaction of two identical pump waves with a signal wave defined at an arbitrary frequency β_3. Our equation is written as follows:

$$a_4(\xi,\theta_4) = i\,C_0\,\tan(\theta_4)\,I_{TPM}^{2nd}\xi\left\{2\exp[0.5i(\beta_3^2-\beta_4^2)\xi]\,\mathrm{sinc}[0.5(\beta_3^2-\beta_4^2)\xi] + \exp[0.5i(2-\beta_3^2-\beta_4^2)\xi]\,\mathrm{sinc}[0.5(2-\beta_3^2-\beta_4^2)\xi]\right\} \quad (3.45)$$

As in the first approximation, the on-axis envelope of the idler wave is also expressed as a function of both TPM integral and LPM terms. Our LPM conditions, described by Eq. (3.20), are reduced to $\beta_4 = \beta_3$ and $\beta_4 = \sqrt{2-\beta_3^2}$, exactly as those obtained from the second approximation [Gadonas et al., 2001]. In Fig. (3.9,right), we depict the angularly resolved spectral intensity of the idler as a function of z for $\beta_3 = 0.01$ (axial wave seed)[1]. Here, we superimposed Eq. (3.45) to Eq. (3.42) to account for the spectral expansion induced by SPM interactions. In other words, the input spatial spectra of the pump waves are defined at the central frequency $\beta_1 = \beta_2 = 1$ as described by Eq. (3.41). As for the signal wave, it is composed of two different spectral components: the central spectral component and a signal wave seed $\beta_3 \approx 0$. In Fig. (3.9,right), we defined this signal wave seed at $\beta_3 = 0.01$. Hence, the expression of the corresponding spectrum is given by:

$$\tilde{S}_3(\beta_3) = \delta(\beta_3 - 1) + \delta(\beta_3 - 0.01) \tag{3.46}$$

The general picture we observe in this figure is qualitatively consistent with our simulation results of the NLSE of Fig. 3.7: the axial wave is amplified along propagation. Here it exhibits weak oscillations and the growth takes the form of a parabola (3.9,d-solid line), which contrasts with the linear and oscillating growth observed numerically. Note here that the signal wave seed, which we defined at $\beta_3 = 0.01$, is assumed to be constant in our FWM model whereas it is actually oscillating along propagation (see Fig. (3.7,d)). Nonetheless, this assumption allows describing some features of the outer ring growth as displayed in Fig. (3.9,d-dashed line): the outer ring grows quasi-linearly in an oscillating fashion, which is in qualitative agreement with the NLSE simulation results. This shows that the oscillating behavior of the idler wave is mainly due to the SPM effect rather than the parametric amplification effect. Another feature described here is the fringe pattern observed for distances $z > 2600\ \mu m$ in Fig. (3.9,c). Notice that about the same pattern is obtained by our FWM model which results from the superposition of the idler generated by both SPM (first approximation) and FWM terms (second approximation).

Particular case where $\beta_4 = 0$: Regarding the particular case where $\beta_4 = 0$, we also consider the interaction of two identical pump waves with a signal wave composed of two frequencies as defined by Eq. (3.46). Here, the axial wave seed in Eq. (3.46) can be defined at $\beta_3 = 0$ instead of 0.01. By superposing the SPM term (Eq. 3.42) to the FWM term (Eq. 3.45), the on-axis evolution of the axial wave can be written as:

$$\begin{aligned} a_4(\xi, \theta_4 = 0) \propto & 6i\, I^{1st}_{TPM0} \exp(0.5i\xi)\, \sin(0.5\xi) \\ & + i\, I^{2nd}_{TPM0}\, [2\,\xi + \exp(i\,\xi)\, \sin(\xi)] \end{aligned} \tag{3.47}$$

where $I^{1st}_{TPM0} = 1/k^2_{r0} \int_0^{\nu_f} J_0^3(\nu)\, \nu\, \mathrm{d}\nu$ and $I^{2nd}_{TPM0} = 1/k^2_{r0} \int_0^{r_f} J_0^2(\nu)\, \nu\, \mathrm{d}\nu$. According to this equation, the on-axis envelope of the idler wave shows two different behaviors: the first is a linear increase in amplitude, i.e. a quadratic increase in intensity as it is the case in Fig. (3.9,d-solid line) where the axial wave seed is defined at $\beta_3 = 0.01$. The second one concerns the oscillating behavior determined by the two sine functions.

Notice that these two sine functions have two different oscillating periods: the SPM term yields an oscillating period of $p_{SPM} = \lambda/n(1-\cos(\theta_0))$ while the FWM term yields of $p_{FWM} =$

[1] Since Eq. (3.45) is not valid for $\beta_4 = 0$, we choose $\beta_3 = 0.01$ instead of 0 so that the spatial frequency for which the LPM condition $\beta_4 = \beta_3$ is satisfied is in the range of validity of our equation.

$p_{SPM}/2$. If we reconsider the NLSE simulation results described in Fig. (3.7) in page 78 (it is re-shown in Fig. (3.11)), we notice a particular feature in the behavior of the axial wave: within the observed oscillations of the axial wave for distances $z > 3500\ \mu m$, we notice weaker sub-oscillations with half the oscillating period of the main oscillations, which is qualitatively described by our model. This particular feature was also observed in Ref. [Gadonas et al., 2001]. Although these sub-oscillations are very weak and may not have any particular effect on the growth of new spectral components, this feature can still be considered as a signature of the efficiency of FWM interactions.

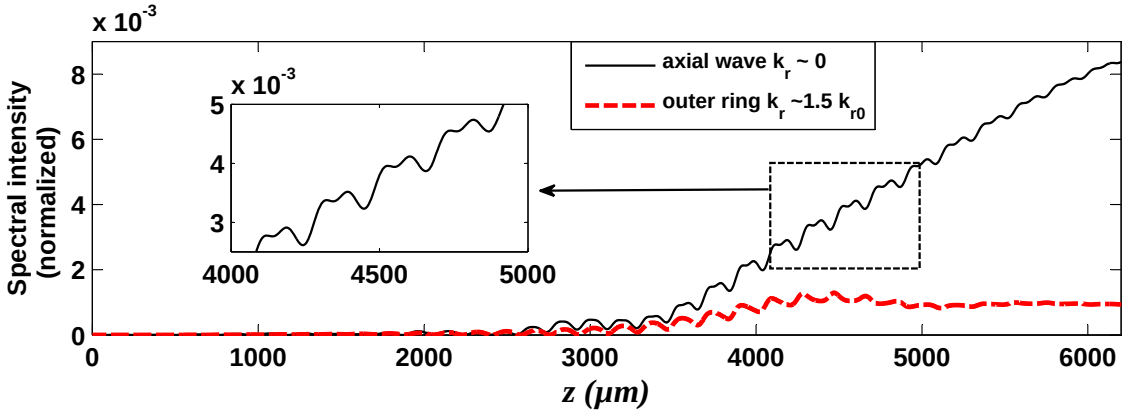

Figure 3.11: Same as Fig. (3.7,d): NLSE simulation results showing the evolution of the axial wave and outer ring along propagation.

Frequency shift of the outer ring: Another point of difference between our theoretical and simulation results is the frequency at which the outer ring is generated. Numerically, the outer ring is generated at $\beta_4 = 1.5$ whereas it is theoretically produced at $\beta_4 = \sqrt{2}$. This point of difference is due to a nonlinear effect that is not included in our FWM model, namely the frequency shift of the beam spatial spectrum due to the compression of the central core of the beam [Polesana et al., 2005, Porras et al., 2004]. In the nonlinear regime, the Bessel frequency k_{r0} was shown to be dependent on the Bessel beam intensity. In a first approximation, it reads [Porras et al., 2004]:

$$\begin{aligned} k_{r0,NL} &= \sqrt{2\,k\,(\delta + \delta_{NL})} \\ &= \sqrt{2\,k\,\delta(1 + \delta_{NL}/\delta)} \\ &= k_{r0}\sqrt{1 + 4\,n_2 I/n\theta^2} \end{aligned} \tag{3.48}$$

where δ and δ_{NL} were defined earlier in this section (page 79). This frequency shift does not affect the phase-matching conditions of the axial wave. In contrast, the LPM condition for the outer ring becomes intensity-dependent as $\beta_4 = \sqrt{2\,\sqrt{1 + 4\,n_2 I_e/n\theta^2}}$. It is clear that the outer ring would also undergo a frequency shift which explains its generation at $\beta_4 \approx 1.5$ rather than $\sqrt{2}$. Note that this expression only describes the frequency shift of the outer ring and can roughly be used to predict its value. One reason is that the intensity I_e in this expression is hard to define. In Ref. [Norfold et al., 2010], I_e was defined as an effective intensity and approximated to $I_e = 0.27 I_{max}$. Considering our

numerical parameters of table (3.1), this LPM condition yields $\beta_4 \approx 1.58$ which is higher than the numerical value ≈ 1.5.

To summarize, our model, along with the theory of Gadonas et al., allows a qualitative understanding of the main features of Kerr-induced spectral distortions in Bessel beams. At low propagation distances, where the peak intensity of the Bessel beam is still low, the input conical pump wave interacts with itself resulting in spectral broadening. Along this process, the seed of the axial wave is generated manifesting an oscillating behavior along propagation. As the propagation distance increases, the peak intensity increases leading to efficient FWM interactions. As a result, the axial wave is significantly amplified which leads in turn to the generation of the outer ring through parametric amplification. In addition, our theory allows describing other features related to the nonlinear evolution of the spatial spectrum of Bessel beams, such as the parabolic-like patterns related to SPM spectral broadening and the fringe-patterns resulting from the superposition of idler waves induced by SPM and FWM interactions. In the next section, we will further investigate the impact of these two components on the input conical beam.

3.2.4/ INTERPRETATION OF LONGITUDINAL INTENSITY MODULATION

Gadonas et al. stated that the appearance of the axial wave is a signature of nonlinear instabilities in Bessel beams [Gadonas et al., 2001] and the observed longitudinal intensity modulation is the result of the interference of the input conical beam with this self-generated component [Gadonas et al., 2001, Polesana et al., 2008] . In Ref. [Polesana et al., 2007], modulation instability analysis showed that both the axial wave and outer ring can be interpreted as unstable modes. Furthermore, the magnitude of nonlinear instabilities was shown to depend on how efficient parametric amplification is. Thus, the interference of outer ring with input conical beam can theoretically also lead to longitudinal intensity modulation. Here, we will investigate the contribution of these two components to on-axis intensity modulation .

Let us consider the spatial spectrum of a Bessel beam superposed to that of a self-generated component defined at β_j (i.e. either the axial wave $\beta_{ax} \approx 0$ or outer ring $\beta_{out} \approx 1.5$). To simplify our computation, we consider ideal J_0 beams whose spatial spectrum is defined by an off-axis Dirac function. Let us define this spectrum at an initial plane $z = 0$. It reads:

$$S(\beta, z = 0) = S_0 \delta(\beta - 1) + S_j \delta(\beta - \beta_j) \tag{3.49}$$

where S_0 and S_j are the spectral amplitudes of the input conical wave and self-generated wave respectively. The subscript j refers to either the axial wave "ax" or the outer ring "out". For simplicity, we fix the value of S_0 to unity ($S_0 = 1$). Using inverse Hankel transform of this equation, we compute the corresponding optical envelope in real space $U(r, z = 0)$. Using the normalized radial coordinate $\nu = k_{r0} r$, it yields:

$$U(\nu, z = 0) = J_0(\nu) + S_j \beta_j J_0(\beta_j \nu) \tag{3.50}$$

To analyze the on-axis evolution of this field, we use the same approach as in Ref. [Čižmár et al., 2009] which was described in chapter 2: we consider longitudinal variations of the central core ($\nu = 0$) and we multiply Eq. (3.50) by the propagator $\exp(ik_{zj}z)$.

We obtain:

$$U(\nu = 0, z) = \exp(ik_{z0}z) + S_j\beta_j\exp(ik_{zj}z) \tag{3.51}$$

We then compute the corresponding squared absolute value (intensity) yielding:

$$I(z) = 1 + \alpha_d^2 + 2\,\alpha_d\cos[(k_{z0} - k_{zj})z] \tag{3.52}$$

where $\alpha_d = S_j\beta_j$ is the on-axis modulation depth. According to this equation, in order to obtain the same modulation depth for both the axial wave (β_{ax}) and outer ring (β_{out}), their spectral amplitudes should satisfy the condition: $S_{out} = S_{ax}\beta_{ax}/\beta_{out}$. Given that $\beta_{ax}/\beta_{out} \ll 1$, the spectral amplitude of the outer ring S_{out} can be far lower than that of the axial wave and still yield the same modulation depth α_d. Considering our numerical results of Fig. (3.7,d), also shown in Fig. (3.11), at $z \approx 2600\ \mu m$, both spectral components have about the same order of magnitude while nonlinear on-axis intensity oscillations have already taken place. We can deduce that the axial wave is not intense enough to efficiently interfere with the input conical beam. Hence, the observed on-axis intensity modulation is mainly due to the interaction of the conical wave with the outer ring rather than the axial wave.

Regarding the nonlinear oscillation period L_{per}, we have mentioned above that numerical results yield $L_{per} = 180.5\ \mu m$. According to Eq. (3.52), L_{per} can be written as:

$$L_{per} = \frac{2\pi}{k\,|\cos(\theta) - \cos(\theta_j)|} \tag{3.53}$$

For the axial wave ($\theta_{ax} \approx 0\ rad$), $L_{per} = 226\,\mu m$ whereas it yields $L_{per} = 180.1\,\mu m$ for the outer ring ($\theta_{out} = 1.5\,\theta_0$). This further proves that the observed nonlinear oscillation are most likely due to the outer ring and not the axial wave. The role of the latter consists mainly in the generation of the outer ring through parametric amplification.

3.2.5/ SUMMARY

In this chapter, we have, so far, meticulously studied nonlinear instabilities in Bessel beams. Using our reduced FWM model combined with the theory of Gadonas et al. [Gadonas et al., 2001], we described and explained the different features related to the growth of new spectral components (axial wave and outer ring) which lead to the appearance of these instabilities.

Numerical simulation results of the standard NLSE showed that the nonlinear evolution of the spatial spectrum of Bessel beams goes through two different stages. In the first stage, the spatial spectrum undergoes an initial spectral broadening. In the plane (k_r, z), this spectral expansion is shaped according to a parabolic-like pattern and gradually reaches the axial wave frequency along the propagation axis. The second stage consists in the generation and amplification of both the axial wave and outer ring which is accompanied by the modulation of the central core intensity of the beam in the real space.

Gadonas et al. has introduced a theoretical model [Gadonas et al., 2001] to explain these phenomena. This theory is based on standard NLSE. The solution to this equation was

developed in a series of solutions. To determine these solutions, they developed approximate nonlinear propagation equations among which two approximate equations were considered.

Of particular interest, this formalism determines the order at which Kerr-induced effect take place. The first approximation describes the interaction of three identical pump waves (input conical waves) according to a SPM-like process which leads to the observed spectral broadening. The second approximation describes the interaction of two pump waves (input conical waves) with a signal wave that is generated through the SPM process. Using phase matching arguments, it was shown that the signal wave is defined at the axial wave frequency ($k_r \approx 0$). This results in the amplification of the axial wave through XPM-like process and the generation of an outer ring $k_r \approx \sqrt{2}k_{r0}$ through parametric amplification. In other words, the SPM process is required to generate an "axial wave seed" so that the subsequent nonlinear effects (XPM and parametric amplification) can take place to generate and amplify the axial wave and outer ring.

However, this theory cannot explain some other features observed in numerical simulation of the NLSE such as the parabolic shape characterizing the spatial spectrum evolution and the evolution along propagation of the axial wave seed. In this regard, we developed a novel theoretical model which we referred to as "reduced FWM model". In this theory, we considered all nonlinear processes involved in the generation of new spectral components.

Our model allows describing the evolution along propagation of the idler wave resulting from the interactions of two pump waves with a signal wave in the spectral domain. We showed that the observed parabolic patterns results from SPM-generated spectral components that are longitudinally phase-mismatched and whose spectral intensity oscillates along propagation. Particularly, the spectral component at the axial wave frequency remains weak and oscillates along propagation. This component (axial wave seed) will then play the role of a signal wave in subsequent nonlinear interactions leading to its amplification. Our model also describes the observed interference patterns as the interference of the idler waves generated by the different nonlinear interactions (SPM, XPM and parametric amplification processes).

Lastly, we have shown that the nonlinear intensity modulation of the central core of Bessel beams results from the interaction of the input conical wave with the outer ring rather than the axial wave. We also explained the frequency shift of the outer ring to high frequency as a result of the ring compression of the Bessel beam main lobe.

3.3/ SOFT AND ABRUPT INTENSITY TRANSITIONS

We mentioned above that nonlinear instabilities can be controlled depending on the exact positioning of Bessel beams with respect to nonlinear media: nonlinear spectral distortions are mitigated for Bessel beams formed progressively inside the nonlinear medium in contrast with those formed before interacting with the sample [Polesana et al., 2007, Sogomonian et al., 2000]. These two input conditions are referred to as smooth and abrupt intensity transitions respectively as depicted in Fig. (3.6,a,b). The decrease in spectral distortions, in the case of smooth transition case, was explained by quenching nonlinear instabilities leading to smooth and spontaneous shaping of the Bessel beam into a stationary and nonlinear stable field, namely the Nonlinear Unbalanced Bessel

Beam (NLUBB). Such smooth transformation is characterized by slow transient dynamics in the transverse space coordinates [Polesana et al., 2007].

Modulation instability analysis showed that the axial wave and outer ring both play the role of unstable modes [Polesana et al., 2007]. The increase in nonlinear instabilities in the case of abrupt transition corresponds then to an exponential amplification of these two modes. In an another work [Dubietis et al., 2007], the abrupt-transient case is assumed to enhance Kerr-nonlinear interactions which lead to significant phase distortions. Thus, this is assumed to relax the constraints for transverse momentum conservation, in contrast with the smooth transition case. In this section, we will use our reduced FWM model to further investigate these features. We show the role of the spectral phase distribution in reducing the efficiency of FWM interactions which then hampers the growth of these unstable modes.

3.3.1/ NUMERICAL ANALYSIS

In order to gain more insight into the tremendous increase in instabilities taking place in abrupt input condition, let's first compare and analyze the evolution of the spatial spectra in both cases. In our simulations, we use the same numerical propagation model based on standard NLSE (Eq. 3.34) where nonlinear losses are neglected. We use the same parameters as in table (3.1) except for the input power. Since Kerr nonlinearity is assumed to be enhanced in the abrupt transition case, we choose a lower value of the input power, namely $P_{in} = 31.2\ MW$ corresponding to a beam peak intensity of $I_{max} = 9$ TW/cm^2. In the linear regime, this Bessel beam reaches its peak intensity at $z = 2160\ \mu m$. Hence, we consider this propagation point as the transition point between the linear and nonlinear regime in the abrupt intensity transition.

We present numerical results in Fig. (3.12) where we compare the nonlinear propagation of the Bessel beam in both cases and compare the corresponding spatial spectra evolution along propagation. Regarding the on-axis intensity evolution, we obtain comparable results as those reported in [Polesana et al., 2007]. In the smooth transition case, the Bessel beam exhibits weak intensity oscillations. In contrast, it undergoes, in the abrupt case, sharp intensity modulation right after entering the nonlinear medium, i.e. at the point $z = 2160\ \mu m$.

We have discussed in the previous section the nonlinear dynamics of the growth of spatial spectra in the case of smooth transition. The beam undergoes a gradual spectral broadening showcasing parabolic-like structures which stretches to the zeroth frequency (axial wave). Here, we notice less intensity growth of both the axial wave and outer ring since we used a lower value of the input power. In the abrupt intensity transition, the initial spectral broadening extends to nearly all frequencies right after entering the medium, in contrast with the seemingly-cascaded broadening observed in smooth transition case. After this initial broadening, the axial wave noticeably increases in intensity which is followed by the growth of the outer ring. Other spectral components, other than those close to the central one, all manifest an oscillating behavior shaped as parabolic-like structures in (β, z) space.

As it is the case in the smooth transition case, the oscillation period is seen to decrease for spectral components that are further from the pump in the abrupt transition case. The axial wave and outer ring also present an oscillating behavior. But since they satisfy longitudinal phase-matching conditions, FWM processes, namely XPM and parametric

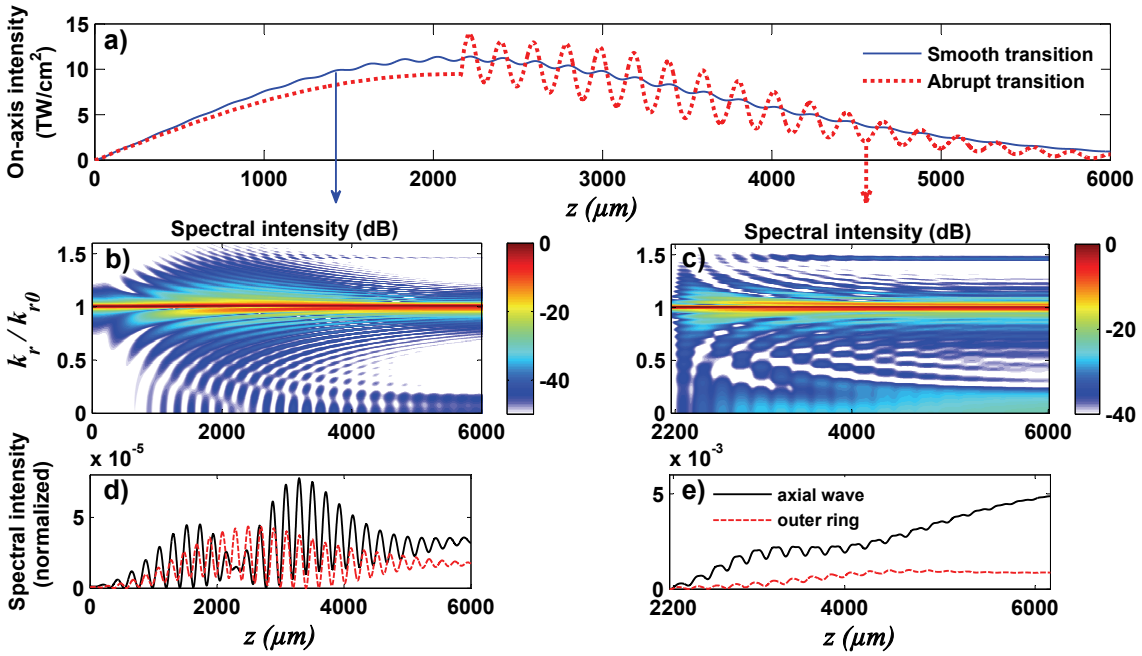

Figure 3.12: (a) On-axis intensity distribution of a Bessel–Gauss beam propagating in a pure nonlinear Kerr medium ($n_2 = 2.4810^{-16}$ cm^2/W) for the smooth (solid line) and abrupt (dotted line); (b-c) the corresponding spatial spectra evolution along the propagation distance (logarithmic scale dB) for both cases respectively and (d-e) the intensity evolution of the corresponding axial wave (black solid line) and outer ring (dashed line) along propagation (spectral intensities are normalized to pump's maximal value). Note that the intensity of newly-generated spectral components in the case of abrupt transition is two order of magnitude higher than the one reached in case of smooth transition.

amplification (second approximation), take place leading to further growth of these two components respectively. In the smooth transition case, however, even though the peak intensity is about the same as the one reached in the abrupt case at $z = 2160\,\mu m$, the axial wave only present an oscillating behavior and no noticeable growth is observed. This may be explained by a more intense axial wave seed in the case of abrupt transition leading to more efficient FWM interactions.

We conclude that the main point of difference between the soft and abrupt transition cases lies in the initial spectral broadening. While the latter is being gradually established in the smooth transition case, it encompasses nearly all frequencies in the other case. Furthermore, it occurs right after the beam enters the nonlinear medium.

3.3.2/ Intuitive interpretation

According to our analysis in the previous section, the nonlinear effect causing such spectral broadening is SPM. We have seen that this effect is also behind the parabolic-like structures, which are also observed in the case of abrupt transition. However, it is clear that there is another factor that affects SPM-induced broadening, which may be related to input conditions related to both cases. We will first provide an intuitive interpretation in this section. We will then provide a detailed interpretation based on our reduced FWM model in the next section.

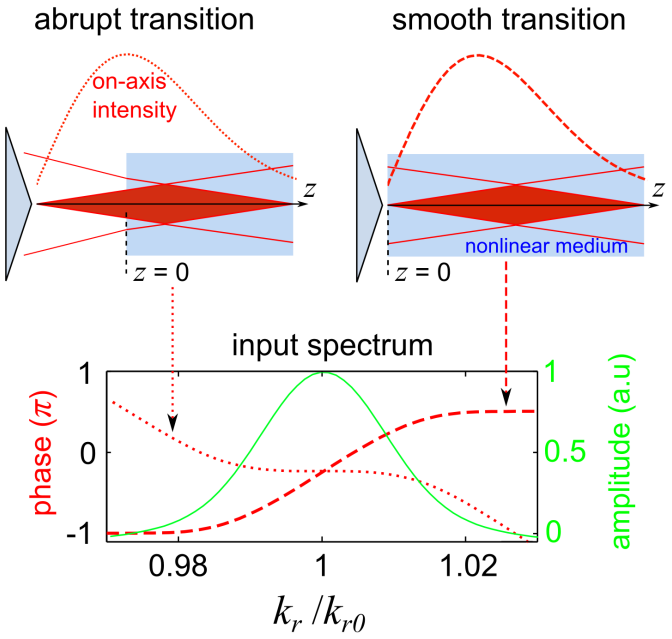

Figure 3.13: Comparison between the input phase distributions (at $z = 0$) of a BG beam at different positions with respect to the nonlinear medium: (red dashed line) smooth and (red dotted line) abrupt intensity transitions.

We compare in Fig. (3.13, bottom) the input spectral amplitude (green) and phase (red) corresponding to both cases (the point $z = 0$ refers to transition point between the linear and nonlinear media). While the input amplitude is naturally the same, we notice that the phase distribution is steeper in the smooth transition case and is quasi-flat in the other. The input amplitude takes the form of a Gaussian function and is mostly in the range $\beta \in [0.98 - 1.02]$). In the following, the Bessel ring will be defined in this spectral range.

A quasi-flat spectral phase implies that spectral components composing the pump wave are nearly in-phase. Hence, if each of these spectral components interacts according to SPM process (first approximation), then each idler wave generated from these interactions will be in phase with the others. The resulting idler wave at a given frequency will then be made of constructive interference of all these waves, which explains the abrupt appearance of spectral components at about all frequencies around the central one. This may also explain the sharp intensity growth of the axial wave seed which leads to more efficient FWM interactions.

In contrast, a steep spectral phase profile, which implies out-of-phase spectral components, may lead to partially-destructive interference and the axial wave seed will then be weaker. This assumption is only valid in case these spectral components remain out-of-phase along the propagation. We compare in Fig. (3.14) the spectral intensity and corresponding spectral phase distributions at two different propagation points, namely $z = 1800$ and $z = 2160\ \mu m$ and compare results with the case of abrupt intensity transition. While the spectral intensity is gradually being shifted to higher frequencies because of the compression of the beam central core [Porras et al., 2004], the spectral phase is gradually being flattened as the beam propagates but remains slightly steeper than in the abrupt transition case. To explain the low intensity rise of the axial wave even though the spectral phase is being flattened, we assume that the axial wave that is generated beforehand

would be superimposed to the one that is generated at later propagation point. Hence, even if the axial wave generation becomes more efficient as the beam propagates, it is bound to destructively interfere with those previously engendered, which makes it relatively less intense. If we reconsider the evolution of the axial wave (Fig. (3.12,d)), we notice that it decreases in intensity and modulation depth around $z = 2160\ \mu m$. Based on our discussion, we can understand it as the result of partial destructive interference. Subsequent intensity increase can be attributed to further FWM interactions (XPM of the second approximation).

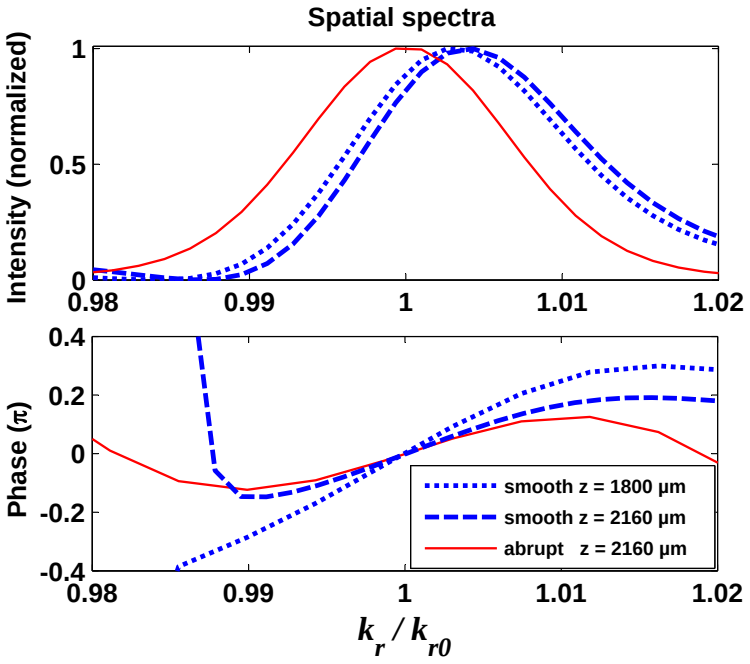

Figure 3.14: NLSE simulation results: Comparison of the spectral intensity and phase distributions in the spectral range of the pump at different propagation points in case of smooth and abrupt intensity transition. Note that the spectral intensity distribution is the same at the transition point between the linear and nonlinear media in both cases.

In a nutshell, the input spectral phase distribution can be the origin of the sharp intensity growth of the axial wave in the case of abrupt intensity transition compared to that of smooth transition. In the following, we will use our reduced FWM model to further investigate the effect of input spectral phase on the growth of nonlinear instabilities.

3.3.3/ THEORETICAL ANALYSIS

3.3.3.1/ THEORETICAL CONSIDERATIONS

Theoretically, we previously (section 3.2.3.1(page 80)) interpreted the growth of nonlinear instabilities by approximating a quasi-Bessel beam to a single-frequency J_0 beam, i.e. we neglected the spectral distribution of the beam. However, the beam spectral distribution should be accounted for to differentiate between the soft and abrupt input conditions. Hence, it is necessary to consider that the interacting waves are composed of multiple frequencies with different input spectral phases. Indeed, according to our intuitive interpretation that we proposed in the previous section, we qualitatively highlighted

the importance of the spectral phase. In order to simplify our analysis, we consider a pump wave composed of only two spectral components defined at β_a and β_b with ϕ_a and ϕ_b being their respective input spectral phases. In the following, we will reconsider the theory of Gadonas et al. [Gadonas et al., 2001] that we previously described in section 3.2.3.1(page 79) and use our FWM model for further analysis.

We reconsider the nonlinear propagation equation described by Eq. (3.36). We recall that its proposed solution B is given by formula (3.37), i.e $B = B_0(\nu) + B_1(\nu,\xi) + B_2(\nu,\xi) + ...$, where B_0 is the input J_0 beam. B_1 and B_2 correspond to solutions to the first and second approximations of the NLSE (3.36).

In order to account for the contribution of two spectral components, we propose to model the input beam B_0 by a superposition of two J_0 beams B_a and B_b as follows:

$$B_0 = B_a + B_b \text{ where } \begin{cases} B_a = J_0(\beta_a \nu)\exp(i\phi_a) \\ B_b = J_0(\beta_b \nu)\exp(i\phi_b) \end{cases} \tag{3.54}$$

We specifically study the impact of input spectral phase on the generation of the axial wave seed (first approximation) and subsequent growth of axial wave and outer ring (second approximation). In this regard, we can further simplify the problem by considering that the two spatial frequencies are nearly equal ($\beta_a \approx \beta_b \approx 1$) and still consider their phase difference. In this case, Eq. (3.54) is reduced to:

$$B_0 = J_0(\nu)[\exp(i\phi_a) + \exp(i\phi_b)] \tag{3.55}$$

3.3.3.2/ FIRST APPROXIMATION: IMPACT ON AXIAL WAVE SEED

According to the first approximation, we have seen that the NLSE can be written as $\frac{\partial B_1}{\partial \xi} - i\Delta_{\perp n} B_1 = i\gamma |B_0|^2 B_0$ (Eq. (3.38)). By inserting formula (3.55) in this equation we obtain:

$$\frac{\partial B_1}{\partial \xi} - i\Delta_{\perp n} B_1 = 2\, i\gamma\, J_0^3(\nu)\,[1 + \cos(\phi_a - \phi_b)]\,[\exp(i\phi_a) + \exp(i\phi_b)] \tag{3.56}$$

The nonlinear term of this equation is then dependent on the phase difference $\Delta\phi = \phi_a - \phi_b$ of the pump spectral components. Specifically, the term $[1 + \cos(\phi_a - \phi_b)]$ shows that Kerr-induced SPM is weaker if $\Delta\phi$ is non-zero, which corresponds to the smooth intensity transition case.

Further analysis of this feature can be performed using our FWM model. We study the evolution of the idler wave resulting from the interaction of identical pump and signal waves, each composed of the two considered spectral components. In this case, the spectral distribution of each of these waves can be written as $\tilde{S}_j(\beta_j) = \delta(\beta_j - 1)\,[\exp(i\phi_a) + \exp(i\phi_b)]$, with $j = 1, 2, 3$. Regarding the TPM integral, it can be seen that it is the same in all nonlinear terms since the interacting waves are supposed to only differ in input spectral phase. Hence, it is defined by Eq. (3.40). Thus, Eq. (3.21) can be written as:

$$\frac{\partial a_4(\xi)}{\partial \xi} \propto \tan(\theta_4) I_{TPM}^{1st} \exp[i\,(1-\beta_4^2)\xi]\,[3\,\mathrm{e}^{i\phi_a} + 3\,\mathrm{e}^{i\phi_b} + \mathrm{e}^{i(2\,\phi_a-\phi_b)} + \mathrm{e}^{i(2\,\phi_b-\phi_a)}] \tag{3.57}$$

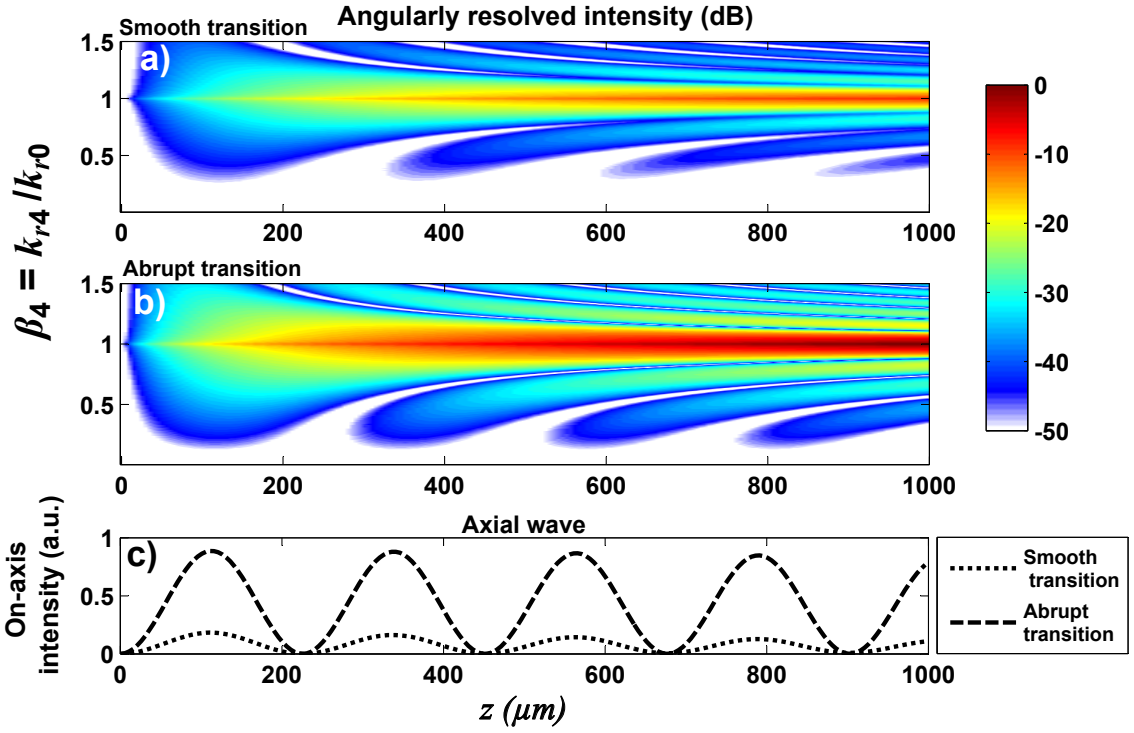

Figure 3.15: Numerical results using our FWM model: Angularly resolved intensity (dB) of the idler wave resulting from the interaction of three waves composed each of three frequencies: $\beta_j = 0.995,\ 1,\ 1.005$ (with j=1,2,3 referring to two pump and signal waves respectively) in case of (a) a varying and (b) flat phase distribution (smooth and abrupt transitions respectively). The input spectral phases related to these frequencies are taken from Fig. (3.13). (c) The corresponding evolution along propagation of the axial wave spectral intensity ($\beta_4 \approx 0$) in linear scale.

where $I_{TPM}^{1st} = 1/k_{r0}^2 \int_0^{\nu_f} J_0^3(\nu) J_0(\beta_4\,\nu)\,\nu\,\mathrm{d}\nu$. Analytically, we are only interested in the evolution along propagation of the idler wave. For a specific frequency, the TPM integral can be reduced to a factor of proportionality since it is constant along propagation. We then integrate over ξ and compute the corresponding on-axis spectral intensity. It yields (see Appendix 3.C, page 156):

$$I_4(\xi,\beta_4) \propto \ \tan^2(\theta_4)\,\xi^2\,\mathrm{sinc}^2[0.5\,(1-\beta_4^2)\xi]\,[1+\cos(\phi_a-\phi_b)]^3 \tag{3.58}$$

The growth of the idler wave intensity is proportional to the term $\xi^2\,\mathrm{sinc}^2[0.5\,(1-\beta_4^2)\xi] \propto \sin^2[0.5\,(1-\beta_4^2)\xi]$ which indicates the above discussed oscillating behavior. Of particular interest, $I_4(\xi,\beta_4)$ is proportional to the cube of the phase-dependent term $[1+\cos(\phi_a-\phi_b)]$ which shows that non-zero phase difference allows reducing the peak value of these oscillations and thus decreases the magnitude of the axial wave seed.

For instance, let's consider the example described in Fig. (3.13). We choose two adjacent spectral components of the pump defined at $\beta_a = 1$ and $\beta_b = 0.995$. Their phase difference is $\Delta\phi_{soft} = 0.88$ rad and $\Delta\phi_{abrupt} = 0.3$ rad in the smooth and abrupt transition cases respectively. Formula (3.58) shows that the magnitude of newly-generated components would be reduced by a factor of about 1.7. This factor can increase considering the contribution of multiple frequencies. However, further analytical analysis requires the integration over multiple frequencies which is too difficult to realize and thus only semi-analytical analysis can be performed.

In Fig. (3.15), we consider the contribution of three spectral components defined at the frequencies β = 0.995, 1, 1.005. We compare the idler wave growth at frequencies in the range $\beta \in [0.005 - 1.5]$. Regarding the input spectral phase relative to these frequencies, we simply extract the corresponding values from the input phase distribution depicted in (Fig. 3.13) using linear interpolation. It is clear that extent of SPM-induced broadening is mitigated in the case of smooth condition with a reduction factor of about 5 as shown in Fig. (3.15,bottom).

3.3.3.3/ FIRST APPROXIMATION: CASCADED FEATURE OF SPECTRAL BROADENING

So far, we have shown how the input spectral phase allows controlling the magnitude of SPM-induced spectral broadening. However, the NLSE numerical results (Fig. (3.7)) showed an apparent-cascaded pattern of this spectral broadening, which has not been explained so far. Indeed, we considered, in the previous section, the contribution of three adjacent spectral components, i.e. $\beta = 0.995,\ 1,\ 1.005$, and studied the behavior along propagation of the corresponding spatial spectrum. As shown in Fig. (3.15), the angularly resolved intensity of the idler wave does not exhibit this cascaded feature. In this regard, it is necessary to consider the contribution of other spectral components, specifically those defined at the tails of Bessel ring. In Fig. (3.16), we take into account the contribution of five spectral components defined in the range $\beta \in [0.96 - 1.04]$, namely $\beta = 0.96,\ 0.98,\ 1,\ 1.02,\ ,1.04$, and plot the evolution of the idler wave spectral intensity along propagation and compare results in smooth and abrupt conditions. The corresponding input spectral phase distributions are also extracted from Fig. (3.13) using linear interpolation.

In the soft input condition, initial spectral broadening is very weak and only cover frequencies that are close to the central one. Notice that it gradually extends to more frequencies for longer propagation distances in cascaded-like fashion, qualitatively as observed numerically. Note here that, in contrast with numerical simulations of the NLSE, the spectral phase profile remains constant. Hence, spectral broadening extension is assumed to be faster if spectral phase flattening could be accounted for. Contrary to these results, the initial spectral broadening covers all frequencies in the abrupt case, which is also in qualitative agreement with numerical simulation results of Fig. (3.12). Regarding the generation of the axial wave seed, we notice that it is initially more intense in the case of abrupt input condition by about two orders of magnitudes, which is also consistent with numerical results.

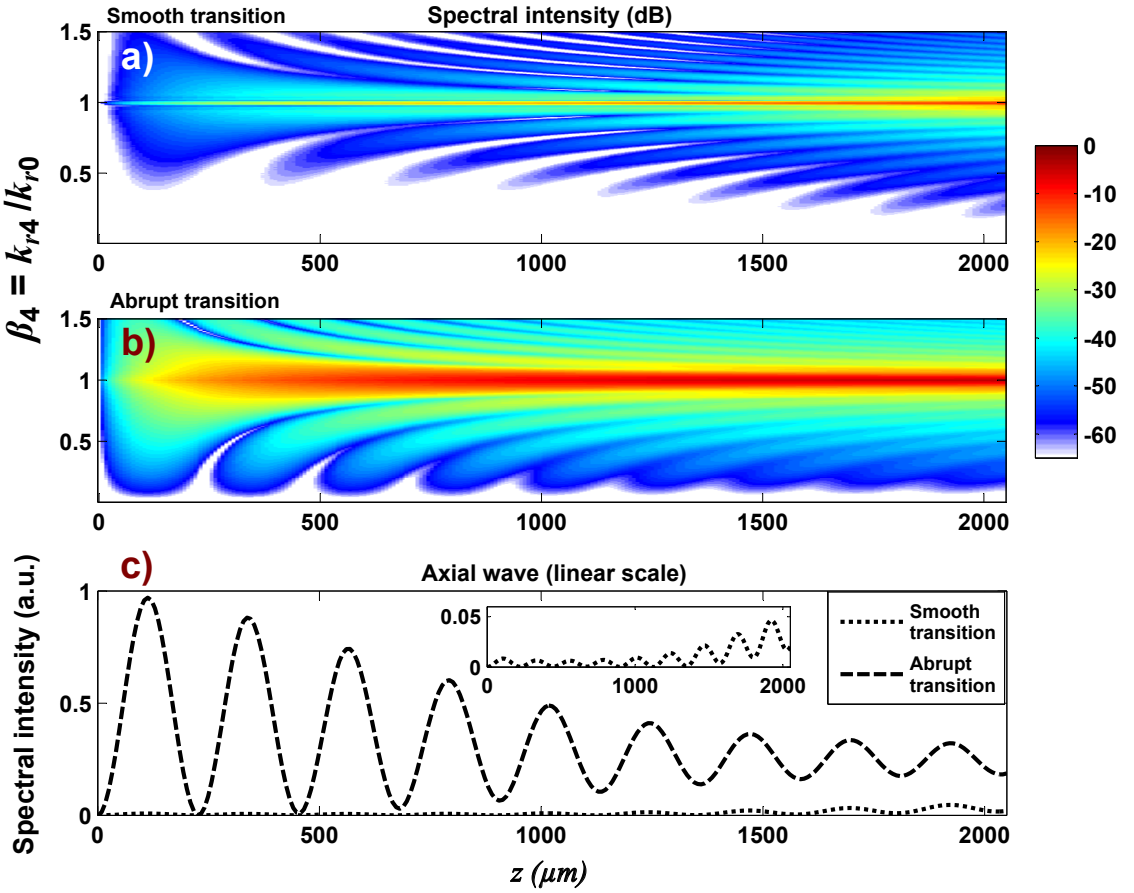

Figure 3.16: Numerical results using our FWM model: Angularly resolved intensity (dB) of the idler wave resulting from the interaction of three waves composed each of five frequencies: $\beta_j = 0.96,\ 0.98,\ 1,\ 1.02,\ ,1.04$ (with j=1,2,3) referring to two pump and signal waves respectively) in case of (a) a varying and (b) flat phase distribution (smooth and abrupt transitions respectively). The input spectral phases related to these frequencies are taken from Fig. (3.13). (c) The corresponding evolution along propagation of the axial wave spectral intensity ($\beta_4 \approx 0$) in linear scale.

3.3.3.4/ SECOND APPROXIMATION: GROWTH OF UNSTABLE MODES

So far, we have studied the effect of the input spectral phase on the initial spectral broadening induced by SPM. We have seen that the intensity of the axial wave seed is weaker in the case of smooth intensity transition compared to the abrupt transition case. We interpreted this difference in intensity to their related input spectral phase profile which is steeper in the case of smooth transition.

By the propagation point where the Bessel beam reaches its peak intensity ($z = 2160\ \mu m$) and the amplification of new spectral components takes place, the spectral phase profile around the central frequency becomes quasi-flat due to linear propagation [Jarutis et al., 2000] (see Fig. (3.14)). Consequently, even in the case of smooth intensity transition, the input phase profile of the pump wave may not have a direct impact on the growth of the axial wave and outer ring. To investigate this point, let's reconsider the second approximation of the NLSE as developed by Gadonas et al. [Gadonas et al., 2001],

i.e. $\frac{\partial B_2}{\partial \xi} - i\Delta_{\perp n} B_2 = i\gamma(2|B_0|^2 B_1 + B_0^2 B_1^*)$. We recall that the solution B_2 specifically refers to the evolution of both the axial wave and outer ring along propagation.

The point here is to study the growth of the solution B_2 depending on the input spectral phase of both B_0 and B_1. We recall that B_0 refers to the input conical wave. We use the same definition we proposed previously as described by Eq. 3.55, i.e. $B_0 = J_0(\nu)[\exp(i\phi_a) + \exp(i\phi_b)]$. As for B_1, which plays the role of a signal wave, we assimilate it to an axial wave seed. This choice is justified since we demonstrated that the axial wave is amplified though an XPM-like interaction and also leads to the generation of an outer ring through parametric amplification. In order to investigate the impact of its spectral phase, we consider the simple case where B_1 is assimilated to a plane wave and is composed of two adjacent spectral components β_{31} and β_{32}, such as $\beta_{31} \approx \beta_{32} \approx 0$. We solely take into account their respective spectral phases ϕ_{31} and ϕ_{32}. Hence, we express the quantity B_1 as:

$$B_1 = \exp(i\phi_{31}) + \exp(i\phi_{32}) \tag{3.59}$$

The second approximate solution of the NLSE thus becomes:

$$\begin{aligned}\frac{\partial B_2}{\partial \xi} - i\Delta_{\perp n} B_2 =& 2\, i\gamma\, J_0^2(\nu)\,[1 + \cos(\phi_a - \phi_b)]\,\sqrt{1 + \cos(\phi_{31} - \phi_{32})} \\ &\times \left[\exp\left(i\frac{\phi_{31} + i\phi_{32}}{2}\right) + \exp\left(i(\phi_a + \phi_b) - i\frac{\phi_{31} + i\phi_{32}}{2}\right)\right]\end{aligned} \tag{3.60}$$

The phase difference between the pump wave spectral components is clearly apparent in the term "$[1 + \cos(\phi_a - \phi_b)]$". Since the input spectral phase is bound to flatten as the beam approaches its peak intensity, even in the smooth transition case, this term will not play a role in reducing the growth of unstable modes. However, notice that growth of B_2 also depends on the phase difference between the axial wave spectral components. In addition, according to the term $\exp\left(i(\phi_a + \phi_b) - i(\phi_{31} + i\phi_{32}/2)\right)$, the phase difference between the pump and signal waves may also influence the evolution of both the axial wave and outer ring. In order to further investigate the impact of this phase difference, we use our reduced FWM model.

Considering the same definitions of the pump and signal waves, the expressions of their respective spectra can be written as:

$$\tilde{S}_j(\beta_j) = \delta(\beta_j - 1)\,[\exp(i\phi_a) + \exp(i\phi_b)], \qquad j = 1, 2 \tag{3.61}$$

$$\tilde{S}_j(\beta_j) = \delta(\beta_3 - \beta_{31})\,[\exp(i\phi_{31}) + \exp(i\phi_{32})] \tag{3.62}$$

We then insert them in the propagation equation (Eq. 3.21) of the idler wave $a_4(\xi)$. We compute its squared absolute value $I_4(\xi, \beta_4) = |a_4(\xi, \beta_4)|^2$ in order to clearly show the impact of the phase distribution of the pump and signal waves on the growth of the idler wave. $I_4(\xi, \beta_4)$ can be expressed as (the demonstration of this formula is in Appendix 3.C, page 156):

$$
\begin{aligned}
I_4(\xi,\beta_4) \propto i\ \tan^2(\beta_4\theta_0)\xi^2[1+\cos(\phi_a-\phi_b)]^2\,[1+\cos(\phi_{31}-\phi_{32})] \\
\times\{\mathrm{sinc}^2[0.5(2-\beta_{31}^2-\beta_4^2)\xi]+4\,\mathrm{sinc}^2[0.5(\beta_{31}^2-\beta_4^2)\xi] \\
+4\,\cos[\phi_a+\phi_b-\phi_{31}-\phi_{32}+(1-\beta_{31}^2)\xi]\,\mathrm{sinc}[0.5(2-\beta_{31}^2-\beta_4^2)\xi]\mathrm{sinc}[0.5(\beta_{31}^2-\beta_4^2)\xi]\}
\end{aligned}
\tag{3.63}
$$

Based on this equation, it is clear that the intensity of the idler wave decreases in case the phase difference between spectral components of the pump wave ($\phi_a-\phi_b$) and that of the signal wave ($\phi_{31}-\phi_{32}$) are higher. However, the term $\cos[\phi_a+\phi_b-\phi_{31}-\phi_{32}+(1-\beta_{31}^2)\xi]$ indicates the phase difference between the pump and signal does not affect the overall growth of the idler wave. Indeed, the phase term $\phi_a+\phi_b-\phi_{31}-\phi_{32}$ does only affect the idler wave growth with a distance lower that its oscillatory period $p=\lambda/n(1-\cos(\theta_0))$. Hence, the only term which may decrease the growth of the idler wave is $[1+\cos(\phi_{31}-\phi_{32})]$. Now, let's analyze the distribution of the spectral phase near the peak intensity of the Bessel beam and investigate the effect of this term.

Previously, we studied the spectral phase distribution propagation point $z=2160\ \mu m$ which is the transition point between the linear and nonlinear medium in the case of abrupt intensity transition. We compared in Fig. (3.14) this phase profile to that obtained in the smooth transition case at the same propagation point (page 92). The spectral phase around the central frequency is quasi-flat in both cases due to linear propagation.

We plot in Fig. (3.17,a) these phase profiles over the range $\beta\in[0\ -\ 1.5]$. We clearly notice that, in the case of abrupt transition, the phase distribution is rapidly varying away from the central frequency whereas it is quasi-flat in the smooth transition case. Hence, according to Eq. (3.63), specifically the term $[1+\cos(\phi_{31}-\phi_{32})]$, one may conclude that the growth of nonlinear spectral distortions should be decreased. However, note that, in the abrupt transition case, the axial wave has yet to be generated at this point. In this regard, one should consider the phase profile at a later propagation point by which the axial wave seed is generated.

We plot in Fig. (3.17,b) the spectral phase profile at 30 μm away from $z=2160\ \mu m$, i.e. $z=2190\ \mu m$. It is clear that the phase profile becomes quasi-flat away from the central frequency, and specifically near the axial wave range. In the smooth transition case, it remains nearly unchanged. Based on these observations, we conclude that since the spectral phase remains quasi-flat near the axial wave range, the growth of both the axial wave and outer ring is inevitable. In other words, one cannot directly control FWM processes leading to the amplification of the axial wave seed and generation of the outer ring depending on input intensity transition case. The input condition only affects these processes indirectly by controlling the intensity of the axial wave seed.

3.3.4/ SUMMARY

In this section, we theoretically and numerically studied the dependence of Kerr-induced instabilities on input conditions of the interaction of the Bessel beams with nonlinear Kerr media. A Bessel beam that is formed progressively inside a Kerr medium yields weak nonlinear modulation of its on-axis intensity (smooth intensity transition). However, if the Bessel beam is formed prior entering the medium (abrupt intensity transition), nonlinear instabilities will be enhanced [Polesana et al., 2007].

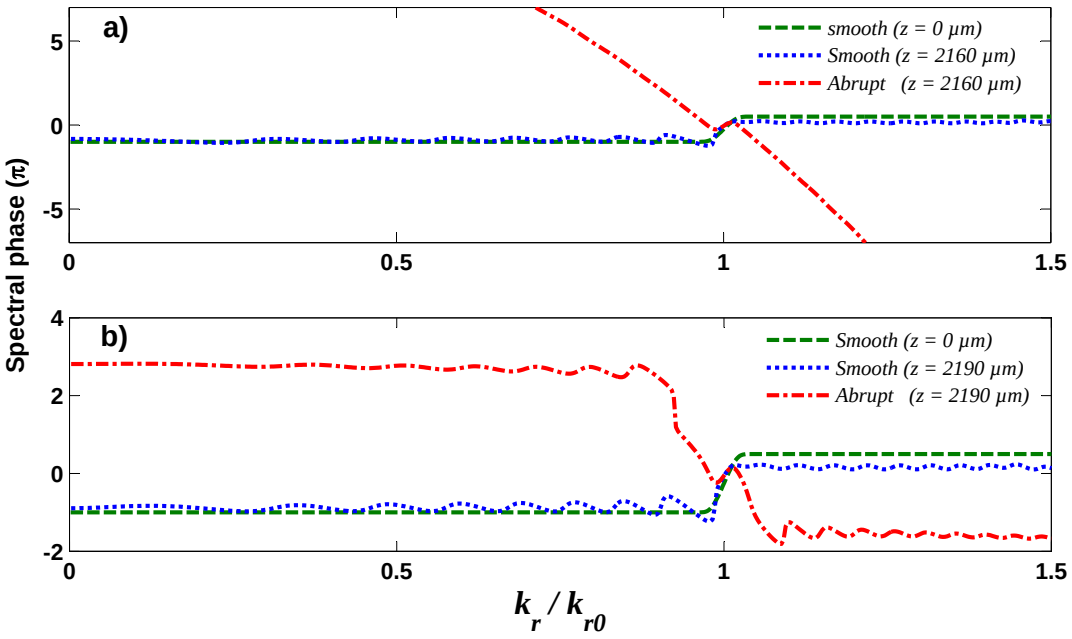

Figure 3.17: NLSE simulation results: Spectral phase distribution at a propagation distance $z = 2190\ \mu m$ in case of abrupt intensity transition. This propagation point is 30 μm away from the transition point between the linear and and nonlinear medium. This spectral phase profile is compared to the one obtained in the smooth intensity transition at the points $z = 0$ and $z = 2190\ \mu m$.

In our numerical simulation of the NLSE, we specifically studied the evolution along propagation of the spatial spectra related to these two cases. In the case of abrupt intensity transition, the initial spectral broadening extends to nearly all frequencies right after entering the medium, in contrast with the gradual spectral broadening observed in smooth transition case. At the propagation point where the central core intensity reaches its peak intensity (transition point in the abrupt transition case), the axial wave seed intensity is found to be lower in the case smooth transition than in case of abrupt transition. Consequently, the subsequent growth of the axial wave is greater in the abrupt transition case, which explains the enhancement of nonlinear instabilities in this case.

We explained the difference in the axial wave seed intensity in terms of the input spectral phase profile. In the abrupt transition case, the spectral phase has a quasi-flat profile, which implies that spectral components composing the pump wave are nearly in-phase. Hence, if each of these spectral components interacts according to SPM process, then each idler wave generated from these interactions will be in phase with the others. The resulting idler wave at a given frequency will then be made of constructive interference of all these waves, which increases the axial wave seed intensity in this case. In contrast, the spectral phase takes the form of a steep ramp profile in the smooth transition case. This implies out-of-phase spectral components, which may lead to partially-destructive interference and the axial wave seed will then be weaker.

Theoretically, we studied the growth of the idler wave resulting from SPM-like interactions of the pump and signal waves. To simplify our analysis, we considered the contribution of only two spectral components. We found that the growth of the idler wave intensity decreases if the phase difference between these two components is higher. This shows that

non-zero phase difference (corresponding to the smooth intensity case) allows reducing the peak value of these oscillations and thus decreases the magnitude of the axial wave seed.

In the case of smooth transition case, our theoretical analysis only applies to the initial spectral broadening where input spectral phase slightly varies. At the peak central core intensity of the Bessel beam, the spectral phase becomes flat due to linear propagation. As a result, there is no longer any difference between the smooth and abrupt transition cases. We conclude that the difference between these two cases resides only in the initial spectral broadening which affects the intensity of the axial wave seed which, in turn, affects subsequent FWM processes.

3.4/ CONTROL OF NONLINEAR INSTABILITIES USING SHAPED INTENSITY PROFILES

In the previous section, we have discussed the dependence of nonlinear instabilities in Bessel beams on the exact positioning of the beam with respect to the nonlinear medium. Specifically, nonlinear instabilities were shown to noticeably decrease if the beam is progressively formed inside the medium (smooth intensity transition). In other words, nonlinear instabilities are expected to decrease if the beam intensity is smoothly increasing inside the sample.

In this section, we will discuss the possibility to control Kerr-induced instabilities depending on the initial intensity rise of the beam inside nonlinear media. In this regard, we will consider quasi-Bessel beams with shaped on-axis intensity profiles as discussed in chapter 2 and numerically study their nonlinear propagation. We will show that nonlinear spectral distortions can be mitigated for Bessel beams with slowly increasing input intensity rise. Based on our theoretical model, we analyze numerical results and specifically discuss the effect of intensity shaping on initial spectral broadening (first approximation) and ensuing growth of new spectral components (second approximation).

3.4.1/ NUMERICAL SIMULATION RESULTS

In our numerical simulations, we use the same nonlinear propagation equation described by formula (3.34). We will still neglect nonlinear losses as to bring out the effect of intensity shaping on the control of Kerr-induced instabilities in Bessel beams. We will later present simulation results taking into account nonlinear losses and show that our results are also valid in the filamentation regime.

We compare the nonlinear propagation of three Bessel beams with different on-axis intensity profiles, i.e. the ones describing their propagation in the linear regime. Their peak maximal intensity is chosen to be the same in order to study the effect of the initial intensity rise on the growth of nonlinear instabilities. These three intensity profiles are depicted in Fig. (3.18,a) and are described as follows: the first profile, denoted profile-1, is that of a conventional Bessel-Gauss beam (green dashed line) identical to that we have used so far. The second profile (profile-2) consists of a linear leading edge followed by a flat-top intensity and parabolic decaying trailing edge (blue dotted line). Profile-3 is identical to profile-2 except that it exhibits a parabolic intensity rise instead of a linear ramp (red solid

line). Numerical parameters are the same as in table (3.1).

The on-axis intensity evolution of these Bessel beams are presented in Fig. (3.18,b). Compared to the case of the BG beam (profile-1), the two other beams present the same longitudinal nonlinear oscillations of the central core intensity but they differ in the oscillation depth. Although the Bessel beams with profile-2 and profile-3 only differ in terms of the initial intensity rise, the oscillation depth is seen to significantly decrease for profile-3.

In the spectral domain (Fig. (3.18,c)), the observed weak on-axis intensity oscillations in case of profile-3 correspond to weak intensity growth of the axial wave below -40 dB up to $z = 4000\ \mu m$ and around -30 dB afterwards. We specifically plot in Fig. (3.18,d) the spectral intensity evolution of the axial wave. In the case of profile-3, the growth of the axial wave seed is slowly established. In addition, while the initial stage of spectral broadening showcases an oscillating behavior of the axial wave seed in the case of profile-1 and profile-2, this oscillating behavior is initially absent in the case of profile-3 and only appears at a propagation distance around $z = 3000\ \mu m$. Following the appearance of these oscillations, both the axial wave and outer ring increase in intensity which indicates that FWM processes become active past this propagation point. However, their growth remains noticeably weaker compared to the other two Bessel beams.

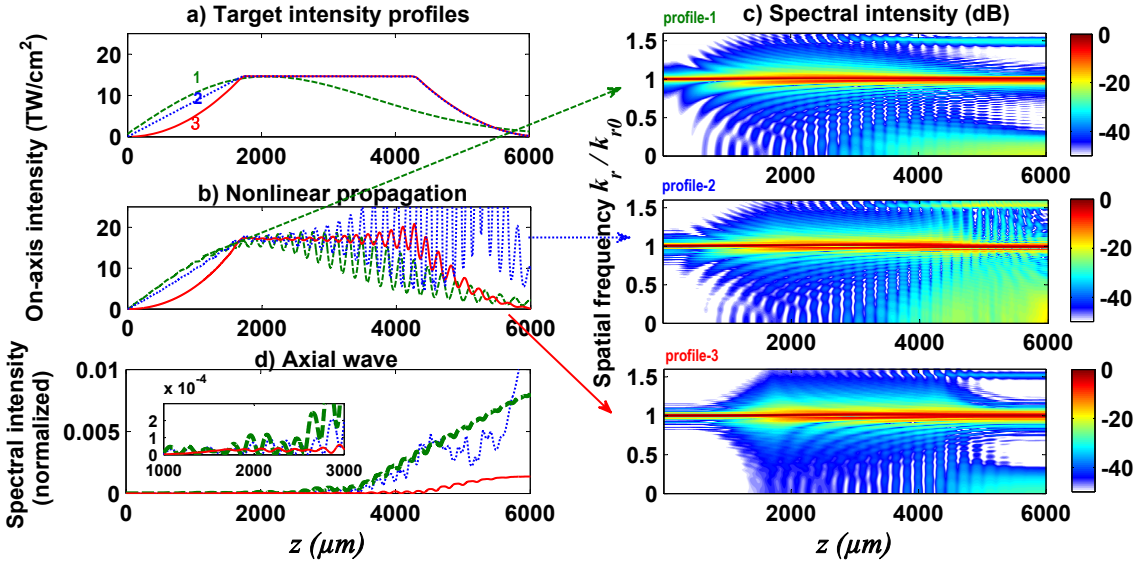

Figure 3.18: Simulation of the nonlinear propagation of three Bessel beams with different (a) target on-axis intensity profiles. Evolution of their respective (b) on-axis intensities, (c) spatial spectra (dB) and (d) spectral intensities of axial wave (linear scale) along propagation. Spectral intensities are normalized to their respective maximal values. Numerical parameters are described in table (3.1).

3.4.2/ INTUITIVE INTERPRETATION

The strong reduction in nonlinear instabilities in the case of profile-3 could be explained by the reduction in the nonlinear propagation length of the Bessel beam thanks to its initial parabolic intensity rise. Indeed, since these Bessel beams propagate according to soft input condition (smooth transition case), the weak intensity rise in the case of profile-3 may lead to a weaker intensity growth of the axial wave seed. To verify this assumption,

further numerical simulations are required.

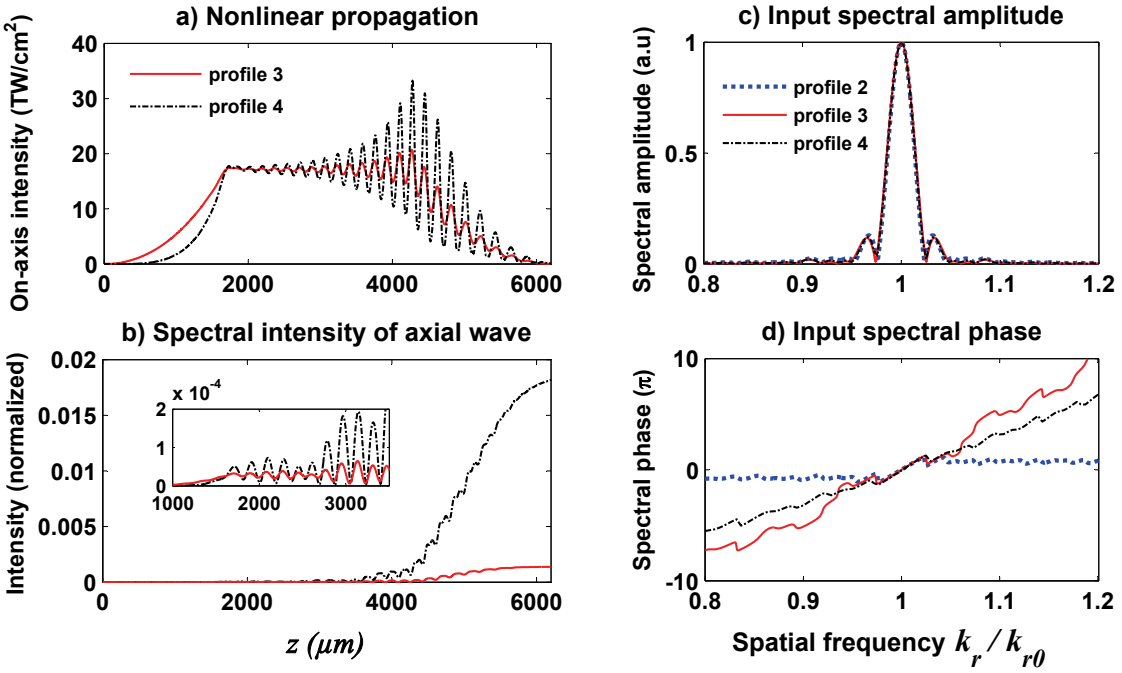

Figure 3.19: NLSE simulation results: Nonlinear propagation of Bessel beams with intensity profiles 3 and 4: plot of (a) the corresponding on-axis intensity and (b) spectral intensity of the axial wave along propagation $I(k_r = 0, z)$. Comparison of their respective (c) amplitude and (d) phase distributions with that of profile-2.

We consider another on-axis intensity profile, denoted profile-4, whose initial intensity rise is proportional to z^4, which is smoother than that of profile-3 for propagation distances below $z = 500\ \mu m$. We compare in Fig. (3.19,a) the nonlinear propagation corresponding to these two profiles. It is clear that nonlinear oscillations are much stronger in the case of profile-4. In the spectral domain (Fig. 3.19,b), although the growth of the axial wave seed is initially weaker in the case of profile-4, this axial wave seed exhibits an oscillating behavior with a higher modulation depth than that obtained for profile-3. This noticeable increase in the axial wave seed intensity cannot be explained by a slightly shorter propagation length where a relatively high intensity (>5 TW/cm^2) is reached.

We also considered different on-axis intensity profiles of the input intensity rise of the form $I(r = 0, z) \propto z^\gamma$ where $\gamma \in \mathbb{Q}^{+*}$ [2]. For $\gamma = 1.5$ and 2.5, numerical results of the NLSE show that the corresponding nonlinear on-axis intensities exhibit slightly higher modulation depth than in case of profile-3 (intensity rise $I(r = 0, z) \propto z^2$). This shows that there is an optimal profile of the initial intensity rise leading to weaker nonlinear instabilities.

Another possible interpretation lies in the input spectral distribution of Bessel beams. Based on our numerical results, the major difference in the nonlinear propagation of our chosen Bessel beams resides in the initial spectral broadening and thus the growth of the axial wave seed. Recall that, in the previous section, the same difference in behavior was observed in the smooth and abrupt transition cases. Hence, we can use the same reasoning we used in the previous section to interpret these results which is based on

[2] positive rational number superior to 0

the input spectral phase distribution. It is therefore not the steepness of the intensity rise than matters, but rather it is the input spectral phase.

Figure (3.19,c,d) shows the spectral amplitude and phase distributions corresponding to profiles 2,3 and 4. The BG beam (profile-1) was studied beforehand (Fig. 3.13). Its input spectral amplitude takes the form of a Gaussian function centered around the central frequency while the spectral phase is in the form a linear ramp in the range ($\beta \in [0.98 \; - \; 1.02]$) and is constant outside this range. In the case of profiles 2,3 and 4, the distribution of their spectral amplitudes is similar between them and takes the shape of a sinc-like function. The spectral phase corresponding to profile-2 is similar to that of profile-1 except that it exhibits a slightly oscillating behavior in the tails of the spectrum. In the case of profiles 3 and 4, however, while the spectral phase also takes the form of a linear ramp in the range $\beta \in [0.98 \; - \; 1.02]$, it varies significantly outside according to an oscillating profile along a ramp.

We estimate the spectral domain of influence of the phase to be in the range $\beta \in [0.8 \; 1.2]$. *Although the input spectral phase is rapidly varying over a wider spectral range, spectral frequencies that contribute to the formation of the Bessel beam are restrained around the central frequency. To investigate the influence of the input spectral phase of spectral components, we vary the input phase outside the main Bessel ring ($\beta \in [0.98 \; - \; 1.02]$) and simulate the linear propagation of the corresponding phase-modified Bessel beam.* Our simulations show that the on-axis intensity is affected by the input phase in the range $\beta \in [0.8 \; - \; 1.2]$ by more than 5% in the linear regime when the phase outside the main Bessel ring is modified. Hence, we estimate that the initial spectral broadening largely depends on the phase distribution in this domain [Ouadghiri-Idrissi et al., 2017].

In the framework of FWM interactions, we interpret the decrease in nonlinear instabilities for profile-3 by the phase mismatch between the pump and signal waves which, as discussed in the previous section, leads to partial destructive interference of the resulting idler wave [Ouadghiri-Idrissi et al., 2017]. Comparing the spectral phase of profiles 3 and 4, we notice that it is steeper in the case of profile-3. This difference in phase distribution can explain the strong decrease in nonlinear instabilities observed for profile-3. In the next section, we will further investigate this hypothesis using our reduced FWM model.

3.4.3/ THEORETICAL ANALYSIS

We investigate the impact of input phase distribution on the initial spectral broadening. We have seen that this spectral broadening is the result of the interaction of the pump with itself, which we referred to as SPM. However, since we estimated that the influence domain of the input phase is extended to the range $\beta \in [0.8 \; - \; 1.2]$, it is necessary to extend the domain of definition of the pump wave over all this spectral range.

Using our reduced FWM model described by Eq. (3.20), we consider the contribution of 27 spectral components in the chosen spectral range. We numerically compute the spectral intensity of the idler wave and compare its evolution for spatial spectra corresponding to profile-1 and profile-3. Numerical computation results are depicted in Fig. (3.20,a,b). Regarding profile-1 (BG beam), we observe about the same features as those obtained in case the pump wave is solely defined in the range $\beta \in [0.96 \; - \; 1.04]$, i.e. the cascaded feature of spectral broadening (see Fig. 3.16). In contrast, this feature is totally absent in the case of profile-3 where spectral broadening only occurs starting from a propagation distance of $z = 1500 \; \mu m$. Particularly, the form of spectral expansion is in qualitative

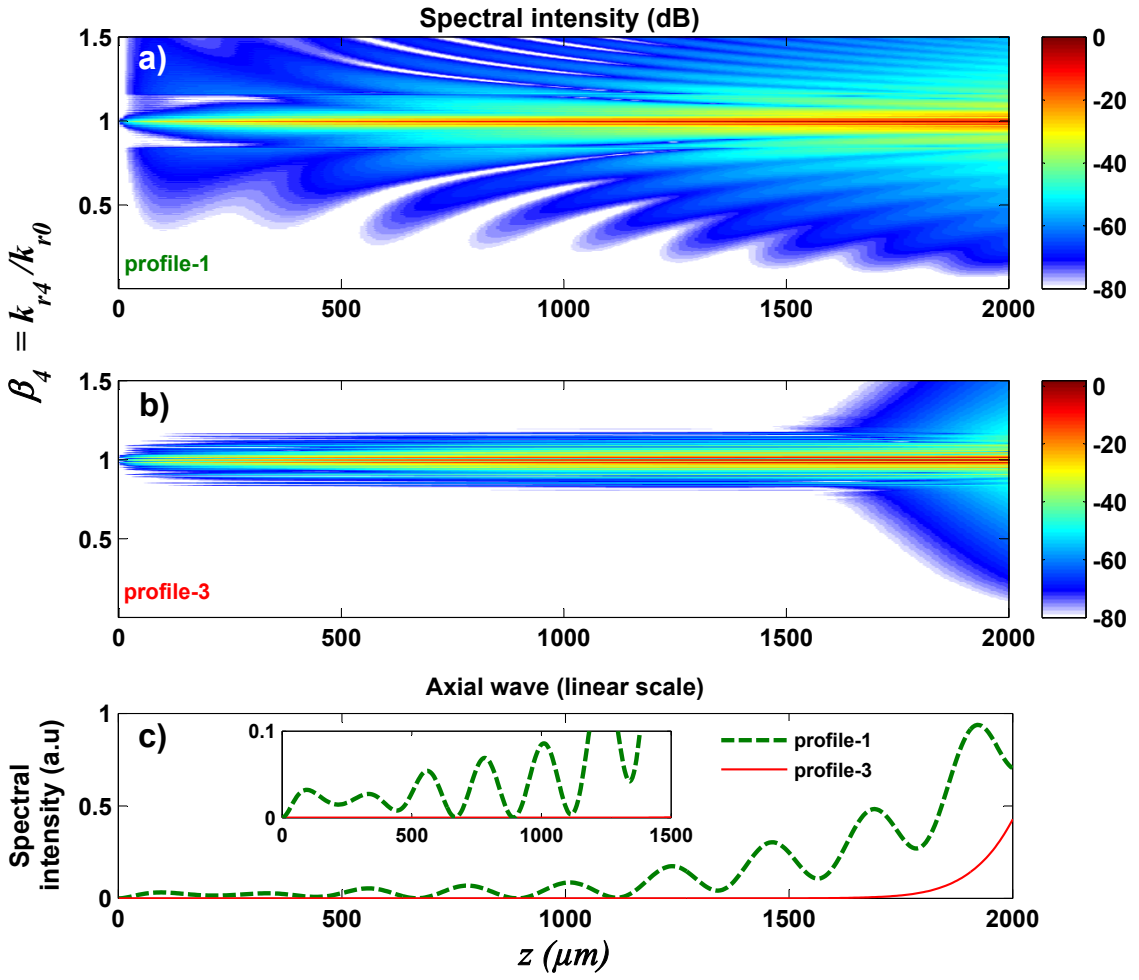

Figure 3.20: Results using our FWM model: Angularly resolved intensity (dB) of the idler wave resulting from the interaction of three waves composed each of twenty-seven frequencies: $\beta_j = [0.805 - 1.195]$ for input phase distributions of (a) profile-1 and (b) profile-3 and (c) the corresponding evolution along propagation of the axial wave intensity ($k_r \approx 0$).

agreement with NLSE simulation results (Fig. 3.18,c).

In Fig. (3.20,c) we compare the evolution of the axial wave intensity corresponding to these two profiles. The absence of axial wave oscillation is clearly seen which is also consistent with numerical simulation results of the NLSE of Fig. (3.18). We then conclude that the low intensity tails of the spatial spectrum also contribute to the initial spectral broadening. Furthermore, related input spectral phase plays a major role in the weak growth of the axial wave.

N.B.: Regarding the results of Fig. 3.20, if we consider the contribution of a lower number of frequencies in the range $\beta = [0.805 - 1.195]$, we do not obtain the same results for the spectral phase distribution related to profile-3. Provided that our calculations are correct, we assume that this disagreement is normal since, in our numerical simulations of the NLSE, we considered the contribution of much more spectral components. We can also conclude that the attenuation of the initial spectral broadening observed for profile-3 is the result of the interference of multiple spatial frequencies in this spectral range.

We stress on the point that these conclusions are only valid in case the phase distribution is conserved along propagation. According to our numerical simulation of the NLSE, the input phase remains about the same up to a propagation point of $z = 1200\ \mu m$. As discussed in the previous section, as the spectral phase flattens because of linear propagation, SPM and FWM interactions become more efficient and inevitably lead to significant growth of the axial wave and outer ring. Hence, the control of input intensity rise only allows controlling the initial spectral broadening. FWM processes responsible for the growth of unstable modes only occur after the generation of an axial wave seed. However, at the propagation point where it appears, the spectral phase distribution becomes quasi-flat as the Bessel beam intensity reaches its peak value. Therefore, the optimization of the input intensity rise of the beam only allows controlling the SPM-induced initial spectral broadening and not the FWM processes of the second approximation. In the next section, we will investigate the possibility to control these FWM processes.

3.4.4/ CONTROL OF THE GROWTH OF UNSTABLE MODES (SECOND APPROXIMATION)

We propose a proof-of-concept approach to directly manipulate FWM processes of the second approximation. As discussed in section 3.2.4, nonlinear oscillations of the on-axis intensity of Bessel beams is the result of the interference of the input conical beam with the self-generated outer ring. This approach is then based on adding an unstable mode to the input Bessel beam to compensate for the one that is induced by Kerr effect. In other words, the unstable mode that is added to the input beam should be in opposition of phase to the Kerr-induced one. In direct-space, the addition of an unstable corresponds to an oscillating target on-axis intensity that will be compensated by Kerr nonlinearity.

To implement our approach, we first study the nonlinear propagation of a Bessel beam and specifically record the on-axis intensity profile. Then, we design, using the theoretical approach described in Chapter 2, a target on-axis intensity with the same oscillation period but with a phase retardation with respect to that obtained in the nonlinear regime.

We present In Fig. (3.21) an example of the application of this approach. The target on-axis intensity and the corresponding input spatial spectrum are depicted in Fig. (3.21,top). In this example, we consider a conventional BG beam (greed line) and compare its nonlinear propagation to a modified BG (MBG) beam which exhibits longitudinal oscillations with an oscillation period of 185 μm (red line). Their spatial spectra are identical except that the MBG beam has an additional spectral component defined at $\beta \approx 1.5$ (outer ring). Notice the spectral phase of this component is defined at 2π whereas it is defined at π for the BG beam. Of course, although BG beams have no spectral component at $\beta \approx 1.5$, a spectral component of weak intensity is generated at this frequency thanks to initial spectral broadening. Hence, we consider that the spectral phase still evolves along propagation in the linear regime and that its initial phase value is determined by input spectral phase of the BG beam, i.e. "π". Supposing that its intensity is low enough to not trigger Kerr nonlinearity, then it will only undergo linear phase shift. In the ideal case, the added outer ring is assumed to remain in opposition of phase to the Kerr-generated one and thus destructively interfere.

In Fig. (3.21,bottom), we present numerical results of the NLSE and compare their respective on-axis intensity evolution as well as the evolution of the outer ring. It is clear

that the MBG exhibits lower longitudinal modulation depth compared to the conventional BG beam, which indicates a decrease in nonlinear instabilities. In the spectral domain, for the BG beam, while the outer ring intensity is lower at low propagation distances, it significantly increases starting from the propagation point $z = 2600\ \mu m$. In contrast, in the case of MBG beam, the spectral intensity of the outer ring does not undergo any noticeable growth and only present an oscillating behavior. This shows then the possibility to manipulate FWM processes of the second approximation via longitudinal intensity shaping of Bessel beams.

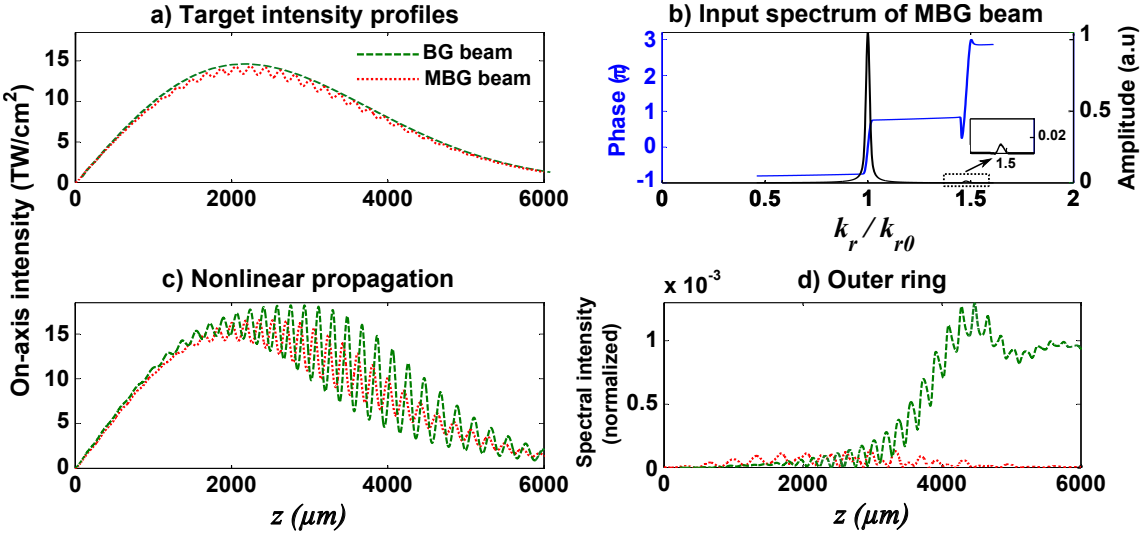

Figure 3.21: (a) Target intensity profiles and (b) input spectrum of the modified Bessel-Gauss (MBG) beam. (bottom) Numerical simulation results of the NLSE: (c) their respective on-axis intensity and (d) spectral intensity of idler wave evolution along propagation for (green dashed line) BG beam and (red dotted line) MBG beam.

Although our approach allows a decrease in nonlinear oscillations, complete suppression of these oscillations remains a difficult challenge, especially regarding the optimal input spectral intensity of the additional wave around $\beta = 1.5$ and the corresponding spectral phase profile. Further theoretical studies are required to complete this approach.

3.4.5/ SUMMARY

We presented a novel approach to control Kerr-induced instabilities depending on the initial intensity rise of the beam inside nonlinear media. By means of numerical simulations of the NLSE, we showed that nonlinear on-axis intensity modulation can be reduced for Bessel beams with slowly increasing input intensity rise and specifically in the form of a parabola. In the spectral domain, this modulation decrease is accompanied by a weak growth of the axial wave and outer ring. As in the case of smooth transition case, we related it to a weak growth of the axial wave seed.

We also explained the difference in the axial wave seed intensity in terms of the input spectral phase profile. In the case of an on-axis intensity profile with parabolic intensity rise (profile-3), the spectral phase has a steeper profile over a wide range of frequencies compared to the case of a Bessel-Gauss beam. This implies that the destructive interference between out-of-phase spectral components leads to a less intense axial wave seed

in the case of the axially shaped Bessel beam (profile-3).

However, this approach only allows controlling the initial spectral broadening and consequently the intensity of the axial wave seed. To control subsequent FWM processes, we proposed a proof-of-concept approach based on adding an unstable mode (outer ring) to the input Bessel beam to compensate for the one that is induced by Kerr effect. In other words, the unstable mode that is added to the input beam should be in opposition of phase to the Kerr-induced one. In direct-space, the addition of an unstable correspond to an oscillating target on-axis intensity that will be compensated by Kerr nonlinearity. This approach opens the possibility to completely suppress Kerr-induced on-axis intensity modulation, but it is a difficult challenge regarding experimental implementation.

3.5/ BESSEL FILAMENTATION USING SHAPED LONGITUDINAL INTENSITY PROFILES

In this section, we will numerically study the nonlinear propagation of longitudinally-shaped Bessel beams in the filamentation regime. We will show the effects of the attenuation of Kerr-nonlinearity on the stability of the beam in presence of nonlinear losses (MultiPhoton Absorption (MPA) and plasma defocusing). We aim to show that our results are also valid in the filamentation regime.

3.5.1/ FILAMENTATION MODEL

We present numerical simulation results using two filamentation models which we briefly discussed in chapter 1. The first was reported in Ref. [Porras et al., 2004] where photoionization is approximated to multiphoton ionization and light-plasma coupling is neglected. It is described by the following equation and will be referred to as "reduced filamentation model":

$$\frac{\partial A}{\partial z} = \frac{i}{2k_0}\Delta_\perp A + ik_0 n_2 |A|^2 A - \frac{1}{2}\sigma_K |A|^{2K-2} K\hbar\omega_0 A \tag{3.64}$$

This nonlinear propagation equation was shown to have a propagation-invariant solution termed "Nonlinear unbalanced Bessel beam" (NL-UBB) which characterizes steady filamentation regime. As discussed in chapter 1, an input Bessel beam can be reshaped into a NL-UBB in case nonlinear losses, and specifically multiphoton absorption, prevail over Kerr self-focusing. Hence, we aim to show that reduced Kerr-nonlinearity in shaped-Bessel beams allows satisfying this condition in a wider range of beam parameters compared to conventional BG beams.

The second model accounts for dispersion and plasma generation. We use the model equations reported in Ref. [Sudrie et al., 2002]. We model the propagation of cylindrically-symmetric envelope A of a linearly polarized electric field E, written as $E = \Re[A\exp(ikz - i\omega_0 t)]$:

$$\frac{\partial A}{\partial z} = \frac{i}{2k}\nabla_{\perp}^2 A - i\frac{k^{(2)}}{2}\frac{\partial^2 A}{\partial t^2} + ik_0 n_2 |A|^2 A - \frac{1}{2}\sigma_K |A|^{2K-2} K\hbar\omega_0 A(1-\rho/\rho_{at}) - \frac{\sigma}{2}(1+i\omega\tau_c)\rho A \quad (3.65)$$

where ρ_{at} is the density of neutral atoms, τ_c is the electron collision time and σ is the cross-section of inverse Bremsstrahlung effect given by:

$$\sigma = \frac{kq^2}{n^2\omega^2\epsilon_0 m_e^*}\frac{\omega\tau_c}{1+\omega^2\tau_c^2} \quad (3.66)$$

where ϵ_0 is vacuum permittivity and m_e^* is the effective free-electron mass. The time evolution equation of laser-generated plasma is written as:

$$\frac{\partial \rho}{\partial t} = \left(\sigma_K |A|^{2K} + \frac{\sigma}{U_i}\rho|A|^2\right)(1-\rho/\rho_{at}) - \rho/\tau_r \quad (3.67)$$

where τ_r is the free-electron relaxation time. Numerical parameters are given for fused silica [Sudrie et al., 2002] and are presented in table 3.2.

$\beta_2\ (fs^2/cm)$	361	$m_e^*\ (Kg)$	$0.635 \times 9.1 \times 10^{-31}$
$U_i\ (eV)$	9	$\rho_{at}\ (cm^{-3})$	2.1×10^{22}
K	6	$\sigma_K\ (cm^9 s^{-1} W^{-6})$	$9.8 \times 10^{-71} \times \rho_{at}$
$\tau_c\ (fs)$	23.3	$\sigma\ (cm^2)$	0.96×10^{18}

Table 3.2: Numerical parameters used in simulations of Bessel filamentation in fused silica.

Input fields: pulsed quasi-Bessel beams : The input field is spatially modeled by a quasi-Bessel beam with a temporal Gaussian envelope. For pulsed BG beams, the input field reads:

$$A_{BG}(r,t,z=0) = A_0 \exp\Big(-\frac{r^2}{w_0^2} - \frac{t^2}{t_p^2} - k\, r\, \sin(\theta)\Big) \quad (3.68)$$

where t_p is the pulse temporal half width defined at 1/e of the central amplitude . For longitudinally shaped Bessel beams, we first compute the complex spatial spectral amplitude corresponding to the desired profile of the longitudinal central core intensity $I(z) \equiv I(r=0,z)$ as described in chapter 2 [Čižmár et al., 2009, Ouadghiri-Idrissi et al., 2016]:

$$S(k_z, z=0) = \frac{1}{k_z}\int_{-\infty}^{+\infty} \sqrt{I(z)}\exp[i(k_{z0}-k_z)z]\mathrm{d}z \quad (3.69)$$

where $k_z = \sqrt{k^2 - k_r^2}$ is the longitudinal frequency coordinate and $k_{z0} = k\cos(\theta)$. The corresponding spatial counterpart is then computed using the inverse Hankel transform HT^{-1}. The input profile of the modified Bessel beam is then defined as:

$$A_{MBB}(r,t,z=0) = A_0 \exp\left(-\frac{t^2}{t_p^2}\right) HT^{-1}[S(k_z, z=0)] \quad (3.70)$$

3.5.2/ DECREASE OF THE CRITICAL INTENSITY ABOVE WHICH MPA PREVAILS OVER KERR EFFECT

The condition for which nonlinear losses prevail over Kerr self-focusing can be satisfied if the Bessel beam peak intensity "I" exceeds a critical value I_c as follows [Couairon et al., 2012]:

$$I \geq I_c \equiv \left(\frac{2k_0 n_2}{\sigma_K U_i}\right)^{1/(K-2)} \tag{3.71}$$

Considering our numerical parameters, $I_c \approx 60\ TW/cm^2$. Hence, we consider, in our simulations, pulsed-Bessel beams whose maximal intensity lower than the critical value: $I_{max} = 25\ TW/cm^2$ as to naturally trigger the unsteady filamentation regime.

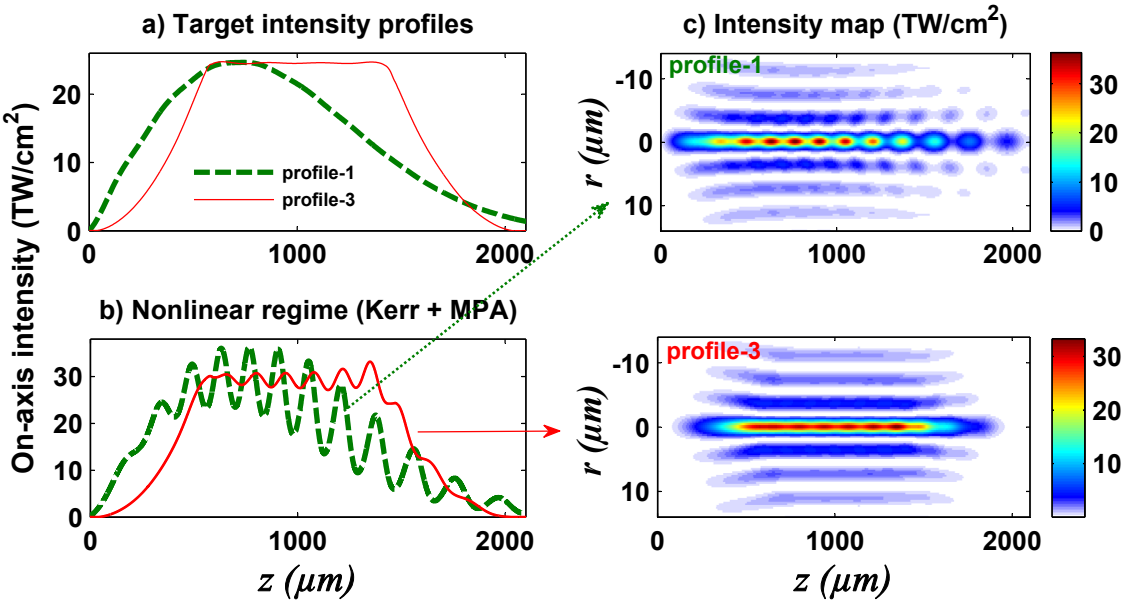

Figure 3.22: Numerical simulation results of the propagation of two Bessel beams in the filamentation regime (we consider the reduced filamentation model of Eq. (3.64) where laser-plasma coupling is neglected) with (a) profile-1 (green dashed line) and profile-3 (red solid line): (b) plot of the peak temporal intensity of the central core along z, and (c) the corresponding intensity distribution in transverse and propagation distances for both beams. Input pulse energy, E_{in} = 3.6 μJ for profile 1 and E_{in} = 3.8 μJ for profile 3, pulse duration 130 fs; cone angle θ= 4°; $I_{max} = 25\ TW/cm^2$ and beam waist $w_0 = 100\ \mu m$.

We compare the propagation of two pulsed Bessel beams with different on-axis intensity profiles (Fig. 3.22,a): profile-1 which refers to a BG beam and profile-3 which allows reducing nonlinear instabilities. We present in Fig. 3.22 numerical simulation results of Eq. (3.64) (plasma terms neglected). Nonlinear evolution of the central core intensity of both beams is shown in Fig. (3.22,b) while the intensity distribution in transverse and longitudinal distance is depicted in Fig. (3.22,c).

As it is expected for the pulsed BG beam, its on-axis intensity presents significant intensity modulation which marks the unsteady filamentation regime. However, we clearly notice that the Bessel beam with target profile-3 exhibits lower intensity modulation which is attributed to reduced Kerr-induced instabilities. We then conclude that the attenuation of Kerr nonlinearity enhances the stabilization of Bessel beams in presence of nonlinear

losses.

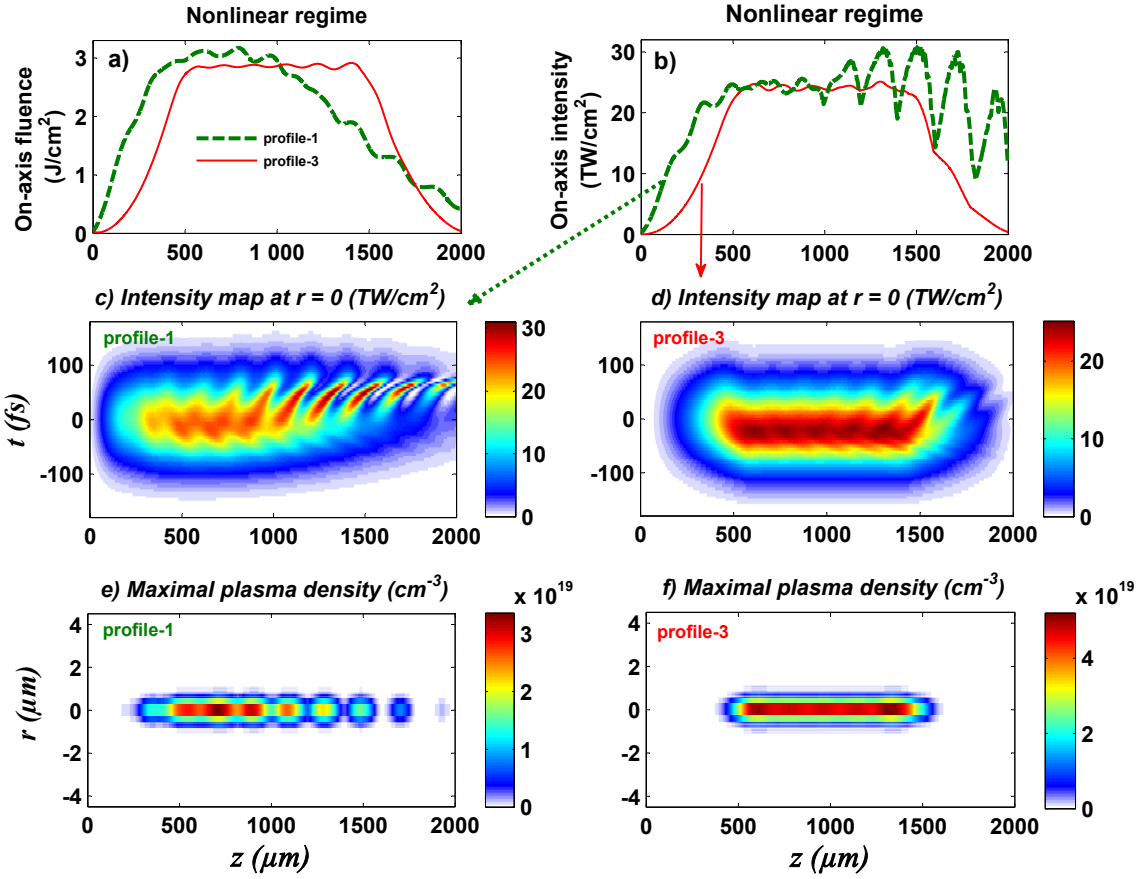

Figure 3.23: Nonlinear propagation of two Bessel beams with profile 1 (green dashed line) and profile 3 (red solid line) in the filamentation regime (accounting for MPA and plasma defocusing): plot of (a) the on-axis fluence (J/cm^2), (b) the peak temporal intensity of the central core along z. Evolution of the central core intensity in time and propagation coordinates for (c) profile-1 and (d) profile-3. Evolution of maximal plasma density in transverse and propagation distances for (e) profile-1 and (f) profile-3.

3.5.3/ CONTROL OF LASER-INDUCED PLASMA CHANNELS

We now consider the full filamentation model described the Eqs. (3.65) and (3.67). We use the same beam parameters as in Fig. (3.22) and consider the same on-axis intensity profiles. Numerical results are shown in Fig. (3.23) where we specically plot in (a) the on-axis fluence and in (b) the peak temporal intensity of the central core along propagation.

Notice that although plasma defocusing has stabilized the BG pulse (Fig. 3.23,a,green dashed line), the corresponding peak temporal intensity presents severe on-axis intensity oscillations (Fig. 3.23,b)). In contrast, the shaped Bessel beam sustains very weak oscillations of the on-axis intensity. These features are apparent in Fig. (3.23,c-d) where we display the time evolution of the central core intensity along propagation: the pulsed BG beam sustains pronounced temporal reshaping, especially after a propagation distance of $z = 1000\ \mu m$ where the pulse undergoes temporal splitting. In contrast, the spatially-

shaped Bessel pulse exhibits weaker temporal reshaping which highlights its stability in the time domain. These weak temporal dynamics can be explained by the reduction in Kerr-induced instabilities as discussed in previous sections.

We show in Fig. (3.23,e-f) the evolution of laser-generated maximal plasma densities as a function of the transverse and longitudinal coordinates for the two intensity profiles. It is clear that the plasma channel generated in the case of profile-3 is more uniform than the one produced in the case of profile-1. In addition, the plasma density is relatively higher in the case of profile-3. We assume that, since the intensity of the spatially-shaped Bessel pulse undergoes weak temporal dynamics, the peak intensity of the pulse remains quasi-constant along propagation allowing the generation of a uniform plasma channel in contrast with the pulsed BG beam.

CONCLUSIONS

In this chapter, we have discussed Kerr-induced nonlinear instabilities and introduced a novel approach based on shaping the on-axis intensity of Bessel beams to reduce their extent in order to generate stable Bessel filaments.

In the first section, we introduced our theoretical model, which we named reduced FWM model, in order to interpret the different features of Kerr-induced instabilities. By means of this model, we investigated the evolution along propagation of Kerr-induced distortions of the spatial spectrum of Bessel beams. This was performed by analyzing the idler wave generated as a result of the interaction of two pump waves with a signal wave in the spectral domain. Although such an analysis cannot be performed using the theory of Gadonas et al. [Gadonas et al., 2001], the latter still allows describing the major Kerr-induced effects causing nonlinear instabilities. Particularly, this theory points out the order at which these nonlinear effects take place as the Bessel beam propagates which cannot be determined using our reduced FWM model. Hence, these two theories complement each other and allow a thorough investigation of nonlinear instabilities.

In the second section, we reviewed the different nonlinear dynamics of Kerr-induced instabilities. Numerical simulation results show that related nonlinear spectral distortions are established in two steps. The first step consists in spectral broadening and the generation of an axial wave seed. The second step lies in the amplification of this axial wave seed and outer ring generation which are a signature of Kerr-induced instabilities. Using the theory of Gadonas et al. and our theoretical model, we showed that the initial spectral broadening is caused by self-phase modulation, i.e. the interaction of the Bessel ring with itself. The growth of signal wave and outer ring were interpreted in terms of FWM interactions as reported in Ref. [Gadonas et al., 2001]. Hence, the control of nonlinear instabilities should reside either in the initial spectral broadening or ensuing FWM processes.

In the third section, we used our FWM model to interpret the dependence of nonlinear instabilities on the positioning of Bessel beams with respect to nonlinear media. Our interpretation is based on the input spectral phase distribution relative to the two cases. In the abrupt intensity transition, the input spectral phase of the Bessel ring is quasi-flat. In the framework of FWM interactions, the pump wave is considered to be made of multiple spectral components, each with nearly the same input phase. At a given spatial frequency, the resulting SPM-generated idler wave will be made of a superposition of in-

phase components which will constructively interfere. As a result, the extent of the initial spectral broadening, and therefore nonlinear instabilities, will be enhanced.

In contrast, the input spectral phase is rapidly-varying in the smooth transition case which will lead to reduced spectral broadening. However, this is only valid in case the input spectral phase remains rapidly-varying along propagation. Indeed, numerical simulations show that the spectral phase becomes quasi-flat by the point the growth of the axial wave takes place. The smooth intensity transition therefore only allows controlling the first stage of nonlinear spectral distortions.

In the fourth section, we introduced our approach to control nonlinear instabilities using shaped-intensity profiles. Our numerical simulations show that nonlinear instabilities are effectively reduced if the initial intensity rise of Bessel beams is slowly established. As in the case of smooth intensity transition, we interpreted results based on the input spectral phase.

However, this approach also only allows controlling the initial spectral broadening. To control subsequent FWM interactions, we proposed the following solution: considering that longitudinal intensity modulation is the result of the interference of the input conical beam with a Kerr-generated outer ring, we proposed to add an additional spectral component to the input beam that is defined at the same frequency as the outer ring but in opposition of phase to it. Our numerical simulations show the potential applicability of this approach since the growth of Kerr-induced outer ring was seen to be reduced along propagation. However, further studies still need to be performed to complete this method.

Finally, we showed that our results are also valid in the filamentation regime. Specifically, reduced Kerr-nonlinearity in shaped Bessel beams allows generating plasma channels that are more uniform compared to those generated by conventional pulsed BG beams.

In our numerical simulations in the filamentation regime, we used nonlinear propagation model that is widely used in the literature. However, it was shown that this model cannot explain some features of Bessel filamentation, particularly the steady propagation regime of Bessel pulses at ablation-level intensities [Courvoisier et al., 2013]. In the next chapter, we will model the filamentation regime of stationary (steady) Bessel beams.

4

FILAMENTATION OF BESSEL BEAMS

INTRODUCTION

In chapter 1, we have shown aspects and applications of Bessel filamentation in transparent media. We have presented the different Bessel filamentation regimes, particularly the steady and unsteady ones.

The first experiments of Bessel filamentation were performed in air using axicon-focused laser beams. Bunkin et al. used a 40-ns pulsed Bessel beam, with high cone angle ($\geq$ 18°) to generate a long and uniform laser spark. Nanosecond Bessel pulses (with low cone angles $\leq$ 10°) were used experimentally to generate quasi-periodic laser sparks in gases [Andreev et al., 1991]. In 1993, Durfee et al. showed that 100-ps Bessel beams can generate uniform plasma waveguides [Durfee et al., 1993]. In 2006, Polesana et al. demonstrated the generation of uniform Bessel filaments in liquid. They later demonstrated that steady and unsteady filamentation regimes can be formed in water depending on the initial positioning of the beam with respect to nonlinear sample [Polesana et al., 2007]. In glass, the propagation of Bessel filaments can generate either permanent (matter modification, ablation) or non-permanent damage. Both steady [Bhuyan et al., 2010, Bhuyan et al., 2011] and unsteady [Gaizauskas et al., 2006] propagation regimes were reported and it was shown that it highly depends on whether the Bessel cone angle is high or low respectively.

Of particular interest, Bhuyan et al. performed many experiments on the filamentation of femtosecond Bessel beams with high cone angle in glass [Bhuyan et al., 2010]. Their results showcased propagation-invariant features of Bessel filaments [Courvoisier et al., 2016b] resulting in inducing high aspect ratio nanochannels.

To interpret these result, previous members of our group numerically investigated the propagation of high cone angle Bessel filaments in glass [Courvoisier et al., 2013]. They used a widely used numerical model which is based on the nonlinear Schrödinger equation (NLSE) for nonlinear light propagation and Drude model for laser-matter coupling [Couairon et al., 2007]. This model was presented in chapter 3 (section 3.5.1, page 107) and it accounts for dispersion, diffraction, Kerr self-focusing, multiphoton absorption and plasma absorption and defocusing.

According to the experimental results, one can expect that the laser-generated plasma channel will be uniform and confined in the volume area of the central core of the beam. However, numerical results are incompatible with experimental ones. They predict the generation of plasma on a wide region, much larger than the void formed. This is even

more apparent for the fluence distribution as shown in Fig. (4.1,c) [Xie et al., 2016].

To obtain results compatible with experiments, it appeared from numerical simulations performed in our group [Xie et al., 2016] and in others [Garzillo et al., 2016], that the collision time must be decreased to the range of 10 to 15 as[1] (see Fig. (4.1)). In this case only, a homogeneous energy deposition could be obtained. Later in this chapter, we will also show experimental results that confirm the stationary behavior of Bessel beams in the ablation regime, and that could not be reproduced with state of the art model.

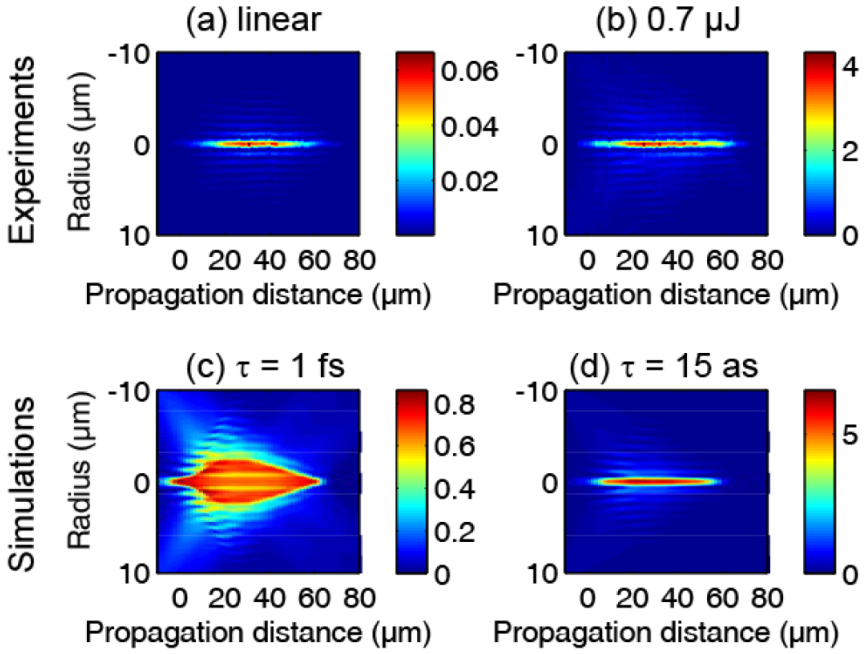

Figure 4.1: Comparison between experimental fluence maps in J/cm^2 (a-b) and simulations with nonlinear Schrödinger model for (c) $\tau_c = 1$ fs and (d) $\tau_c = 15$ as. Image taken from Ref. [Xie et al., 2016].

In this chapter, we will discuss the validity of filamentation models based on the above described NLSE and time evolution equation of plasma density. In the first section, we will first recall the steps and approximations used to derive the NLSE.

In the second section, we will present our experimental results on the filamentation of femtosecond Bessel beams in fused silica. We will discuss, based on numerical results reported in literature, the possible improvements that can be introduced in the filamentation model. We will then introduce our proposed improvements and compare the corresponding numerical simulations with experimental results.

4.1/ FILAMENTATION MODELING

The filamentation of pulsed laser beams is modeled using Maxwell equations coupled with matter equations. Maxwell equations describe the pulse propagation in nonlinear self-modified media. Although Maxwell equations can perfectly describe the propagation

[1]The collision time of dense electronic plasma was experimentally measured and is around 1 fs [Sun et al., 2005]. A value of the order of 10 as has yet to be demonstrated.

of optical fields, their numerical simulations are time consuming, hence the need to resort to approximations in order to simplify the propagation model.

Matter equations describe the matter modification induced by the laser field. They also describe the evolution of laser-generated plasma of electron-holes in time and its action on the laser field. These equations are originally very complicated and the physical processes involved are hard to model. Their numerical resolution is then also time consuming and there is a need to simplify them through appropriate approximations. These approximations are also needed to simplify the physical interpretation and descriptions of the processes involved. In this section, we will recall these approximations. Their validity in modeling the filamentation of Bessel beams will be discussed later in this chapter.

4.1.1/ NONLINEAR PROPAGATION EQUATIONS AND RELATED APPROXIMATIONS

Let us first summarize the different steps leading to the derivation of nonlinear Schrödinger equation (NLSE), following the approach of Ref. [Couairon et al., 2011]. We consider an electric field **E** propagating in a homogeneous, isotropic and nonmagnetic dielectric medium. Starting from Maxwell equations, one can express the vectorial wave equation in the time domain as follows [Couairon et al., 2011]:

$$\nabla^2\mathbf{E} - \nabla(\nabla\,.\,\mathbf{E}) - \frac{1}{c^2}\frac{\partial^2}{\partial t^2}\int_{-\infty}^{t}\epsilon(t-t')\mathbf{E}(\mathbf{r},t',z)\mathrm{d}t' = \frac{1}{\epsilon_0\,c^2}\left(\frac{\partial\mathbf{J}}{\partial t} + \frac{\partial^2\mathbf{P}_{NL}}{\partial t^2}\right) \tag{4.1}$$

where $\mathbf{P}_{NL}$ is the nonlinear polarization, **J** refers to the current density of free charges, c is the light velocity in vacuum. All fields depend on space transverse coordinates $\mathbf{r} \equiv (x, y)$, propagation variable z and time t.

It is actually more convenient to solve this equation in space-frequency to avoid the time-convolution term. Provided that the spectral counterpart of the time derivative is $\partial_t = -i\,\omega$, the vectorial wave equation is written as follows:

$$\nabla^2\hat{\mathbf{E}} - \nabla(\nabla\,.\,\hat{\mathbf{E}}) + \frac{\omega^2 n^2(\omega)}{c^2}\hat{\mathbf{E}} = \frac{1}{\epsilon_0\,c^2}\,(-i\,\omega\hat{\mathbf{J}} - \omega^2\hat{\mathbf{P}}_{NL}) \tag{4.2}$$

where $n^2(\omega) = \epsilon(\omega)$ refers to the linear complex refractive index of the sample. Later in this section, we will express this quantity as a function of time. The hat functions refer to the Fourier transforms of **E**, $\mathbf{P}_{NL}$, **J**

4.1.1.1/ SCALAR WAVE EQUATION

The first approximation used to simplify this propagation equation is the scalar one: the electric field is assumed to be linearly polarized and transverse to the propagation axis determined by the wavevector **k**. This applies also to the medium response, namely the current **J** and the nonlinear polarization $\mathbf{P}_{NL}$. Furthermore, the electric field is assumed to maintain its polarization state along the propagation distance.

Firstly, these assumptions imply that the term $\nabla(\nabla.\mathbf{E})$ can be neglected [Couairon et al., 2011]. This approximation is valid for weakly focused beams or conical beams with sufficiently low cone angles. Secondly, the linear polarization assumption implies that Eq. (4.2) can be written in a scalar form [Couairon et al., 2011]:

$$(\partial_z^2 + \nabla_\perp^2)\hat{E} + k^2(\omega)\hat{E} = -\frac{1}{\epsilon_0 c^2}(i\omega\hat{J} + \omega^2\hat{P}_{NL}) \tag{4.3}$$

where $k(\omega) = \dfrac{n(\omega)\omega}{c}$ is the medium dispersion relation.

4.1.1.2/ NONLINEAR ENVELOPE EQUATION

From laboratoty to pulse time frame: To further simplify the propagation equation and reduce the constraint on numerical sampling, the electric field is expressed as a superposition of a pulse envelope $\mathcal{E}$ with a carrier wave of angular frequency ω_0. Furthermore, the propagation equation is expressed in the pulse reference frame $(\xi, \tau = t - z/v_g)$ instead of the laboratory frame (z, t) where v_g is the pulse group velocity and is given by $v_g^{-1} = \dfrac{\partial k(\omega)}{\partial\omega}\,|_{\omega_0}$. The electric field is written as:

$$E(\mathbf{r},\tau,\xi) = \mathcal{E}(\mathbf{r},\tau,\xi)\exp[i(k - \frac{\omega_0}{v_g})\xi - i\omega_0\tau] \tag{4.4}$$

A similar decomposition holds for the nonlinear polarization and the free charge current whose envelopes are respectively denoted $\mathcal{P}_{NL}$ and $\mathcal{J}$. The expression of the propagation equation becomes:

$$\partial_\xi^2\hat{\mathcal{E}} + 2i\kappa(\omega)\partial_\xi\hat{\mathcal{E}} = -\nabla_\perp^2\hat{\mathcal{E}} - [k^2(\omega) - \kappa^2(\omega)]\hat{\mathcal{E}} - \frac{\omega^2}{c^2}\frac{\hat{\mathcal{P}}_{NL}}{\epsilon_0} - i\frac{\omega}{c^2\epsilon_0}\hat{\mathcal{J}} \tag{4.5}$$

where $\kappa(\omega) = k + \dfrac{\omega - \omega_0}{v_g}$ corresponds to space-time focusing [Brabec et al., 1997, Polesana et al., 2008].

Minimal approximation: The minimal approximation consists in neglecting the second derivative of the pulse envelope with respect to the propagation coordinate ∂_ξ^2. Hence, the nonlinear envelope equation becomes:

$$\partial_\xi\hat{\mathcal{E}} = \frac{i}{2\kappa(\omega)}\nabla_\perp^2\hat{\mathcal{E}} + i[k(\omega) - \kappa(\omega)]\hat{\mathcal{E}} + i\frac{[k(\omega) - \kappa(\omega)]^2}{2\kappa(\omega)}\hat{\mathcal{E}} + \frac{i}{2\kappa(\omega)}\frac{\omega^2}{c^2}\frac{\hat{\mathcal{P}}_{NL}}{\epsilon_0} - \frac{\omega}{2\kappa(\omega)c^2\epsilon_0}\hat{\mathcal{J}} \tag{4.6}$$

This approximation implies many assumptions. Physically, it is assumed that the field amplitude and phase are evolving sufficiently slowly along propagation [Couairon et al., 2011]. Notice that this equation is unidirectional. In other words, potential back-reflected light is assumed to be very small compared to the one propagating in the forward direction [Couairon et al., 2011].

Slowly Varying Envelope Approximation (SVEA): The SVEA states that the pulse envelope must slowly vary over a propagation distance of the wavelength order [Brabec et al., 1997]. It consists in assimilating the group velocity to phase velocity. In the other words, we approximate $k(\omega)$ and ω to k and ω_0 respectively [Couairon et al., 2011]. The nonlinear envelope equation becomes:

$$\partial_\xi \hat{\mathcal{E}} = i\frac{(\omega-\omega_0)^2}{2}k^{(2)}\hat{\mathcal{E}} + \frac{i}{2k}\nabla_\perp^2\hat{\mathcal{E}} + i\frac{\omega_0^2}{2c^2k}\frac{\hat{\mathcal{P}}_{NL}}{\epsilon_0} - \frac{\omega_0}{2c^2\epsilon_0 k}\hat{\mathcal{J}} \tag{4.7}$$

In the time domain, this equation reads:

$$\partial_\xi \mathcal{E} = \frac{i}{2k}\nabla_\perp^2\hat{\mathcal{E}} - i\frac{k^{(2)}}{2}\frac{\partial^2\mathcal{E}}{\partial\tau^2} + i\frac{\omega_0^2}{2c^2k}\frac{\mathcal{P}_{NL}}{\epsilon_0} - \frac{\omega_0}{2c^2\epsilon_0 k}\mathcal{J} \tag{4.8}$$

where $k^{(2)}$ is the group velocity dispersion coefficient. Let us now develop the expressions of nonlinear polarization $\mathcal{P}_{NL}$ and plasma current density $\mathcal{J}$.

4.1.2/ Laser-matter coupling terms of nonlinear propagation equation

4.1.2.1/ Nonlinear polarization

In Kerr media, $\mathbf{P}_{NL}$ refers to the third order nonlinear polarization which was described earlier in chapters 1 and 3. It reads:

$$\mathbf{P}_{NL} = \varepsilon_0\chi^{(3)}\mathbf{EEE} \tag{4.9}$$

where $\chi^{(3)}$ is the third order susceptibility. We simply write the corresponding envelope as follows:

$$\mathcal{P}_{NL} = \epsilon_0 n n_2 \mathcal{I}\mathcal{E} \tag{4.10}$$

where $\mathcal{I}$ is the intensity defined by $\mathcal{I} = \epsilon_0 nc \mid \mathcal{E} \mid^2 /2$, n_2 is the nonlinear refraction index which is expressed in m^2/W as $3\chi^{(3)}/4\epsilon_0 n^2 c$.

4.1.2.2/ Nonlinear absorption

Although the term **J** refers to current density, one must also consider nonlinear absorption processes which lead to the generation of free-electrons. In this regard, the expression of the current **J** becomes: $\mathbf{J} \equiv \mathbf{J}_{abs} + \mathbf{J}_p$ where $\mathbf{J}_{abs}$ accounts for nonlinear absorption and $\mathbf{J}_p$ refers to plasma current density [Couairon et al., 2011].

Nonlinear absorption is described by an effective current $\mathbf{J}_{abs}$ such that the averaged dissipated power corresponds to the one necessary for the ionization of the sample [Couairon et al., 2011]. This quantity depends then on the ionization potential U_i and an intensity dependant ionization rate $W_{PI}(\mathcal{I})$. It is expressed as [Couairon et al., 2011]:

$$\mathbf{J}_{abs}\mathbf{E}^* = 2W_{PI}(\mathcal{I})K\hbar\omega_0 \tag{4.11}$$

where K is the number of photons absorbed to overcome the potential gap U_i and liberate one electron. Using the scalar approximation, and in terms of envelopes, Eq. (4.11) becomes:

$$\frac{\mathcal{J}_{abs}}{n\epsilon_0 c} = \frac{W_{PI}(\mathcal{I})}{\mathcal{I}} K\hbar\omega_0 \mathcal{E} \tag{4.12}$$

The expression of the probability of photoionization W_{PI} was introduced in chapter 1 (section 1.2.2.2, page 21): it can be described by Keldysh formula as follows [Sudrie et al., 2002]:

$$W_{PI} = \frac{2\omega_0}{9\pi}\left(\frac{\omega_0 m}{\hbar\sqrt{\Gamma}}\right)^{3/2} Q(\gamma, U_i, \omega_0) \tag{4.13}$$

where ω_0 is the angular frequency, m is the reduced mass of electron and hole, $\Gamma = \gamma^2/1+\gamma^2$ and $\gamma = \omega_0\sqrt{mU_i}/qE$ is referred to as adiabaticity parameter with q is the electric charge and E is the electric envelope. Q is a function of laser and material parameters.

If we use the multiphoton absorption approximation to model the nonlinear ionization especially in case the field peak intensity is inferior to 35 TW/cm^2. W_{PI} is:

$$W_{PI}(\mathcal{I}) \equiv \sigma_K \mathcal{I}^K \tag{4.14}$$

4.1.2.3/ PLASMA CURRENT DENSITY

We have briefly presented in chapter 1 the effect of free-electron plasma on the propagating laser pulse. It induces a reduction in refraction index and thus reduces the pulse intensity. This description actually stems from Drude model and is widely used in filamentation modeling to describe the plasma current density J. Here we briefly recall this model and show how to develop the expression of this quantity.

Drude model is based on a classical description of free electrons that undergo Lorentz force and a friction force, determined by a collision time τ_c. This characteristic time corresponds to the time between two collisions with the ions. The time evolution equation of plasma velocity is then given by:

$$m_e\frac{\partial \mathbf{v}_p}{\partial t} = -q\mathbf{E} - \frac{m_e}{\tau_c}\mathbf{v}_p \tag{4.15}$$

where $\mathbf{v}_p = -\mathbf{J}_p/q\rho$. We replace this relation in Eq. (4.15):

$$\frac{\partial \mathbf{J}_p}{\partial t} = \frac{q^2\rho}{m_e}\mathbf{E} + \mathbf{J}_p\left[\frac{\partial\rho/\partial t}{\rho} - 1/\tau_c\right] \tag{4.16}$$

The evolution equation of the plasma current density has an additional term $\mathbf{J}_p\partial_t\rho/\rho$ with respect to the state of the art [Couairon et al., 2011, Couairon et al., 2007, Courvoisier et al., 2013, Sudrie et al., 2002, Polesana et al., 2008]. According to Eq. (4.16), neglecting this additional term implicitly implies that the rate of laser-induced ionization is very small compared to the electron collision frequency $1/\tau_c$. Let us, in a first

step, neglect this term. If we consider the envelope counterpart written in the pulse reference frame, Eq. (4.16) becomes:

$$\frac{\partial \mathcal{J}_p}{\partial \tau} = \frac{q^2 \rho}{m_e} \mathcal{E} + \mathcal{J}_p (i\omega_0 - 1/\tau_c) \tag{4.17}$$

where $\partial_\tau J = \exp[i(k - \omega_0/v_g) - i\omega_0 t](\partial_\tau - i\omega_0)\mathcal{J}$ [Couairon et al., 2011]. This equation can be solved in Fourier domain and we express the spectral counterpart of the current envelope as follows:

$$\hat{\mathcal{J}}_p = \frac{q^2 \tau_c}{m_e(1 + \omega_0^2 \tau_c^2)} (1 + i\omega_0 \tau_c) \Big(1 - i(\omega - \omega_0) \frac{\tau_c}{1 - i\omega_0 \tau_c}\Big)^{-1} \widehat{\rho \mathcal{E}} \tag{4.18}$$

The space-time counterpart of Eq. (4.18 can be written as [Gulley et al., 2010]:

$$\mathcal{J}_p = \frac{q^2 \tau_c}{m_e(1 + \omega_0^2 \tau_c^2)} (1 + i\omega_0 \tau_c) \Big(1 + \frac{i}{\omega_0} g \partial_\tau\Big)^{-1} \rho \mathcal{E} \tag{4.19}$$

where $g = \dfrac{-i\omega_0 \tau_c}{1 - i\omega_0 \tau_c}$. Gulley et al. defined an operator G as follows [Gulley et al., 2010]:

$$G^{-1} = (1 + \frac{i}{\omega_0} g \partial_\tau)^{-1} \tag{4.20}$$

This operator accounts for the variation of the refractive index as a function of time and it stands for dispersion of plasma. In the literature, however, this operator is usually neglected in the modeling of Bessel filamentation. This simplification can be seen as an application of the slowly varying envelope approximation which states that $\omega \approx \omega_0$. The expression of the current density envelope in the time domain then becomes:

$$\frac{\mathcal{J}_p}{n\, \epsilon_0 c} = \sigma (1 + i\omega_0 \tau_c) \rho \mathcal{E} \tag{4.21}$$

where σ is the cross section of inverse Bremsstrahlung effect.

$$\sigma = \frac{k q^2}{n^2 \omega^2 \epsilon_0 m_e} \frac{\omega \tau_c}{1 + \omega^2 \tau_c^2} \tag{4.22}$$

4.1.2.4/ EQUATION OF PLASMA DENSITY EVOLUTION IN TIME AND AVALANCHE IONIZATION

The nonlinear propagation model is coupled to a time evolution equation of plasma current density [Couairon et al., 2011]. It is written in the form of a rate equation as follows [Couairon et al., 2011]:

$$\frac{\partial \rho}{\partial t} = (W_{PI} + W_{ava} \rho)(1 - \rho/\rho_{at}) - \rho/\tau_r \tag{4.23}$$

where W_{PI} is the photoionization rate that was previously defined. W_{ava} refers to avalanche ionization. This ionization process was presented in chapter 1 (section 1.2.2.3, page 22). It describes the process according to which electrons in the valance band are ionized by highly energetic conduction band electrons generated beforehand by photoionization. τ_r is the electron recombination time.

The most simple model of avalanche ionization rate is based on the double-flux approximation [Stuart et al., 1996]. It states that each free-electron, right after reaching a critical energy ε_{crit}, will generate a second free-electron via collisions. This assumption also indicates that the collision rate is much higher than that of energy gain of free-electrons. The avalanche ionization rate is assumed to be proportional to pulse intensity and is written as [Couairon et al., 2007]:

$$W_{ava} = \frac{\sigma}{U_i}|\mathcal{E}|^2 \tag{4.24}$$

4.2/ BESSEL FILAMENTATION IN FUSED SILICA: EXPERIMENTS AND SIMULATION

As mentioned in the introduction, the filamentation model described in the previous section was used by our group to study filamentation of Bessel beams at ablation-level intensities [Courvoisier et al., 2013]. While experimental results showed that Bessel beams propagate according to a propagation-invariant regime of filamentation [Xie et al., 2016] leading to uniform energy deposition along propagation [Bhuyan et al., 2010, Courvoisier et al., 2013], numerical results using this model showed non-uniform and weak deposition of energy. In our work, we aim to improve our numerical model to better describe our experimental results.

In this section, we will firstly present our experimental results and describe the different features of Bessel filamentation. Then, we will recall the limitations of the above described filamentation model and discuss possible improvements that can be introduced. Finally, we will present our numerical results and discuss the validity of these improvements.

4.2.1/ EXPERIMENTAL RESULTS

4.2.1.1/ EXPERIMENTAL SETUP AND METHODOLOGY

The experimental setup is similar to the one we used in our linear propagation experiments as described in chapter 2 (section 2.3.1, page 45): the light source is an amplified Ti:Sapphire laser emitting 130 fs pulses with a central wavelength of 800 nm. It is obliquely incident on a SLM and the back-reflected light passes through a 4f system to filter out all undesired diffraction orders. In the image plane of this system, light amplitude distribution is demagnified by a factor 278. The Bessel beam onsets from the image focal plane of the microscope objective where the samples under consideration are positioned.

Fluence distribution imaging: To compare numerical maps of fluence distribution with experimental ones, the nonlinear propagation must be avoided from the plane z of con-

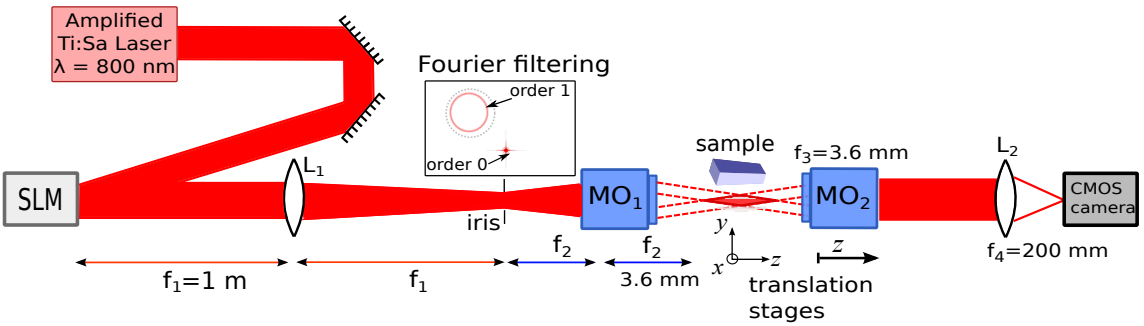

Figure 4.2: Experimental setup used for measurement of 3D fluence distribution of Bessel pulses in glass.

sideration to the camera. Therefore, in our experiments, the fluence distribution was reconstructed by recording the fluence at the exit side of the sample and progressively translating the beam across the exit side. 3D fluence distribution (in J/cm^2) of the Bessel beam is produced after energy calibration of the camera.

We also measure the energy evolution along propagation to estimate the energy loss due to nonlinear and plasma absorption. This is performed by means of spatial integration of the measured fluence. More details are presented in Refs. [Xie et al., 2015, Courvoisier et al., 2016a].

4.2.1.2/ EXPERIMENTAL PARAMETERS AND RESULTS

Figure (4.3) shows the evolution of fluence distribution and energy along propagation for different values of the input energy. For these experiments, the pulse duration was 130 fs and the Bessel-Gauss beam was characterized by a cone angle of 26° in air (17° in fused silica) and a Gaussian waist of $w_0 = 15\ \mu m$.

We observe that the Bessel beams propagate in the steady filamentation regime. The analysis of the samples shows that long and uniform sub-micron channels were generated for an input energy higher than $E_{in} = 0.72\ \mu J$. For $E_{in} = 0.26\ \mu J$, only refractive index modification was observed.

For $E_{in} = 0.26\ \mu J$, we notice an intensity clamping feature where the fluence remains quasi-constant after reaching a value of $F = 1.85$ J/cm^2 at a propagation distance of $z = 20\ \mu m$. At this point, we notice the beginning of energy attenuation. This shows that nonlinear absorption takes place leading to a decrease in the pulse fluence. The total energy loss is between 8 to 11 $\%$ of the input energy.

For $E_{in} = 0.72\ \mu J$, the intensity clamping effect takes place twice along propagation, in contrast with the case of an input energy of $E_{in} = 0.26\ \mu J$. The fluence keeps increasing to reach a maximal value of approximately 3.9 J/cm^2. This is accompanied by a significant decrease in energy in the range 33-37 $\%$ of the energy at $z = 17\ \mu m$. The same observations hold for $E_{in} = 1.6\ \mu J$ where the energy loss is around 56-58 $\%$ of the input value.

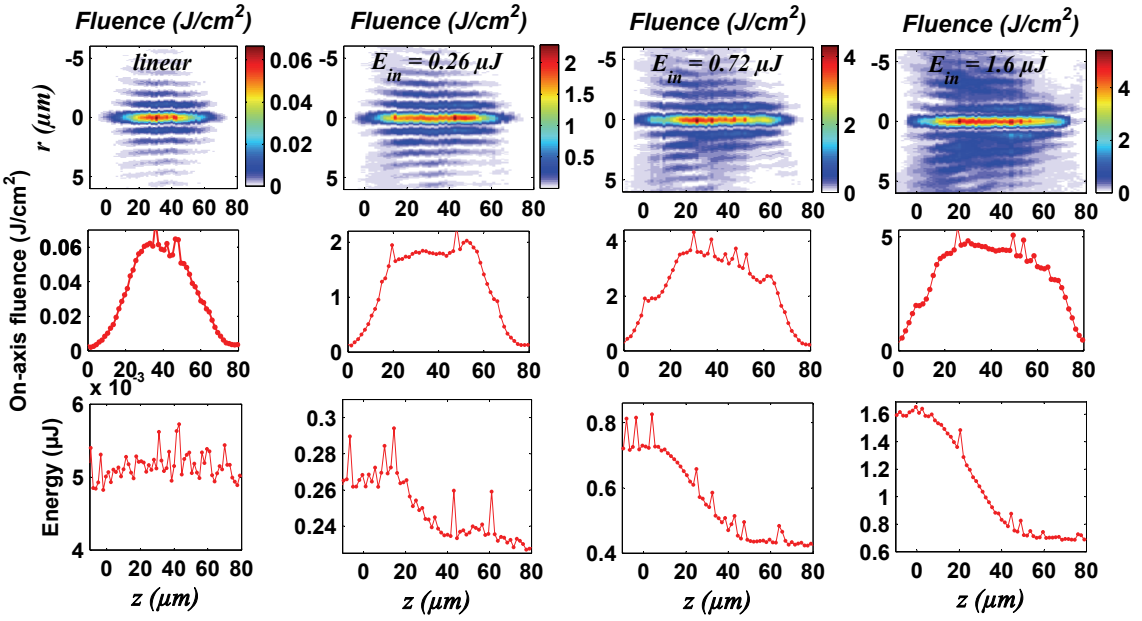

Figure 4.3: Experimental results of the propagation of 130 fs Bessel-Gauss beams in fused silica: (top) evolution of fluence distribution in the transverse and propagation coordinates (middle) the corresponding on-axis fluence ($r = 0$) and (bottom) energy evolution along propagation for different input energies (from left to right columns): 6 nJ (linear regime), 0.26 μJ, 0.72 μJ, 1.6 μJ.

4.2.2/ NUMERICAL RESULTS AND DISCUSSION

4.2.2.1/ FILAMENTATION MODEL AND IMPROVEMENTS

Let us first briefly recall the discrepancies discussed in previous works and discuss the validity of approximations used in the above described model.

Limitation of our filamentation model: We specifically consider previous results of our group reported in Ref. [Courvoisier et al., 2013, Xie et al., 2016] where the propagation of high cone angle Bessel filaments in glass was investigated.

Experimental results showed the formation of propagation-invariant Bessel filaments yielding high aspect-ratio nano-channels. One then can expect that the laser-generated plasma channel is uniform and is confined in the volume area of the central core of the beam. However, numerical results using this model showed strong transverse spreading in space of pulsed Bessel beams which contrasts with experimental observations as one can see from Fig. (4.1,c) (page 114). In addition, although laser-generated plasma reaches a density superior to the critical one $\rho_{cr} \approx 10^{21}\, cm^{-3}$, its density drastically decreases along propagation which indicates inefficient energy deposition [Courvoisier et al., 2013].

To obtain a better consistency with experiments, numerical simulation were performed while neglecting avalanche ionization. However, although the plasma channel is uniform, the maximal plasma density reached is inferior to the critical value by an order of magnitude, which might be insufficient to cause ablation [Bulgakova et al., 2015]. In Ref.

[Garzillo et al., 2016], it was estimated that ablation requires plasma densities superior to ρ_{cr} or even of the order of neutral atom density $\rho_{at} = 2.2\,10^{21}\,cm^{-3}$, but this hypothesis has yet to be verified especially since their numerical results were obtained for an "unphysical" value of the collision time $\tau_c \approx 10 - 15\ as$ [Xie et al., 2016]. We recall that the collision time of dense electronic plasma was experimentally measured and is around 1 fs [Sun et al., 2005].

Validity of approximations involved in the NLSE: We discussed in the first section the different approximations used to derive the nonlinear envelope equation. The first approximation considered is the scalar one where the electric field is assumed to be linearly polarized in the transverse plane of the wavevector direction. It was stated that this approximation is only valid for low cone angles. Hence, since we use a very high cone angle, this approximation may not be valid. The other approximations concern a slowly evolving pulse envelope which states that the phase and group velocity are nearly equal.

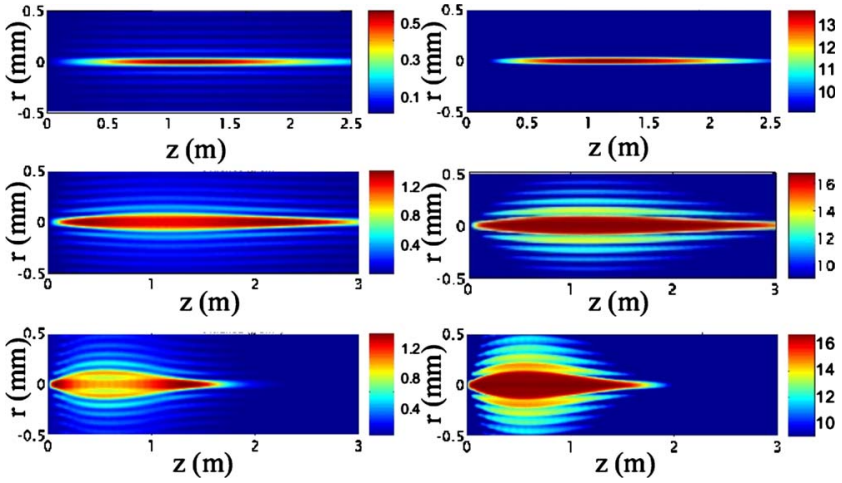

Figure 4.4: Fluence distribution (first column) and plasma channels (second column) generated by Bessel filamentation. The color bar units are in J/cm^2 for the fluence (left-hand column) and in decades $16 \equiv 10^{16}\,cm^{-3}$ for the electron densities (right-hand column). The input Bessel-Gauss pulse has pulse duration of 50 fs and a cone angle $\theta \approx 0.25°$. First line, $E_{in} = 1.44\ mJ$, $w_0 = 10\ mm$; second line, $E_{in} = 14.\ mJ$, $w_0 = 10\ mm$; third line, $E_{in} = 14.4\ mJ$, $w_0 = 5\ mm$. Image taken from Ref. [Polesana et al., 2008].

In Ref. [Polesana et al., 2008], Polesana et al. used a similar filamentation model as the one used by our group. The point of difference lies in the approximations involved in the derivation of the NLSE: while laser-plasma coupling equation are nearly identical, they did not consider the slowly varying envelope approximation. Furthermore, in their numerical simulations, Polesana et al. used Bessel beams with very low cone angles (less than 1°). Hence, the scalar approximation discussed above can be considered to be valid.

In Fig. (4.4), we present some of their numerical results showing the fluence and plasma density distributions of femtosecond low cone angle Bessel-Gauss beams. For a low intensity (low input energy $E_{in} = 1.44\ mJ$ and high beam waist $w_0 = 10\ \mu m$), the plasma density is confined in central core of the beam along propagation distance yielding a uniform plasma channel. However, for higher intensities, the fluence distribution of the

pulse shows that its central core undergoes a spatial expansion accompanied by non-confinement of the pulse-generated plasma density. These results are qualitatively similar to those reported later by our group in Ref. [Courvoisier et al., 2013] as discussed above. Hence, although there are less approximations in the nonlinear envelope equation used by Polesana et al. [Polesana et al., 2008] than in Ref. [Courvoisier et al., 2013], similar features regarding the behavior of plasma density are observed.

We then assume that the observed disagreement between experiment and simulations is mainly due to laser-plasma coupling and not necessarily the nonlinear envelope equation. In this case, we can simply express the propagation equation using the simplest approximation, i.e. the slowly varying envelope approximation, which is the one used in Ref. [Courvoisier et al., 2013].

4.2.2.2/ NUMERICAL MODEL AND PARAMETERS

Based on the above discussion, the filamentation equation we numerically solve is given by:

$$\partial_\xi \mathcal{E} = \frac{i}{2k}\nabla_\perp^2 \hat{\mathcal{E}} - i\frac{k^{(2)}}{2}\frac{\partial^2 \mathcal{E}}{\partial \tau^2} + ik_0 n_2 |\mathcal{I}|^2 \mathcal{E} - \frac{W_{PI}(\mathcal{I})}{2\mathcal{I}} K\hbar\omega_0 \mathcal{E} - \frac{1}{2c\epsilon_0 n}\mathcal{J}_p \tag{4.25}$$

We express the photoionization rate W_{PI} according to Keldysh formulation. Its variation as a function of the intensity is depicted in Fig. (4.5).

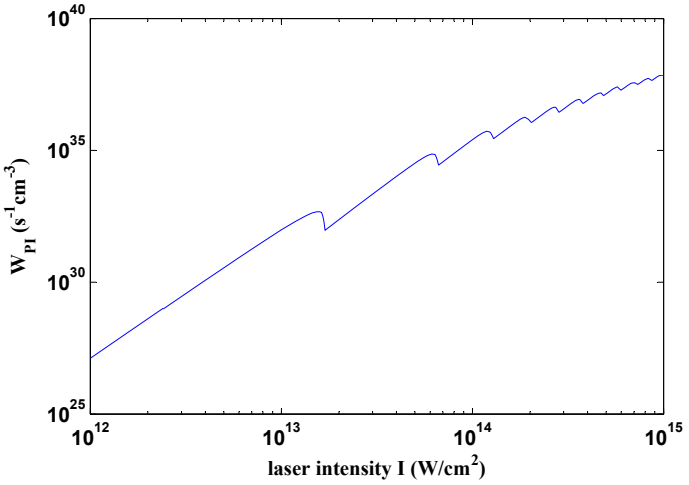

Figure 4.5: Nonlinear ionization rate as a function of optical intensity according to the theory of Keldysh.

We express the time evolution equation of plasma density in its general form as defined by Eq. (4.23): $\partial_t \rho = (W_{PI} + W_{ava}\,\rho)(1 - \rho/\rho_{at}) - \rho/\tau_r$. We will show numerical simulation results considering different models of plasma related terms, namely the current density envelope $\mathcal{J}_p$ and the avalanche ionization term $W_{ava}\rho$. Numerical resolution of these equations is described in Ref. [Couairon et al., 2011, Couairon et al., 2002].

Numerical parameters used in our simulations are presented in table (4.1). The value of the collision time is $\tau_c = 1.28\ fs$ unless otherwise mentioned.

$\lambda\ (\mu m)$	0.8
n	1.453
$n_2\ (m^2/W)$	$2.48\ 10^{-20}$
$\theta\ (^\circ)$(in air)	26
$k^{(2)}\ (fs^2/cm)$	361
$U_i\ (eV)$	7.2
$\tau\ (fs)$	1.28
$w_0\ (\mu m)$	15
$\rho_{at}\ (cm^{-3})$	2.1×10^{22}

Table 4.1: Numerical parameters used in our simulations of 130-fs Bessel beams in fused silica.

In the following, we will compare experimental data with simulation results of the fluence (computed by integrating the pulse intensity over the time coordinate) and the energy (computed by integrating the fluence over the transverse coordinates). We also present results for plasma density as the maximal value reached in the time domain.

4.2.2.3/ RESULTS FOR AN INPUT ENERGY OF 0.26 μJ

We begin our analysis of numerical results with $E_{in} = 0.26\ \mu J$. We use the same expressions of the current density and avalanche ionization as in Ref. [Courvoisier et al., 2013], i.e. $\mathcal{J}_p/n\epsilon_0 c = \sigma(1 + i\omega_0\tau_c)\rho\mathcal{E}$ and $W_{ava} = \sigma\mathcal{I}/U_i$. We show in Fig. (4.6) the evolution of the energy, fluence and plasma density along propagation for two different values of the collision time τ_c. We also compare results with available experimental data.

Our experimental method to image Bessel filaments allows to adjust numerical modeling and parameters to give a better understanding of the physical effects involved in filamentation [Courvoisier et al., 2016a]. For instance, experimental measurements of the collision time at ablation threshold yields a mean value of around 1.28 fs [Sun et al., 2005]. However, in the case of an input energy of 0.26 μJ, we did not observe any ablation traces. Hence, we adjusted the value of τ_c to obtain a better consistency with experiments.

Numerical results for $\tau_c = 4$ fs show a better agreement with experimental data than in case $\tau_c = 1.28$ fs. Firstly, there is a good consistency regarding the energy behavior between experiments and simulation results for $\tau_c = 4$ fs whereas the energy loss is overestimated in the case $\tau_c = 1.28$ fs. Furthermore, simulation of the fluence distribution shows that the pulse undergoes a slight spatial expansion for $\tau_c = 1.28$ fs whereas it preserves its initial spatial size in the case of $\tau_c = 4$ fs. The latter case is more consistent with experimental data although the maximal fluence value is higher than the experimental one by a factor of 1.5 (see Fig. (4.6,b)). Hence, the model used in Ref. [Courvoisier et al., 2013] is sufficient to describe filamentation below ablation.

NB: the low fluence rise in the experimental curve compared to the numerical one is due to spherical aberrations which are neglected in numerical simulations.

Regarding plasma density, its distribution is more localized and confined in space in the case of $\tau_c = 4$ fs. The maximal value reached in both cases is higher than $10^{21}\ cm^{-3}$ but still lower than the critical density $\rho_{cr} = 1.7\ 10^{21}\ cm^{-3}$ over which the plasma becomes opaque. Since no ablation traces are observed, we assume that laser-generated plasma

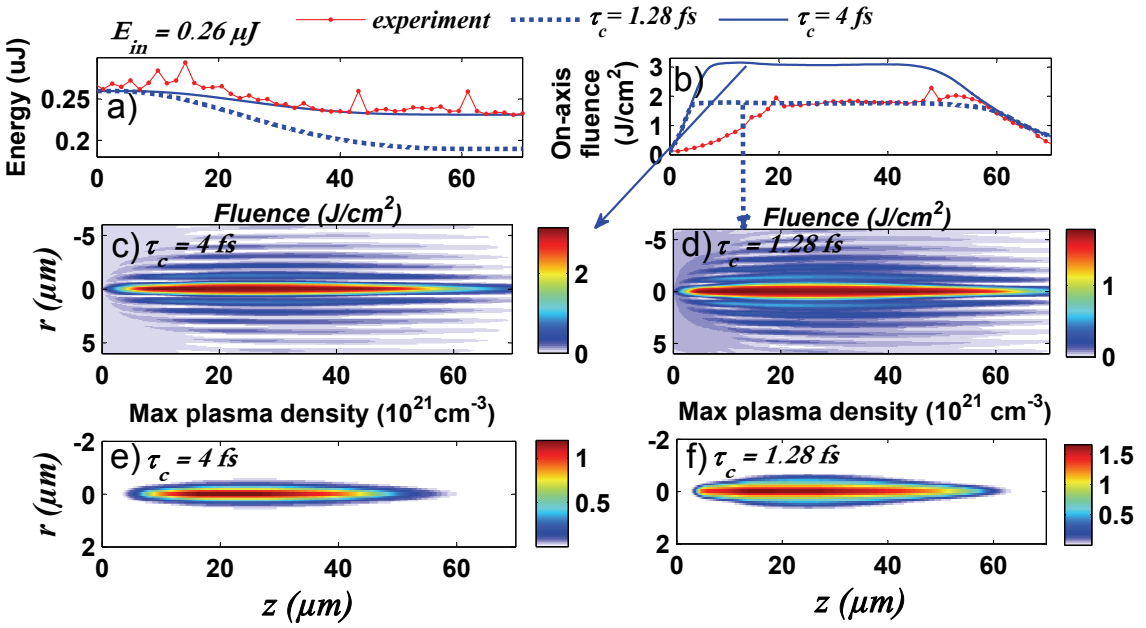

Figure 4.6: Numerical simulation results of Eqs. (4.25), (4.21) and (4.23) where $W_{ava} = \sigma \mathcal{I}/U_i$ for $E_{in} = 0.26\,\mu J$ (a) energy and (b) central core fluence evolution along propagation for (blue dotted line) $\tau_c = 1.28$ fs and (blue solid line) $\tau_c = 4$ fs and (red line) comparison with experiments. (c-d) Fluence map and (e-f) evolution of plasma density in the radial and propagation coordinates corresponding to two values of collision time [i.e. $\tau_c = 4$ fs (c-e) and $\tau_c = 1.28$ fs (d-f)].

densities below the critical value are insufficient to cause ablation in glass as proposed in [Garzillo et al., 2016]. Nevertheless, experimental measurements of plasma density are still required to verify this claim.

4.2.2.4/ RESULTS FOR AN INPUT ENERGY OF 0.72 μJ

For $E_{in} = 0.72\ \mu J$, Bessel filaments induce ablation traces in fused silica. Using the same model and parameters as in the previous section, we observe about the same results as those reported in Ref. [Courvoisier et al., 2013]; as shown in Fig. (4.7), the Bessel pulse undergoes pronounced spatial expansion and the maximal fluence value is much lower than the experimental one. As for plasma density, it increases significantly at low propagation distances to exceed the critical value ρ_{cr}. It then expands in transverse spatial plane and decreases along the pulse propagation. The only observed consistency is related to energy variation along propagation.

Note that although increasing the value of the collision time leads to the stabilization of the fluence distribution, the energy loss and plasma density are underestimated compared to experimental results. Let us now consider improved models of laser-plasma coupling in our numerical simulations. We begin with the plasma current density.

Current density and plasma dispersion: When deriving Drude model in section 4.1.2.3 (page118), we have neglected the term $\mathbf{J}_p \partial_t \rho/\rho$ in the expression of current density (4.17), provided that the ionization rate is small. However, if we assume that

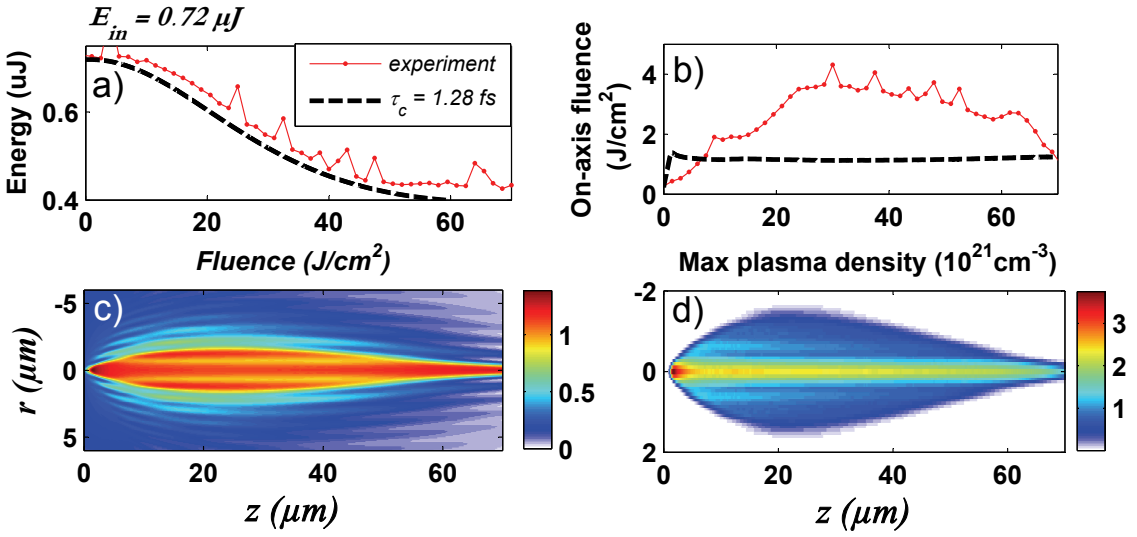

Figure 4.7: Numerical simulation results of Eqs. (4.25), (4.21) and (4.23) for $E_{in} = 0.72\,\mu J$ where $W_{ava} = \sigma \mathcal{I}/U_i$ (a) energy and (b) central core fluence evolution along propagation for (black dashed line) $\tau_c = 1.28$ fs and (red line) comparison with experiments. (c) Fluence map and (d) evolution of plasma density in the radial and propagation coordinates.

over-critical plasma densities can be reached within few tens of fs (i.e. few optical cycles) [Rethfeld, 2004], then this term becomes on the same order of magnitude as the collision frequency $1/\tau_c$. Here, we will correct the propagation equation if this term is not neglected. Equation then (4.16) becomes:

$$\frac{\partial\left(\mathcal{J}_p/\rho\right)}{\partial\tau} = \frac{q^2}{m_e}\mathcal{E} + \frac{\mathcal{J}_p}{\rho}(i\omega_0 - \nu) \tag{4.26}$$

We solve this equation in the spectral domain as in section 4.1.2.3. We obtain:

$$\widehat{\left(\frac{\mathcal{J}_p}{\rho}\right)} = \frac{q^2\tau_c}{m_e(1+\omega_0^2\tau_c^2)}(1+i\omega_0\tau_c)\Big(1 - i(\omega-\omega_0)\frac{\tau_c}{1-i\omega_0\tau_c}\Big)^{-1}\hat{\mathcal{E}} \tag{4.27}$$

It can be expressed in the time domain as:

$$\frac{1}{n\,\epsilon_0 c}\frac{\mathcal{J}_p}{\rho} = \sigma(1+i\omega_0\tau_c)G^{-1}\mathcal{E} \tag{4.28}$$

In Ref. [Gulley et al., 2010], the operator $G^{-1} = (1 + \frac{i}{\omega_0}g\partial_\tau)^{-1}$ is actually applied to the product $\rho\mathcal{E}$ while, in our case, it is only applied to the pulse envelope $\mathcal{E}$. In the general case, one can compute the current density by numerically solving Eq. (4.26) to implicitly consider plasma dispersion.

Considering the corrected expression of the current density (4.27) in our numerical simulations, our results show nearly no difference with the state of the art [Xie et al., 2016] as shown in Fig. (4.7). Actually, even if we numerically compute the current density by solving the corresponding time evolution equation (4.26), we still obtain the same results. This shows that plasma dispersion plays no significant role in our case. This might be due to the fact that avalanche ionization is much more important.

Avalanche ionization model: Rethfeld's model. The model we took earlier ($W_{ava} = \sigma \mathcal{I}/U_i$) to describe avalanche ionization rate is very basic since it is only a two-level system, which does not describe the progressive capture of photons before impact ionization. In Ref. [Rethfeld, 2004], Rethfeld introduced another model to describe the gradual process of energy gain. Rethfeld suggested that free-electrons generated through photoionization are initially at the lowest edge of the conduction band with an energy close to zero $\varepsilon_1 \approx 0$ (Fig. (4.8)). These free-electrons will then gradually absorb single light photons which define discrete energy levels $\varepsilon_l = \varepsilon_1 + l\,\hbar\omega_0$, where l is an integer. Impact ionization occurs when a free-electron absorbs enough energy to surpass a threshold value ε_{crit} corresponding to $p = \left[\frac{\varepsilon_{crit}}{\hbar\omega_0} + 1\right]$ photons, where $[x]$ denotes an integer. ε_{crit} was defined as follows:

$$\varepsilon_{crit} = 1.5\,(U_i + U_{osc}) \tag{4.29}$$

where U_{osc} is the energy of free-electron oscillation in the laser field.

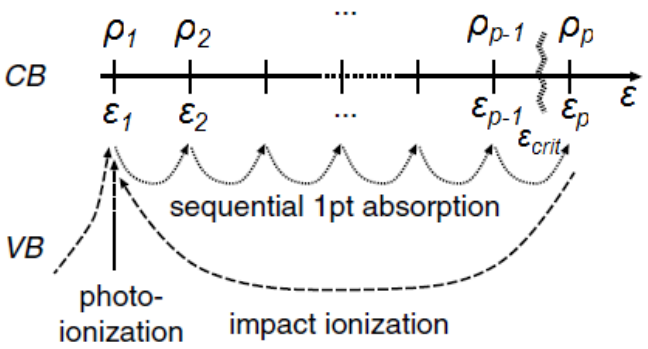

Figure 4.8: Illustration of the processes providing changes in the density and the energy, respectively, of free electrons in the conduction band of a dielectric ([Rethfeld, 2004])

This process was then expressed in the form of multiple rate equations (MRE) as follows:

$$\begin{aligned}
\frac{\partial \rho_1}{\partial t} &= \bar{W}_{PI}\rho_0 + 2\bar{W}_{ava}\rho_p - W_{pl}\rho_1 - \rho_1/\tau_r \\
\frac{\partial \rho_2}{\partial t} &= W_{pl}\rho_1 - W_{pl}\rho_2 - \rho_2/\tau_r \\
&\vdots \\
\frac{\partial \rho_p}{\partial t} &= W_{pl}\rho_{p-1} - \bar{W}_{ava}\rho_p - \rho_p/\tau_r
\end{aligned} \tag{4.30}$$

where W_{pl} is the probability of one-photon absorption and $\bar{W}_{ava}$ denotes avalanche ionization rate. In Ref. [Rethfeld, 2004], it was not expressed as $W_{ava} = \sigma \mathcal{I}/U_i$ (Eq. (4.24)) but was given a fixed value ($\bar{W}_{ava} > 10^{15} s^{-1}$). Adding up these equation yields:

$$\frac{\partial \rho}{\partial t} = \bar{W}\rho_0 + \bar{W}_{ava}\rho_p - \rho/\tau_r \tag{4.31}$$

where $\rho = \sum_l^p \rho_l$ and $\rho_0 = \rho_{at} - \rho$. This equation is only different from that of Eq. (4.23) (page 119) in terms of the quantity ρ_p: while Eq. (4.23) assumes that all free-electrons

can simultaneously trigger avalanche ionization, Eq. (4.31) states that only a fraction of free-electrons (ρ_p instead of ρ) is involved in this process.

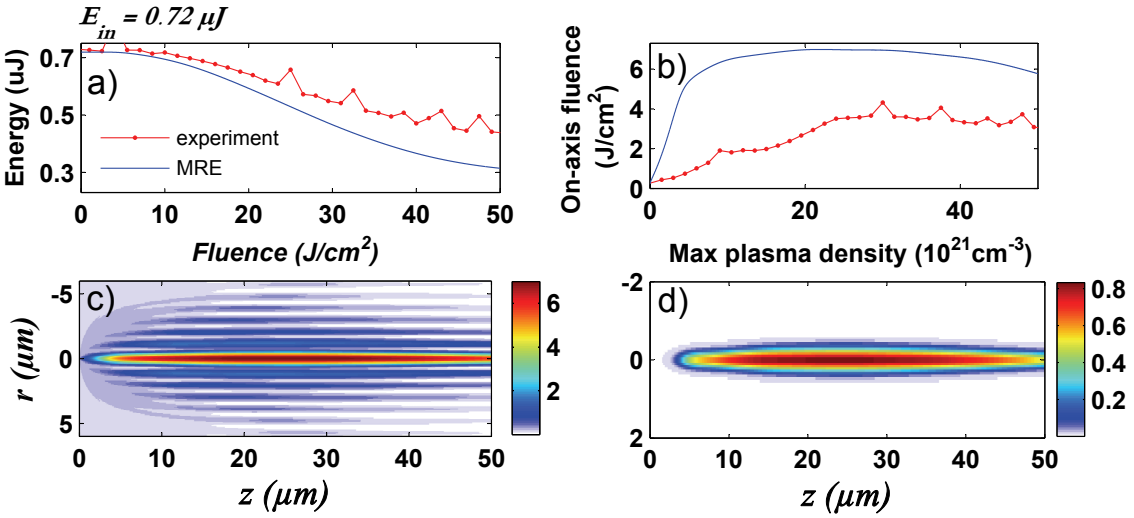

Figure 4.9: Numerical simulation results of Eqs. (4.25), (4.21) and (4.30) for $E_{in} = 0.72$ μJ (a) energy and (b) central core fluence evolution along propagation for (solid line) $\tau_c = 1.28$ fs and (red line) comparison with experiments. (c) Fluence map and (d) evolution of plasma density in the radial and propagation coordinates.

Numerical simulation results considering this avalanche ionization model are shown in Fig. (4.9). We used fourth order Runge-Kutta to solve each of the $p = \left[\frac{\varepsilon_{crit}}{\hbar\omega_0} + 1\right]$ rate equations. The evolution of the pulse fluence along propagation shows a propagation-invariant feature as it is the case in experiments, whereas the peak fluence is overestimated. However, it is clear that the energy loss is overestimated compared to experimental data. Despite this, the maximal plasma density is one order of magnitude lower than that of the critical density $\rho_{cr} = 1.7\,10^{21}\,cm^{-3}$. This result is similar to that obtained in Ref. [Courvoisier et al., 2013] where avalanche ionization is neglected. This suggests that avalanche ionization is probably underestimated in this model.

Avalanche ionization using a Maxwellian distribution: We have tested another model for avalanche from the literature. In fact, this ionization process is originally modeled using Keldysh formulation [Chimier et al., 2011]. For a particular energy distribution of free-electrons $f_e(\varepsilon)$, avalanche ionization rate is written as:

$$W_{ava}(\varepsilon) = \int_0^{+\infty} \alpha_{ava}(\varepsilon) f_e(\varepsilon) \mathrm{d}\varepsilon \tag{4.32}$$

$$\text{with } \alpha_{ava}(\varepsilon) = \begin{cases} \alpha_0(\varepsilon/\varepsilon_{crit} - 1)^2, & \varepsilon > \varepsilon_{crit} \\ 0, & \text{otherwise} \end{cases} \tag{4.33}$$

where α_{ava} is the impact probability of a free-electron of energy ε to collide with a bound electron. Equation (4.33) shows that this probability only has non-zero values in case

the free-electron energy is superior a critical value ε_{crit}. In case the masses of free-electrons and holes are considered equal, the expression of ε_{crit} is defined by Eq. (4.29). α_0 is a rate constant that is related to the material and can be empirically evaluated [Penano et al., 2005]. For fused silica, it is 1.5 fs^{-1}.

The resolution of Eq. (4.32) is very complicated since one needs to solve the kinetic equation related to the energy distribution function $f_e(\varepsilon)$ [Stuart et al., 1995, Stuart et al., 1996]. Chimier et al. proposed to describe the distribution function f_e using Fermi distribution [Chimier et al., 2011]. In this case, this equation is coupled to other equations to determine other quantities such electron temperature and electron heating capacity. Considering the fact that all these equations should be coupled to the nonlinear propagation equation, then the resolution of the overall filamentation model becomes more difficult and time consuming.

In this regard, even though the distribution function f_e is non-Maxwellian [Stuart et al., 1995, Stuart et al., 1996], some authors have proposed to use the Maxwellian distribution to simplify the resolution of Eq. (4.32) and include it in filamentation models [Penano et al., 2005, Hallo et al., 2007]. In this case, the avalanche ionization rate is written as:

$$\begin{aligned} W_{ava}(\gamma) =& \alpha_0(15/4\gamma^2 - 3\,\gamma + 1)\,\mathrm{erfc}(\sqrt{1/\gamma}) \\ &+ \frac{\alpha_0}{\sqrt{\pi}}\exp(-1/\gamma)(7.5\gamma^{3/2} - \gamma^{1/2}) \end{aligned} \tag{4.34}$$

where $erfc(x) = 1 - (2/\sqrt{\pi})\int_0^x \exp(-t^2)\mathrm{d}t$ stands for the complementary error function, $\gamma = \varepsilon/\varepsilon_{th}$ and ε_{th} is the electron thermal energy. The latter can be determined using the following equation:

$$\frac{\partial(\rho\,\varepsilon_{th})}{\partial t} = J\,E - 2U_i\,W_{ava}\,\rho \tag{4.35}$$

It states that free-electrons gain energy through Joule heating ($J\,E$) and lose energy because of avalanche ionization ($2U_i\,W_{ava}\,\rho$). Note that, in this model, the electron collision frequency $\nu_c = 1/\tau_c$ is varying in time and is defined as the sum of the electron-neutral ν_{en} and electron-ion ν_{ei} collision frequencies which are expressed in s^{-1} as: $\nu_{en} = 2\,10^{-7}(\rho_a t - \rho)(cm^{-3})T_e(eV)$ and $\nu_{ei} = 2.91\,10^{-6}\rho(cm^{-3})\Lambda T_e^{-3/2}(eV)$ where Λ is Couloub logarithm and was given values higher than 2 [Penano et al., 2005].

In our simulations, we expressed the quantities J and E as $J = \mathcal{J}\cos(\omega_0\tau)$ and $E = \mathcal{E}\cos(\omega_0\tau)$ respectively. The current density envelope is computed by solving the corresponding time evolution equation (4.26).

Figure (4.10) shows numerical results using this avalanche ionization model: we still observe the good agreement between the experimental and numerical curves of energy evolution along propagation. Although plasma density reaches a value superior to the critical value, the fluence distribution exhibits significant spatial expansion which is in opposition to experimental results.

Toy-model for avalanche: we suggested a possible correction of the plasma density evolution equation (4.23) following the idea that not all free electrons can contribute to

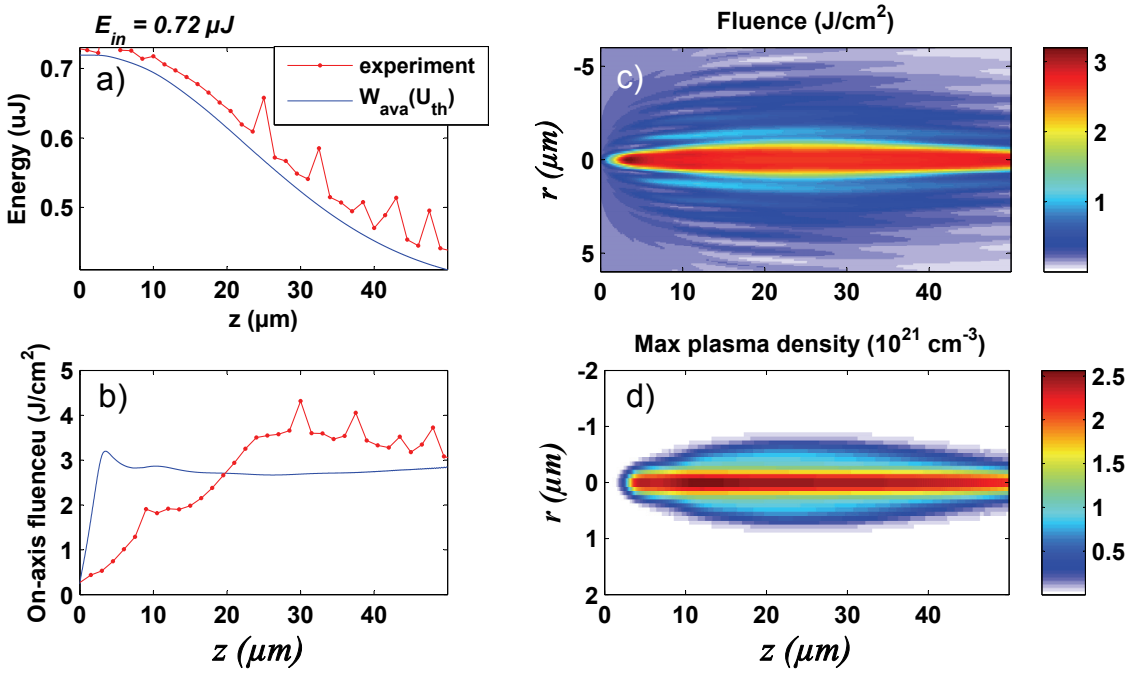

Figure 4.10: Numerical simulation results of Penano's model [Penano et al., 2005] using Eqs. (4.25) and (4.34) (4.35). Additional parameters can be found in the same reference. (blue solid line): (a) Energy and (b) central core fluence evolution along propagation and (red line) comparison with experiments. (c) Fluence map (d) Evolution of plasma density in the radial and propagation coordinates.

avalanche ionization. Considering an intensity-dependent avalanche ionization rate, we write Eq. (4.23) in the same form as (4.31):

$$\frac{\partial \rho}{\partial t} = [W_{PI} + \sigma \mathcal{I}/U_i(\eta\rho)]\,(1-\rho/\rho_{at}) - \rho/\tau_r \tag{4.36}$$

where $\eta = \rho_p/\rho$ is assumed to be an arbitrary constant parameter. Hence, in our simulations, we consider that only a fixed fraction of the total plasma density participates in avalanche ionization. We show in Fig. (4.11) our numerical results for two values of η, namely 0.1 and 0.2:

With regard to total energy loss, there is a very good consistency between experimental and numerical curves as it is the case in Fig. (4.7). We assume that since both plasma and nonlinear absorption contribute to nonlinear losses, then if one energy absorption process decreases in efficiency, the efficiency of other process will increase and vice versa.

In addition, the fluence distribution is more consistent with experiments and specifically for $\eta = 0.1$. The distribution of plasma density can also be seen to be in agreement with experiment since it does not significantly expand in the transverse direction. Although the maximal plasma density does not exceed the critical value, it is still unclear if this density is enough to trigger the formation of a void channel as discussed above.

Finally, we note that even though this toy model works well for $E_{in} = 0.72\ \mu J$, the results of $E_{in} = 1.6\ \mu J$ could not be reproduced. This shows that some of the approximations

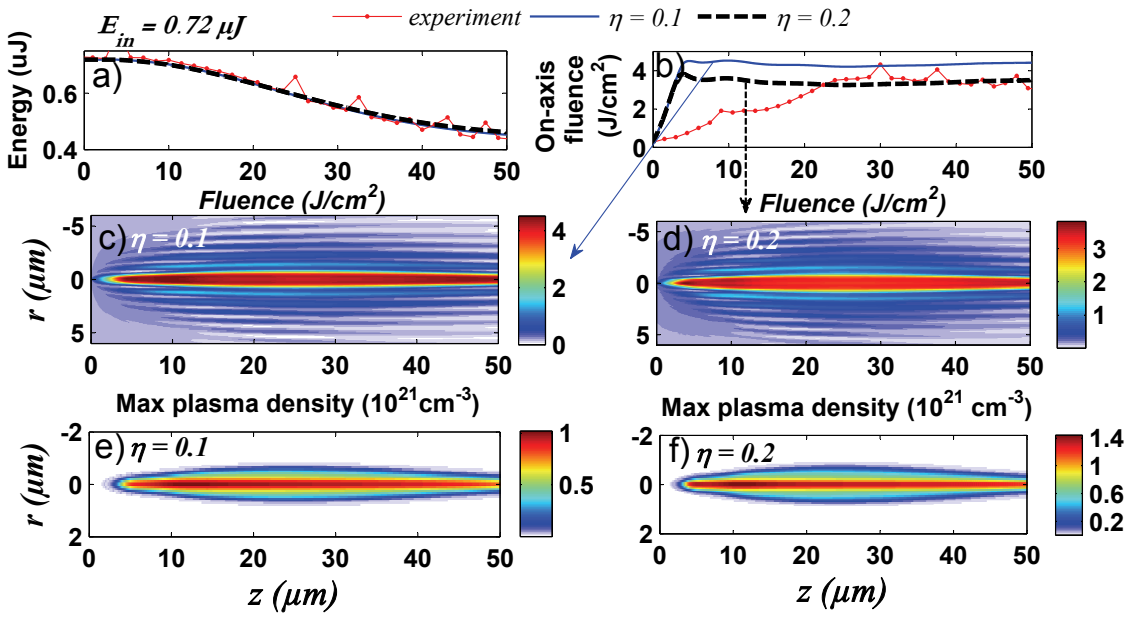

Figure 4.11: Numerical simulation results of Eqs. (4.25) and (4.36) (a) energy and (b) central core fluence evolution along propagation for (blue solid line) $\eta = 0.1$ and (black dashed line) $\eta = 0.2$ and (red line) comparison with experiments. (c-d) Fluence map and (e-f) evolution of plasma density in the radial and propagation coordinates corresponding to two values of collision time [i.e. $\eta = 0.1$ (c-e) and $\eta = 0.2$ (d-f)]

involved in these models are not valid or that there are other physical effects that are not accounted for.

4.3/ CONCLUSIONS

In this chapter, we investigated filamentation of femtosecond Bessel beams of high cone angle in fused silica. Experimental results showcase the formation of propagation-invariant Bessel filaments leading to the generation of high aspect-ratio nano-channels. These observations suggest an efficient energy deposition along the propagation distance and that laser-generated plasma channels are uniform and confined in the volume of the central lobe of Bessel beams.

We studied Bessel filamentation using numerical simulations based on nonlinear Schrödinger equation (NLSE) for pulse propagation and Drude model for laser-plasma coupling. Numerical results obtained before this thesis showed a pronounced spatial expansion of the central lobe of Bessel filaments which is accompanied by non-uniform plasma channels. To investigate the discrepancy between experiments and simulations, we investigated the different approximations used to develop this model.

In the NLSE, we considered plasma dispersion effect in the expression of the current density. Nevertheless, numerical results show the same discrepancies. We obtained better consistency with experiments by correcting avalanche ionization. We firstly considered Rethfield's multiple rate equation model which, in principle, better describes the dynamics of avalanche ionization

We also considered another avalanche ionization model from the literature where the energy distribution of free-electrons is assumed to be Maxwellian. Simulations showed that although the maximal plasma density remains superior to the critical value along propagation, the central core of the beam undergoes a transverse spatial expansion which contrasts with experiments.

Finally, we proposed a toy-model considering that only a fixed fraction of the free-electron plasma density contributes to avalanche. Our simulations can be considered to be in agreement with experiments. However, the maximal density of the laser-generated plasma remains inferior to the critical density, which might be insufficient to cause ablation. Moreover, inconsistencies are observed if the input energy is further increased. The models considered in this thesis are then insufficient to describe Bessel filamentation. In this regard, additional experiments and more appropriate physical modeling are required to explain the exceptional characteristics of ablation with a Bessel pulses.

CONCLUSION AND PERSPECTIVES

This thesis was dedicated to the study of arbitrary on-axis intensity shaping of Bessel beams and its application in controlling Kerr-induced nonlinear instabilities and laser-generated plasma.

We developed, in a first step, an experimental technique to arbitrarily shape the on-axis intensity of Bessel beams. This approach requires the shaping of both the spatial amplitude and phase of an incident beam. We used a technique that enables exact encryption of the amplitude and phase of the target Bessel beam on a phase-only spatial light modulator (SLM). Beam shaping is performed from direct-space and thus ensures a much higher energy throughput than Fourier-space shaping. We numerically studied physically realizable target on-axis intensity profiles depending on physical limitations imposed by laser wavelength and numerical aperture of experimental setup. We showed that these limitations can be expressed as a convolution product of the target intensity profile and a sinc-shaped function which may yield undesired on-axis intensity oscillations.

We presented our experimental results for two different target on-axis intensity profiles. Our results showed a very good agreement between simulation and experiment which validate our chosen experimental approach. We also discussed the energy throughput of our technique. Our measurements showed that it is typically around 10 % and that it depends largely on the transverse size of the target beam. We also discussed the possibility to improve the energy throughput by means of intensity shaping of the incident laser field.

In the second part of this thesis, we analytically and numerically discussed Kerr-induced nonlinear instabilities and their control using on-axis intensity shaping of Bessel beams. Kerr-induced instabilities refer to the modulation of central core intensity of Bessel beams along propagation. This modulation was interpreted as the interference of the input Bessel beam with new spectral components (axial wave and outer ring) resulting from four wave mixing (FWM) interactions. In our work, we further investigated the underlying features of these instabilities by means of our model (reduced FWM model) in addition to the theory of Gadonas et al. [Gadonas et al., 2001]. We showed that nonlinear spectral distortions go through two stages: a Bessel beam first undergoes self-phase modulation (SPM) leading to an initial expansion of its spatial spectrum and the generation of an axial wave "seed". The second stage lies in the amplification of the axial wave seed and outer ring generation as a result of cross-phase modulation (XPM) and parametric amplification respectively. Our results then show that the control of nonlinear instabilities resides either in the initial spectral broadening or ensuing FWM processes.

We interpreted previous results on the control of nonlinear instabilities in Bessel beams depending on whether they are formed progressively inside or prior entering nonlinear media (smooth and abrupt transition). We showed that the input phase profile determines the SPM-induced broadening in the first stage.

We then introduced our approach to control nonlinear instabilities using shaped-intensity profiles. Our numerical simulations show that these instabilities are effectively reduced if the initial intensity rise of Bessel beams is slowly established. Our interpretation of results is also based on input spectral phase profile as in the case of smooth and abrupt transitions. We showed that our results are also valid in the filamentation regime. Specifically, reduced Kerr-nonlinearity in shaped Bessel beams allows generating plasma channels that are more uniform compared to those generated by conventional pulsed Bessel-Gauss beams.

In the last chapter, we investigated the validity of filamentation modeling of femtosecond Bessel beams in glass at ablation-level intensities. Experimental results highlight the formation of propagation-invariant Bessel filaments leading to the generation of high aspect-ratio nano-channels. Numerical results obtained using extended nonlinear Schrödinger equation and Drude model showed a pronounced spatial expansion of the central lobe of Bessel filaments which is accompanied by non-uniform plasma channels. We reconsidered the different approximations used to develop this model in order to investigate the observed disagreement between experiments and simulations.

Our work showed that only by correcting avalanche ionization one can obtain a better consistency with experiments. We suggested a toy-model considering that only a fixed fraction of free electron plasma density contributes to avalanche. Our simulations could be somehow in agreement with experiments. However, the maximal density of the laser-generated plasma remains inferior to the critical density, which might be insufficient to cause ablation. We concluded that the models considered in this thesis are insufficient to describe Bessel filamentation. In this regard, additional experiments and physical modeling are required to explain the exceptional characteristics of ablation with Bessel pulses.

At the conclusion of my thesis, we conceive three axis of potential research. The first concerns direct applications of on-axis intensity shaping of Bessel beams in high power laser applications. Our technique allows to generate a superposition of Bessel beams of different cone angles and with controllable on-axis intensity profiles. This approach can be easily extended to Bessel vortices.

Regarding our reduced FWM model, we have, so far, neglected temporal contribution. We think it would be interesting to generalize our model to time domain as to investigate the impact of on-axis intensity shaping on temporal spectral broadening, anti-Stokes generation [Dubietis et al., 2007] and other related nonlinear phenomena. Another possible axis of research concerns Plasma-induced instabilities in gases as reported in [Cooley et al., 2006].

Finally, we believe that the control of filamentation by initial shaping will provide interesting new pathways for the applications of filamentation and plasma generation: in ultrafast-laser matter interaction studies, laser materials processing, secondary sources such as THz generation.

LIST OF FIGURES

1.1 Transverse spatial distribution of Bessel beam in (left) near and (right) far fields. 7

1.2 Transverse intensity distribution of a Bessel beam (solid line) and Gaussian beam (dashed line) whose width is equal to that of the Bessel central core. (right) On-axis intensity evolution of (solid line) an apertured Bessel beam and (dashed line) a Gaussian beam. [From Ref. [Durnin, 1987]]. 7

1.3 Geometrical estimation of the Bessel zone. [After Ref. [Durnin, 1987]]. . . . 8

1.4 Self-reconstruction property of Bessel beams. [From Ref. [McGloin et al., 2005]] 9

1.5 Experimental scheme for Direct-space Bessel beam generation using phase-only modulation. 11

1.6 Experimental scheme for Fourier-space Bessel beam generation using amplitude-only modulation. 11

1.7 Bessel beam generator based on a annular aperture placed at the object focal plane of a lens. [From Ref. [Durnin et al., 1989]] 12

1.8 Bessel beam generation using an axicon. 13

1.9 Example of a binary-amplitude hologram for Bessel beam generation (left) without and (right) with carrier frequency. [from Ref. [Vasara et al., 1989]] . 14

1.10 Experimental setup for femtosecond Bessel beam generation from direct-space using a phase-only SLM. Image taken from Ref. [Froehly et al., 2014]. 15

1.11 Group velocity of a Bessel pulse for two types of Bessel beam generators: a) refractive and b) diffractive axicon. Image taken from [Klewitz et al., 1998]. 17

1.12 (left) Simulation of Bessel beam propagation in a thick medium as reported in [Fahrbach et al., 2010] and (right) comparison depth imaging performance of Gaussian and Bessel beams. Images taken from [Fahrbach et al., 2010]. 18

1.13 Setup for manipulation of particles placed in two different cells separated by a distance of 3 mm. Image taken from Ref. [Garces-Chavez et al., 2002]. 18

1.14 (a) A photograph of the self-guided filament in fused silica at input energy of 2 μJ. (b) Measured diameter of the filament along its propagation compared to that measured in linear propagation regime at low input energy (50 nJ). Figures taken from Ref. [Tzortzakis et al., 2001]. 20

1.15 Illustration of Kerr effect which acts as a focusing lens. Image taken from Ref. [Couairon et al., 2007]. 20

1.16 Ionization rate for fused silica with gap U_i =9 eV computed with Keldysh's formulation for multiphoton ionization ($\gamma \gg 1$, dotted curve) and tunnel ionization ($\gamma \ll 1$, dash-dotted curve) and from the general formula valid in the intermediate regime (solid line). The multiphoton rate is shown by the dashed line. Figure taken from Ref. [Couairon et al., 2005]. 21

1.17 Illustration of multiphoton (left) and tunnel (right) ionizations. E_{1ph} refers to the energy of a single photon. [After Ref.[Couairon et al., 2007]]. 22

1.18 Illustration of avalanche ionization. Image taken from Ref. [Vogel et al., 2005]. 22

1.19 Illustration of plasma defocusing effect. Image taken from Ref. [Couairon et al., 2007]. 23

1.20 Illustration of filament formation according to a cycle of nonlinear focusing and defocusing effects. Image taken from Ref. [Couairon et al., 2007]. . . . 24

1.21 (left) Evolution of the central core intensity along propagation in the linear (1) and nonlinear regimes (2-4) where nonlinearity is increased from (2) to (4). (right) Experimental observation of spatial spectrum of Bessel beam transmitted through a benzene cell in the nonlinear regime. Images taken from Ref. [Gadonas et al., 2001]. 26

1.22 Numerical results: radial compression of Bessel beams in a Kerr medium for increased peak amplitude. Image taken from [Johannisson et al., 2003]. 27

1.23 Magnification of the fluence profile (logarithmic scale of normalized units) of the reshaped Bessel beam (BB) (solid line) after the nonlinear propagation through a 5-mm-long fused silica sample, compared with the linearly propagated Bessel beam (dotted line) through the same sample. Image taken from Ref. [Polesana et al., 2006]. 28

1.24 Simulation results of the filamentation of two Bessel beam beams with different cone angles: Fluence distribution along propagation for (left) $\theta = 0.15°$ and (right) $\theta = 0.05°$. Image taken from [Polesana et al., 2008]. . . 29

1.25 Shadowgrams of channels formed in argon for different pressures: (a) 200 torr, (b) 280 torr, (c) 300 torr, (d) 340 torr, (e) 370 torr, and (f) 420 torr. Laser pulse: 100 ps FWHM, $\lambda = 1064$ nm, and peak intensity 5×10^{13} W/cm^2; and axicon base angle $25°$. Image taken from Ref. [Cooley et al., 2006]. 30

1.26 Calculation of 30 torr Argon time response to a 100 ps laser pulse with a peak intensity of 400 TW/cm^2, a spot size of 10 μm and a wavelength of 1.064 μm. The rapid rise in electron density at early times was seen to be due to direct ionization by the laser. The pulse, Gaussian in time, peaks at 0.125 ns. Image taken from Ref. [Durfee et al., 1993]. 31

1.27 Experimental setup for guiding laser pulses using laser-generated plasma channel using (a) a lens and (b) using an axicon. (c) Fluorescence images from sparks generated by Gaussian pulses in Argon for different delays and (d) fluorescence images of (top) Bessel-induced spark and (bottom) the scattered light of the second pulse at a delay of 15 ns at the channel entrance and exit. Images taken from [Durfee et al., 1993]. 32

1.28 Guiding of electric discharge using laser sparks generated by a) a pulsed Gaussian beam and b) a Bessel pulse. Image taken from Ref. [Clerici et al., 2015]. 32

1.29 Transverse intensity distribution of THz radiations generated by (left) Bessel beam and (right) Gaussian beam [Akhmedzhanov et al., 2009]. . . . 33

1.30 Timescale of the physical phenomena associated with the interaction of laser pulses with transparent materials. The green bars represent typical timescales for the relevant process. Image taken from Ref. [Gattass et al., 2008]. 34

1.31 Impact of increased spherical aberrations in elongating laser induced-channels [Ahmed et al., 2014]. 35

1.32 (top) SEM image of a nanochannel drilled by a single-shot femtosecond Bessel beam [Bhuyan et al., 2010] and (bottom) Sequence of glass drilling using Bessel beams [Courvoisier et al., 2016b]. 36

2.1 (left) phase-only hologram for arbitrary on-axis intensity shaping and (right) comparison between numerical and experimental results of the generation of a Bessel beam with constant on-axis intensity profile. Images taken from [Čižmár et al., 2009]. 43

2.2 Numerical and experimental data of a Bessel beam whose intensity profile is made of three separate flat-top shapes (a) 3D intensity map and (b) the corresponding on-axis intensity profiles. Images taken from [Vieira et al., 2014]. 44

2.3 Experimental setup for amplitude and phase shaping using an amplitude-only hologram. Exp: beam expander, Pol: polarizer, Anl: analyzer and CA: circular aperture mask. Figure is taken from [Vieira et al., 2014]. 44

2.4 Principle of amplitude and phase beam shaping using a single phase-only hologram. Images taken from Ref. [Davis et al., 1999] 45

2.5 Experimental setup using LCOS-SLM . A_{inc} is the amplitude of the incident laser beam, $U_{SLM}(m,n)$ is the beam spatial envelope reflected on the SLM, $S(k_r, z=0)$ is the spatial spectrum and $U_{ret}(r, z=0)$ is the retrieved Bessel beam envelope (b) Example of the phase mask applied on the SLM; (c) Experimentally measured Bessel beam intensity distribution. 46

2.6 Qualitative comparison of the method of Davis et al. [Davis et al., 1999] and that of Bolduc et al. [Bolduc et al., 2013]. The target intensity profile purposely has small features to accentuate the difference between the two methods. The experimentally recorded images are taken in the far-field of a HOLOEYE SLM. Image taken from [Bolduc et al., 2013]. 48

2.7 Comparison of the spatial spectra for two flat-top on-axis intensity profiles with and without parabolic ramps. The two truncations of the spectrum at $k_z = k$ and $k_z = k_z^{min}$ are specifically shown. The spectrum is expressed in the image plane of the SLM ($\theta = 13°$). (bottom) Retrieved on-axis intensity for the target intensity profile (b) without and (c) with parabolic variations (with typical variation length of about $\Delta H = 33\ \mu m$ for our experimental conditions). 54

2.8 (left) Modulus of the spatial spectrum retrieved for the target on-axis intensity profile I_{cst} defined Eq. (2.30) and (right) the corresponding input spatial amplitude for (dashed dotted line) cone angle $\theta = 6.1°$ and $w_b = 75\ \mu m$ and (dotted black line) cone angle $\theta = 13°$ and $w_b = 26\ \mu m$. 55

2.9 Image of the incident beam intensity at the SLM plane, (b) phase mask corresponding to a uniform light illumination ($A_{inc} = 1$) and (c) phase mask corresponding to the incident laser beam. 58

2.10 Computation of the field distribution at the common focal plane of the lens and microscope objective (see setup of Fig. (2.5), page 45) of our 4f system (a) before and (b) after spatial filtering and centering. Reconstruction of the optical field distribution in the image space at (c) $z = 0\ \mu m$ and (d) $z = 60\ \mu m$. the subscripts "f" and "4f" added to the transverse coordinates (x_f, y_f and x_{4f}, y_{4f}) refer to the Fourier plane and image plane of the 4f system respectively 58

2.11 Comparison of (green line) target on-axis intensity profile with the one retrieved in case (blue dashed line) the Bessel beam is computed directly from the target on-axis intensity [ideally retrieved] and (dotted red line) in case it is generated by the SLM. 59

2.12 Comparison between the target on-axis intensity profile of a modified Bessel beam with flat on-axis intensity and the ones retrieved using (triangles) the approximation proposed in Ref. [Bolduc et al., 2013] and (circles) our implementation of this method [Ouadghiri-Idrissi et al., 2016]. 60

2.13 Numerical and experimental data of the intensity distribution along the propagation axis of Bessel beams with (left) uniform and (right) uniformly growing on-axis intensity profiles. 61

3.1 Numerical simulation results of Ref. [Polesana et al., 2008] comparing the on-axis fluence of a pulsed Bessel beam in the case of smooth (solid line) and abrupt (dotted line) intensity transitions. The abrupt intensity transition is considered at the interface between air (linear medium) and water (nonlinear medium) at the point $z = 2$ cm. 64

3.2 Comparison between (right) Fig. (2) of Ref. [Gadonas et al., 1999] and (left) our numerical computation of Eq. 3.23. The parameters β_3 and β_4 are denoted p and q in Ref. [Gadonas et al., 1999]. 71

3.3 Comparison between the variation of $J_0(\nu)$, defined by the Matlab function "*besselj*(0,ν)", with its approximate expression given by Eq. 3.24 where $\nu_0 = 1.1$. 72

3.4 (blue line) Analytical and (red dotted line) numerical computation of the TPM integral given by Eq. 3.25. 74

3.5 Figure (2) of Ref. [Gadonas et al., 2001]: Results of the numerical computation of the TPM integral written as: $I_{TPM} = \int_0^{+\infty} \exp(-2\nu^2/g^2) J_0^2(\nu)\ J_0(\beta_3\,\nu)\, J_0(\beta_4\,\nu)\,\nu\,\mathrm{d}\nu$. The parameters β_3 and β_4 are denoted p and q in Ref. [Gadonas et al., 2001]. 75

3.6 Input conditions for numerical simulations reported in (left) Ref. [Polesana et al., 2008] and (right) Ref. [Gadonas et al., 2001]. 76

3.7 NLSE simulation results: (a) intensity distribution of a Bessel–Gauss (BG) beam propagating in a pure nonlinear Kerr medium ($n_2 = 2.4810^{-16}$ cm^2/W), as a function of the radial and propagation distances r and z, (b) the corresponding on-axis intensity, (c) the spatial spectrum distribution $|S(k_{rj}|^2/|S(k_{r0}|^2|$ along the propagation distance (logarithmic scale dB) and (d) the on-axis spectral intensity of the axial wave (solid line) and outer ring in linear scale (dashed line). The intensity of both spectral components are normalized to the maximal intensity value of the central frequency. 78

3.8 Numerical computation of the TPM integral in the case of the first approximation according to Eq. (3.8, (solid line) and $\tan(\theta_4)\, I^{1st}_{TPM}$ (dashed line). These two quantities are normalized to their specific maximal value. 80

3.9 Evolution of angularly-resolved intensity (dB) of the idler wave along propagation in case (a-b) the idler wave is generated by SPM only (first approximation: $\beta_1 = \beta_2 = \beta_3 = 1$, i.e. the input spatial spectra of the pump and signal waves are defined by Eq. (3.41)) and (c-d) the idler wave is resulted from both SPM and other FWM interactions [second approximation: i.e. the spatial spectrum of pump wave is defined by Eq. (3.41) while that of the signal wave is written by Eq. (3.46), i.e. $\tilde{S}_3(\beta_3) = \delta(\beta_3 - 1) + \delta(\beta_3 - 0.01)$]. 81

3.10 Illustration of FWM interactions of the second approximation, described by Eq. (3.39) satisfying the corresponding LPM conditions. 83

3.11 Same as Fig. (3.7,d): NLSE simulation results showing the evolution of the axial wave and outer ring along propagation. 85

3.12 (a) On-axis intensity distribution of a Bessel–Gauss beam propagating in a pure nonlinear Kerr medium ($n_2 = 2.4810^{-16}$ cm^2/W) for the smooth (solid line) and abrupt (dotted line); (b-c) the corresponding spatial spectra evolution along the propagation distance (logarithmic scale dB) for both cases respectively and (d-e) the intensity evolution of the corresponding axial wave (black solid line) and outer ring (dashed line) along propagation (spectral intensities are normalized to pump's maximal value). Note that the intensity of newly-generated spectral components in the case of abrupt transition is two order of magnitude higher than the one reached in case of smooth transition. 90

3.13 Comparison between the input phase distributions (at $z = 0$) of a BG beam at different positions with respect to the nonlinear medium: (red dashed line) smooth and (red dotted line) abrupt intensity transitions. 91

3.14 NLSE simulation results: Comparison of the spectral intensity and phase distributions in the spectral range of the pump at different propagation points in case of smooth and abrupt intensity transition. Note that the spectral intensity distribution is the same at the transition point between the linear and nonlinear media in both cases. 92

3.15 Numerical results using our FWM model: Angularly resolved intensity (dB) of the idler wave resulting from the interaction of three waves composed each of three frequencies: $\beta_j = 0.995,\ 1,\ 1.005$ (with j=1,2,3 referring to two pump and signal waves respectively) in case of (a) a varying and (b) flat phase distribution (smooth and abrupt transitions respectively). The input spectral phases related to these frequencies are taken from Fig. (3.13). (c) The corresponding evolution along propagation of the axial wave spectral intensity ($\beta_4 \approx 0$) in linear scale. 94

3.16 Numerical results using our FWM model: Angularly resolved intensity (dB) of the idler wave resulting from the interaction of three waves composed each of five frequencies: $\beta_j = 0.96,\ 0.98,\ 1,\ 1.02,\ ,1.04$ (with j=1,2,3) referring to two pump and signal waves respectively) in case of (a) a varying and (b) flat phase distribution (smooth and abrupt transitions respectively). The input spectral phases related to these frequencies are taken from Fig. (3.13). (c) The corresponding evolution along propagation of the axial wave spectral intensity ($\beta_4 \approx 0$) in linear scale. 96

3.17 NLSE simulation results: Spectral phase distribution at a propagation distance $z = 2190\ \mu m$ in case of abrupt intensity transition. This propagation point is 30 μm away from the transition point between the linear and and nonlinear medium. This spectral phase profile is compared to the one obtained in the smooth intensity transition at the points $z = 0$ and $z = 2190$ μm. 99

3.18 Simulation of the nonlinear propagation of three Bessel beams with different (a) target on-axis intensity profiles. Evolution of their respective (b) on-axis intensities, (c) spatial spectra (dB) and (d) spectral intensities of axial wave (linear scale) along propagation. Spectral intensities are normalized to their respective maximal values. Numerical parameters are described in table (3.1). 101

3.19 NLSE simulation results: Nonlinear propagation of Bessel beams with intensity profiles 3 and 4: plot of (a) the corresponding on-axis intensity and (b) spectral intensity of the axial wave along propagation $I(k_r = 0, z)$. Comparison of their respective (c) amplitude and (d) phase distributions with that of profile-2. 102

3.20 Results using our FWM model: Angularly resolved intensity (dB) of the idler wave resulting from the interaction of three waves composed each of twenty-seven frequencies: $\beta_j = [0.805 - 1.195]$ for input phase distributions of (a) profile-1 and (b) profile-3 and (c) the corresponding evolution along propagation of the axial wave intensity ($k_r \approx 0$). 104

3.21 (a) Target intensity profiles and (b) input spectrum of the modified Bessel-Gauss (MBG) beam. (bottom) Numerical simulation results of the NLSE: (c) their respective on-axis intensity and (d) spectral intensity of idler wave evolution along propagation for (green dashed line) BG beam and (red dotted line) MBG beam. 106

3.22 Numerical simulation results of the propagation of two Bessel beams in the filamentation regime (we consider the reduced filamentation model of Eq. (3.64) where laser-plasma coupling is neglected) with (a) profile-1 (green dashed line) and profile-3 (red solid line): (b) plot of the peak temporal intensity of the central core along z, and (c) the corresponding intensity distribution in transverse and propagation distances for both beams. Input pulse energy, E_{in} = 3.6 μJ for profile 1 and E_{in} = 3.8 μJ for profile 3, pulse duration 130 fs; cone angle θ= 4°; $I_{max} = 25\ TW/cm^2$ and beam waist $w_0 = 100\ \mu m$. 109

3.23 Nonlinear propagation of two Bessel beams with profile 1 (green dashed line) and profile 3 (red solid line) in the filamentation regime (accounting for MPA and plasma defocusing): plot of (a) the on-axis fluence (J/cm^2), (b) the peak temporal intensity of the central core along z. Evolution of the central core intensity in time and propagation coordinates for (c) profile-1 and (d) profile-3. Evolution of maximal plasma density in transverse and propagation distances for (e) profile-1 and (f) profile-3. 110

4.1 Comparison between experimental fluence maps in J/cm^2 (a-b) and simulations with nonlinear Schrödinger model for (c) $\tau_c = 1$ fs and (d) $\tau_c = 15\ as$. Image taken from Ref. [Xie et al., 2016]. 114

4.2 Experimental setup used for measurement of 3D fluence distribution of Bessel pulses in glass. 121

4.3 Experimental results of the propagation of 130 fs Bessel-Gauss beams in fused silica: (top) evolution of fluence distribution in the transverse and propagation coordinates (middle) the corresponding on-axis fluence ($r = 0$) and (bottom) energy evolution along propagation for different input energies (from left to right columns): 6 nJ (linear regime), 0.26 μJ, 0.72 μJ, 1.6 μJ. 122

4.4 Fluence distribution (first column) and plasma channels (second column) generated by Bessel filamentation. The color bar units are in J/cm^2 for the fluence (left-hand column) and in decades $16 \equiv 10^{16}\ cm^{-3}$ for the electron densities (right-hand column). The input Bessel-Gauss pulse has pulse duration of 50 fs and a cone angle $\theta \approx 0.25°$. First line, $E_{in} = 1.44\ mJ$, $w_0 = 10\ mm$; second line, $E_{in} = 14.\ mJ$, $w_0 = 10\ mm$; third line, $E_{in} = 14.4\ mJ$, $w_0 = 5\ mm$. Image taken from Ref. [Polesana et al., 2008]. 123

4.5 Nonlinear ionization rate as a function of optical intensity according to the theory of Keldysh. 124

4.6 Numerical simulation results of Eqs. (4.25), (4.21) and (4.23) where $W_{ava} = \sigma \mathcal{I}/U_i$ for $E_{in} = 0.26\ \mu J$ (a) energy and (b) central core fluence evolution along propagation for (blue dotted line) $\tau_c = 1.28$ fs and (blue solid line) $\tau_c = 4$ fs and (red line) comparison with experiments. (c-d) Fluence map and (e-f) evolution of plasma density in the radial and propagation coordinates corresponding to two values of collision time [i.e. $\tau_c = 4$ fs (c-e) and $\tau_c = 1.28$ fs (d-f)]. 126

4.7 Numerical simulation results of Eqs. (4.25), (4.21) and (4.23) for $E_{in} = 0.72$ μJ where $W_{ava} = \sigma \mathcal{I}/U_i$ (a) energy and (b) central core fluence evolution along propagation for (black dashed line) $\tau_c = 1.28$ fs and (red line) comparison with experiments. (c) Fluence map and (d) evolution of plasma density in the radial and propagation coordinates. 127

4.8 Illustration of the processes providing changes in the density and the energy, respectively, of free electrons in the conduction band of a dielectric ([Rethfeld, 2004]) 128

4.9 Numerical simulation results of Eqs. (4.25), (4.21) and (4.30) for $E_{in} = 0.72$ μJ (a) energy and (b) central core fluence evolution along propagation for (solid line) $\tau_c = 1.28$ fs and (red line) comparison with experiments. (c) Fluence map and (d) evolution of plasma density in the radial and propagation coordinates. 129

4.10 Numerical simulation results of Penano's model [Penano et al., 2005] using Eqs. (4.25) and (4.34) (4.35). Additional parameters can be found in the same reference. (blue solid line): (a) Energy and (b) central core fluence evolution along propagation and (red line) comparison with experiments. (c) Fluence map (d) Evolution of plasma density in the radial and propagation coordinates. 131

4.11 Numerical simulation results of Eqs. (4.25) and (4.36) (a) energy and (b) central core fluence evolution along propagation for (blue solid line) $\eta = 0.1$ and (black dashed line) $\eta = 0.2$ and (red line) comparison with experiments. (c-d) Fluence map and (e-f) evolution of plasma density in the radial and propagation coordinates corresponding to two values of collision time [i.e. $\eta = 0.1$ (c-e) and $\eta = 0.2$ (d-f)] 132

List of Tables

2.1 SLM characteristics used in our experiments. 45

3.1 Numerical parameters used in simulations. The values of n and n_2 correspond to those of fused silica [Gulley et al., 2010]. 77

3.2 Numerical parameters used in simulations of Bessel filamentation in fused silica. 108

4.1 Numerical parameters used in our simulations of 130-fs Bessel beams in fused silica. 125

APPENDIXES

APPENDIX OF CHAPTER 2

2.A DEMONSTRATION OF THE LIGHT FIELD EXPRESSION AT THE FIRST DIFFRACTION ORDER

As discussed in chapter 2, section 2.3.2, we expressed the phase mask $\psi(x,y)$ designed to modulate the amplitude and phase of in incident field $U_{inc}(x,y)$ as follows:

$$\psi(x,y) = M(x,y).F(x,y) \tag{37}$$

where $M(x,y)$ is an amplitude modulation term such as $\leq M(x,y) \leq 1$ and $F(x,y)$ is phase function wrapped over 2π. In the following, we will omit writing the (x,y) related to the different quantities for simplicity.

After interacting with the SLM, the incident light field U_{inc}, with a spatial amplitude A_{inc} and phase ϕ_{inc}, will acquires the phase term ψ in the form of the multiplicative $\exp(i\psi)$. Considering the spatial phase ϕ_{inc} of an incident laser beam is quasi-flat, the expression of the light field at the SLM plane U_{SLM} is given by :

$$U_{SLM} = A_{inc}\exp(i\psi) \tag{38}$$

We first expand the exponential term in a Taylor series. We obtain:

$$U_{SLM} = A_{inc}\sum_{p=0}^{+\infty}\frac{(i\,M)^p}{p!}F^p \tag{39}$$

Here, we separated the amplitude and phase term in order to expand the latter in a Fourier series:

$$U_{SLM} = A_{inc}\sum_{p=0}^{+\infty}\frac{(i\,M)^p}{p!}\sum_{n=-\infty}^{+\infty}A_n\exp(i\,n\,F) \tag{40}$$

where $A_n = \int_0^{2\pi}\frac{1}{2\pi}F^p\exp(-i\,n\,F)\mathrm{d}F$. Then, we can write the whole expression of U_{SLM} in the form of a Fourier series as follows:

$$U_{SLM} = A_{inc}\sum_{n=-\infty}^{+\infty}T_n\exp(i\,n\,F) \tag{41}$$

where the Fourier coefficient T_n is written as : $T_n = \frac{1}{2\pi}\int_0^{2\pi}\left\{\sum_{p=0}^{+\infty}\frac{(i\,M\,F)^p}{p!}\right\}\exp(-i\,n\,F)\mathrm{d}F$

This expression can be further simplified by writing the Taylor-expanded term $\sum_{p=0}^{+\infty}\frac{(i\,M\,F)^p}{p!}$ as $\exp(i\,M\,F)$ and then computing the integral. The expression of T_n then becomes:

$$
\begin{aligned}
T_n &= \frac{1}{2\pi}\int_0^{2\pi}\exp(i\,M\,F)\exp(-i\,n\,F)\mathrm{d}F \\
T_n &= \frac{1}{2\pi}\left[\frac{\exp\{i(M-n)F\}}{i(M-n)}\right]_0^{2\pi} \\
T_n &= \frac{1}{2\pi}\frac{\exp\{2\pi\,i(M-n)\}-1}{i(M-n)} \\
T_n &= \exp\{i(M-n)\,\pi\}\frac{\exp\{i(M-n)\,\pi\}-\exp\{-i(M-n)\,\pi\}}{2\pi\,i(M-n)}
\end{aligned}
\tag{42}
$$

Then, the coefficient T_n can be written as :

$$T_n = \exp\{i(M-n)\,\pi\}\mathrm{sinc}\{(M-n)\,\pi\} \tag{43}$$

where the sinc function is defined as $\mathrm{sinc}\{(M-n)\,\pi\} = \sin\{(M-n)\,\pi\}/((M-n)\,\pi)$. The expression of U_{SLM} then becomes :

$$U_{SLM} = A_{inc}\sum_{n=-\infty}^{+\infty}\exp\{i(M-n)\,\pi\}\mathrm{sinc}\{(M-n)\,\pi\}\exp\{i\,n\,F\} \tag{44}$$

At the first diffraction order ($n = 1$), where the target light field is retrieved, the expression of the light field U_{ret} is given by :

$$U_{ret} = -A_{inc}\mathrm{sinc}\{(M-1)\,\pi\}\exp\{i\,(\pi\,M+\,F)\} \tag{45}$$

By identifying Eq. (45) to the expression of a target field $U_{tar} = A_{tar}\exp(i\phi_{tar})$

$$M(x,y) = 1 + \frac{1}{\pi}\mathrm{sinc}^{-1}(A_{tar2}(x,y)) \tag{46}$$

$$F(x,y) = \phi_{tar}(x,y) - \pi M(x,y) \tag{47}$$

where $A_{tar2} = A_{tar}/A_{inc}$ and should be normalized : $0 \leq A_{tar2} \leq 1$.

2.B Analytical computation of the spatial spectrum

In this appendix, we present analytical formula of spatial spectra related to two different on-axis intensity profiles :

CASE OF A FLAT-TOP PROFILE WITH PARABOLIC RAMPS

This on-axis intensity profile, denoted I_{cst}, is given by:

$$I_{cst} = \begin{cases} I_{max}(z/z_i)^2 & ,0 \leq z \leq z_i \\ I_{max} & z_i \leq z \leq z_f \\ I_{max}(1 - \dfrac{z - z_f}{z_{max} - z_f})^2 & ,z_f \leq z \leq z_{max} \\ 0 & ,\text{otherwise} \end{cases} \tag{48}$$

The corresponding spatial spectrum is computed using Eq. (2.5): $S_{cst}(\sqrt{k^2 - k_z^2}, z = 0) = \dfrac{1}{k_z}\int_{-\infty}^{+\infty} \sqrt{I_{cst}} e^{i(k_{z0}-k_z)z}\,dz$. Inserting Eq. (48) in Eq. (2.5) we obtain :

$$\begin{aligned} S_{cst}(\sqrt{k^2 - k_z^2}, z = 0) = \frac{\sqrt{I_{max}}}{k_z}\Bigg\{ & \int_0^{z_i} (z/z_i) e^{i(k_{z0}-k_z)z}\,dz + \int_{z_i}^{z_f} e^{i(k_{z0}-k_z)z}\,dz \\ & + \int_{z_f}^{z_{max}} (1 - \frac{z - z_f}{z_{max} - z_f}) e^{i(k_{z0}-k_z)z}\,dz \Bigg\} \end{aligned} \tag{49}$$

The expression of the spatial spectrum is then made of the sum of the spatial spectra of each segment of the on-axis intensity profile. After resolving these integral, we obtain:

$$\begin{aligned} S_{cst}(\sqrt{k^2 - k_z^2}, z = 0) = \frac{\sqrt{I_{max}}}{k_z}\Bigg\{ & \frac{1}{-z_i a^2}\left[\exp(i\,a\,z_i)\,(i\,a\,z_i - 1) + 1\right] \\ & + \frac{\exp(i\,a\,z_f) - \exp(i\,a\,z_i)}{i\,a} \\ & + \frac{1}{(z_{max} - z_f)\,a^2}\left[\exp(i\,a\,z_{max})\,(i\,a\,z_{max} - 1) - \exp(i\,a\,z_f)\,(i\,a\,z_f - 1)\right] \\ & + (1 + \frac{z_f}{z_{max} z_f})\frac{\exp(i\,a\,z_{max}) - \exp(i\,a\,z_f)}{i\,a} \Bigg\} \end{aligned} \tag{50}$$

where $a = k_{z0} - k_z$.

CASE OF A LINEAR RAMP PROFILE WITH PARABOLIC DECAY

This on-axis intensity profile, denoted I_{ramp}, is given by:

$$I_{ramp} = \begin{cases} I_{max} z/z_i & ,0 \leq z \leq z_f \\ I_{max}(1 - \dfrac{z - z_f}{z_{max} - z_f})^2 & ,z_f \leq z \leq z_{max} \\ 0 & ,\text{otherwise} \end{cases} \tag{51}$$

We resolve Eq. (2.5) in the same way as described in Eq. (49). The spatial spectrum S_{ramp} corresponding to this profile is given by:

$$S_{ramp}(\sqrt{k^2 - k_z^2}, z=0) = \frac{\sqrt{I_{max}}}{k_z}\left\{ \int_0^{z_f} \sqrt{z/z_f} e^{i(k_{z0}-k_z)z}\, dz + \int_{z_f}^{z_{max}} (1 - \frac{z - z_f}{z_{max} - z_f}) e^{i(k_{z0}-k_z)z}\, dz \right\} \tag{52}$$

where the second integral of this equation is the same as the third integral in the right hand side (r. h. s.) of Eq. (49) and its resolution is described by the third and fourth terms on (r. h. s) of Eq. (50). The solution of the first integral, $S_{ramp1} = \int_0^{z_f} \sqrt{z/z_f} e^{i(k_{z0}-k_z)z}\, dz$, written as:

$$S_{ramp1}(\sqrt{k^2 - k_z^2}, z=0) = \frac{1}{z_f}\left\{ \frac{z_f}{a} [\sin(a\, z_f) i \cos(a\, z_f)] + \frac{\sqrt{\pi/2}}{a^{3/2}} [\mathrm{SinF}(\sqrt{2\, a\, z_f/\pi}) - i\, \mathrm{CosF}(\sqrt{2\, a\, z_f/\pi})] \right\} \tag{53}$$

where a was previously defined as $a = k_{z0} - k_z$. and the functions sinF and CosF stand for the sine and cosine Fresnel integrals and are defined as follows:

$$\mathrm{SinF}(x) = \int_0^x \sin\left(\frac{\pi}{2} t^2\right) dt \tag{54}$$

$$\mathrm{CosF}(x) = \int_0^x \cos\left(\frac{\pi}{2} t^2\right) dt \tag{55}$$

APPENDIX OF CHAPTER 3

3.A DERIVATION OF HELMHOLTZ EQUATION FOR A J_0 FUNCTION

In this appendix, we show how Eq. (3.9) (page 67) is obtained. The propagation equation is given by:

$$\Delta \mathbf{E}_4 - \frac{\varepsilon_r}{c^2}\frac{\partial^2 \mathbf{E}_4}{\partial t^2} = \mu_0 \frac{\partial^2 \mathbf{P}_{NL}^{(4)}}{\partial t^2} \tag{56}$$

where

$$\mathbf{E}_4 = \frac{1}{2}\mathbf{x}\,(A_4 \exp[i(\omega_0 t - k_{z4} z)] \; + \; c.c) \tag{57}$$

$$A_4 = a_4(z)\, J_0(k_{r4} r) e^{i\phi_4} \tag{58}$$

We ignore complex conjugate terms "c.c" and consider that all waves are polarized along axis **x**. Eq. (56) becomes:

$$\begin{aligned} \Delta\left[A_4 e^{i(\omega_0 t - k_{z4} z)}\right] - \frac{\varepsilon_r}{c^2}\frac{\partial^2}{\partial t^2}\left[A_4 e^{i(\omega_0 t - k_{z4} z)}\right] &= \mu_0 \frac{\partial^2}{\partial t^2}\left[p^{(4)}_{NL,\,\omega_0} e^{i(\omega_0 t - k_{z4} z)}\right] \\ \Delta\left[A_4 e^{-i\,k_{z4} z}\right] + \frac{\omega_0^2 \varepsilon_r}{c^2}\left[A_4 e^{-i\,k_{z4} z}\right] &= -\frac{\omega_0^2}{\varepsilon_0 c^2}\left[p^{(4)}_{NL,\,\omega_0} e^{-i\,k_{z4} z}\right] \end{aligned} \tag{59}$$

where

$$\begin{aligned} p^{(4)}_{NL,\,\omega_0} = \frac{3}{4}\varepsilon_0 \chi^{(3)} \Big[& |A_4|^2 A_4 + 2\,(|A_1|^2 + |A_2|^2 + |A_3|^2) A_4 \\ & + \sum_{j=1}^{3} (A_j^2 A_4^* e^{-i(2k_{zj} - 2k_{z4})z}) + 2\,(A_1 A_2 A_3^* e^{-i(k_{z1} + k_{z2} - k_{z3} - k_{z4})z} \\ & + A_1 A_2^* A_3 e^{-i(k_{z1} - k_{z2} + k_{z3} - k_{z4})z} + A_1^* A_2 A_3 e^{-i(-k_{z1} + k_{z2} + k_{z3} - k_{z4})z}) \Big] \end{aligned} \tag{60}$$

We have:

$$\Delta\left[A_4 e^{-i\,k_{z4} z)}\right] = \left(\frac{\partial^2}{\partial r^2} + \frac{1}{r}\frac{\partial}{\partial r} + \frac{\partial^2}{\partial z^2}\right) a_4(z)\, J_0(k_{r4} r) e^{i\phi_4} e^{-i\,k_{z4} z} \tag{61}$$

For derivative terms along variable "r" we have:

$$\begin{aligned} \frac{1}{r}\frac{\partial J_0(k_{r4} r)}{\partial r} &= -\,k_{r4}\frac{J_1(k_{r4} r)}{r} \\ \frac{\partial^2 J_0(k_{r4} r)}{\partial r^2} &= -\,k_{r4}\frac{\partial J_1(k_{r4} r)}{\partial r} \\ &= +\,k_{r4}\frac{J_1(k_{r4} r)}{r} - k_{r4}^2 J_0(k_{r4} r) \end{aligned}$$

For derivative terms along variable "z" we have:

$$\begin{aligned}\frac{\partial^2 a_4(z)\mathrm{e}^{-i\,k_{z4}z}}{\partial z^2} &= \frac{\partial}{\partial z}\frac{\partial a_4(z)\mathrm{e}^{-i\,k_{z4}z}}{\partial z}\\ &= \frac{\partial}{\partial z}(\frac{\partial a_4(z)}{\partial z}\mathrm{e}^{-ik_{z4}z} - ik_{z4}a_4(z)\mathrm{e}^{-ik_{z4}z})\\ &= \frac{\partial^2 a_4(z)}{\partial z^2}\mathrm{e}^{-i\,k_{z4}z} - 2ik_{z4}\frac{\partial a_4(z)}{\partial z}\mathrm{e}^{-ik_{z4}z} - k_{z4}^2 a_4(z)\mathrm{e}^{-ik_{z4}z}\end{aligned}$$

According to the slowly varying envelop approximation, we neglect the second derivate of $a_4(z)$. Eq. (61) becomes:

$$\Delta\left[A_4\mathrm{e}^{-i\,k_{z4}z)}\right] = -[(k_{r4}^2 + k_{z4}^2)a_4(z) + 2ik_{z4}\frac{\partial a_4(z)}{\partial z}]J_0(k_{r4}r)\mathrm{e}^{-ik_{z4}z}\mathrm{e}^{i\phi_4} \tag{62}$$

We have $k^2 = k_{r4}^2 + k_{z4}^2 = \varepsilon_r\frac{\omega_0^2}{c^2}$, [Durnin, 1987]. Then, Eq. (59) becomes:

$$2ik_{z4}\frac{\partial a_4(z)}{\partial z}J_0(k_{r4}r)\mathrm{e}^{i\phi_4} = \frac{k^2}{n^2\varepsilon_0}p^{(4)}_{NL,\,\omega_0} \tag{63}$$

where $\varepsilon_r = n^2$ and n is the linear refractive index.

3.B Analytical computation of a TPM integral defined for $\beta_1 = \beta_2$ and $\beta_3 = \beta_4$

We analytically develop the expression of transverse phase matching (TPM) integral introduced in chapter 3 (section 3.25, page 73). It is defined for two identical pump waves ($\beta_1 = \beta_2$) interacting with a signal wave to yield an idler wave identical to the latter ($\beta_4 = \beta_3$):

$$I_{TPM} = 1/k_{r0}^2\int_0^{\nu_f} J_0^2(\beta_1\,\nu)\,J_0^2(\beta_4\,\nu)\,r\,\mathrm{d}r \tag{64}$$

We use the approximate expression of the J_0 function:

$$J_0(\beta\,\nu) \approx \begin{cases} 1-(\beta\,\nu)^2/4 & ,0 \le \nu \le \nu_0 \\ \sqrt{\dfrac{2}{\pi\beta\,\nu}}\cos\left(\beta\,\nu - \pi/4\right) & ,\nu_0 \le \nu \end{cases}$$

The breakpoints of the Bessel functions $J_0(\beta_1\,\nu)$ and $J_0(\beta_4\,\nu)$ are $\nu_1 = 1.1/\beta_1$ $\nu_4 = 1.1/\beta_4$ respectively. In our calculations, we compute I_{TPM} as a function of β_4 for a given value of β_1. Since the breakpoint ν_4 varies as a function of β_4, the approximative expression of I_{TPM} integral depends on whether $\nu_1 < \nu_4$ or $\nu_1 > \nu_4$.
In the case where $\beta_4 < \beta_1$ ($\nu_1 < \nu_4$), the integral (64) can be written as $I_{TPM1} = I_1 + I_2 + I_3$ where:

$$I_1 = \int_0^{\nu_1} 1/k_{r0}^2 (1 - \frac{(\beta_1\,\nu)^2}{4})^2 (1 - \frac{(\beta_4\,\nu)^2}{4})^2 \nu\,\mathrm{d}\nu \qquad , \ \nu\epsilon[0,\nu_1] \tag{65}$$

$$I_2 = \int_{\nu_1}^{\nu_4} \frac{2}{k_{r1}\,\pi} \cos^2(\beta_1\,\nu - \pi/4)\,(1 - \frac{(\beta_4\,\nu)^2}{4})^2 \mathrm{d}\nu \qquad , \ \nu\epsilon[\nu_1,\nu_4] \tag{66}$$

$$I_3 = \int_{\nu_4}^{\nu_f} \frac{4}{k_{r1}\,k_{r4}\,\pi^2} \frac{\cos^2(\beta_1\,\nu - \pi/4)\cos^2(\beta_4\,\nu - \pi/4)}{\nu} \mathrm{d}\nu \qquad , \ \nu\epsilon[\nu_4,\nu_f] \tag{67}$$

Their analytical solutions are given by:

$$\begin{aligned} I_1 = \frac{1}{256}\Big[& \frac{\beta_1^4\beta_4^4\nu^{10}}{10} - \beta_1^2\beta_4^2(\beta_1^2 + \beta_4^2)\nu^8 - 32(\beta_1^2 + \beta_4^2)\nu^4 \\ & + \frac{8}{3}(\beta_1^4 + \beta_4^4 + 4\beta_1^2\beta_4^2)\nu^6 + 128\,\nu^2 \Big]_0^{\nu_1} \end{aligned} \tag{68}$$

$$\begin{aligned} I_2 = \frac{1}{1920\beta_1^5}\Big[& 4\beta_4^5\nu^4(3\beta_4^4\nu^4 - 40\beta_4^2\nu^2 + 240) \\ & + 30\beta_1\beta_4^4\nu[2\beta_1^2(\beta_4^2\nu^2 - 4) - 3\beta_4^2]\,\sin(2\beta_1\nu) \\ & - 15\{2\beta_1^4(\beta_4^2\nu^2 - 4)^2 + \beta_1^2(8_b eta_4^2 - 6\beta_4^4\nu^2) + 3\beta_4^4\}\,\cos(2\beta_1\nu) \Big]_{\nu_1}^{\nu_4} \end{aligned} \tag{69}$$

$$\begin{aligned} I_3 = \frac{1}{2\,k_{r1}k_{r4}\pi^2}\Big[& -\mathrm{Ci}[2(\beta_1 + \beta_4)\,\nu] + \mathrm{Ci}[2(\beta_1 - \beta_4)\,\nu] \\ & + 2\,\mathrm{Si}(2\beta_1\,\nu) + 2\,\mathrm{Si}(2\beta_4\,r) + \ln(\nu) \Big]_{\nu_4}^{\nu_f} \end{aligned} \tag{70}$$

In the case $\beta_4 > \beta_1$ ($\nu_1 > \nu_4$), the integral (64) can be similarly written as $I_{TPM2} = I_2 + I_4 + I_6$ where:

$$I_4 = \int_0^{\nu_4} 1/k_{r0}^2 (1 - \frac{(\beta_1\,\nu)^2}{4})^2 (1 - \frac{(\beta_4\,\nu)^2}{4})^2 \nu\,\mathrm{d}\nu \qquad , \ \nu\epsilon[0,\nu_4] \tag{71}$$

$$I_5 = \int_{\nu_4}^{\nu_1} \frac{2}{k_{r0}k_{r4}\,\pi} \cos^2(\beta_4\,\nu - \pi/4)\,(1 - \frac{(\beta_1\,\nu)^2}{4})^2 \mathrm{d}\nu \qquad , \ \nu\epsilon[\nu_4,\nu_1] \tag{72}$$

$$I_6 == \int_{\nu_1}^{\nu_f} \frac{4}{k_{r1}\,k_{r4}\,\pi^2} \frac{\cos^2(\beta_1\,\nu - \pi/4)\cos^2(\beta_4\,\nu - \pi/4)}{\nu} \mathrm{d}\nu \qquad , \ \nu\epsilon[\nu_1,\nu_f] \tag{73}$$

Similarly, the solutions to these integrals are written as:

$$\begin{aligned} I_4 = \frac{1}{256}\Big[& \frac{\beta_1^4\beta_4^4\nu^{10}}{10} - \beta_1^2\beta_4^2(\beta_1^2 + \beta_4^2)\nu^8 - 32(\beta_1^2 + \beta_4^2)\nu^4 \\ & + \frac{8}{3}(\beta_1^4 + \beta_4^4 + 4\beta_1^2\beta_4^2)\nu^6 + 128\,\nu^2 \Big]_0^{\nu_4} \end{aligned} \tag{74}$$

$$I_5 = \frac{1}{1920\beta_4^5}\Big[4\beta_1^5\nu^4(3\beta_1^4\nu^4 - 40\beta_1^2\nu^2 + 240) + 30\beta_4\beta_1^4\nu[2\beta_4^2(\beta_1^2\nu^2 - 4) - 3\beta_1^2]\,\sin(2\beta_4\nu) - 15\{2\beta_4^4(\beta_1^2\nu^2 - 4)^2 + \beta_1^2(8_b eta_1^2 - 6\beta_4^4\nu^2) + 3\beta_1^4\}\,\cos(2\beta_4\nu)\Big]_{\nu_4}^{\nu_1} \tag{75}$$

$$I_6 = \frac{1}{2\,k_{r1}k_{r4}\pi^2}\Big[-\mathrm{Ci}[2(\beta_1+\beta_4)\,\nu] + \mathrm{Ci}[2(\beta_1-\beta_4)\,\nu] + 2\,\mathrm{Si}(2\beta_1\,\nu) + 2\,\mathrm{Si}(2\beta_4\,r) + \ln(\nu)\Big]_{\nu_1}^{\nu_f} \tag{76}$$

The total integral (64) is then written as:

$$I_{TPM} = I_{TPM1} + I_{TPM2}\begin{cases} I_1 + I_2 + I_3 & ,\beta_4 < \beta_1 \\ I_4 + I_5 + I_6 & ,\beta_4 > \beta_1 \end{cases}$$

where $\mathrm{Ci}(x)$ and $\mathrm{Si}(x)$ stand for the cosine and sine integrals respectively. They are defined as follows:

$$\mathrm{Ci}(x) = \int_0^{+\infty} \frac{\cos(t)}{t}\mathrm{d}t \tag{77}$$

$$\mathrm{Si}(x) = \int_0^{+\infty} \frac{\sin(t)}{t}\mathrm{d}t \tag{78}$$

3.C Expression of the idler wave for two-frequency pump and signal waves

We recall the expression of the growth rate of the idler wave axial envelope defined in chapter 3 (section 3.21, page 70):

$$\frac{\partial a_4(\xi,\theta_4)}{\partial\xi} = i\,C_0\tan(\theta_4)\int_0^{+\infty}\mathrm{d}\beta_1 S_1(\beta_1)\int_0^{+\infty}\mathrm{d}\beta_2 S_2(\beta_2) \times \int_0^{+\infty}\mathrm{d}\beta_3 S_3(\beta_3)\,I_{TPM}\sum_{m=1}^{3}\exp(i\Delta\phi_m + i\Delta\beta_{zm}\xi) \tag{79}$$

where I_{TPM} is defined as:

$$I_{TPM} = \frac{1}{k_{r0}^2}\int_0^{\nu_f} J_0(\beta_1\nu)\,J_0(\beta_2\nu))\,J_0(\beta_3\nu)\,J_0(\beta_4\nu)\,\nu\,\mathrm{d}\nu \tag{80}$$

and $\nu_f = k_{r0}r_f$ and $S_j(\beta_j)$, $j = 1,2,3$, stand for the amplitude distribution of the spectral components of the pump and signal waves respectively. The complex spatial spectra are given by: $\tilde{S}_j(\beta_j) = S_j(\beta_j)\exp[i\phi_j]$.

We consider two identical pump waves defined at the central frequency $\beta_1 = \beta_2 = 1$ Their respective input phases are denoted ϕ_a and ϕ_b. We define a signal wave at two adjacent frequencies β_{31} and β_{32} ($\beta_{31} \approx \beta_{32}$) with input phases ϕ_{31} and ϕ_{32} respectively. Their respective spatial spectra are then written as:

$$\tilde{S}_j(\beta_j) = \delta(\beta_j - 1)\,[\exp(i\phi_a) + \exp(i\phi_b)], \qquad j = 1, 2 \tag{81}$$

$$\tilde{S}_j(\beta_j) = \delta(\beta_3 - \beta_{31})\,[\exp(i\phi_{31}) + \exp(i\phi_{32})] \tag{82}$$

We insert Eq. (82) in Eq. (79):

$$\begin{aligned}\frac{\partial a_4(\xi,\theta_4)}{\partial \xi} = i\,C_0 \tan(\theta_4) I^{ab2}_{TPM}\Big[&\mathrm{e}^{i(2-\beta_{31}^2-\beta_4^2)\xi}\,\{\exp[i(2\phi_a - \phi_{31})] + \exp[i(2\phi_b - \phi_{31})] \\ &+ \exp[i(\phi_a + \phi_b - \phi_{31})] + \exp[i(\phi_a + \phi_b - \phi_{32})]\} \\ &+ \exp[i(2\phi_a - \phi_{32})] + \exp[i(2\phi_b - \phi_{32})] \\ &+ 4\,\mathrm{e}^{i(\beta_{31}^2-\beta_4^2)\xi}\,[\exp(i\phi_{31}) + \exp(i\phi_{32})][1 + \cos(\phi_a - \phi_b)]\Big]\end{aligned} \tag{83}$$

where $I^{ab2}_{TPM} = \dfrac{1}{k_{r0}^2}\int_0^{\nu_f} J_0^2(\nu)\,J_0(\beta_{31}\nu)\,J_0(\beta_4\nu)\,\nu\,\mathrm{d}\nu$

We further develop this equation using trigonometric relations:

$$\begin{aligned}\frac{\partial a_4(\xi,\theta_4)}{\partial \xi} =& 2i\,C_0 \tan(\theta_4) I^{ab2}_{TPM}[1 + \cos(\phi_a - \phi_b)]\,\sqrt{1 + \cos(\phi_{31} - \phi_{32})} \\ &\times\Big[\mathrm{e}^{i(2-\beta_{31}^2-\beta_4^2)\xi}\exp[i(\phi_a + \phi_b - \frac{\phi_{31} + \phi_{32}}{2})] + 2\,\mathrm{e}^{i(\beta_{31}^2-\beta_4^2)\xi}\exp[0.5\,i(\phi_{31} + \phi_{32})]\Big]\end{aligned} \tag{84}$$

We now integrate this equation over ξ: $a_4(\xi,\theta_4) = \int_0^{\xi}[\partial a_4(\xi,\theta_4)/\partial\xi]$:

$$\begin{aligned}a_4(\xi,\theta_4) =& 2i\,C_0 \tan(\theta_4) I^{ab2}_{TPM}[1 + \cos(\phi_a - \phi_b)]\,\sqrt{1 + \cos(\phi_{31} - \phi_{32})} \\ &\times\Big[\exp[i(\phi_a + \phi_b - \frac{\phi_{31} + \phi_{32}}{2})]\frac{\exp[i(2 - \beta_{31}^2 - \beta_4^2)\xi] - 1}{i(2 - \beta_{31}^2 - \beta_4^2)} \\ &+ 2\exp[0.5\,i(\phi_{31} + \phi_{32})]\frac{\exp[i(\beta_{31}^2 - \beta_4^2)\xi] - 1}{i(\beta_{31}^2 - \beta_4^2)}\Big]\end{aligned} \tag{85}$$

$$\begin{aligned}a_4(\xi,\theta_4) =& 2i\,C_0 \tan(\theta_4) I^{ab2}_{TPM}\,\xi[1 + \cos(\phi_a - \phi_b)]\,\sqrt{1 + \cos(\phi_{31} - \phi_{32})} \\ &\times\Big[\exp[i(\phi_a + \phi_b - \frac{\phi_{31} + \phi_{32}}{2})]\mathrm{e}^{0.5\,i(2-\beta_{31}^2-\beta_4^2)\xi}\mathrm{sinc}[0.5\,(2 - \beta_{31}^2 - \beta_4^2)\xi] \\ &+ 2\exp[0.5\,i(\phi_{31} + \phi_{32})]\mathrm{e}^{0.5\,i(\beta_{31}^2-\beta_4^2)\xi}\mathrm{sinc}[0.5\,(\beta_{31}^2 - \beta_4^2)\xi]\Big]\end{aligned} \tag{86}$$

Expression of $I_4(\xi,\beta_4)$ for identical two-pump waves and a different signal wave

We compute the squared absolute value $I_4(\xi,\theta_4) = |a(\xi,\theta_4)|^2$ of Eq. (86):

$$I_4(\xi,\beta_4) \propto i\ \tan^2(\beta_4\theta_0)\xi^2[1+\cos(\phi_a-\phi_b)]^2\,[1+\cos(\phi_{31}-\phi_{32})] \tag{87}$$
$$\times\{\mathrm{sinc}^2[0.5(2-\beta_{31}^2-\beta_4^2)\xi]+4\,\mathrm{sinc}^2[0.5(\beta_{31}^2-\beta_4^2)\xi]$$
$$+4\,\cos[\phi_a+\phi_b-\phi_{31}-\phi_{32}+(1-\beta_{31}^2)\xi]\,\mathrm{sinc}[0.5(2-\beta_{31}^2-\beta_4^2)\xi]\mathrm{sinc}[0.5(\beta_{31}^2-\beta_4^2)\xi]\}$$

Expression of $I_4(\xi,\beta_4)$ for identical two-frequency pump and signal waves

In this particular case, we just replace the expression of the signal wave by that of the pump, i.e. $\tilde{S}_3(\beta_j)=\delta(\beta_3-1)\,[\exp(i\phi_a)+\exp(i\phi_b)]$ in the expression of Eq. (86). We then find the expression of the corresponding $I_4(\xi,\theta_4)$ presented in chapter 3 (section 3.58, page 94).

$$I_4(\xi,\beta_4) \propto\ \tan^2(\theta_4)\,\xi^2\,\mathrm{sinc}^2[0.5\,(1-\beta_4^2)\xi]\,[1+\cos(\phi_a-\phi_b)]^3 \tag{88}$$

BIBLIOGRAPHY

[Agrawal, 2013] Agrawal, G. (2013). **Chapter 10 - four-wave mixing**. In Agrawal, G., editor, *Nonlinear Fiber Optics (Fifth Edition)*, Optics and Photonics, pages 397 – 456. Academic Press, Boston, fifth edition edition.

[Ahmed et al., 2014] Ahmed, F., Shamim Ahsan, M., Seop Lee, M., et Jun, M. B. G. (2014). **Near-field modification of femtosecond laser beam to enhance single-shot pulse filamentation in glass medium**. *Appl. Phys. A*, 114(4):1161–1165.

[Akhmedzhanov et al., 2009] Akhmedzhanov, R. A., Ilyakov, I. E., Mironov, V. A., Suvorov, E. V., Fadeev, D. A., et Shishkin, B. V. (2009). **Plasma mechanisms of pulsed terahertz radiation generation**. *Radiophysics and Quantum Electronics*, 52(7):482.

[Alexeev et al., 2002] Alexeev, I., Kim, K. Y., et Milchberg, H. M. (2002). **Measurement of the superluminal group velocity of an ultrashort bessel beam pulse**. *Phys. Rev. Lett.*, 88:073901.

[Amako et al., 2003] Amako, J., Sawaki, D., , et Fujii, E. (2003). **Microstructuring transparent materials by use of nondiffracting ultrashort pulse beams generated by diffractive optics**. *J. Opt. Soc. Am. B*, 20(12).

[Andreev et al., 1991] Andreev, N. E., Aristov, Y. A., Polonskii, L. Y., et Pyatnitskii, L. N. (1991). **Bessel beams of electromagnetic waves**. *Zh. Eksp. Teor. Fiz.*, 100:1756–1766.

[Arlt et al., 2001] Arlt, J., Garces-Chavez, V., Sibbett, W., et Dholakia, K. (2001). **Optical micromanipulation using a Bessel light beam**. *Opt. Commun.*, 197(4):239 – 245.

[Arrizón et al., 2005] Arrizón, V., Méndez, G., et de La-Llave, D. S. (2005). **Accurate encoding of arbitrary complex fields with amplitude-only liquid crystal spatial light modulators**. *Opt. Express*, 13(20):7913–7927.

[Arrizón et al., 2007] Arrizón, V., Ruiz, U., Carrada, R., et González, L. A. (2007). **Pixelated phase computer holograms for the accurate encoding of scalar complex fields**. *J. Opt. Soc. Am. A*, 24(11):3500–3507.

[Bhuyan et al., 2011] Bhuyan, M., Courvoisier, F., Phing, H., Jedrkiewicz, O., Recchia, S., Trapani, P. D., et Dudley, J. (2011). **Laser micro- and nanostructuring using femtosecond Bessel beams**. *Eur. Phys. J. Special Topics*, 199:101–110.

[Bhuyan et al., 2010] Bhuyan, M. K., Courvoisier, F., Lacourt, P.-A., Jacquot, M., Salut, R., Furfaro, L., et Dudley, J. M. (2010). **High aspect ratio nanochannel machining using single shot femtosecond Bessel beams**. *Appl. Phys. Lett.*, 97(081102).

[Bhuyan et al., 2014] Bhuyan, M. K., Velpula, P. K., Colombier, J. P., Olivier, T., Faure, N., et Stoian, R. (2014). **Single-shot high aspect ratio bulk nanostructuring of**

fused silica using chirpcontrolled ultrafast laser Bessel beams. *Appl. Phys. Lett.*, 104(021107).

[Bitman et al., 2012] Bitman, A., Moshe, I., et Zalevsky, Z. (2012). **Improving depth-of field in broadband thz beams using nondiffractive Bessel beams**. *Opt. Lett.*, 37(19):4164–4166.

[Bolduc et al., 2013] Bolduc, E., Bent, N., Santamato, E., Karimi, E., et Boyd, R. W. (2013). **Exact solution to simultaneous intensity and phase encryption with a single phase-only hologram**. *Opt. Lett.*, 38(18):3546–3549.

[Bowlan et al., 2009] Bowlan, P., Valtna-Lukner, H., ohmus, M. L., Piksarv, P., Saari, P., et Trebino, R. (2009). **Measuring the spatiotemporal field of ultrashort Bessel-X pulses**. *Opt. Lett.*, 34(15):2276–2278.

[Brabec et al., 1997] Brabec, T., et Krausz, F. (1997). **Nonlinear optical pulse propagation in the single-cycle regime**. *Phys. Rev. Lett.*, 78:3282–3285.

[Braun et al., 1995] Braun, A., Korn, G., Liu, X., Du, D., Squier, J., et Mourou, G. (1995). **Self-channeling of high-peak-power femtosecond laser pulses in air**. *Opt. Lett.*, 20(1):73–75.

[Brodeur et al., 1997] Brodeur, A., Chien, C. Y., Ilkov, F. A., Chin, S. L., Kosareva, O. G., et Kandidov, V. P. (1997). **Moving focus in the propagation of ultrashort laser pulses in air**. *Opt. Lett.*, 22(5):304–306.

[Bulgakova et al., 2015] Bulgakova, N. M., Zhukov, V. P., Sonina, S. V., et Meshcheryakov, Y. (2015). **Modification of transparent materials with ultrashort laser pulses: What is energetically and mechanically meaningful**. *Journal of Applied Physics*, 118(23):233108.

[Bunkin et al., 1983] Bunkin, F. V., Korobkin, V. V., Kurinyi, Y. A., Polonskii, L. Y., et Pyatnitskii, L. N. (1983). **Laser spark with a continuous channel in air**. *Sov. J. Quantum. Electron*, 13:254–255.

[Bystrov et al., 2005] Bystrov, A. M., Vvedenskii, N. V., et Gildenburg, V. B. (2005). **Generation of terahertz radiation upon the optical breakdown of a gas**. *Journal of Experimental and Theoretical Physics Letters*, 82(12):753–757.

[Chattrapiban et al., 2003] Chattrapiban, N., Rogers, E. A., Cofield, D., W. T. Hill, I., et Roy, R. (2003). **Generation of nondiffracting Bessel beams by use of a spatial light modulator**. *Opt. Lett.*, 28(22):2183–2185.

[Chiao et al., 2009] Chiao, R. Y., Gustafson, T., et Kelley, P. (2009). **Self-Focusing of Optical Beams**, pages 129–143. Springer New York, New York, NY.

[Chichkov et al., 1996] Chichkov, B. N., Momma, C., Nolte, S., von Alvensleben, F., et Tünnermann, A. (1996). **Femtosecond, picosecond and nanosecond laser ablation of solids**. *Applied Physics A*, 63(2):109–115.

[Chimier et al., 2011] Chimier, B., Uteza, O., Sanner, N., Sentis, M., Itina, T., Lassonde, P., Legare, F., Vidal, F., et Kieffer, J. C. (2011). **Damage and ablation thresholds of fused-silica in femtosecond regime**. *Phys. Rev. B*, 84(094104).

[Clark et al., 2016] Clark, T. W., Offer, R. F., Franke-Arnold, S., Arnold, A. S., et Radwell, N. (2016). **Comparison of beam generation techniques using a phase only spatial light modulator**. *Opt. Express*, 24(6):6249–6264.

[Clerici et al., 2015] Clerici, M., Hu, Y., Lassonde, P., Milián, C., Couairon, A., Christodoulides, D. N., Chen, Z., Razzari, L., Vidal, F., Légaré, F., Faccio, D., et Morandotti, R. (2015). **Laser-assisted guiding of electric discharges around objects**. *Science Advances*, 1(5).

[Cooley et al., 2006] Cooley, J. H., Antonsen, T. M., Milchberg, H. M., Fan, J., Margolin, L., et Pyatnitskii, L. (2006). **Parametric instability in the formation of plasma waveguides**. *Phys. Rev. E*, 73:036404.

[Couairon et al., 2011] Couairon, A., Brambilla, E., Corti, T., Majus, D., de J. Raminez-Gongora, O., et Kolesik, M. (2011). **Practitioner's guide to laser pulse propagation models and simulation**. *Eur. Phys. J. Special Topics*, 199:5–76.

[Couairon et al., 2012] Couairon, A., Lotti, A., Panagiotopoulos, P., Abdollahpour, D., Faccio, D., Papazoglou, D. G., Tzortzakis, S., Courvoisier, F., et Dudley, J. M. (2012). **Ultrashort laser pulse filamentation with airy and Bessel beams**. *SPIE Proc.*, 8770(87701E-1).

[Couairon et al., 2007] Couairon, A., et Mysyrowicz, A. (2007). **Femtosecond filamentation in transparent media**. *Physics Reports*, pages 47–189.

[Couairon et al., 2002] Couairon, A., S.Tzortzakis, Bergé, L., Franco, M., Prade, B., et Mysyrowicz, A. (2002). **Infrared femtosecond light filaments in air: simulations and experiments**. *J. Opt. Soc. Am. B*, 19(5):1117–1131.

[Couairon et al., 2005] Couairon, A., Sudrie, L., Franco, M., Prade, B., et Mysyrowicz, A. (2005). **Filamentation and damage in fused silica induced by tightly focused femtosecond laser pulses**. *Phys. Rev. B*, 71:125435.

[Courvoisier et al., 2016a] Courvoisier, F., Giust, R., Xie, C., Jukna, V., Furfaro, L., Meyer, R., Rapp, L., Jacquot, M., Dudley, J. M., et Couairon, A. (2016a). **Imaging of bessel filaments in fused silica and impact on modelling the underlying light-matter physics**. In *2016 Progress in Electromagnetic Research Symposium (PIERS)*, pages 2428–2428.

[Courvoisier et al., 2016b] Courvoisier, F., Stoian, R., et Couairon, A. (2016b). **Ultrafast laser micro and nano processing with nondiffracting and curved beams**. *J. Opt. Las. Tech.*, 80:125–137.

[Courvoisier et al., 2013] Courvoisier, F., Zhang, J., Bhuyan, M., Jacquot, M., et Dudley, J. (2013). **Applications of femtosecond Bessel beams to laser ablation**. *Appl. Phys. A*, 112:29–34.

[Cox et al., 1991] Cox, A. J., et Dibble, D. C. (1991). **Holographic reproduction of a diffraction-free beam**. *Appl. Opt.*, 30(11):1330–1332.

[Davis et al., 1999] Davis, J. A., Cottrell, D. M., Campos, J., Yzuel, M. J., et Moreno, I. (1999). **Encoding amplitude information onto phase-only filters**. *Appl. Opt.*, 38(23):5004–5013.

[Davis et al., 1993] Davis, J. A., Guertin, J., et Cottrell, D. M. (1993). **Diffraction-free beams generated with programmable spatial light modulators**. *Appl. Opt.*, 32(31):6368–6370.

[DLMF,] DLMF. *NIST Digital Library of Mathematical Functions*. http://dlmf.nist.gov/, Release 1.0.19 of 2018-06-22. F. W. J. Olver, A. B. Olde Daalhuis, D. W. Lozier, B. I. Schneider, R. F. Boisvert, C. W. Clark, B. R. Miller and B. V. Saunders, eds.

[Dota et al., 2012] Dota, K., Pathak, A., Dharmadhikari, J. A., Mathur, D., et Dharmadhikari, A. K. (2012). **Femtosecond laser filamentation in condensed media with Bessel beams**. *Phys. Rev. A*, 86(023808).

[Dubietis et al., 2004] Dubietis, A., Kučinskas, E., Tamošauskas, G., Gaižauskas, E., Porras, M. A., et Trapani, P. D. (2004). **Self-reconstruction of light filaments**. *Opt. Lett.*, 29(24):2893–2895.

[Dubietis et al., 2007] Dubietis, A., Polesana, P., Valiulis, G., Stabinis, A., Trapani, P. D., et Piskarskas, A. (2007). **Axial emission and spectral broadening in self-focusing of femtosecond Bessel beams**. *Opt. Express*, 15:4168.

[Durfee et al., 1995] Durfee, C. G., Lynch, J., et Milchberg, H. M. (1995). **Development of a plasma waveguide for high-intensity laser pulses**. *Phys. Rev. E*, 51:2368–2389.

[Durfee et al., 1993] Durfee, C. G., et Milchberg, H. M. (1993). **Light pipe for high intensity laser pulses**. *Phys. Rev. Lett.*, 71:2409–2412.

[Durnin, 1987] Durnin, J. (1987). **Exact solutions for nondiffracting beams. i. the scalar theory**. *J. Opt. Soc. Am. A*, 4(4):651–645.

[Durnin et al., 1989] Durnin, J., et Miceli, J. J. (1989). **Diffraction-free beams**. *Phys. Rev. Lett.*, 58(15):1499–1501.

[Fahrbach et al., 2012] Fahrbach, F. O., et Rohrbach, A. (2012). **Propagation stability of self-reconstructing Bessel beams enables contrast-enhanced imaging in thick media**. *Nat. Commun.*, 3(632).

[Fahrbach et al., 2010] Fahrbach, F. O., Simon, P., et Rohrbach, A. (2010). **Microscopy with self-reconstructing beams**. *Nat. Photonics*.

[Fan et al., 2002] Fan, J., Parra, E., Kim, K. Y., Alexeev, I., Milchberg, H. M., Cooley, J., et Antonsen, T. M. (2002). **Resonant self-trapping of high intensity Bessel beams in underdense plasmas**. *Phys. Rev. E*, 65:056408.

[Fang et al., 2017] Fang, Q., Curatolo, A., Wijesinghe, P., Yeow, Y. L., Hamzah, J., Noble, P. B., Karnowski, K., Sampson, D. D., Ganss, R., Kim, J. K., Lee, W. M., et Kennedy, B. F. (2017). **Ultrahigh-resolution optical coherence elastography through a micro-endoscope: towards in vivo imaging of cellular-scale mechanics**. *Biomed. Opt. Express*, 8:5127–5138.

[Froehly et al., 2014] Froehly, L., Jacquot, M., Lacourt, P.-A., Dudley, J. M., , et Courvoisier, F. (2014). **Spatiotemporal structure of femtosecond Bessel beams from spatial light modulators**. *J. Opt. Soc. Am. A*, 31(4):790.

[Gadonas et al., 1999] Gadonas, R., Jarutis, V., Marcinkevicius, A., Smilgevicius, V., Stabinis, A., et Vaicaitis, V. (1999). **Transverse phase-matching in stimulated Raman scattering by a Bessel beam**. *Opt.Commun.*, 169:189–197.

[Gadonas et al., 2001] Gadonas, R., Jarutis, V., Paskauskas, R., Smilgevicius, V., Stabinis, A., et Vaicaitis, V. (2001). **Self-action of Bessel beam in nonlinear medium**. *Opt. Commun.*, 196:309–316.

[Gaizauskas et al., 2006] Gaizauskas, E., Vanagas, E., Jarutis, V., Juodkazis, S., Mizeikis, V., et Misawa, H. (2006). **Discrete damage traces from filamentation of Gauss–Bessel pulses**. *Opt. Lett.*, 31:80–82.

[Gamaly et al., 2013] Gamaly, E. G., et Rode, A. V. (2013). **Physics of ultra-short laser interaction with matter : From phonon excitation to ultimate transformations**. *Progress in Quantum Electronics*, 37:215–323.

[Garces-Chavez et al., 2002] Garces-Chavez, V., Mcgloin, D., Melville, H., Sibbett, W., et Dholakia, K. (2002). **Simultaneous micromanipulation in multiple planes using a self-reconstructing light beam**. *Nature*, 419:145–147.

[Garzillo et al., 2016] Garzillo, V., Jukna, V., Couairon, A., Grigutis, R., Di Trapani, P., et Jedrkiewicz, O. (2016). **Optimization of laser energy deposition for single-shot high aspect-ratio microstructuring of thick bk7 glass**. *Journal of Applied Physics*, 120(1):013102.

[Gattass et al., 2008] Gattass, R. R., et Mazur, E. (2008). **Femtosecond laser micromachining in transparent materials**. *Nat. Photonics*, 2:219–225.

[Gil-Villalba et al., 2015] Gil-Villalba, A., Xie, C., Salut, R., Furfaro, L., Giust, R., Jacquot, M., Lacourt, P.-A., Dudley, J. M., et Courvoisier, F. (2015). **Deviation from threshold model in ultrafast laser ablation of graphene at sub-micron scale**. *Applied Physics Letters*, 107(6):061103.

[Golub et al., 2010] Golub, I., Chebbi, B., Shaw, D., et Nowacki, D. (2010). **Characterization of a refractive logarithmic axicon**. *Opt. Lett.*, 35(16):2828–2830.

[Gong et al., 2013] Gong, L., Y., Xue, G., Wang, Q., Zhou, J., Zhong, M., Wang, Z., et Li, Y. (2013). **Generation of nondiffracting Bessel beam using digital micromirror device**. *Appl. Opt.*, 52(19):4566–4575.

[Gulley et al., 2010] Gulley, J. R., et Dennis, W. M. (2010). **Ultrashort-pulse propagation through free-carrier plasmas**. *Appl. Phys. A*, 81:033818.

[Hallo et al., 2007] Hallo, L., Bourgeade, A., Tikhonchuk, V. T., Mezel, C., et Breil, J. (2007). **Model and numerical simulations of the propagation and absorption of a short laser pulse in a trasnparent dielectric material: Blast-wave launch and cavity formation**. *Phys. Rev. B*, 76(024101).

[Hamster et al., 1993] Hamster, H., Sullivan, A., Gordon, S., White, W., et Falcone, R. W. (1993). **Subpicosecond, electromagnetic pulses from intense laser-plasma interaction**. *Phys. Rev. Lett.*, 71:2725–2728.

[Herbstman et al., 2010] Herbstman, J. F., et Hunt, A. J. (2010). **High-aspect ratio nanochannel formation by single femtosecond laser pulses**. *Opt. Express*, 18(16):16840–16848.

[Hine et al., 2016] Hine, G. A., Goers, A. J., Feder, L., Elle, J. A., Yoon, S. J., et Milchberg, H. M. (2016). **Generation of axially modulated plasma waveguides using a spatial light modulator**. *Journal of Biomedical Optics*, 41(15):3427–3430.

[Iwasaki et al., 2003] Iwasaki, A., Aközbek, N., Ferland, B., Luo, Q., Roy, G., Bowden, C., et Chin, S. (2003). **A lidar technique to measure the filament length generated by a high-peak power femtosecond laser pulse in air**. *Applied Physics B*, 76(3):231–236.

[Jarutis et al., 2000] Jarutis, V., Paškauskas, R., et Stabinis, A. (2000). **Focusing of Laguerre–Gaussian beams by axicon**. *Optics Communications*, 184(1):105 – 112.

[Johannisson et al., 2003] Johannisson, P., Anderson, D., Lisak, M., et Marklund, M. (2003). **Nonlinear besel beams**. *Opt. Commun.*, 222:107–115.

[Jui et al., 2013] Jui, S. K., Kamaraj, A. B., et Sundaram, M. M. (2013). **High aspect ratio micromachining of glass by electrochemical discharge machining (ecdm)**. *Journal of Manufacturing Processes*, 15(4):460 – 466.

[Kim et al., 2009] Kim, J. K., Kim, J., Jung, Y., Ha, W., S.Jeong, Y., Lee, S., Tünnermann, A., et Oh, K. (2009). **Compact all-fiber bessel beam generator based on hollow optical fiber combined with a hybrid polymer fiber lens**. *Opt. Lett.*, 34(19):2973–2975.

[Kirk et al., 1971] Kirk, J. P., et Jones, A. L. (1971). **Phase-only complex-valued spatial filter**$*$. *J. Opt. Soc. Am.*, 61(8):1023–1028.

[Klewitz et al., 1998] Klewitz, S., Sogomonian, S., Woerner, M., et Herminghaus, S. (1998). **Stimulated Raman scattering of femtosecond Bessel pulses**. *Opt. Commun.*, 154:186–190.

[Lambert et al., 2016] Lambert, A., Atchison, D., et M.Suheimat (2016). **Improvements to phakometry through use of Bessel beams**. In *Imaging and Applied Optics 2016*, page AOM3C.5. Optical Society of America.

[Lee et al., 2008] Lee, K. S., et Rolland, J. P. (2008). **Bessel beam spectral-domain high-resolution optical coherence tomography with micro-optic axicon providing extended focusing range**. *Opt. Lett.*, 33(15):1696–1698.

[Lei et al., 2008] Lei, M., et Yao, B. (2008). **Multifunctional darkfield microscopy using an axicon**. *Journal of Biomedical Optics*, 13(044024).

[Li et al., 2014] Li, L., Lee, W. M., Xie, X., Krolikowski, W., Rode, A. V., et Zhou, J. (2014). **Shaping self-imaging bottle beams with modified quasi-Bessel beams**. *Opt. Lett.*, 39(8):2278–2281.

[Lloyd et al., 2003] Lloyd, J., Wang, K., Barkan, A., et Mittleman, D. M. (2003). **Characterization of apparent superluminal effects in the focus of an axicon lens using terahertz time-domain spectroscopy**. *Appl. Phys. Lett.*, 219:289–294.

[McGloin et al., 2005] McGloin, D., et Dholakia, K. (2005). **Bessel beams: Diffraction in a new light**. *Contemporary Physics*, 46(1):15–28.

[McLeod, 1954] McLeod, J. H. (1954). **The axicon: A new type of optical element**. *J. Opt. Soc. Am.*, 44(8):592–597.

[McLeod, 1960] McLeod, J. H. (1960). **Axicons and their uses**. *J. Opt. Soc. Am.*, 50(2):166–169.

[Mendoza-Yero et al., 2014] Mendoza-Yero, O., Mínguez-Vega, G., et Lancis, J. (2014). **Encoding complex fields by using a phase-only optical element**. *Opt. Lett.*, 39(7):1740–1743.

[Mitra et al., 2015] Mitra, S., Chanal, M., Clady, R., Mouskeftaras, A., et Grojo, D. (2015). **Millijoule femtosecond micro-Bessel beams for ultra-high aspect ratio machining**. *Appl. Opt.*, 54(24):7358–7365.

[Mlejnek et al., 1998] Mlejnek, M., Wright, E. M., et Moloney, J. V. (1998). **Dynamic spatial replenishment of femtosecond pulses propagating in air**. *Opt. Lett.*, 23(5):382–384.

[Neto et al., 1996] Neto, L. G., Roberge, D., et Sheng, Y. (1996). **Full-range, continuous, complex modulation by the use of two coupled-mode liquid-crystal televisions**. *Appl. Opt.*, 35(23):4567–4576.

[N.Kim et al., 2017] N.Kim, Piao, Y., et Wu, H. (2017). **Holographic optical elements and application**. In Naydenova, I., editor, *Holographic Materials and Optical Systems*, chapter 5. InTech, Rijeka.

[Norfold et al., 2010] Norfold, A. W., et Grace, E. J. (2010). **New beat length for writing periodic structures using Bessel beams**. *Optics Communication*, 283:447–450.

[Ouadghiri-Idrissi et al., 2017] Ouadghiri-Idrissi, I., Dudley, J., et Courvoisier, F. (2017). **Controlling nonlinear instabilities in Bessel beams through longitudinal intensity shaping**. *Opt. Lett.*, 42:3785–3788.

[Ouadghiri-Idrissi et al., 2016] Ouadghiri-Idrissi, I., Giust, R., Froehly, L., M. Jacquot, L. F., Dudley, J., et Courvoisier, F. (2016). **Arbitrary shaping of on-axis amplitude of femtosecond Bessel beams with a single phase-only spatial light modulator**. *Opt. Express*, 24:11495–11504.

[Paterson et al., 1996] Paterson, C., et Smith, R. (1996). **Higher-order bessel waves produced by axicon-type computer-generated holograms**. *Opt. Commun.*, 124(1):121 – 130.

[Penano et al., 2005] Penano, J. R., Sprangle, P., Hafizi, B., Manheimer, W., et Zigler, A. (2005). **Transmission of intense femtosecond laser pulses in dielectrics**. *Phys. Rev. E*, 772(036412).

[Polesana et al., 2007] Polesana, P., Couairon, A., Faccio, D., Parola, A., Porras, M. A., Dubietis, A., Piskarskas, A., et Trapani, P. D. (2007). **Observation of conical waves in focusing, dispersive, and dissipative kerr media**. *Phys. Rev. Lett.*, 99(223902).

[Polesana et al., 2006] Polesana, P., Dubietis, A., Porras, M. A., Kučinskas, E., Faccio, D., Couairon, A., et Di Trapani, P. (2006). **Near-field dynamics of ultrashort pulsed Bessel beams in media with kerr nonlinearity**. *Phys. Rev. E*, 73:056612.

[Polesana et al., 2005] Polesana, P., Faccio, D., Trapani, P. D., Dubietis, A., Piskarskas, A., Couairon, A., et Porras, M. A. (2005). **High localization, focal depth and contrast by means of nonlinear Bessel beams**. *Opt. Express*, 13(16):6160–6167.

[Polesana et al., 2008] Polesana, P., Franco, M., Couairon, A., Faccio, D., et Trapani, P. D. (2008). **Filamentation in kerr media from pulsed Bessel beams**. *Phys. Rev. A*, 77(043814).

[Porras et al., 2004] Porras, M. A., Parola, A., Faccio, D., Dubietis, A., et Trapani, P. D. (2004). **Nonlinear unbalanced Bessel beams: Stationary conical waves supported by nonlinear losses**. *Phys. Rev. Lett.*, 93(153902).

[Porras et al., 2015] Porras, M. A., Ruiz-Jimenez, C., et Losada, J. C. (2015). **Underlying conservation and stability laws in nonlinear propagation of axicon-generated Bessel beams**. *Phys. Rev. A*, 92(063826).

[Pyragaite et al., 2006] Pyragaite, V., Regelskis, K., Smilgevicius, V., et Stabinis, A. (2006). **Self-action of Bessel light beams in medium with large nonlinearity**. *Opt. Commun.*, 257(1):139 – 145.

[Rethfeld, 2004] Rethfeld, B. (2004). **Unified model for the free-electron avalanche in laser-irradiated dielectrics**. *Phys. Rev. Lett.*, 92(18).

[Rodenburg et al., 2014] Rodenburg, B., Mirhosseini, M., na Loaiza, O. S. M., et Boyd, R. W. (2014). **Experimental generation of an optical field with arbitrary spatial coherence properties**. *J. Opt. Soc. Am. B*, 31(6):A51–A55.

[Saari et al., 1997] Saari, P., et Reivelt, K. (1997). **Evidence of x-shaped propagation-invariant localized light waves**. *Phys. Rev. Lett.*, 79(21):4135–4138.

[Shen, 1975] Shen, Y. R. (1975). **Self-focusing : Experimental**. *Prog. Quant. Electr.*, 4:1–34.

[Shen, 2009] Shen, Y. R. (2009). **Self-Focusing and Filaments of Light: Past and Present**, pages 3–19. Springer New York, New York, NY.

[Sochacki et al., 1993] Sochacki, J., Jaroszewicz, Z., Staroński, L. R., et Kołodziejczyk, A. (1993). **Annular-aperture logarithmic axicon**. *J. Opt. Soc. Am. A*, 10(8):1765–1768.

[Sogomonian et al., 2000] Sogomonian, S., Barille, R., et Rivoire, G. (2000). **Spatial distortions of a Bessel beam in a Kerr type medium**. *SPIE Proc.*, 4060:70–77.

[Steinvurzel et al., 2011] Steinvurzel, P., Tantiwanichapan, K., Goto, M., et Ramachandran, S. (2011). **Fiber-based Bessel beams with controllable diffraction-resistant distance**. *Opt. Lett.*, 36(23):4671–4673.

[Stuart et al., 1996] Stuart, B. C., Feit, M. D., Herman, S., Rubenchik, A. M., Shore, B. W., et Perry, M. D. (1996). **Nanosecond-to-femtosecond laser-induced breakdown in dielectrics**. *Phys. Rev. B*, 53:1749–1761.

[Stuart et al., 1995] Stuart, B. C., Feit, M. D., Rubenchik, A. M., Shore, B. W., et Perry, M. D. (1995). **Laser-induced damage in dielectrics with nanosecond to subpicosecond pulses**. *Phys. Rev. Lett.*, 74:2248–2251.

[Sudrie et al., 2002] Sudrie, L., Couairon, A., Franco, M., Lamouroux, B., Prade, B., Tzortzakis, S., , et Mysyrowicz, A. (2002). **Femtosecond laser-induced damage and filamentary propagation in fused silica**. *Phys. Rev. Lett.*, 89(186601).

[Sun et al., 2005] Sun, Q., Jiang, H., Liu, Y., Wu, Z., Yang, H., et Gong, Q. (2005). **Measurement of the collision time of dense electronic plasma induced by a femtosecond laser in fused silica**. *Opt. Lett.*, 30(3):320–322.

[Tewari et al., 1996] Tewari, S. P., Huang, H., et Boyd, R. W. (1996). **Theory of third-harmonic generation using Bessel beams, and self-phase-matching**. *Phys. Rev. A*, 54:2314–2325.

[Tiwari et al., 2012] Tiwari, S. K., Mishra, S. R., Ram, S. P., et Rawat, H. S. (2012). **Generation of a Bessel beam of variable spot size**. *Appl. Opt.*, 51(17):3718–3725.

[Tricoles, 1987] Tricoles, G. (1987). **Computer generated holograms: an historical review**. *Appl. Opt.*, 26(20):4351–4360.

[Turunen et al., 1988] Turunen, J., Vasara, A., et Friberg, A. T. (1988). **Holographic generation of diffraction-free beams**. *Appl. Opt.*, 27(19):3959–3962.

[Tzortzakis et al., 2001] Tzortzakis, S., Sudrie, L., Franco, M., Prade, B., et Mysyrowicz, A. (2001). **Self-guided propagation of ultrashort ir laser pulses in fused silica**. *Phys. Rev. Lett.*, 87(213902).

[Vasara et al., 1989] Vasara, A., Turunen, J., et Friberg, A. T. (1989). **Realization of general nondiffracting beams with computer-generated holograms**. *J. Opt. Soc. Am. A*, 6(11):1748–1754.

[Čižmár et al., 2009] Čižmár, T., et Dholakia, K. (2009). **Tunable Bessel light modes: engineering the axial propagation**. *Opt. Express*, 17(18):15558–15570.

[Čižmár et al., 2008] Čižmár, T., Kollárová, V., Tsampoula, X., Gunn-Moore, F., Sibbett, W., Bouchal, Z., et Dholakia, K. (2008). **Generation of multiple Bessel beams for a biophotonics workstation**. *Opt. Express*, 16(18):14024–14035.

[Vieira et al., 2015] Vieira, T. A., Gesualdi, M. R. R., Zamboni-Rached, M., et Recami, E. (2015). **Production of dynamic frozen waves: controlling shape, location (and speed) of diffraction-resistant beams**. *Opt. Lett.*, 40(24):5834–5837.

[Vieira et al., 2014] Vieira, T. A., Zamboni-Rached, M., et Gesualdi, M. R. R. (2014). **Modeling the spatial shape of nondiffracting beams: Experimental generation of frozen waves via holographic method**. *Optics Communications*, 315:374 – 380.

[Vogel et al., 2005] Vogel, A., Noack, J., Hüttman, G., et Paltauf, G. (2005). **Mechanisms of femtosecond laser nanosurgery of cells and tissues**. *Applied Physics B*, 81(8):1015–1047.

[White et al., 2008] White, Y. V., Li, X., Sikorski, Z., Davis, L. M., et Hofmeister, W. (2008). **Single-pulse ultrafast-laser machining of high aspect nano-holes at the surface of SiO2**. *Opt. Express*, 16(19):14411–14420.

[Wu et al., 2010] Wu, B., Kumar, A., et Pamarthy, S. (2010). **High aspect ratio silicon etch: A review**. *Journal of Applied Physics*, 108(5):051101.

[Xie et al., 2016] Xie, C., Giust, R., Zhang, J., Jukna, V., Meyer, R., Furfaro, L., Jacquot, M., Froehly, L., Dudley, J. M., Couairon, A., et Courvoisier, F. (2016). **Enhanced absorption and plasmon excitation in the bulk of fused silica with femtosecond**

bessel beams. In *Conference on Lasers and Electro-Optics*, page STh3Q.2. Optical Society of America.

[Xie et al., 2015] Xie, C., Jukna, V., Milian, C., Giust, R., Ouadghiri-Idrissi, I., Itina, T., Dudley, J. M., Couairon, A., et Courvoisier, F. (2015). **tubular filamentation for laser material processing**. *scientific reports*, 5(8914).

[Zamboni-Rached, 2004] Zamboni-Rached, M. (2004). **Stationary optical wave fields with arbitrary longitudinal shape by superposing equal frequency Bessel beams: Frozen waves**. *Opt. Express*, 12(17):4001–4006.

[Zamboni-Rached et al., 2005] Zamboni-Rached, M., Recami, E., et Hernández-Figueroa, H. E. (2005). **Theory of "frozen waves": modeling the shape of stationary wave fields**. *J. Opt. Soc. Am. A*, 22(11):2465–2475.

[Zhang et al., 2014] Zhang, Q., Cheng, X. M., Chen, H. W., B. He, Z. Y. R., Zhang, Y., et Bai, J. T. (2014). **Diffraction-free, self-reconstructing Bessel beam generation using thermal nonlinear optical effect**. *Appl. Phys. Lett.*, 111(161103).

[Zhang et al., 2011] Zhang, Z., et Buma, T. (2011). **Terahertz imaging in dielectric media with quasi-Bessel beams**. *SPIE Proc.*, 7938(7938-8).

Document generated with LaTeX and:
the LaTeX style for PhD Thesis created by S. Galland — http://www.multiagent.fr/ThesisStyle
the tex-upmethodology package suite — http://www.arakhne.org/tex-upmethodology/